Equal Channel Angular Pressing (ECAP) of AA6082: Mechanical Properties, Texture and Microstructural Development

by

Jens Christofer Werenskiold

A thesis submitted to
The Norwegian University of Science and Technology (NTNU)
in partial fulfilment of the requirements for the degree of

Doktor Ingeniør

Trondheim
Oktober 2004

NTNU
Norwegian University of
Science and Technology
Doctoral theses
for the degree of Doktor Ingeniør
Faculty of Natural Science
and Technology
Department of Materials Technology

IMT-report 2004:63.

ISBN 82-471-6481-7 (electronic)

ISBN 82-471-6482-5 (printed)

I. PREFACE

This work has been carried out at the Norwegian University of Science and Technology, (NTNU), Faculty of Natural Science and Technology, Department of Materials Technology. The research was carried out as part of the COMPFORM project and funded by the Norwegian Research Council and Hydro Aluminium AS.

This work has given me the opportunity to work in a new field of materials technology at NTNU and has been very educating. Hopefully, the initiation of this work will result in new insight in the field of severe plastic deformation (SPD) in coming years.

The thesis consist of a general introduction to equal channel angular pressing (ECAP), aluminium alloys and deformation mechanisms, followed by a detailed strain analysis of ECAP'ed materials, mechanical properties and finally a study of the microstructural and textural development resulting from equal channel angular pressing.

The main results presented in this thesis have been published (chapter 5), or are in the process of being published (chapter 6 and 7), in international journals and conference proceedings.

II. ABSTRACT

This thesis deals with the concept of ECAP applied to a commercial Al-Mg-Si alloy (AA6082.50). A detailed analysis of the strains introduced by ECAP in a single passage through the die has been made, based on direct measurements on partially pressed samples.

Further, the mechanical properties of ECAP'ed samples have been investigated. The effect of initial material temper and post-ECAP artificial aging was investigated in addition to the effect of strain accumulation and processing route.

Finally, a detailed study of the textural and microstructural development was made. The continuous evolution of texture and microstructure was followed through the ECAP deformation zone up to an accumulated strain of 2 (2 passes) by route A, and linked to strain measurements from the same zone.

Strain measurements on sectioned samples have validated the plane strain assumption for ECAP. The shear angle has been measured and some typical features of ECAP have been corroborated, i.e. friction and material temper affect the strain distribution, the strain homogeneity and the work-piece corner angle, friction being the most significant here. Also, new conclusions have been drawn. The analysis of material element deformation histories along path lines reveals that ECAP can be interpreted as the combination of shearing and stretching (i.e. tension and/or compression). Furthermore, the final shear strain angle obtained in ECAP appears to be friction and material temper independent in the zone of homogeneous deformation.

The 6082 alloy has been successfully processed by ECAP at room temperature to strains $\varepsilon=6$ to $\varepsilon=8$. The alloy has been pressed in the solutionized, T4, homogenized and soft annealed states. The highest tensile

strength was obtained from the solutionized material, followed by T4, homogenized and soft annealed. This behaviour is linked to the solid solution content prior to ECAP and the potential for dynamic precipitation during ECAP processing.

The tensile elongation to failure drops to a constant level between 4% and 9% after ECAP and is highest for the soft annealed and lowest for the solutionized material. The ductility in the solutionized material can, however, recover to ~18% elongation to failure (i.e. an increase by a factor 2-3) by low temperature heat treatment with only a small drop in tensile strength.

Soft annealed and ECAP'ed material has been compared to cold rolling to similar strains. The tensile strength response to accumulated strain is similar, but the ductility and post uniform deformation is different. However, the ECAP'ed material can be processed to higher strains and, thus, achieving higher strength.

The tensile yield strength behaviour of the homogenized and ECAP'ed material can be described by a simple relation to the grain size and the fraction high and low angle boundaries.

The typical texture components related to ECAP of aluminium, pressed by route A, have been identified. The typical ECAP texture starts to develop already at ~25% strain and increases in intensity during the first pass. In the second pass, two of the stable texture components continue to increase in intensity, while the other texture components decrease.

The microstructural development during the first pass is dominated by deformation banding leading to grain-subdivision. The average linear intercept distance (grain size) is reduced from ~80μm to ~4μm for high angle boundaries and from ~10μm to ~0.7μm for low angle boundaries. During the second pass, the linear intercept distance is further reduced to ~1.8μm for high angle and ~0.3μm for low angle boundaries.

Deformation twins are observed during the second pass and are believed to play an important role in severe plastic deformation when the grains reach the sub-micron or nano-metre scale.

The deformation banding have been explained in terms of the low energy dislocation structure (LEDS) theory, and has been shown to be an important mechanism in the early stages of grain subdivision, and is further believed to be the main source of high angle grain boundary formation by grain subdivision down to a grain size of approximately ~0.6μm, when other deformation mechanisms may be energetically more favourable.

III. ACNOWLEDGEMENTS AND CONTRIBUTIONS

This research was carried out as part of the COMPFORM project and funded by the Norwegian Research Council and Hydro Aluminium AS.

I would like to thank my main supervisor, Prof. Hans Jørgen Roven for his great contributions and stimulating discussions and for motivating me during this work.

I would like to give a special to thank Dr. Stéphane Dumolin for his contribution to chapter 5: Strain analysis in ECAP. His involvement in strain measurements and aid in mathematical and continuum mechanical calculations is greatly acknowledged.

I would also like to thank Mr. Hans Bjerkaas for fruitful discussions regarding EBSD analysis, Mr. John Rasmus Leinum for help with XRD texture measurements, Mr. Håkon Atle Nesbø for his contributions to chapter 6 in performing the post ECAP heat treatments and mechanical testing, and Mr. Simen Olsen for sharing my office and lots of interesting discussions the last years.

Finally, I would like to thank my one and only Laila Beate Kjønstad for her patience, encourage and support over the past years.

IV. CONTENTS

I. Preface ... 3
II. Abstract ... 5
III. Acnowledgements and contributions ... 9
IV. Contents ... 11

1. Introduction ... 14

2. Theoretical background ... 16
2.1 General introduction to Equal Channel Angular Pressing ... 16
2.1.1 Introduction ... 16
2.1.2 The shearing characteristics associated with ECAP ... 17
2.1.3 Grain refinement by ECAP ... 23
2.1.4 Estimation of the strain in ECA Pressing ... 26
2.1.5 Mechanical properties at room temperature ... 28
2.1.6 High Strain Rate Superplasticity ... 29
2.1.7 Textures by ECAP ... 32
2.2 Aluminium alloys and deformation mechanisms ... 34
2.2.1 Non-heat treatable aluminium alloys ... 34
2.2.2 Heat-treatable aluminium alloys ... 35
2.2.3 Deformation structures ... 36
2.2.3.1 Dislocation slip and stored energy ... 36
2.2.4 Grain refinement mechanisms ... 38
2.2.4.1 Grain refinement by subdivision ... 38
2.2.5 Alloying effects on subdivision ... 45
2.2.5.1 Solute atoms ... 45
2.2.5.2 Non-deformable particles ... 46
2.2.5.3 Dislocation density in the grain interior ... 47
2.2.6 Band formation in plastic deformation ... 48
2.2.6.1 Bands of secondary glide ... 49
2.2.6.2 Kink bands ... 49
2.2.6.3 Stria bands ... 50
2.2.6.4 Regular deformation bands ... 50
2.2.6.5 Transition bands ... 52
2.2.6.6 Hybrid / regular transition bands ... 52
2.2.6.7 Shear bands ... 52
2.2.7 Deformation banding in relation to the LEDS theory ... 55
2.2.8 Theory of co-incidence site lattice boundaries ... 61
2.3 Basic polycrystal plasticity ... 63
2.3.1 The Sachs model ... 64
2.3.2 The Taylor model ... 65

3 ECAP die design 69
3.1 The Piston 69
3.2 The control system 69
3.3 The Die 70
3.3.1 Version 1.1 70
3.3.2 Version 1.2 71

4 Experimental procedures 75
4.1 Strain analysis (referring to chapter 5) 75
4.2 Mechanical properties (referring to chapter 6) 77
4.3 Microstructure and texture (referring to chapter 7) 78

5 Strain Analysis in ECAP 80
5.1 Introduction 80
5.2 Theoretical analysis 80
5.2.1 Strain Analysis 82
5.2.2 Flow and Deformation History Analysis 86
5.3 Conclusion 90

6 Mechanical properties in AA6082 subjected to ECAP 91
6.1 Introduction 91
6.2 Results 93
6.2.1 The effect of ECAP on different initial material states 93
6.2.2 The effect of processing route and tensile test strain rate 99
6.2.3 Comparison to conventional T6 heat treated non-ECAP'ed material 100
6.2.4 Comparison with cold rolling 100
6.2.5 The effect of post-ECAP artificial aging 101
6.3 Discussion 103
6.3.1 Influence of SPD strain accumulation 103
6.3.2 Influence of initial temper 105
6.3.3 Strain path and cold rolling 108
6.3.4 Further comments on precipitation 110
6.3.5 The grain size effect: Homogenized, route A 114
6.4 Conclusions 118

7 Microstructure and texture development in the deformation zone 120
7.1 Introduction 120
7.2 Experimental 120
7.3 Strain measurements in the deformation zone 124
7.4 Texture development 129
7.4.1 Introduction 129
7.4.2 Identification of the ideal texture components 130
7.4.3 Texture development through the deformation zone in the 1st pass 136
7.4.4 Texture development through the deformation zone in the 2nd pass 142
7.5 Microstructural development 150

7.5.1 Introduction to the Aligned Cell Structure (ACS) 152
7.5.2 Introduction to Deformation Bands (DB) 154
7.6 Microstructural observations through the deformation zone: First pass 156
7.6.1 25% strain 156
7.6.2 50% strain 165
7.6.3 60% strain 172
7.6.4 70% strain 182
7.6.5 80% strain 187
7.6.6 100% strain (full passage through the deformation zone) 195
7.7 Microstructural observations through the deformation zone: Second pass 197
7.7.1 10% strain in 2nd pass 197
7.7.2 30% strain in 2nd pass 199
7.7.3 50% strain in 2nd pass 204
7.7.4 75% strain in 2nd pass 211
7.7.5 95% to 105% strain in 2nd pass 215
7.8 Deformation twins 222
7.9 Discussion 226
7.9.1 Texture evolution 226
7.9.2 Microstructural development 230
7.9.3 Deformation banding in ECAP explained by the LEDS theory 241
7.10 Conclusions 249

8 General conclusion 250

9 References 253

1. INTRODUCTION

Materials processing by severe plastic deformation (SPD) have received vast focus in the research community the last five to ten years due to the unique physical and mechanical properties obtainable by SPD processing.

The process of SPD is based on intense plastic deformation of a work-piece, resulting in alteration of the microstructure and texture, in principal reduction of the grain size to the sub-micron or the nano-metre scale.

The most common process of SPD is the equal channel angular pressing (ECAP), which involves pressing a billet through a die consisting of two channels of equal cross sections, intersecting at an angle, typically 90°. The process of ECAP allows us to introduce very large plastic deformations to a work-piece without altering the overall geometry of the work-piece.

In the present thesis, the ECAP process has been applied to a commercial 6xxx series aluminium alloy. The deformation characteristics have been investigated by direct strain measurements on ECAP'ed samples. Further, the mechanical properties have been investigated for a series if processing parameters and finally, a detailed study of the texture development and deformation mechanisms have been made.

In the present work, the main focus has been to gain a better understanding of the deformation mechanisms operating in the ECAP process, which leads to the observed intense grain refinement. In this process, a vast amount of EBSD measurements was carried out, including two processing routes (route A and Bc) and eight accumulated strain levels, corresponding to eight ECAP passes.

Due to the enormous amount of collected data, it proved impossible to collect all results and observations in this thesis; therefore, the main focus was set on the early stages of grain subdivision, i.e. the first two ECAP

passes by route A. However, some results obtained at higher strains, i.e. higher number of passes, are included, such as grain size and misorientation distributions. The most important results on the microstructural development at higher strains will be published in international journals after the submission of the present thesis.

2. THEORETICAL BACKGROUND

2.1 General introduction to Equal Channel Angular Pressing

2.1.1 Introduction

The ECAP process was first developed by V.M. Segal in the former USSR in 1977 [1]. This is a process employed to realize a "near ideal" deformation to the material. In 1950 A. Nadai realized that pure shear is the "ideal" deformation for extrusion and drawing [2]. With the ECAP method one can have a "near ideal" deformation by simple shear in the system [3]. The general principle for the method is shown in Figure 2.1. The tool is a block with two intersecting channels of identical cross-section. A well lubricated billet of the same cross-section is placed into one of the channels, and a punch then presses it into the second channel. Under these conditions the billet will move as a rigid body, and deformation is achieved ideally by simple shear in a thin layer at the crossing plane of the channels. When the punch is finished it is retreated and the billet has been uniformly deformed, except for a small zone in the lower part of the sample and in the end regions.

The die geometry is defined by the cross section area and the two angles Φ and Ψ, the angle of intersection between the two channels, and the arc of curvature at the outer point of intersection respectively. It is possible to calculate, from the two angles, the shear strain or the effective von Mises strain resulting from pressing through the die.

The advantage with the ECAP method is that it is possible to introduce severe plastic deformation (SPD) by repeated pressing of the billet without any significant change in the cross section. Altering the billet orientation after each press, thereby modifying the shear plane and shear direction,

makes it possible to control the microstructure and texture of the material, thus, altering the mechanical properties.

The principal of sample rotation was first noted by Segal [4] in 1995. The principal has been demonstrated in several recent experiments, i.e. [5-8].

It is now clear that the microstructural characteristics, and in particular the evolution of the microstructure during ECA pressing, depend upon the precise pressing conditions, and therefore upon the characteristics of the shearing introduced in each passage through the die. Furukawa et al. [6] were the first to analyze the shearing characteristics for several different pressing and rotation modes.

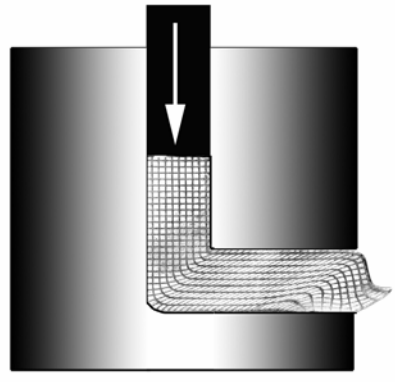

Figure 2.1: Principally sketch of ECA pressing.

2.1.2 The shearing characteristics associated with ECAP

There are several different processing routs for ECA pressing. They differ in the way the sample is rotated between each press. The most common are (I) not rotated, (II) rotated by +90° or ±90° between each consecutive pressing or (III) rotated +180° between pressings (Figure 2.2).

The shearing characteristics for these routes and in addition, two other processing routs have been analyzed by M. Furukawa et al. [6].

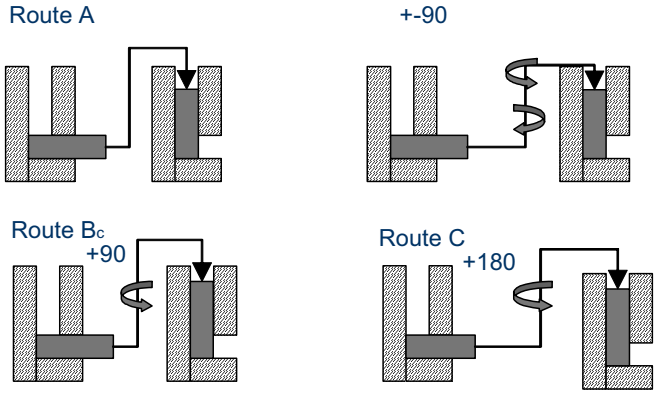

Figure 2.2: Different processing routes.

The analysis is conducted for standard conditions where Φ=90° and Ψ=0°. It has been shown in [9-13] that in this condition a potential difficulty arises, as revealed by finite element modelling, in filling the outer corner at the intersection of the two channels when friction is present. This analysis therefore, applies to an ideal frictionless condition, or more appropriate, to the central regions of the pressed sample where friction effects are small.

Schematic drawings of a cubic element contained within the test sample, on its passage through the die, is shown in Figure 2.3 to Figure 2.5, where the shaded plane at the lower left represents the theoretical shear plane and the planes X, Y and Z define three mutually orthogonal planes of sectioning that lie perpendicular to the longitudinal axis of the pressed sample and parallel either to the side faces or to the top face of the sample at the point of exit from the die, respectively.

It is apparent from Figure 2.3 that a single pressing through the die shears the cubic element into a rhombohedra shape. However, it is also apparent that the deformation occurring in subsequent pressings will depend upon the nature of any rotation of the sample.

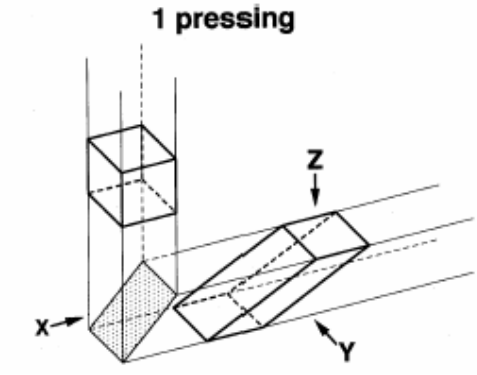

Figure 2.3: Schematic illustration of shearing in a single pressing through the die: *X, Y* and *Z* define three orthogonal planes of observations [6]**.**

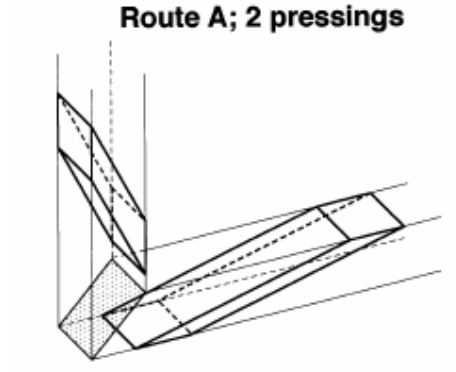

Figure 2.4: Schematic illustration of shearing after two pressings with no rotation (route A) [6]**.**

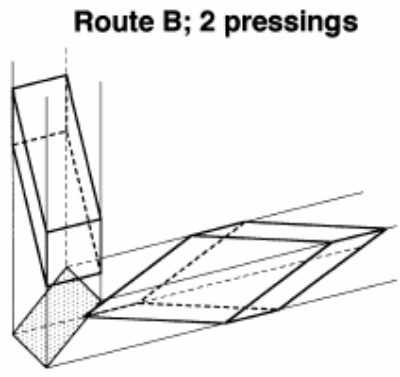

Figure 2.5: Schematic illustration of shearing after two pressings with rotation of 90° (route B) [6]**.**

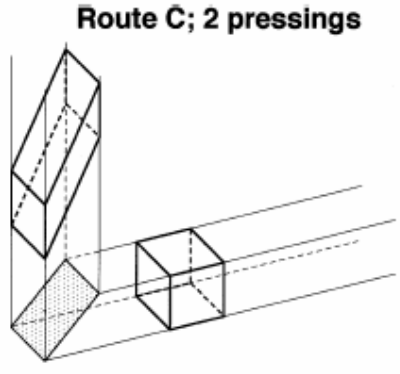

Figure 2.6 Schematic illustration of shearing after two pressings with rotation of 180° (route C) [6]**.**

The effect of the second passage through the die is shown in Figure 2.4 to Figure 2.6 for the situation where the sample is either non-rotated (route A), rotated 90° (route B) or rotated 180° (route C), using the notation by Segal [4] and Ferrasse et al. [8]. It is clear from the figures that route A serves to markedly increase in distortion of the rhombohedra, route B increases the distortion in the *X* and *Z* planes and route C restores the cubic element so that strain has been introduced to the element without any distortion of the bulk sample.

To make it more clear, Table 2.1 shows the definition of the 6 different processing routes. It is important to note the difference between B_A and B_C and the combinations B_A-A and B_C-A.

What happens to the cubic element shown in Figure 2.3 during subsequent pressings is illustrated schematically in Table 2.2, where the cubic element is viewed in planes of sectioning cut in the three orthogonal *X, Y* and *Z* planes.

Close inspection of Table 2.2 leads to several important conclusions concerning the effect of using these different processing routes.

Firstly, as noted earlier, route B_A (0°–90°–0°–90°) has shearing characteristics similar to route A, whereas route B_C (0°–90°–180°–270°) has characteristics similar to route C.

Secondly, route A exhibits continuous changes in the *X* and *Y* planes but no deformation of the cubic element in the *Z* plane, and route B_A exhibits continuous changes in all three planes. By contrast, the cubic element is restored after 4*n* passes in route B_C and 2*n* passes in route C, where *n* is an integer. In addition, there is no deformation in the *Z* plane when using route C. Thirdly, it is possible to make use of these tabulated characteristics to reach conclusions concerning the optimum processing route. Thus, routes B_C and C appear preferable to routes B_A and A because of the ultimate restoration of the cubic element, and route B_C appears preferable to route C because of the lack of deformation in the Z plane in route C. By contrast, the processing route B_A–A is clearly not attractive because of the increased distortion with further pressings in each of the three orthogonal planes, but route B_C-A, combining elements or routes B_C and A, may represent an optimum pressing condition because it combines both the introduction of high shear strains in each plane and their consequent recovery to restore the cubic element after a total of 8*n* pressings.

Table 2.1: Definition of the rotations in the different pressing routes [6]**.**

Route	Number of pressings						
	2	3	4	5	6	7	8
A	0°	0°	0°	0°	0°	0°	0°
B_A	90° ↖	90° ↘	90° ↖	90° ↘	90° ↖	90° ↘	90° ↖
B_C	90° ↖	90° ↖	90° ↖	90° ↖	90° ↖	90° ↖	90° ↖
C	180°	180°	180°	180°	180°	180°	180°
B_A-A	90° ↖	0°	90° ↘	0°	90° ↖	0°	90° ↘
B_C-A	90° ↖	0°	90° ↖	0°	90° ↖	0°	90° ↖

Table 2.2: Schematics of the deformation of a unit element after *n* passages through the die [6]**.**

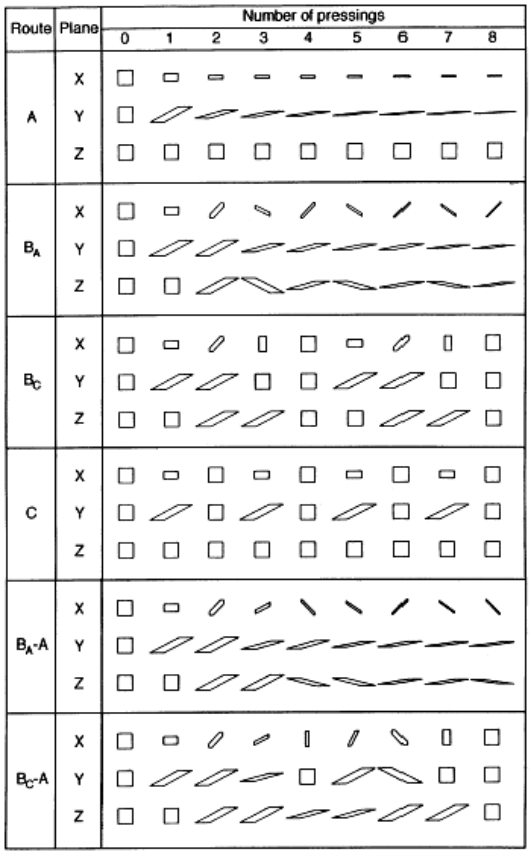

2.1.3 Grain refinement by ECAP

Iwahashi et al. seem to be the first to make a detailed systematic research on the microstructural evolution during ECAP in 1997 [7]. Earlier reports had described the use of ECAP and the subsequent stability of the ultra fine grains produced in Al-Mg [14-17] and Al-Mg-Li-Zr alloys [18]. Iwahashi et al. conducted detailed experiments on pure (99.99%) aluminium in order to investigate the development end evolution of the ultra fine grains during ECAP for the routes A and C.

It was shown [7] that pure Al with an initial grain size of ~1.0 mm could obtain grain structures at the micrometer level (~4 μm) after a single pass through the die with an introduced effective strain of ~1.05. The microstructure after the first press consists of bands of elongated sub-grains. There is a rapid evolution with further pressings into an array of equiaxed grains.

The initial massive reduction in grain size is achieved in the first passage through the die because the original grains break up into bands of sub grains. These sub-boundaries subsequently evolve with further pressings into high angle grain boundaries, giving ultimately a reasonable equiaxed microstructure.

When samples of pure Al, with a coarse grain size, are cold rolled to reductions of ~15% to 30% ,the grains become divided into bands of elongated sub grains and the average size of these sub grains is typically of the order of ~1 - 2 μm [19-21]. These sub grain bands appear to be the precursor of the well-defined and regular band structure, which is visible also in ECA pressed samples, after a single passage through the die to a strain of ~1.05 (Figure 2.7).

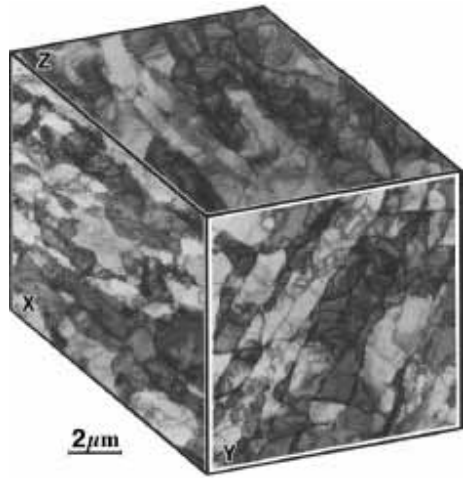

Figure 2.7: Grain structure after 1 pass [5] **(X, Y and Z denote the plane normals, coordinate system is the same as in Figure 2.3).**

In order to understand the nature of grain refinement at the high strains associated with ECA pressing, and in particular the influence of the processing route, it is necessary to examine the shearing patterns which develop within each sample during repetitive passages through the die.

These patterns are illustrated schematically, in the form of the dominant directions of shearing, for routes A, B and C in Figure 2.8. It is apparent from Figure 2.8 that the shearing patterns are significantly different between the three separate routes.

In route Bc, where the sub grain boundaries evolve most rapidly into high angle grain boundaries, the two shearing directions lie on planes which intersect at 120°. As a result of this duality in the shearing directions, sub grain bands are developed on repetitive pressings along two separate and intersecting sets of planes (Figure 2.9) and this leads rapidly to an evolution in the boundary structure into a reasonably equiaxed array of high angle boundaries. Thus, it is reasonable to conclude that route B_C is the preferable procedure for use in ECAP experiments. By contrast, route A has two shearing planes intersecting at 90° and route C repeats shearing on the same

plane. It is demonstrated in Figure 2.10, and also confirmed in an earlier investigation [7], that route C is preferable to route A in developing an array of high angle boundaries. Although the reason for this observation has not been established in detail, it probably arises because route C permits the shear to build continuously on a single set of planes whereas in route A the extent of shearing is divided equally between two sets of orthogonal planes.

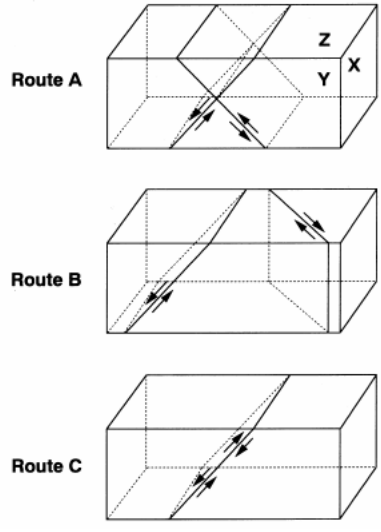

Figure 2.8: Shearing patterns associated with ECA pressing through routes A, B and C, respectively [5].

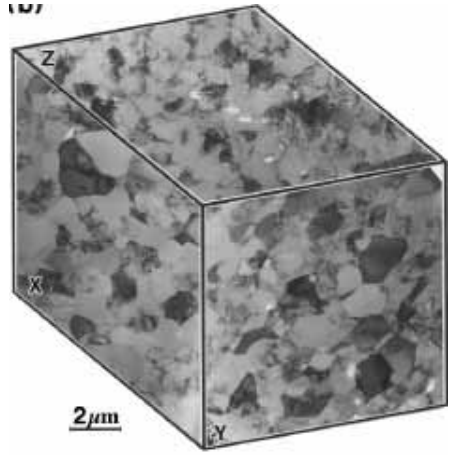

Figure 2.9: Microstructure after 3 passes with route B_C [5].

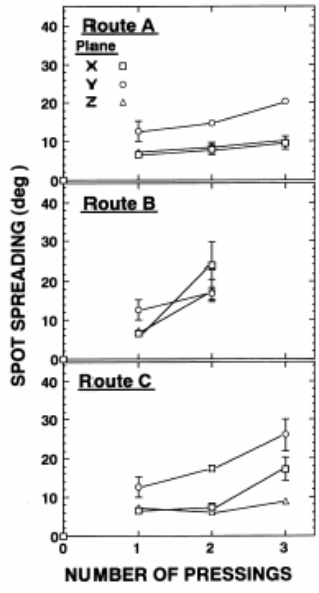

Figure 2.10: Spot spreading from selected area electron diffraction (SAED) patterns describing the angle of misorientation between the grains. Route B has the most equiaxed grain structure [5]**.**

2.1.4 Estimation of the strain in ECA Pressing

The shear strain γ for simple shear is defined as in Figure 2.11b), $\gamma = a/h$. Simple shear involves a shape change produced by displacement along a single set of parallel planes. The shear strain introduced by the ECA pressing will first be derived for the case of simple shear, assuming a square cut die and neglecting the friction effects.

Figure 2.11a) shows a cubic element *abcd* along the centreline in the ECAP die. The die is defined by the angles Φ and Ψ. If we follow the element through the die, we will end up with the orthogonal element *a'b'c'd'*, deformed by shear during the passage through the die. Following the notation in Figure 2.11, it follows that the shear strain, γ, is given by

$$\gamma = \frac{a'u}{d'u} = \frac{rc'+as}{ad} = \frac{\psi \cdot ad \cdot \cos ec\left(\frac{\phi}{2}+\frac{\psi}{2}\right) + ad \cdot \cot\left(\frac{\phi}{2}+\frac{\psi}{2}\right) + ad \cdot \cot\left(\frac{\phi}{2}+\frac{\psi}{2}\right)}{ad}$$

Equation 2.1

which is reduced to

$$\gamma = \psi \cos ec\left(\frac{\phi}{2}+\frac{\psi}{2}\right) + 2\cot\left(\frac{\phi}{2}+\frac{\psi}{2}\right)$$

Equation 2.2

The resulting deformation with the directions of the principal strains is shown in Figure 2.12.

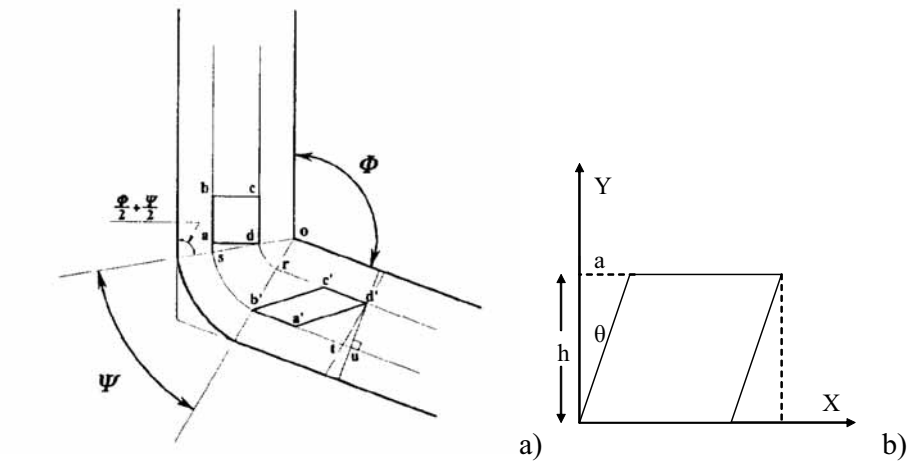

Figure 2.11: Schematic drawings of a deforming element moving through the ECAP die

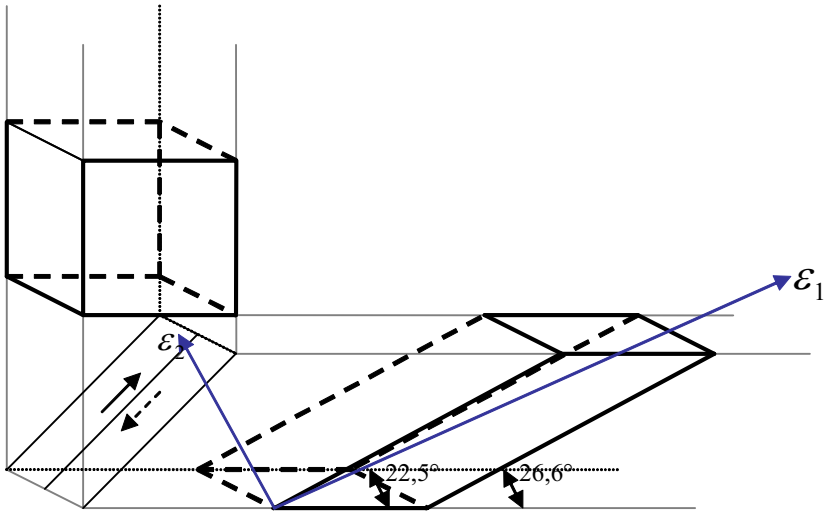

Figure 2.12: Resulting deformation of a cubic element moved through the ECAP die. ε_1 and ε_2 are the directions of the principal strains.

2.1.5 Mechanical properties at room temperature

The mechanical properties of ECAP processed aluminium alloys normally show a significant increase in yield strength and ultimate tensile strength while the tensile ductility at room temperature is decreased after the first pass and stays relatively unchanged by increasing number of passes.

Numerous works have been published on the mechanical properties of aluminium alloys after ECAP. Non-heat treatable alloys such as the Al-Mg [22-34], Al-Mn [35], and Al-Mn-Mg [36] alloys have shown improvements in strength and some also in ductility after ECAP.

Heat treatable alloys such as Al-Cu-Zr [37], Al-Mg-Si [38-41], Al-Cu-Mg-Mn [42], Al-Mn-Si [43],Al-Zn-Mg [35, 44-46], Al-Li [18, 47-49] and Al-Mg-Sc [50-52] have been reported to achieve positive developments after ECAP. A majority of these studies show that tensile ductility is decreased after multiple ECAP presses, and flow stress is generally increasing with ECAP strain accumulation.

There are several parameters determining the mechanical properties of ECA processed aluminium. Except from the alloy composition, the processing conditions are vital. Recent experiments on 6xxx alloys show that the initial material temper is the most important, following the number of ECAP passes, the pressing temperature and post ECAP heat treatment.

Heat treatable alloys, such as the 6082 treated in this thesis, can yield a significant increase in strength *and* ductility compared to conventional T6 heat treatment by using the proper processing parameters. The highest strength is reached by ECA processing directly from solid solution heat treatment at sub-ambient or cryogenic temperatures followed by post ECAP heat treatment at low temperatures, typically 80-120°C [38, 42]. The low temperature ECA pressing hinders or slows down deformation induced precipitation, thus keeping as much alloying elements in solid solution as possible. A low temperature post ECAP heat treatment will then lead to a combined effect of releasing residual stresses, which increases the ductility and slightly lowering the strength, and secondly, precipitation strengthening. A low heat treatment temperature is vital, as the precipitation kinetics is highly accelerated in the highly deformed material. At conventional heat treatment temperatures the deformed structure is unstable and recrystallization may occur before the precipitates starts to pin the structure. As an example, the 6082 alloy has typical UTS of ~340MPa and elongation to failure of about 11% in the T6 condition. After ECAP and low temperature heat treatment, this alloy reaches ~460MPa and ~16% elongation simultaneously.

2.1.6 High Strain Rate Superplasticity

High strain rate superplasticity (HSR SP) is defined as the ability to achieve high superplastic tensile elongations at strain rates faster than $10^{-2}s^{-1}$ [53]. It is now well established that the high tensile ductility associated with

superplastic flow occur at intermediate strain rates of the order of ~10^{-4} – 10^{-3} s^{-1}, in materials having small grain sizes lying typically in the range of ~2 – 10μm. In practice, these rates are so slow that superplastic forming operations will normally take up to 30 minutes, i.e. too slow for any high volume – low cost applications.

Langdon et al. have shown that since the strain rate in superplastic forming is inversely proportional to the square of the grain size, a decrease in grain size displaces the superplastic regime to faster strain rates [54]. The ECAP technology can produce grain sizes in the sub-micrometer range, thus, it should be feasible to use ECAP in order to fabricate materials which are capable of exhibiting superplasticity at high strain rates. It has been demonstrated by several recent reports [55-60] that high superplastic ductility can be achieved at strain rates >$10^{-2}s^{-1}$ in a range of aluminium based alloys processed by ECAP.

It has been shown that the choice of processing routes used during the ECA pressing is vital to the superplastic behaviour of the material [53, 56, 61-64], i.e. see Figure 2.13 and Figure 2.14 for a comparison of routes A, Bc and C. ECAP initially introduces an array of closely-spaced sub-grain bands, but this structure evolves with further straining into an array of ultra-fine equiaxed grains separated by boundaries having high angles of missorientation [5, 7]. The precise nature of the microstructure produced by ECAP is dependent upon the processing route. It has been suggested by several authors that processing route B_C with $\Phi = 90°$ is the most efficient in producing superplastic alloys [53, 65, 66].

Reports show that superplasticity has been obtained in several commercial alloys such as Al-Cu-Zr (AA2004) and Al-Mg-Li-Zr cast alloys [55], Al-Mg-Sc [56] and an Al-3Fe (AA2024) powder alloy. Komura et al. obtained an elongation of 2280% at 400°C with a strain rate of 10^{-2} for an Al-3Mg-0.2Sc alloy pressed 8 times by route B_C at RT [53]. In this case the

grain size was reduced from ~200μm to 0.2μm after 8 passes, i.e. a total strain equal to 8.

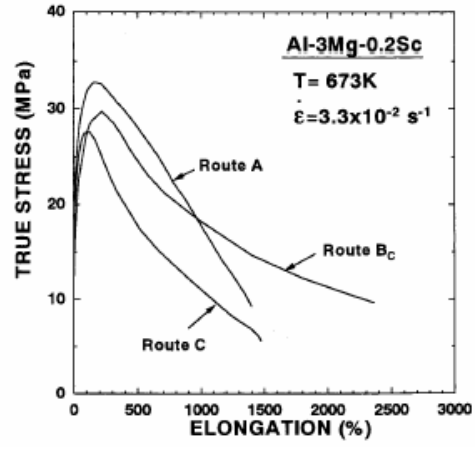

Figure 2.13: Superplasticity: True stress vs. elongation for samples pressed using routes A, B_C and C [53]**.**

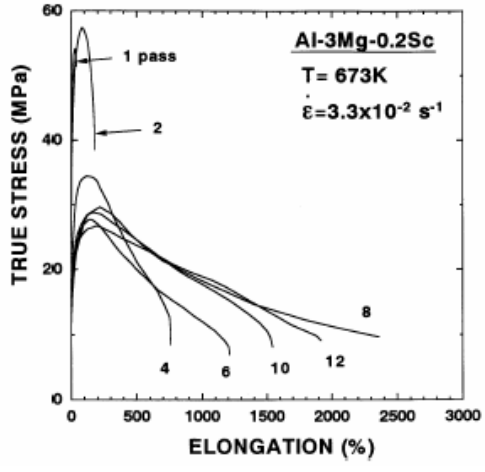

Figure 2.14: Superplasticity: True stress versus elongation for samples after ECAP using route B_C for one to 12 passes [53]**.**

The characteristics of the microstructure introduced by ECAP play an important role in determining the magnitude of the post processed elongations. High superplastic elongations are achieved through ECAP only

when the microstructure has evolved from the banded sub-grain structure introduced initially in ECAP at low strains to a homogenous array of uniform and equiaxed grains separated by high angle grain boundaries at high strains. These high angle grain boundaries are a prerequisite for superplasticity because flow occurs predominantly by grain boundary sliding.

2.1.7 Textures by ECAP

Much work has been made to understand the texture development in ECAP'ed materials, with the main emphasis on texture modelling. Maybe the most important experimental work is that of Tóth et al. [67] in identifying the stable texture components.

Published work on the textures generated during ECAP of Al and Cu have noted the presence of {100}<110> and {112}<110> components on the partial β-fibre. However, although the texture ideally is symmetric in the mirror plane of the die, the positions of maximum intensity have been reported to be rotated away from the "extrusion direction" by 10-20°, often referred to as the "tilts" of texture components from their ideal positions known in simple shear.

There have been several different explanations and disagreements on how the texture develops in regard to alignment to the shear zone and re-alignment of the texture components between successive ECAP passes.

There have however, to the present authors knowledge, not been made any detailed texture measurements through the deformation zone in order to continuously follow the texture development, and no serious attempts have been made to explain how the various texture components generates in the microstructure.

Lots of different texture simulations have been made by several authors. The earliest texture simulations used a hypothetical simplified flow field

and were applied to predict the texture evolution in ECAP with the Taylor polycrystal model in a 90°, sharp cornered die. The self-consistent (SC) model of polycrystal viscoplasticity has also been used to predict texture evolution in iron [68] with the discontinuous shear approach (shear occurs at the intersection of the ECAP channels, not gradually through a zone). More recently, the Taylor polycrystal plasticity model was incorporated into finite element calculations to predict the textures and hardening of aluminium [69]. Gholinia et al. [70] have studied the flow field experimentally and then used the Taylor polycrystal model to predict the texture evolution in an Al alloy. They have identified the "tilts" of texture components from their ideal positions known in simple shear. Beyerlein et al. [71] used the viscoplastic self-consistent polycrystal code in its full anisotropic formulation together with the discontinuous shear approach to predict the texture evolution in copper. They examined the effect of grain shape changes on texture evolution resulting from grain subdivision during ECAP. Tóth et al. [67] used a new flow field which uses an analytical flow function to significantly improve the accuracy of the texture predictions in copper.

The most important works on ECAP textures can be found in [67, 69-88].

2.2 Aluminium alloys and deformation mechanisms

2.2.1 Non-heat treatable aluminium alloys

Non-heat treatable aluminium alloys constitute a class of alloys that owe their strength mainly to elements in solid solution, but also to some types of particles. A heat-treatment of such an alloy will generally not produce any strengthening precipitates as in the heat treatable alloys (an exception is the dispersoids formed in Al-Mn alloys). The strength may in fact decrease during heat treatment due to the removal of solute atoms. The alloy systems belonging to this class are the AA1xxx system (commercially pure with small amounts of mainly Fe and Si), the AA3xxx system (as AA1xxx with manganese and magnesium additions), the AA5xxx system (as AA1xxx with magnesium addition) and the AA8xxx system (as AA1xxx, but with higher alloy additions).

The strength of these alloys depends strongly on the content of alloying elements. In Figure 2.15 the ultimate tensile strength of a number of commercial non-heat treatable alloys are shown as a function of the amount of alloying elements. An interesting observation is that the tensile strength is approximately linearly dependent on the total alloying addition in wt%, irrespective of element type, and follows the simple equation given in Figure 2.15. It is here distinguished between the O-temper, i.e. annealed condition, and the H18/H38 condition, i.e. cold rolled or cold rolled and stabilized of the same alloys. These curves indicate a large work hardening potential in these alloys. The dotted and the full lines illustrate the difference between the alloys where solution hardening is most important (AA5xxx) and where the particle hardening dominates (AA1xxx, AA8xxx). In the AA3xxx alloys the strength results from both Mn and Mg in solid solution and particles/dispersoids.

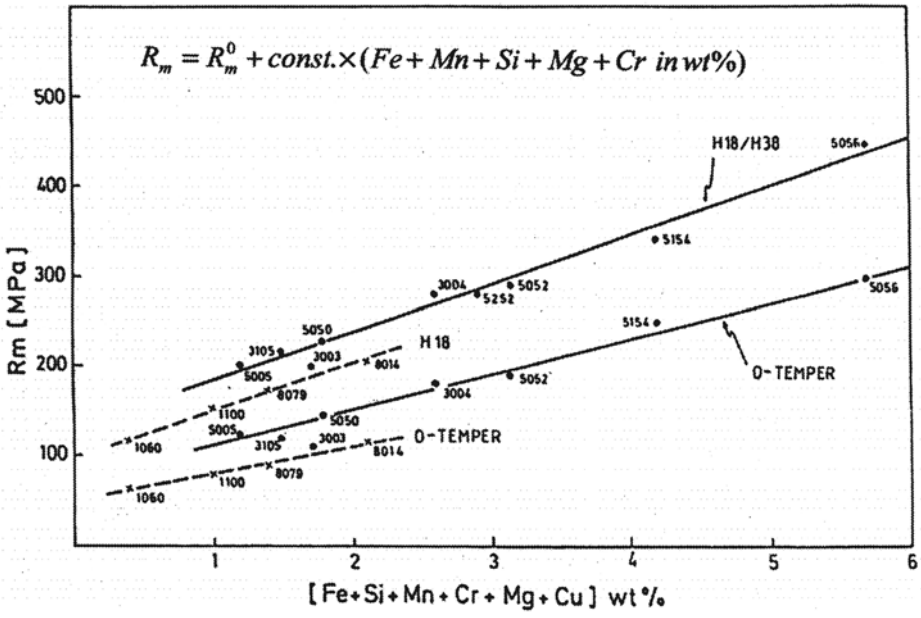

Figure 2.15: Ultimate tensile strength as a function of alloying additions for a wide range of commercial non-heat treatable aluminium alloys. Both O-temper and cold rolled conditions of the same alloys are plotted [89].

2.2.2 Heat-treatable aluminium alloys

The heat-treatable aluminium alloys get their strength mainly from precipitate particles, and collect the AA2xxx, AA6xxx and AA7xxx alloy systems. These alloys are first solution heat-treated, i.e. heated to the single-phase area of the phase diagram where alloying elements are more or less dissolved into solid solution. A rapid quench freezes the atoms in a supersaturated solid solution (ssss) from where the precipitation sequence starts. Here is an example from AA6xxx alloy showing the phase transformation sequence in this alloy:

AA6xxx: ssss → GP zones → β" → β'(Mg_2Si) → β(Mg_2Si)

Precipitation can occur at room temperature (natural ageing), but an artificial ageing treatment is normally used in order to achieve a more stabilized material with as high a strength as possible. Following the sequence from the left to the right, the size of the microstructural feature increases, and the coherency between the matrix and the precipitate is gradually lost. The maximum strength generally occurs when there is a mixture of coherent and semi-coherent precipitates. Overageing produces stable incoherent particles, giving a lower strengthening effect (e.g. so-called Orowan hardening).

2.2.3 Deformation structures

The large plastic deformation that a piece of aluminium is exposed to during rolling or extrusion has great impacts on the microstructure and the crystallographic texture of the material. These changes will influence its mechanical properties, in terms of e.g. strength and anisotropy, and its behaviour during subsequent annealing. In this section a brief overview is given on the current general knowledge of deformation structure and texture. It is important to notice, however, that because of the large number of different microstructural features developing during deformation, a unified and complete description of deformation structures has appeared to be difficult to obtain. In many cases the description and interpretation of observed features is a question of definition by the experimentalist.

2.2.3.1 Dislocation slip and stored energy

The generation and migration of dislocations and dislocation loops, and the subsequent interaction, storage and recovery of the dislocations are the fundamentals of the evolution of the deformation structure (see e.g. [90, 91]). Aluminium has relatively high stacking-fault energy (γ_{sfe}) which makes the dissociation into partial dislocations difficult. Hence cross-slip, and consequently also dynamic recovery, is promoted. In cold forming of

aluminium alloys it is a common assumption that all slip occur on the {111}<110> slip systems and that dislocation climb is limited. At higher temperatures however, the existence of non-octahedral slip on the {100}, {110} and {112}-planes is observed [92]. As the slip systems intersect, the mobile dislocations will interact with each other, as well as with obstacles like solute atoms and particles. When the dislocations are stored in the material, they will lead to an increase in the total stored energy:

$$E \equiv \rho\Gamma$$

Equation 2.3

where ρ is the dislocation density [m^{-2}] and Γ is the line tension of dislocations [N] which is estimated to

$$\Gamma \approx \frac{Gb^2}{2}$$

Equation 2.4

where G is the shear modulus [Pa] and b is the Burgers vector [m]. The system will, as any other system, try to minimize its energy. For the case of aluminium this can be achieved either by organizing the dislocations into low-energy configurations, or through dynamic recovery processes where dislocations annihilate each other.

An important aspect is that cold deformation of metals normally is considered to be limited to the temperature regime of <0.1Tm, which for aluminium is below 70°C. For most practical applications, cold rolling is performed at room temperature, and due to the plastic work the temperature in the material will rise. So what is generally referred to as cold rolling therefore involves temperatures well above 0.1Tm. Thus cold rolling of

aluminium is associated with thermally activated processes, and a considerable amount of dynamic recovery involving both cross-slip and climb of dislocations is expected. This is particularly true for commercial cold rolling, where the temperature of the sheet may reach 100-150°C due to the strain rates being of the order 50-100s^{-1}.

2.2.4 Grain refinement mechanisms

2.2.4.1 Grain refinement by subdivision

According to the general framework [93, 94], dislocation structures organize incidental dislocation boundaries (IDBs) and geometrical necessary boundaries (GNBs). When strain increases, GNBs evolve in a few steps: (I) reorganization into deformation bands (DBs), (II) decrease of spacing to a cell size, (III) rotation to a total flow direction and (IV) increase in missorientation angles (MOA) [95]. Simultaneous changes in microstructure and texture during such an evolution lead to material hardening or softening. Depending on the material and deformation mode, hardening may extend continuously to large strains while softening may interrupt that by localized flow at moderate strains.

If softening becomes predominant, continuous evolution is substituted by flow localization in shear bands (SBs). Shearbands are planar thin material layers accommodating strains which are significantly larger than in the surrounding areas. The average distance between bands approximates to the cell size outside the bands. Crystallographic multi-slip activity in SBs results in gradually increased MOAs along their boundaries. SBs have non-crystallographic orientations that always follow to continual principal shears and they may penetrate a few grains without noticeable deviation. Upon origination, SBs substitute pre-existing structures and define the final structure of heavily deformed metals.

During most deformation processes the original grains in a material will be extensively subdivided. New boundaries are introduced separating volume elements by a misorientation between their lattice orientations. A range of misorientations arises and the spacing of the boundaries is continuously decreased as deformation proceeds. An extensive study of the boundary spacing was provided by Gil Sevillano et al. [96]. They collected cell size data from a range of materials, normalized them to the cell size at $\varepsilon=1.5$ and plotted them against the strain. Figure 2.16 shows that the evolution in cell size with strain is similar for all the investigated alloys, and that the size decreases continuously up to very large strains. Also plotted in the diagram is the inverse of the cell size, which shows a linear dependence on strain above $\varepsilon=1$. Also the boundary misorientation changes significantly during deformation and various authors have reported a range of misorientation results. A collection of reported misorientations are given in Figure 2.17, and suggests something between saturation at about 2-3° and a continuous development in aluminium alloys [97-99] [100-102].

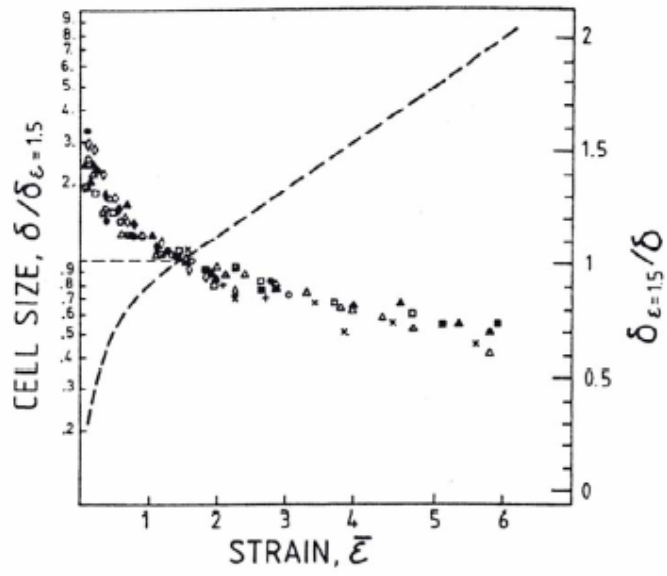

Figure 2.16: Cell size,δ normalized to cell size at ε=1.5 ($\delta_{\varepsilon=1.5}$) for a range of materials. Broken lines shows 1/δ vs. strain [96]

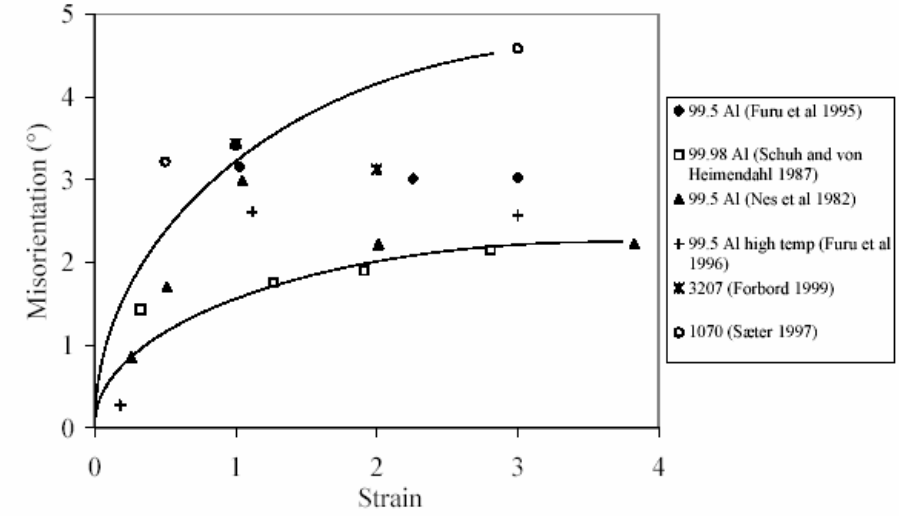

Figure 2.17: Evolution in sub-grain misorientation with strain reported by several authors for aluminium and aluminium alloys [103]**.**

During recent years, a group at Risø National Laboratory has given a very detailed description of deformation structures, e.g. [93, 104-107]. These works are dealing with cold rolled pure aluminium and nickel (which in this context is very similar to aluminium in terms of crystal structure and stacking fault energy, and hence also deformation structure). An overview of some of their observations and considerations is given in the following. Their description starts with the assumption that within one grain the combination and number of simultaneously active slip systems vary from place to place. The number of active slip systems at each location is generally lower than the five predicted by the Taylor theory (see section 2.6.2), as this is energetically favourable. Thereby, the grain starts to subdivide into volume elements. Within one element the slip pattern is different from that in the neighbouring elements, but collectively they fulfil the Taylor assumption for strain accommodation.

The volume elements correspond to an experimentally observed feature denoted *cell block* (CB) which, as the name indicates, consists of a number of adjacent cells. The boundaries between neighbouring CBs arise out of geometrical necessity, as the selection of slip systems is different on either side of them. Hence, they are termed geometrically necessary boundaries (GNBs). Several types of GNBs are described, e.g. dense dislocation walls (DDWs), observed at small to moderate strains, and laminar boundaries (LBs), separating flat elongated CBs at large strains. Microbands (MBs) are plate-like zones bounded by dislocation sheets which tend to develop from the DDWs, and thereby separate CBs. Within the CBs there are cells separated by cell boundaries. These boundaries are formed through mutual trapping of mobile and stored dislocations, and thereby they are termed incidental dislocation boundaries (IDBs). A schematic illustration of the

cells, cell blocks, GNBs and MBs at a moderate strain level is given in Figure 2.18.

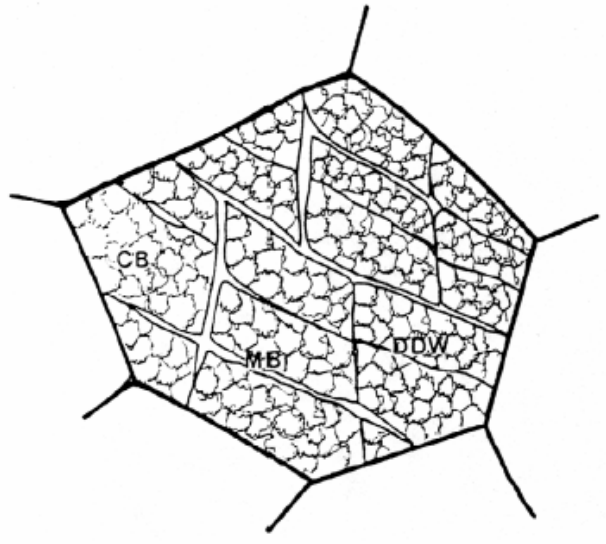

Figure 2.18: Schematic drawing of the early deformation structure in a cell-forming metal [108]**.**

The grain subdivision starts during the early stages of deformation, and already after 10% cold rolling a well-developed cell block structure has evolved in favourably oriented grains [106]. At small to moderate strains (up to ε=0.7) most of the GNBs are DDWs and MBs. The majority of them are inclined to the rolling direction by an angle of approximately 40°. A schematically presentation of the substructure at 30% and 50% rolling reduction is shown in Figure 2.19 (a, b).

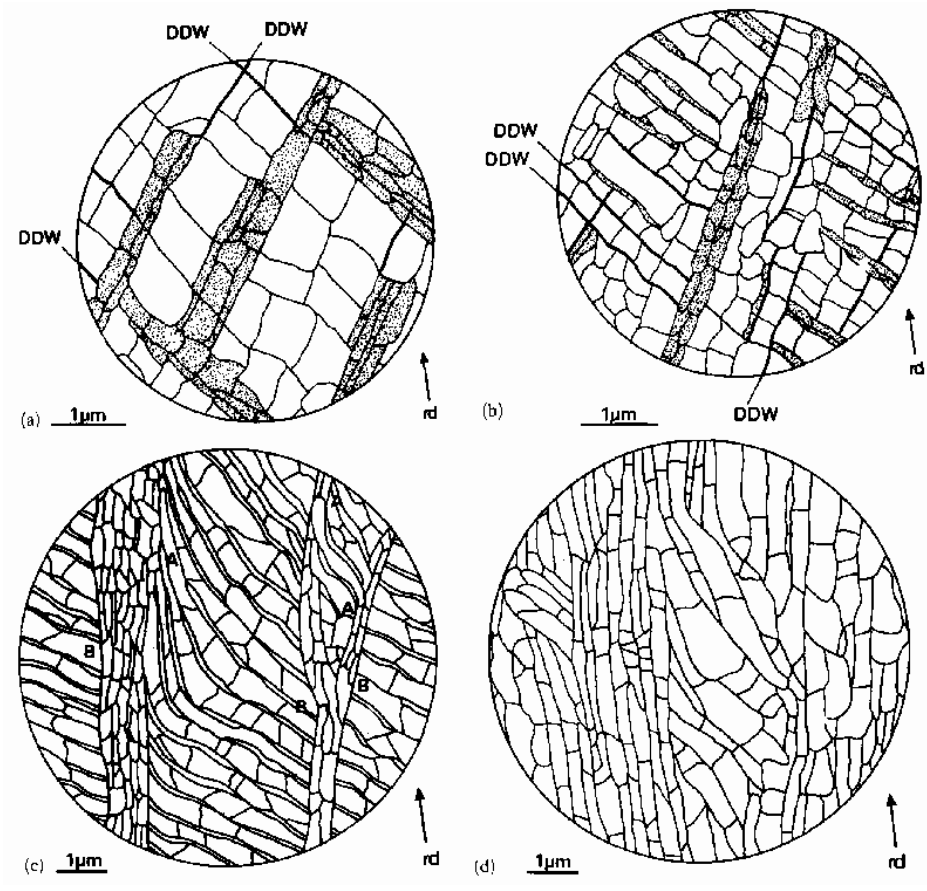

Figure 2.19: Schematic illustrations of the changes in microstructure during cold rolling. (a) 30% (ε=0.36), (b) 50% (ε=0.69), (c) 70% (ε=1.2), (d) 90% (ε=2.3). In (a) and (b) the DDWs are drawn as thick lines and subgrains in MBs are dotted. [105]

At higher rolling reductions (ε>0.7) layers of elongated cells or sub-grains are formed. The sub-grains are grouped in bands of a lamellar structure nearly parallel to the rolling direction. A lamella is essentially a cell block with only one sub-grain between its boundaries. The GNBs of this structure therefore appear as lamellar boundaries (LBs); see Figure 2.19(c, d).

The spacing of both GNBs and IDBs decrease with increasing deformation. Obviously the GNB spacing is larger than the IDB spacing, but the difference diminishes at large strains as the cell blocks finally contain only one cell across its width. This is shown in Figure 2.20 for small to moderate strains in aluminium, and in Figure 2.21 for a wide strain range in nickel. Also the variation in the misorientation across GNBs and IDBs with strain is shown in Figure 2.21. The GNB misorientation is higher and increases more rapidly with strain as compared to the IDBs. While the IDB misorientation increases slowly to about 3° at large strains, the GNB misorientation increases up to 15-20°. Eventually, the GNBs turn into high-angle boundaries (>15°), and no saturation in the misorientation is observed for these boundaries at a strain of 4.5.

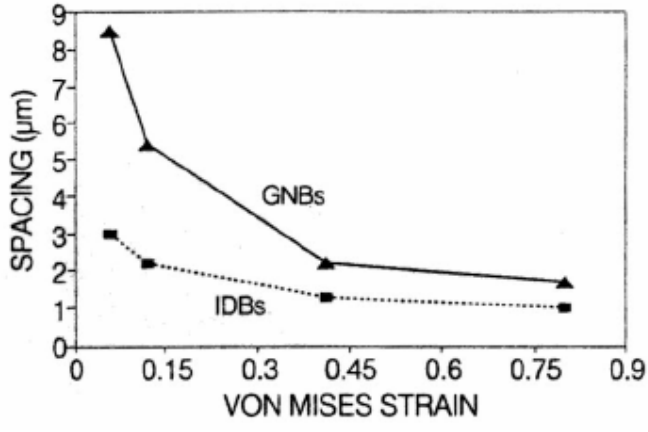

Figure 2.20: Spacing of GNBs as a function of rolling strain in pure aluminium [106]**.**

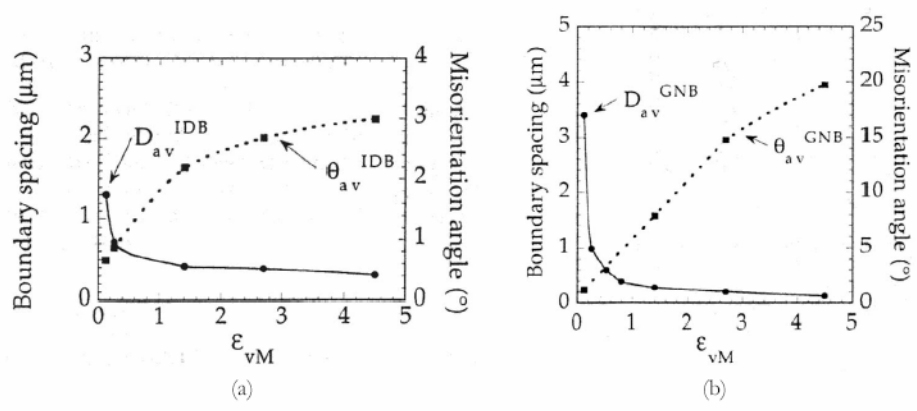

Figure 2.21: Observed boundary spacing (*D*) and misorientation (*θ*) as a function of rolling strain in pure nickel. (a) Geometrically necessary boundaries, (b) incidental dislocation boundaries. [107]

2.2.5 Alloying effects on subdivision

2.2.5.1 Solute atoms

Not all materials build up a well-defined cell structure as described in section 2.2.4. By introducing a considerable amount of solute atoms to an alloy, the friction stress is increased and the dislocation mobility reduced due to solute-dislocation interactions. This causes large constraints on the dislocation rearrangement, which is essential in the creation of cell boundaries. Instead, a different dislocation structure evolves, known as a Taylor lattice (e.g. [108]). A Taylor lattice consists of uniform arrays of edge dislocations along the primary slip planes. It is characterized by a nearly uniform distribution of dislocations, multiple Burgers vectors of dislocations within the array and the dislocations are organized along {111}-planes. So, instead of clustering the dislocations to minimize their energy such as in cell walls, they organize into arrays of alternating sign, a process that also lowers their energy. The Taylor lattice is an incidental dislocation structure, i.e. the dislocations are trapped incidentally, or

statistically. On a larger scale, geometrically necessary boundaries (GNB's) are created in order to account for the variations in selection of slip system between neighbouring volumes. This is analogous to the DDWs appearing in cell-forming metals described in the previous section. However, in non-cell forming alloys they appear as domain boundaries (DBs). The difference between domain boundaries and DDWs is that domain boundaries are parallel to the {111} slip planes whereas DDW's tend not to be crystallographic in nature. Microbands also appear frequently in non-cell forming alloys [109]. These microstructural features are illustrated schematically in Figure 2.22. Note the difference between this subdivision pattern and the one in cell-forming metals in Figure 2.18.

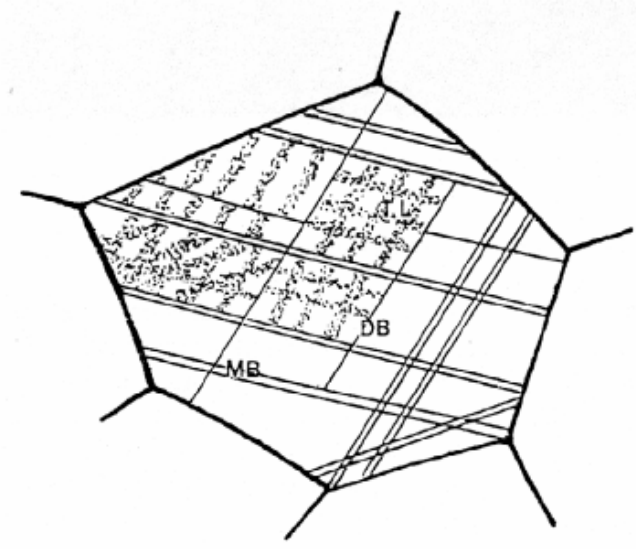

Figure 2.22: Illustration of the grain subdivision in a non-cell forming alloy. TL: Taylor lattice, DB: domain boundary, MB: microband. [108]

2.2.5.2 Non-deformable particles

When a matrix containing hard second phase particles is deformed, strain incompatibilities arise around the particles. In order to account for this

geometrical effect, an arrangement of geometrically necessary dislocations has to be introduced [110]. This results in the occurrence of deformation zones around the particles, as illustrated by Figure 2.23(a). The deformation zones consist of small subgrains that build up an orientation gradient between the particle surface and the matrix, see Figure 2.23(b). It is found that the misorientation increases with both strain and particle radius [91]. Additionally, the presence of second phase particles is observed to increase the overall dislocation density and to reduce the average subgrain size.

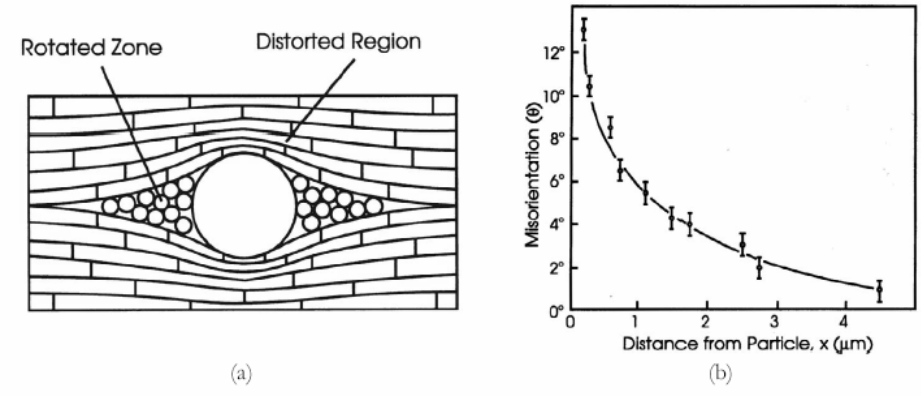

Figure 2.23: (a) Sketch of a deformation zone around a particle in a rolled polycrystal. (b) Lattice misorientations as a function of distance from the particle as observed in [91]**.**

2.2.5.3 Dislocation density in the grain interior

As mentioned earlier, dislocation loops are generated and expanded during deformation. A large number of these dislocations are used to build up sub-boundaries, but some of them will be stored as a 3-D network in the subgrain interior instead. Even an annealed metal will contain a considerable amount of dislocations, typically 10^{10}-10^{12} m^{-2} [90], but the density increases rapidly, and a severely cold worked material may have an overall dislocation density of up to 10^{16} m^{-2}. It was observed by Nord-

Varhaug et al. [111] that the density of dislocations inside the subgrains saturated in the early stage of deformation. Figure 2.24 shows a constant dislocation density of around 10^{14} m^{-2} in the strain range of ε=0.03-2 for two commercial aluminium alloys. The density was somewhat higher in the AA3207 alloy, containing 0.4 wt% Mn, than in the more pure AA1050. This is consistent with the observations in the classical work of Langford and Cohen [112], where iron was wire-drawn to very large strain. They concluded that most of the dislocations were confined to cell walls and that the density within the cells was comparatively low.

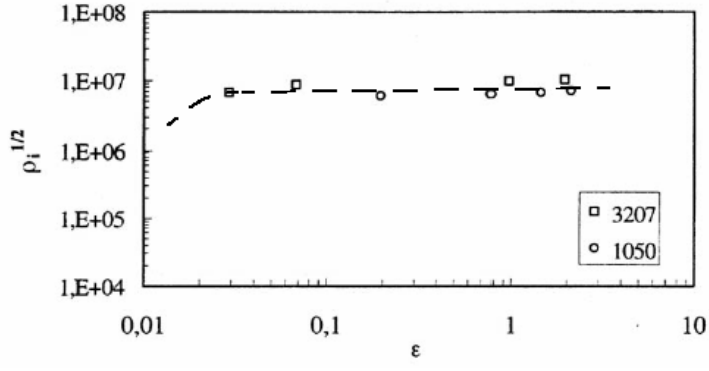

Figure 2.24: Density of dislocations inside the cells / subgrains of the commercial alloys AA1050 and AA3207, covering a strain range up to a strain of 2 [111].

2.2.6 Band formation in plastic deformation

Bands of different types are very common in plastic deformation-in fact in all types of material, independent of crystal dislocation behaviour. Basically, they are due to the fact that, without diffusional processes, solids can locally deform only through shearing in a fixed direction on planar or prismatic planes, and that the intersection of deformation zones with different slip directions requires an increased stress. The different kinds of bands are outlined briefly below. The following features have commonly

accepted names and they are basically other features than what the Risø-group has put their names to (GNB's, DDW's, DB's etc.)

2.2.6.1 Bands of secondary glide

Bands of secondary glide, observed mostly in later stage I, are zones with strongly decreased primary glide activity in which secondary or "unpredicted" glide is concentrated. They are slightly inclined against the primary glide plane [113-115], and are accentuated near orientations of multiple glide [116]. According to [115] they are localizations compensatory coplanar (on the primary slip plane) glide due to the deviation of the primary Burgers vector direction from the direction of maximum shear stress.

2.2.6.2 Kink bands

These bands are generally normal to both the operative slip plane and to the slip direction. Further, the lattice in the bands is rotated with respect to the rest of the crystal about an axis lying in the slip plane and perpendicular to the slip direction. The kink bands may form when the crystal is loaded in compression, and deforms by a localized region of the crystal suddenly snapping into a tilted position with a sudden shortening of the crystal. The kinking behaviour is illustrated in Figure 2.25.

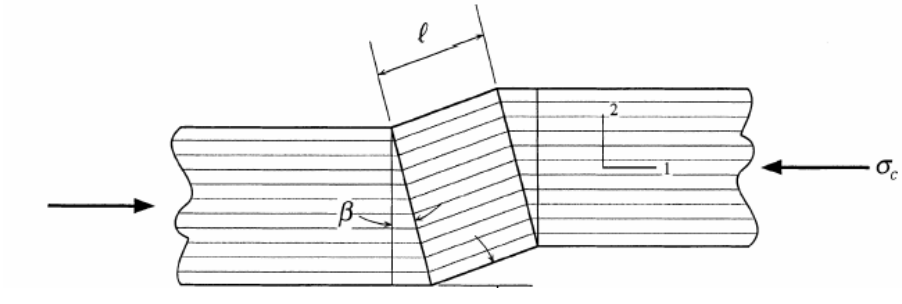

Figure 2.25: Schematic figure of a kinked crystal experiencing the critical compression stress for kinking, σ_c, resulting in a kink band of width *l*, tilted an angle β with respect to the crystal.

2.2.6.3 Stria bands

The typical appearance of stria bands is that they are slightly inclined to primary slip lines. However, in the regions of stria, the primary slip system is poorly developed or completely absent, while slip lines from other (secondary) systems can be present. The explanation of stria formation from [117] is that the grains developing stria are stiffer than the neighbouring grains. The constrained condition within such a grain is overcome by the formation of separated bands with primary and multiple slip, i.e. primary slip and stria bands respectively.

2.2.6.4 Regular deformation bands

Regular deformation bands are typical slab-like parallel sequences of volume elements with alternating average lattice orientation, which are caused by the local simultaneous operation of fewer slip systems than would be required for homologous deformation. Regular deformation bands are subdivided into dislocation cells and apparently by twins in planar glide. In either case, they terminate at grain boundaries.

The free energy change due to deformation bands consists of: (I) the reduced elastic strain energy through a lowered flow stress on account of a decreased number of simultaneously acting slip systems; (II) the deformation band energy; and (III) the strain energy of internal stresses, i.e. the specifically misfit stresses caused by opposite deviations from homologous strain in neighbouring deformation bands.

According to an overview by Kuhlmann-Wilsdorf [118], the deformation bands can be explained by the LEDS theory “beyond reasonable doubt”.

- LEDS hypothesis: "*Among all microstructures that are in equilibrium with the applied stresses and are in principal accessible to dislocations, those are formed which minimize the energy of the **system** composed of the deforming material and the applied tractions".*

Orientation splitting in FCC metals by deformation banding has been studied in detail by Akef and Driver 1991 [119], Maurice and Driver 1992 [120], Basson and Driver 2000 [121], Paul, Driver and Jasienski 2002 [122] and Paul, Driver, Maurice and Jasienski 2003 [123]. Their focus has been on explaining the orientation splitting of cube-oriented FCC crystals in plane strain compression. The main findings are:

- Plane strain compression of (001)[010] and (001)[110] aluminium single crystals leads to the development of deformation bands by lattice rotations of opposite sign about the transverse axis [100]. The decomposition process is preceded by a stage of relatively homogeneous deformation up to a critical strain $\varepsilon_c \approx 0.2\text{-}0.3$.
- The (001)[110] orientation separates into two stable, complementary copper {112}<111> type texture components after a strain of 1.2. The (001)[010] orientation develops two complementary {049}<094> after similar strains; these texture components are unstable and probably decomposes further at higher strains into four S-type texture components.
- The decomposition process can in certain cases be related to the type of dislocation interactions; within a given band the number of active slip systems is reduced either to one or two which interact weakly.
- At temperatures less than 300°C the cube orientation splits up into deformation bands separated by cube oriented transition bands (see below).

- At temperatures above 300°C the cube orientation is stable, and slip takes place on the {110}<1-10> systems.
- The (001)[110] orientation deforms by octahedral slip and breaks up into deformation bands with two symmetric {112}<11-1> type orientations.

2.2.6.5 Transition bands

In transition bands the lattice orientation changes gradually, i.e. they exhibit systematic strain gradient(s) on at least one slip system across a width significantly larger than the diameter of the participating dislocation cells.

2.2.6.6 Hybrid / regular transition bands

Hybrid / regular transition bands are like regular deformation bands in one direction and transition bands in another.

2.2.6.7 Shear bands

Shear bands are narrow regions of intense shear and are a kind of plastic instability. They appear in materials subjected to heavy deformation, such as cold rolling. The bands are non-crystallographic, and in a rolled sheet they are normally aligned about ±35° to the rolling direction and parallel to the transverse direction. Often they intersect several grains and may cross a whole plate leading to failure.

Shear bands have been observed in high-purity aluminium rolled at room temperature. But it is upon the addition of magnesium that shear banding really becomes frequent. The mechanisms involved in shear banding are not fully understood, but Dillamore et al. (1979) [124] analyzed the phenomenon in terms of a plastic instability. In plane strain compression, or rolling, the condition for this instability is written as:

$$\frac{1}{\sigma}\cdot\frac{d\sigma}{d\varepsilon}=\frac{n}{\varepsilon}+\frac{m}{\dot{\varepsilon}}+\frac{1+n+m}{M}\cdot\frac{dM}{d\varepsilon}-\frac{m}{\rho}\cdot\frac{d\rho}{d\varepsilon}<0$$

Equation 2.5

where n and m are the strain hardening and strain rate exponents, ρ is the dislocation density and M is the Taylor factor. It follows that instability is favoured by negative strain rate sensitivity (m), which is the case in AlMg alloys, and a negative dM/dε. The latter term corresponds to geometric softening, i.e. that instability is favoured if it causes a lattice rotation into a softer orientation. A more recent contribution to the knowledge of shear banding has been provided by Inagaki and Kohara (1997) [125]. They studied the shear banding in polycrystalline binary AlMg alloys with 0.5-5% Mg, given cold rolling reductions up to 95%. The shear band density increased with both Mg-content and strain, and a critical concentration between 2 and 3% Mg was experienced, above which shear bands formed readily. The suggested mechanism is that stress concentrations and misfit strains arise at the grain boundaries, and thereby lead to the formation of offsets on the boundaries, see Figure 2.26(a). It was observed that shear bands grew out of these offsets, and hence the grain boundaries served as nucleation sites for the bands (Figure 2.26(b)). This effect is enhanced by the presence of Mg-atoms, as they suppress the dislocation movement and give an even more inhomogeneous deformation. However, the orientation difference between the grains on each side of the boundary influences the misfit strain and plays an important role in the formation of offsets. Therefore, not all boundaries are able to nucleate shear bands.

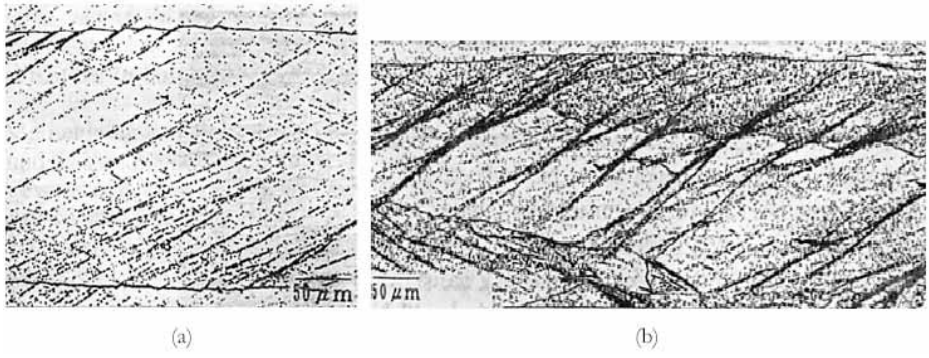

Figure 2.26: (a) Formation of offsets on a grain boundary in AlMg5 cold rolled to 50%. (b) Shear bands crossing a grain boundary after cold rolling to 70%. [125]

The mechanism described above applies only to alloys with more than 2.5% Mg. The low-Mg alloys, on the other hand, did not form any offsets on the grain boundaries. Instead, shear bands were formed by necking of elongated grains. After large rolling reductions the internal stress state varies considerably along the length of a grain, leading to subdivision of the grain and diffuse and localized necking. This mechanism depends on the thickness of the grains, with necking occurring easily in thin grains. It is suggested by Inagaki et al. (2002) [126] that shear banding may be one of the methods to accommodate strain in hard oriented grains. Material softening has also been related to shear banding [127]. Geometrical softening, caused by non-uniform lattice reorientation, influences the localization process, as channels of softened material and concentrated strain are formed. The shear banding is also associated with negative strain rate sensitivity, caused by solute-dislocation interactions which hinder the dislocation mobility.

Lloyd (1986) [128] observed a lesser extent of shear banding at low temperatures (77K) and high temperatures (473K) than at room temperature in an AlMg4.5 alloy. Only in the ambient temperature regime,

corresponding to the dynamic strain ageing regime, shear banding was extensive.

2.2.7 Deformation banding in relation to the LEDS theory

For the formation of a deformation band to be energetically favourable, the reduction of elastic strain energy due to a reduction of simultaneously acting slip systems must be larger than the energy created in the DB boundaries and the excess elastic strain energy on account of accommodation stresses.

In the framework of the LEDS theory, if a reduction of simultaneously acting slip systems reduces the flow stress from τ to $\tau(1-\delta_N)$, the corresponding energy density is

$$U_{eB} = (1/2G)[\tau(1-\delta_N)]^2$$

Equation 2.6

for a reduction of the elastic strain energy of

$$-U_e = (1/2G)\left[\tau^2 - \tau^2(1-\delta_N)^2\right] = (2\delta_N - \delta_N^2)\frac{\tau^2}{2G} \cong \delta_N \tau^2 / G$$

Equation 2.7

the last approximation being valid provided δ_N is less than, at most, 0.5.

The accommodation stresses are assumed to be concentrated at the end faces in a zone of length $\lambda_a W$. If so, a local stress increase in the band zones

to $\tau(1+\delta_a)$ with typically, $\delta_a <\approx 1/2$ the excess elastic strain energy density on account of accommodation stresses is

$$U_a = \left(2\lambda_a \frac{W}{L}\right)\left(2\delta_a + \delta_a^2\right)\frac{\tau^2}{2G} \cong \left(2\lambda_a \delta_a \frac{W}{L}\right)\frac{\tau^2}{G}$$

Equation 2.8

U_e is further counteracted by the boundary energy of the banding, i.e.

$$U_B = \Gamma_{DB}\left(\frac{1}{W} + \frac{1}{T} + \frac{1}{L}\right) \approx \frac{\Gamma_{DB}}{W}$$

Equation 2.9

assuming the same value of the specific surface energy, Γ_{DB}, for all band boundaries. The necessary condition for deformation band formation then is

$$\delta_N \frac{\tau_{DB}^2}{G} >\approx \left\{\left(\frac{W}{L}\right)\frac{\tau_{DB}^2}{G} + \frac{\Gamma_{DB}}{W}\right\}$$

Equation 2.10

Here the variable τ_{DB}, signifying the local shear stress at the time of DB formation, is introduced in lieu of τ because once formed, a deformation band appears to retain its length and width except for participating in the distortion of the material as a whole.

Once Equation 2.10 is fulfilled, the band morphology is found from minimizing $U_a + U_B$ as a function of the band width, *W*. This yield

$$\left(\frac{\lambda_a}{L}\right)\left(2\delta_a + \delta_a^2\right)\frac{\tau_{DB}^2}{G} = \frac{\Gamma_{DB}}{W^2}$$

Equation 2.11

for

$$W = \left\{\frac{\Gamma_{DB} LG}{\lambda_a\left(2\delta_a + \delta_a^2\right)\tau_{DB}^2}\right\}^{\frac{1}{2}} \cong \left\{\frac{\Gamma_{DB} LG}{2\lambda_a \delta_a \tau_{DB}^2}\right\}^{\frac{1}{2}}$$

Equation 2.12

U_a and U_B are proportional and inversely proportional to W, respectively, so that at energy minimum, $U_a = U_B$ and Equation 2.10 reduces to

$$\delta_N >\approx 2\frac{W}{L} \geq 2\frac{W}{D_G}$$

Equation 2.13

with D_G the grain size. This explains why small grains exhibit thin deformation bands and, since L is limited by the cell size, why small grains may not exhibit deformation banding at all.

All of the band boundaries will be, piecewise, dislocation rotation boundaries, being low energy dislocation boundaries (LEDS) with an average spacing among the dislocations of

$$d = \frac{b}{2\sin(\varphi/2)} \cong \frac{b}{\varphi}$$

Equation 2.14

Therefore, their local specific dislocation line energy is

$$U_D \cong Gb^2 \left\{ \frac{(1-\upsilon/2)}{4\pi(1-\upsilon)} \right\} \ln\left(\frac{1}{\varphi}\right)$$

Equation 2.15

since the upper cut-off radius of the individual dislocations' stress fields is necessarily comparable to *d*. Here Poisson's ratio appears to average over the participation of edge and screw dislocations.

For any particular value of φ, the geometrically necessary dislocation line length per unit area depends modestly on the type and geometrical arrangement of the dislocations in the boundary, but is always near $1/d$. This dislocation content is supplemented by redundant or "filler" dislocations due to tangling and imperfect mutual annihilation of ±dislocations arriving at the opposite sides of the wall. As a result the dislocation line length per unit wall area is $M_r \left[2\sin(\varphi/2)\right]/b$ where the ratio of total to geometrically necessary dislocation content is M_r. Furthermore, Poisson's ratio never ranges far from $\upsilon = 0.3$. The specific energy of an isolated boundary of constant rotation angle φ is

$$\Gamma \cong M_r Gb \left\{ \frac{(1-\upsilon/2)}{4\pi(1-\upsilon)} \right\} \sin\left(\frac{\varphi}{2}\right) \ln\left(\frac{1}{\varphi}\right) \cong 0.1 M_r Gb \sin\left(\frac{\varphi}{2}\right) \ln\left(\frac{1}{\varphi}\right)$$

Equation 2.16

Equation 2.15 and Equation 2.16 breaks down for $\varphi > 1/e[rad] \cong 21^\circ$, the maximum angle of $\Gamma(\varphi)$. Beyond $\varphi = 21^\circ$, Equation 2.16 is replaced by

$$\Gamma_{(\varphi \geq 21^\circ)} \cong M_r Gb \left\{ \frac{(1-\upsilon/2)}{4\pi(1-\upsilon)} \right\} \sin\left(\frac{21^\circ}{2} \right) \ln\left(\frac{1}{21^\circ} \right) \cong 0.035 M_r Gb$$

Equation 2.17

Below $T_M/2$, the best present value is $M_r = 2$, which does not seem to depend much on strain or deformation temperature.

When Equation 2.16 and Equation 2.17 are only valid if φ_{DB} is much larger than the average misorientation angle φ_C of cell walls within the band volumes on either side. The effect of φ_C may be accounted for by a correction factor, *F*, for the specific surface energy of deformation band boundaries in the presence of dislocation cell walls. A typical value for *F* is 0.7 when $\varphi \geq 21^\circ$ and $\varphi_C \approx 2^\circ$. The approximate relation between *F*, φ and φ_C is shown in Figure 2.28 [118]. Equation 2.17 may be written, accounting for the cell walls, as:

$$\Gamma_{DB} = 0.035 F M_r Gb$$

Equation 2.18

The unknown parameters λ_a and δ_a regarding the accommodation energy may be evaluated numerically; λ_a must compare to unity and δ_a is limited to ~0.4 by the level at which a previously latent system is triggered and thereby the strain propagated into the next band.

$$\xi = \frac{\left[\lambda_a\left(2\delta_a + \delta_a^2\right)\right]}{FM_r} \approx 0.035b\left(\frac{L}{W^2}\right)\left(\frac{G}{\tau_{DB}}\right)^2 \approx 2\lambda_a\delta_a$$

Equation 2.19: Unknown parameters regarding the accommodation energy.

The calculated values for ζ are listed in Table 7.6. A reasonable value for ζ is assumed to be ~0.8 [118].

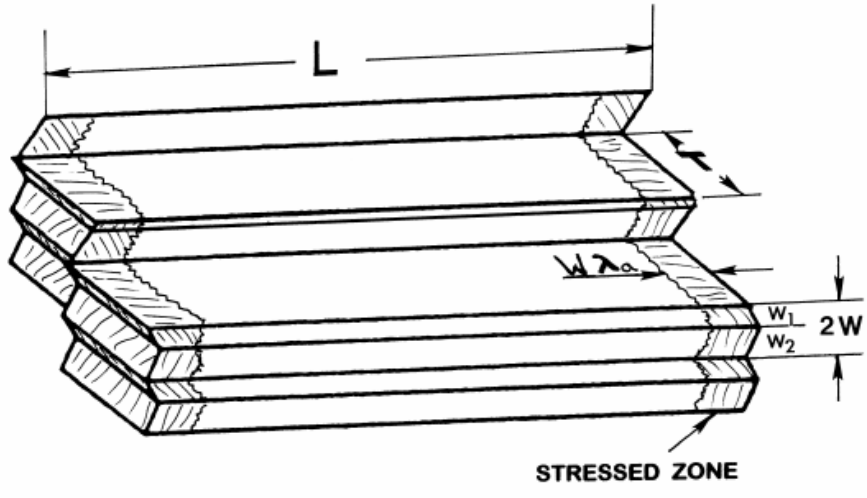

Figure 2.27: Definition of size parameters related to deformation bands [118]**.**

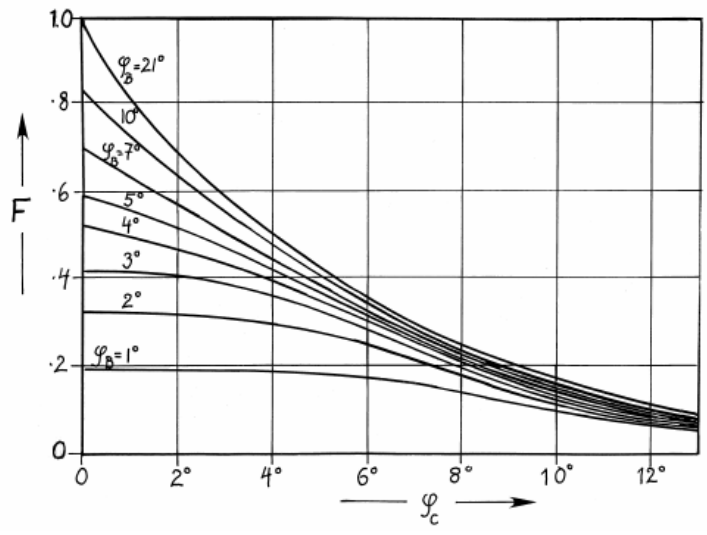

Figure 2.28: Approximate value of F as a function of cell wall misorientation [118]**.**

2.2.8 Theory of co-incidence site lattice boundaries

The theory of co-incidence site lattice (CSL) boundaries is important regarding low energy grain boundary configurations. Two grains which do not have the same orientation may still possess common lattice sites. If this is the case, the atoms occupying these sites constitute a new lattice, which is called the co-incidence site lattice. The ratio between the numbers of atoms per volume in the original lattice to the number of atoms in the CSL defines a number Σ that characterizes the relation between the two grains:

$$\Sigma = \frac{n_{orig}}{n_{CSL}}$$

Equation 2.20

where n_{orig} is the atom density in the original lattice and n_{CSL} is the atom density in the co-incidence site lattice. This number also characterizes the boundary between the grains which is called a "sigma-*n*" boundary, where *n*

equals the number *Σ*. Only certain values of *Σ* are allowed. In cubic symmetry, *Σ3* is the highest degree of symmetry, then comes *Σ5, Σ7, Σ9* etc. Each *Σ*-boundary is characterized by a specific axis/angle pair, describing the misorientation and rotation axis separating the two grains. The axis/angle pairs for *Σ*-values up to 33 are shown in Table 2.3.

Table 2.3: Axis/angle pairs for Σ values up to 33 [129]

Σ	φ	Axis	Σ	φ	Axis
3	60	111	21b	44.41	211
5	36.86	100	23	40.45	311
7	38.21	111	25a	16.26	100
9	38.94	110	25b	51.68	331
11	50.47	110	27a	31.59	110
13a	22.62	100	27b	35	210
13b	27.79	111	29a	43.6	100
15	48.19	210	29b	46.4	221
17a	28.07	100	31a	17.9	111
17b	61.9	221	31b	52.2	211
19a	26.53	110	33a	20.1	110
19b	46.8	111	33b	33.6	311
21a	21.78	111	33c	59	110

The CSL boundaries possess a degree of symmetry which makes them particularly interesting. For a Σ-n boundary, at least every n'th atom is common, however, the boundary plane will normally orient itself to obtain a higher degree of symmetry. One preferred boundary plane can be found using an alternative description of the CSL. A Σ-boundary can be described by a 180° rotation about a <*hkl*> axis where

$$h^2 + k^2 + l^2 = \Sigma$$

Equation 2.21

and the boundary plane is the *(hkl)*-plane. All the atoms in this plane will be common to the two lattices, and thus, minimizing the energy of the boundary. If the boundary is forced to move in a different direction than given by the *(hkl)*-plane, the grain boundary energy will be minimized by introducing a stepped structure.

2.3 Basic polycrystal plasticity

Several models for anisotropic behaviour are suggested in the literature, and the classical Sachs and Taylor models are presented below. They are both related to the simple analysis by Schmid (1924) [130] in which a critical resolved shear stress was deduced. Consider Figure 2.29, where a single crystal with cross-section area A is loaded in tension. A {111} plane with <110> directions are shown, and the angles between the tensile axis and the considered <110> direction and a chosen {111} plane normal are denoted λ and ϕ, respectively. The resolved shear stress on this particular slip system is then given by Equation 2.22

$$\tau_c = \frac{F}{A}\left(\cos\lambda \cdot \cos\phi\right)$$

Equation 2.22

F/A is the same as the applied stress on the crystal, σ, and $\cos\lambda \cdot \cos\phi$ is referred to as the Schmid factor, m, for the considered slip system. The critical resolved shear stress giving crystallographic slip is then:

$$\tau_c = m\sigma$$

Equation 2.23

There are twelve different independent slip systems in fcc-metals. The Schmid factor will vary with the orientation of the slip system relative to the loading direction, and each slip system will have a value of $m \leq 0.5$.

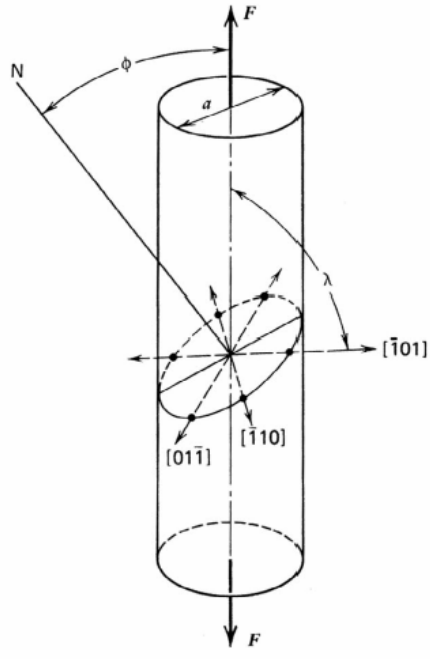

Figure 2.29: Single crystal in tension with slip plane and slip directions

2.3.1 The Sachs model

In the Sachs model it is assumed that each grain deforms independently of its neighbours, and on the slip system that has the highest resolved shear stress [131]. For a tensile test this corresponds to a maximum m, Equation 2.23. The Sachs model also says that the stress state is the same in all the grains, i.e. the same as the macroscopic stress. For a tensile test the Sachs model uses Schmid's law, Equation 2.22, to determine the active slip systems, in fcc-metals between one and eight slip systems. However, this simple deformation model does not require compatibility of the strain field

between the grains, and is therefore not very realistic, except for very small deformations and for single crystals. The theory is known as the lower bound model and is observed to underestimate the stress. Modified Sachs models have also been proposed, giving more successful descriptions of polycrystal plasticity (e.g. [132]).

2.3.2 The Taylor model

Unlike the Sachs model, where the *stress* equilibrium is required, the Taylor model requires *strain* compatibility [133]. It rests on some assumptions, where a kinematical equation and an energetic assumption are essential elements:

(I) All grains in a polycrystalline aggregate experience the same strain, equal to the global strain. The macroscopic velocity gradient tensor is equal to the microscopic velocity gradient:

$$L_{ij} = l_{ij}$$

Equation 2.24

which for a tension test is given by:

$$L_{ij} = \begin{bmatrix} 1 & 0 & 0 \\ 0 & -\dfrac{r}{1+r} & 0 \\ 0 & 0 & -\dfrac{1}{1+r} \end{bmatrix} \cdot \dot{\varepsilon}$$

Equation 2.25

where $\dot{\varepsilon}$ is the strain rate and r is the plastic strain ratio, i.e. the ratio between the width strain and the thickness strain: $r = \varepsilon_w / \varepsilon_t$. A kinematical

equation is deduced for the velocity gradient tensor, where the lattice rotation is separated:

$$l_{ij} = \dot{\Omega}_{ij}^{L} + \sum_{s=1}^{12} b_i^s n_j^s \dot{\gamma}^s$$

Equation 2.26

where $\dot{\Omega}_{ij}^{L}$ is the rate of rotation of the crystal lattice, $\dot{\gamma}^s$ is the slip rate on slip system s, and *b* and *n* are the unit vectors of the slip direction and slip plane normal, respectively. The kinematical equation says that the combination of all slip processes active at the moment determines what happens to the crystallite. The symmetric part of l_{ij} becomes the strain rate tensor:

$$d_{ij} = \frac{1}{2} \sum_{s=1}^{12} \left(b_i^s n_j^s + b_j^s n_i^s \right) \dot{\gamma}^s$$

Equation 2.27

where Taylor's assumption is that $d_{ij}=D_{ij}$, i.e. the strain rate at the microscopic level equals the strain rate prescribed at the macroscopic level. The expression $\frac{1}{2}\left(b_i^s n_j^s + b_j^s n_i^s \right)$ is the generalized Schmid factor, which in uniaxial tension reduces to $\cos\lambda \cdot \cos\phi$. The strain rate tensor, Equation 2.27 gives a set of five independent equations, but twelve unknown $\dot{\gamma}^s$. Therefore additional requirements are needed in order to solve the equations.

(II) The energetic assumption of Taylor suggests that the slip systems are chosen so that the internally dissipated frictional work is minimized:

$$\dot{W} = \sum_{s=1}^{12} \tau_c^s \cdot \left| \dot{\gamma}^s \right| = \min.$$

Equation 2.28

where τ_c^s is the critical resolved shear stress on slip system s.

Slip occurs on the active slip systems, for which the shear stress τ^s reaches τ_c^s. This requirement gives a stress relation when considering the active slip systems only:

$$\frac{1}{2} \sum \left(b_i^s n_j^s + b_j^s n_i^s \right) \sigma_{ij} = \tau_c^s$$

Equation 2.29

from which σ_{ij}, the deviatoric stress tensor in each grain, may be obtained.

(III) If the critical resolved shear stress is assumed to be identical in all slip systems, which is a commonly used approximation, no unique solution is obtained for the stress. This will give several sets of (five) non-zero $\dot{\gamma}^s$-values which make $\dot{W}$ minimal. Consequently an ambiguity, referred to as the Taylor ambiguity, arises about which set of slip systems shall be active. Solving the ambiguity can in the simplest case be done by picking one of the solutions by random.

The Taylor factor, *M*, may be defined as the ratio between the shear strain increments on the slip systems and the global strain increment on the crystal:

$$M = \frac{\sum_s \left|\dot{\gamma}^s\right|}{\dot{\varepsilon}} = \frac{\sigma}{\tau_c}$$

Equation 2.30

where it is assumed that all τ_C^S are equal and σ is the equivalent stress. By comparing Equation 2.23 and Equation 2.30, we see that the Taylor factor, M, is analogous to the inverse Schmid factor, 1/*m*. As they rely on different assumptions regarding the crystal deformation, they will obtain different values. The average Taylor factor for a polycrystalline aggregate is normally larger than the average 1/*m*, and the Taylor factor is often referred to as an upper bound model. In a tensile test of a FCC polycrystal with randomly oriented grains, the average Taylor factor is calculated to be *M*=3.06.

In a modified Taylor model, known as the relaxed constraints model (RC), some of the strain compatibility restrictions between the grains are relaxed in favour of better stress homogeneity. This result in fewer slip systems involved; in the so-called "pancake" model the number of active slip systems in each grain is reduced from five to three. This can be justified by the shape of a flat, elongated grain. The interface area between two grains on the thin side is so small that no big errors are introduced if the requirement of strain compatibility is relaxed here. For comparison, the Sachs model may be considered as a zero constraints model. A more comprehensive review of the Taylor model may be found e.g. in [134, 135].

3 ECAP DIE DESIGN

The ECAP die used in all experiments had to be constructed from scratch as there was very limited knowledge about ECAP at NTNU at the start of this work. Many parameters had to be taken into consideration regarding sample shape, sample size, working temperature, and maximum work load. We decided to use a 90° die with a square section of 20 x 20mm^2 cross section and sample length of 100mm which should be capable of a maximum workload of 600kN. In addition we wanted the possibility of heating the die to a maximum of 550°C.

3.1 The Piston

The piston is made from the same steel quality as the die, e.g. Orvar Supreme. It is mounted to the ram by two steel disks. The piston can be adjusted ± 2.5 mm in all directions for perfect alignment with the die. The piston cross section has a taper of 0.1 x 0.1mm, 10mm from the front to avoid sticking friction along the whole piston length.

3.2 The control system

The process is monitored by a computer program written in LabWiev 6.1 from National Instruments. The die temperature is controlled by a Eurotherm unit with 4 x 950W heating elements and a 4kW surrounding heating element. Temperature is measured 3mm from the channel wall in 2 positions and directly on the sample surface in the exit channel. The ram force is monitored by the same computer program, but cannot be preset or controlled in any way; it is determined by the sample strength. A simple standard press with 60 metric tons capacity was used. The ram displacement is measured by a Mitutoyo displacement measuring unit, and has been

implemented in the LabWiev program. This gives the possibility of monitoring the pressing speed.

3.3 The Die

3.3.1 Version 1.1

The first die was made from the Orvar 2 tool steel, hardened to approximately 46HCR. The channel surfaces were nitrated for increased wear resistance. The die is horizontally split, 6mm up from the bottom of the exit channel. Further, it has a 90º bend with inner and outer radius of curvature 1 mm and 6 mm respectively. The cross section area for the entrance channel is 20 x 20mm with 1mm radius of curvature in the corners. The entrance channel accepts 100 mm samples and the exit channel has a cross section reduction to 19.5.x.19.5 which expands to 20.5 x 20.5mm 25mm from the centre of the entrance channel.

The die worked as expected at room temperature but started cracking in the upper-channel corners after some hundred pressing cycles. The stress concentration in the channel corners was simply too large and the die had to be redesigned in order to withstand the internal pressure without cracking.

Figure 3.1: ECAP die Version 1.1 mounted on working table with the four heating elements. Entrance channel at the top and exit channel pointing towards the reader.

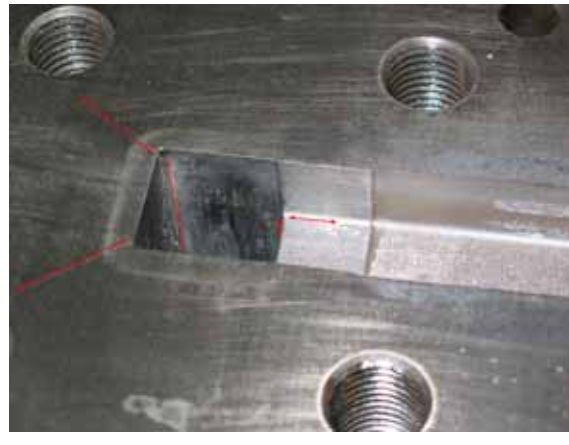

Figure 3.2: Cracking in the upper channel corners in Version 1.1

3.3.2 Version 1.2

The second version of the die was made from Orvar Supreme tool steel, which has higher strength and ductility at room temperature than Orvar 2. The overall geometry is the same as the first version (V1.1).

In order to make the die withstand the high forces without cracking in the channel corners, some computer simulations were made to get a view of the forces present in the die at the maximum work load.

The first calculations showed that it was impossible for the die to withstand an inner pressure of 1GPa without exceeding the yield stress of the material in the channel corners, no matter what outer dimensions used. In order to overcome this problem we had to “remove” the corners in the entrance channel by splitting the inner part of the die in four sections from the corners. This will result in compressive stresses on these sections and which will be below the yield stress of the “Orvar Supreme”. The four sections will transfer the forces onto a larger area and the idea was to reduce the stresses to an acceptable level. However, the deformations in the open corners would still become unreasonably large. In order to create deformations as small as possible, the solution seemed to be to make a pre-tensioned ring which surrounds the four inner sections which form the square hole. The pre-tensioning can be achieved by thermal fitting of the ring. The proper diameters are 30mm for the inner section containing the square hole, 50mm for the pre-tensioned ring and 200mm for the total diameter of the die.

The simulations were made on a symmetric section of the die as shown in Figure 3.4. The pre-tension of the middle ring is achieved by a temperature difference of 310°C resulting in 0.2mm expansion of the hole. Calculations of the shrink-tensions / pre-tension are shown in Figure 3.5. At zero work load, the inner ring is in compression bearing a stress of ~600MPa. When the die is loaded by an inner pressure of 1GPa, the tension distribution will be as shown in Figure 3.6.

The die produced on these principles has, at the time of writing, successfully reached more than 1500 pressing cycles without problems.

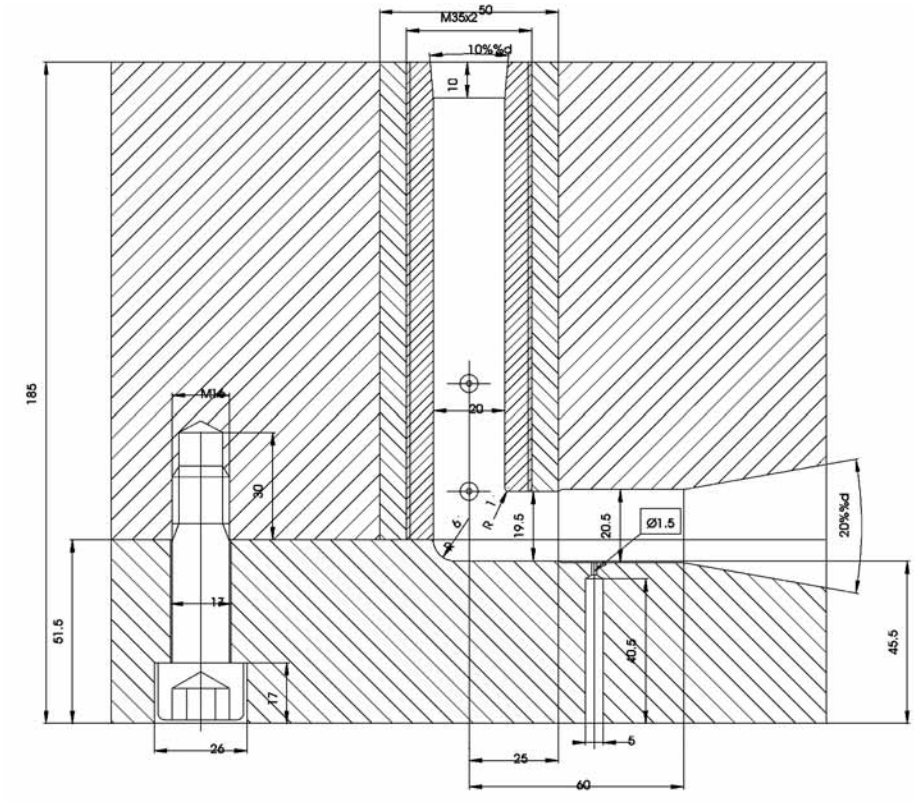

Figure 3.3: Schematic cross sectional drawing of the ECAP die V.1.2. Entrance channel at top and exit channel to the right. Position of the thermo couple channel is also shown.

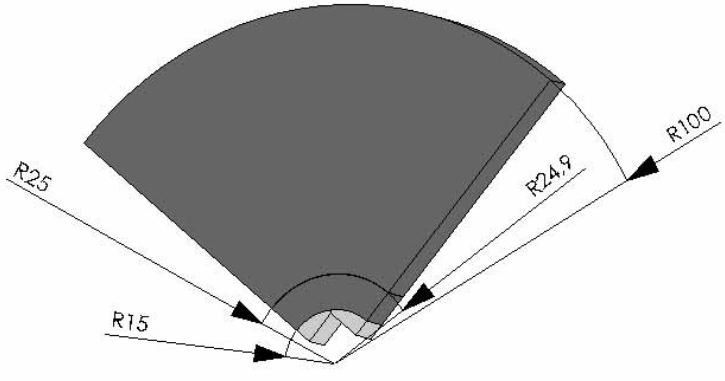

Figure 3.4: Section of the die used in calculations of stress distributions.

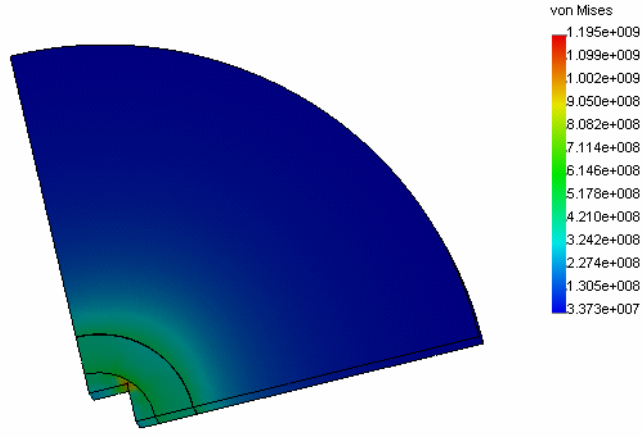

Figure 3.5: Stress distribution as a result of pre-tensioning of the middle ring. The colour scale shows the effective Von Mises stress [Pa].

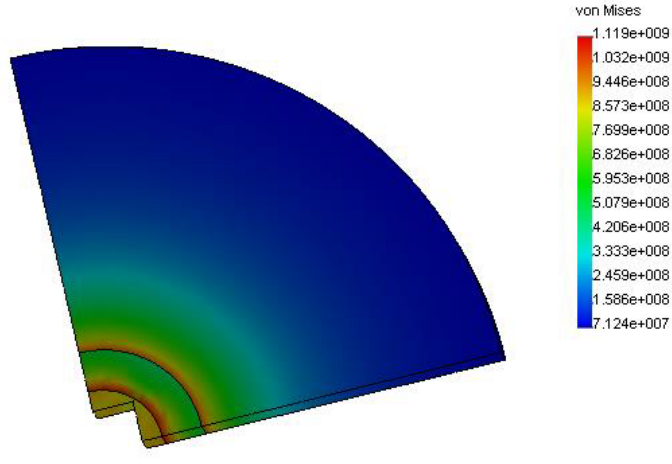

Figure 3.6: Stress distribution with an inner channel pressure of 1GPa. The colour scale shows the effective Von Mises stress [Pa].

4 EXPERIMENTAL PROCEDURES

The material used in the present study is a commercial Al-Mg-Si aluminium alloy (AA6082.50) supplied by Hydro Aluminium AS. The actual chemical composition is given in Table 4.1.

Table 4.1: Chemical composition of the Al-Mg-Si 6082.50 alloy

Element:	Si	Mg	Mn	Fe	Ti	Cr	Contaminants	Al
wt%:	0.98	0.64	0.51	0.19	0.012	0.004	0.018	balance

The material was supplied in two different conditions, i.e. industrially homogenized (03-temper) and room temperature stabilized after quenching from solutionizing temperature (T4). Billets of dimensions $19.5\times19.5\times100mm^3$ were machined from the received materials.

All ECA pressings are performed with the die design described in chapter 3.3.

4.1 Strain analysis (referring to chapter 5)

Two different pre-deformation material tempers were studied: (i) the as received T4 temper and (ii) a homogenized temper (853 K/3 hours followed by air cooling at 300 K/hour). These tempers provide high yield stress/high work hardening and low yield stress/lower work hardening conditions respectively.

The ECA pressings were carried out at room temperature. Before each pressing, the channels were cleaned and then coated with lubricant OMEGA99®. Two different friction conditions were applied: (i) high friction; direct contact between the samples and the lubricant, and (ii) low friction; the samples were wrapped into a 0.35 mm thick Teflon foil. The

initial sample dimensions were 19.5x19.5x100 mm^3 in high friction conditions and 19x19x100 mm^3 in low friction conditions.

The T4 samples were cut into five parts (one half the width and four sections $1/8^{th}$ the width). Then a rectangular grid network was introduced on these sections before pressing. An example of how the specimens were cut and marked with grids is shown in Figure 4.1. The homogenized sample consisted of two parts and was pressed for each friction condition.

Each part of the samples was mechanically grinded to 4000mesh grinding paper. A grid was etched on one face of the specimen by an electrochemical marking process from Lectroetch®. The different parts were stacked together such that no grid was facing another and then partially pressed in the die. The die was then dismounted and the sample was carefully removed in order to analyze the strains on the sub-specimens.

The grid was mapped using the commercially available strain analysis software ASAME® and analyzed by in-house software. The grid size was $1 \times 1 mm^2$ with line thickness of ~0.1mm.

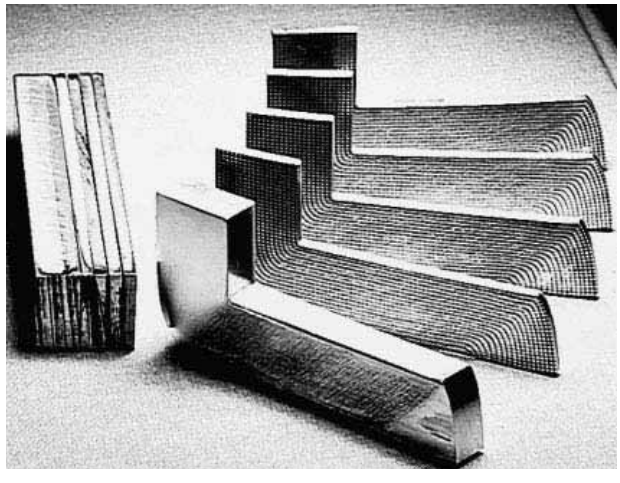

Figure 4.1: Example of a specimen cut into 5 sub-specimens, or parts, with their respective grids (squared 1x1mm^2).

4.2 Mechanical properties (referring to chapter 6)

Four different initial states were investigated with regard to post ECAP mechanical properties: (I) as cast and homogenized (as-received, 03-temper), (II) solution treated (W-temper), (III) naturally aged (as-received, T4) and (IV) soft-annealed (see Table 4.2).

Table 4.2: Initial heat treatments before ECAP

Homogenized (03)	580°C for 3h → cooling at 300°C h^{-1}
Solution treated (W)	540°C for 40min → water quench
Naturally aged (T4)	565°C for 4h10min → water quench → stabilized at RT
Soft annealed	Start with T4 → 440°C for 2h → cooling to 250°C during 2 hours → holding at 250°C for 4h → air cooling

The material was processed to different strains by ECAP at room temperature by route A (i.e. no rotation of the sample between passes) and a few additional pressings by route Bc (90° sample rotation between passes), using a constant ram speed of approximately 3 mm/s. The billets were coated with petroleum and graphite based lubricant, OMEGA99® before pressing. For comparison, cold rolling (CR) was performed on the soft annealed material, starting with a machined billet of 19.5×19.5×100mm^3. The CR was done in the longitudinal direction by successive thickness reductions up to 97.2% corresponding to an equivalent strain of 4.2.

Tensile specimens from the ECAP processed material were machined from the centre of the processed billets, in the longitudinal direction, with a gauge length of 30mm and diameter 3.8mm. The samples were taken from a zone which is believed to carry an approximate homogeneous deformation. For further details concerning the homogeneous zone, please see chapter 5.

The effect of post-ECAP artificial low-temperature aging was investigated on samples pressed in the solutionized state. Post-ECAP heat

treatments were made at 90, 110 and 130°C for different aging times corresponding to peaks in the post-ECAP aging curves.

The tensile specimens from the cold rolled sheets were flat specimens, machined in the rolling direction with a gauge length of 33mm, 12.9mm width and carrying the actual thickness (1.9 to 0.5mm).

The tensile tests were performed at room temperature in a 100kN servo-hydraulic MTS 880 test machine, at constant ram speeds, giving initial strain rates of ~10^{-4}, 10^{-3}, 10^{-2} and ~10^{-1} s^{-1} in the various tests performed.

The grain size of ECAP processed billets was measured from electron backscatter diffraction (EBSD) data. The preparation and equipment was the same as described below (see 4.3 Microstructure and texture). Samples were observed in the XY-plane (Figure 5.1). Grain size was calculated from the "grain area" corresponding to areas surrounded by continuous boundaries with misorientations larger than 2°. The averaging of the grain size is further normalized to the number fraction.

4.3 Microstructure and texture (referring to chapter 7)

The microstructure and texture have been investigated for the homogenized material (as received, 03 temper), pressed at room temperature by route A.

The billets were coated with petroleum and graphite based lubricant, OMEGA99® before pressing.

The ECAP sample consisted of two parts with equal dimensions of 100×19.5×9.75mm^3. A grid was applied to one face (the XY-plane) of the first part of the sample, facing the second part of the sample. The sample was then pressed halfway through the die and carefully removed by disassembling the die. The strains introduced by ECAP in the deformation zone was measured and analyzed by the same technique as described in

"Strain analysis", section 4.1, before a small sample was cut, containing the shear deformation zone, for EBSD analysis (Figure 4.2).

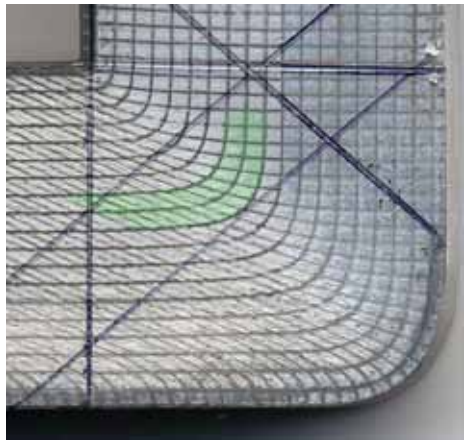

Figure 4.2: Work piece used for strain analysis, including the sample used in EBSD measurements (green area corresponds to strain paths used in strain tensor calculations in section 7).

Texture and microstructural data was obtained by electron backscatter diffraction (EBSD) established in a Hitachi S-4300SE FE-SEM, equipped with a Nordif EBSD detector and the TSL OIM EBSD software, and analyzed by OIM Analysis 4.0 software from the company TSL.

EBSD was performed at 20kV, 15-20mm working distance and 70° tilt. Samples for EBSD analysis were mechanically grinded and polished to 1μm, followed by polishing in a diluted OPS solution (10%), electrochemically polished in a 30% HNO_3 – 60% methanol solution at -30°C (90-120s at 11V) and finally mechanically polished again for 10 to 20s in 1% OPS solution before cleaning in a plasma cleaner.

The texture has also been measured by XRD after 1, 2, 3, 4, 6 and 8 passes by route A in a Siemens D5000 difractometer and analyzed by the "Van Houtte" software. Sample preparation in this case consisted of mechanical polishing to 1μm followed by electrochemical polishing at 15°C in the A2 electrolyte.

5 STRAIN ANALYSIS IN ECAP

5.1 Introduction

A survey of the current knowledge on shear strain and strain distribution in ECAP shows that it is mainly based on analytical [136-140] and numerical approaches [9, 11-13, 141-145]. Since experimental measurements are rather seldom in the literature [79, 141, 146], the present study thus aims at providing (i) data of quasi-3D strain measurements depending on (ii) the friction conditions and (iii) the initial material properties, after one pass of ECAP at room temperature.

The strains appeared in multi-sectioned billets pressed through the die are analyzed using a grid marking technique. Effects of friction and initial material properties on the strain distribution and the specimen shape in the die angle region are investigated by pressing samples with different tempers under different friction conditions. Furthermore, focus is set on the deformation history of flow along material path lines.

5.2 Theoretical analysis

The principle of ECAP has been outlined in chapter 2.1 and is schematically described in Figure 5.1. Two channels of equal cross sections intersect at an angle θ with an outer arc of curvature, or die corner angle, delineated by an angle ψ.

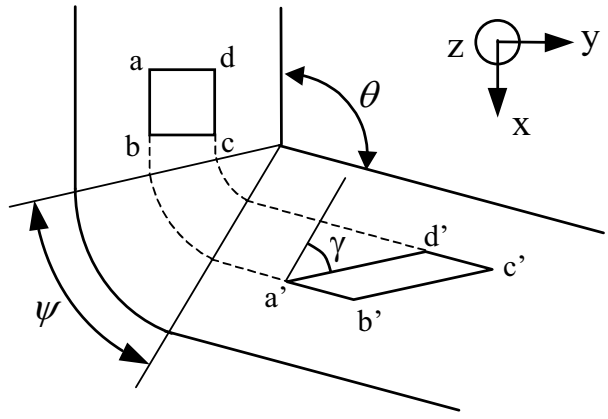

Figure 5.1: Definition of ECAP geometrical parameters, coordinate system, material flow lines and shear angle as adapted in the present work.

A small initially square element *abcd* is deformed into a non-square element *a'b'c'd'* after undergoing shear through the die. Since such a process gives rise to large strains, it is thus necessary to use an appropriate measure of strain e.g. the Lagrangian description. Therefore, it can be shown that the Green-Lagrange finite strain tensor $\overline{\overline{E}}$, for simple shear, can be written in the (xyz) coordinate system as:

$$E = \begin{bmatrix} E_{xx} & E_{xy} \\ E_{xy} & E_{yy} \end{bmatrix} = \begin{bmatrix} 0 & g/2 \\ g/2 & g^2/2 \end{bmatrix}$$

Equation 5.1

where, according to [138]:

$$g = 2\cot\left(\frac{\theta}{2} + \frac{\psi}{2}\right) + \psi\,\mathrm{cosec}\left(\frac{\theta}{2} + \frac{\psi}{2}\right)$$

Equation 5.2

The shear strain angle γ is defined as being the change of angle of two initially orthogonal material lines and can be written in the (xyz) coordinate system as:

$$\sin\gamma = \frac{2E_{xy}}{\sqrt{1+2E_{xx}}\sqrt{1+2E_{yy}}}$$

Equation 5.3

Please note that and g and γ are linked through the relationship $g = \tan\gamma$.

The effective plastic strain is determined using the Hencky, or logarithmic, strain tensor $\overline{\overline{H}}$:

$$E_{eff} = \sqrt{\frac{2}{3}\left(H_I^2 + H_{II}^2\right)}$$

Equation 5.4

where $H_k = \ln\sqrt{1+2E_k}$, E_k being the principal values of the Green-Lagrange strain tensor. Please note that the latter formula will provide a value different from the commonly assumed one (i.e. $g/\sqrt{3}$) [136, 137], i.e., here having the value 0.95 instead of 1.05.

5.2.1 Strain Analysis

For each sub-specimen, the coordinates of each grid intersection were determined using the commercially strain analysis software ASAME® [147]. The strains on each part were then computed using an in-house program and plotted using a commercial data viewer.

Figure 5.2 shows the effective plastic strain (see Equation 5.4) on each part of the T4 sample pressed under low friction. The first and most important result emerging from this analysis is the relatively good similarity between all the strain distributions in all sections within the experimental accuracy of ±2%. Please note that the theoretical value of the effective plastic strain, under the assumption of homogeneous strains, is 0.95, which is in good agreement with the present observed strains. Moreover, the absolute thickness strains, i.e. the strains in the z-direction, obtained from the assumption of incompressibility, are generally lower than 8%. Therefore, from the present analysis it can be stated that ECAP is a plane-strain process. (So far, this has only been an assumption in the literature).
These results also validate some typical characteristics usually observed in numerical or experimental analyses of ECAP [9, 13, 145] [141, 146].

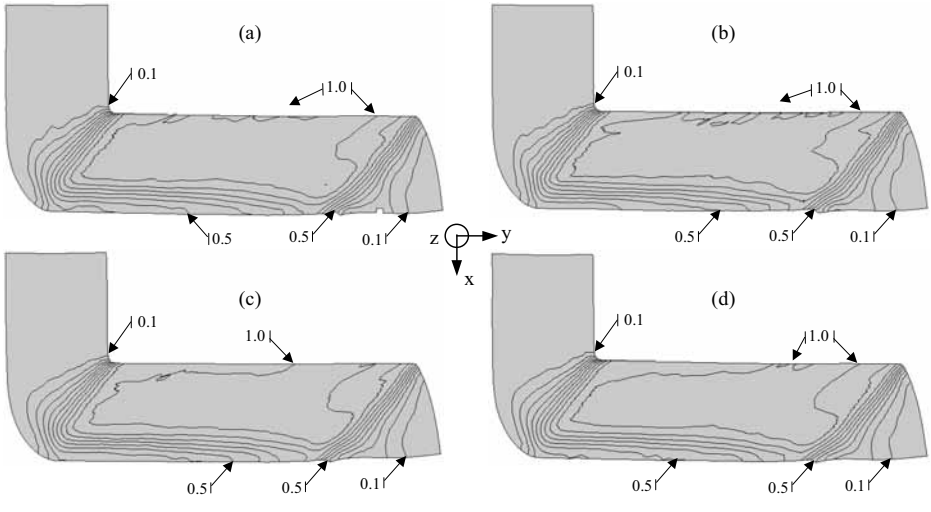

Figure 5.2: Experimental effective plastic strain in different sections of the T4 sample under low friction conditions; initial position from the surface: (a) z=2.4mm, (b) z= 4.8mm, (c) z=7.2mm and (d) z=9.6mm, i.e. the sample centre plane.

The ECAP process does not generate homogeneous strains all over the sample but rather in a restricted volume. The front-end undergoes low

strains since it is not sheared through the die angle and bends up due to the difference of stress states between the upper (tensile) and lower (compressive) part of the sample. A strain gradient appears behind that area revealing where the sample started shearing. The lower part of the sample experiences heterogeneous strains mainly due to flow path dissimilarity and friction.

Furthermore, even though the outer arc of curvature, ψ, is small, the shear in the work-piece angle does not ideally take place along a line but rather over a wide zone (in the following denoted the deformation zone). Therefore, a strain gradient arises across the deformation zone thus generating a complex deformation mode resulting from a combination of simple shear, pure shear and stretching [138, 139].

The next figure, Figure 5.3, shows, for the first time, the shear strain angle γ in ECAP. The figure illustrates the shear angle in mid-samples, for each friction/temper combination. The theoretical value for g, obtained from Equation 5.2, is 1.83, equivalent to a shear angle of 1.07 radians. It is worth noting the good agreement between the experiments and the theory. Nevertheless, as seen for the effective plastic strain, the shear angle is not constant in the whole sample. The same comments can be done regarding to the repartition of the shear strain angle over the sample, such as lower strains in the front-end of the sample and in the lower part. In the following, all statements done are also valid for the effective plastic strain E_{eff}, g and the principal strains E_k.

This comparison provides some noticeable details about the strain repartition and the shape of the work-piece corner angle (the work-piece equivalent of ψ, now on denoted ψ_{sample}). First, a closer look at the strain distribution reveals that the deformation becomes more homogeneous when friction increases. Thus, under high friction, the strain gradient in the

deformation zone is higher, i.e. a narrower deformation zone, the strains in the front-end become more homogeneous and the homogeneous zone is wider (i.e. a higher strain gradient in the lower part). Furthermore, the deformation in the front-end is more homogeneous for the T4 sample than for the homogenized one. Secondly, the work-piece corner angle, ψ_{sample}, is affected by both friction and temper: it is the smallest for the T4 sample pressed under high friction (Figure 5.3c) and seem to be the widest for the homogenized sample under low friction (Figure 5.3b). Therefore, the work-piece corner angle, ψ_{sample}, would decrease when friction and strain hardening increase, which is in disagreement with finite element simulations reported in the literature [11].

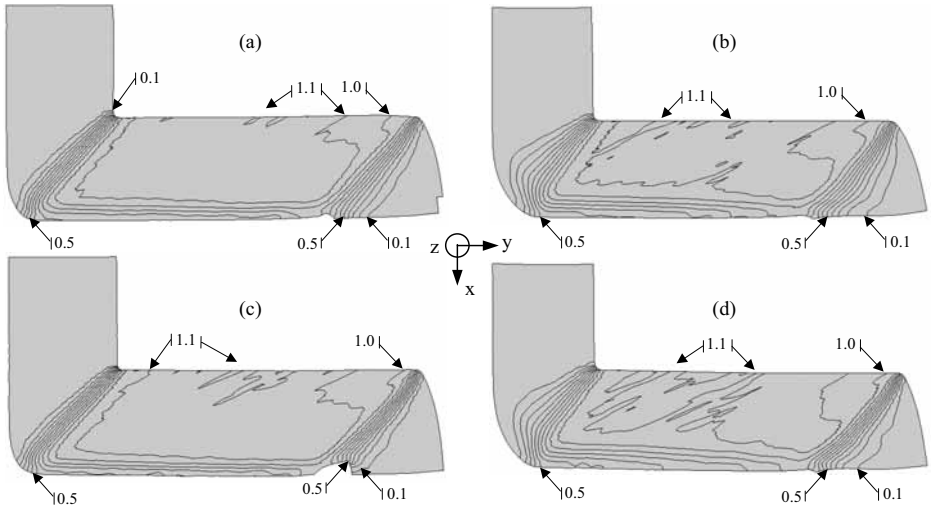

Figure 5.3: Comparison of experimentally observed shear strain angle (in radians) in mid-samples, z=9.6 mm, for different temper and friction conditions: (a) homogenized - high friction; (b) homogenized - low friction, (c) T4 - high friction and (d) T4 - low friction.

5.2.2 Flow and Deformation History Analysis

In order to understand how the work-piece undergoes deformation during pressing, especially when crossing through the die angle, the deformation history of a material element along different path lines is investigated as shown in Figure 5.4a. Here, each grid element along a given path line is rotated and translated into the path-line coordinate system, *s*-*n*, in order to be superimposed on the first one.

In Figure 5.4, deformation histories, in the mid-thickness, are plotted along three different paths: close to the bottom, near the centre and close to the top of the sample. All path lines start from and end up on the same section (dotted lines in Figure 5.4a), i.e. the same number of grid elements is considered for all paths. The numbers denoted in Figure 5.4(1) to (3) indicate the position of the grid element along the path line. The labels *s* and *n* refer to the path line coordinate system.

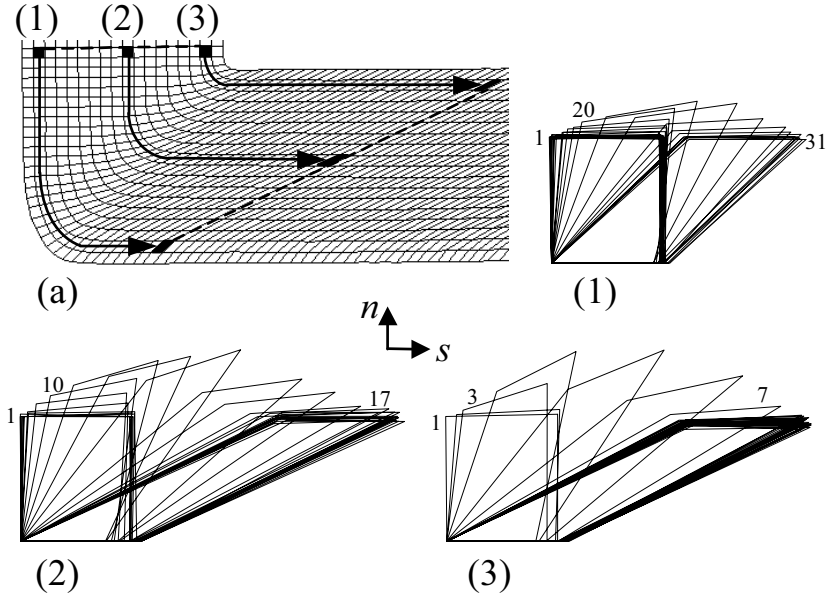

Figure 5.4: Experimental deformation history of material elements, in the mid-thickness, for the homogenized sample under high friction along the different path lines as shown in (a). Numbers 1-31 represents the grid number starting at the dashed line at the top of (a).

The first and important result drawn from this analysis is the deformation history dissimilarity, as could have been expected. Since each material element does not flow through the deformation zone at the same time, the flow history across the width of the sample will differ. While a material element along path (3) exits the shear zone and travels in the exit channel, its counterpart along path (2) enters the zone and the third one is still in the entry channel. This thus leads to shear of the work-piece and tilts an initial straight section relatively to the sample axes.

Moreover, due to friction and corner gap formation, i.e. the dissimilarity between ψ and ψ_{sample}, lower strains are present in the bottom of the work-piece, thus leading to lower shear (see Figure 5.4(1)). As can be seen in Figure 5.3, this low strain zone extends only over a few millimetres and therefore, above this zone, the flow along any path line will generate approximately the same shear.

This means that each flow line represents the deformation history of an element passing through the deformation zone and therefore reveals the deformation features of ECAP. It clearly appears that a material element passing through the deformation zone is subjected, in addition to shear, to a significant amount of stretching, i.e. tension and compression, in both the *s* and *n* directions.

Therefore, this analysis demonstrates that the deformation during ECAP can be interpreted as a combination of shear, occurring tangentially to the path line, and stretching in both the *s* and *n* directions.

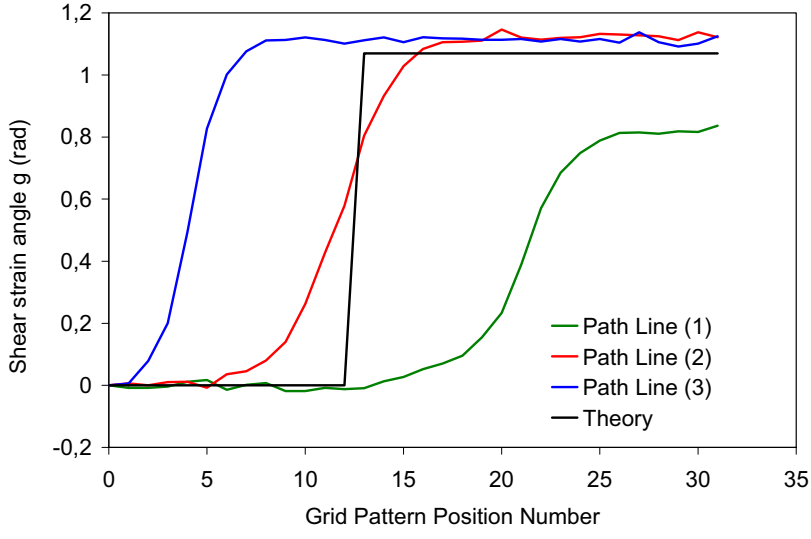

Figure 5.5: Comparison of the measured shear strain angle (γ) histories for the path lines plotted in Figure 5.4(a). The solid line represents the theoretical value of the shear angle from the discontinuous shear approach.

Figure 5.5 shows the comparison of the shear angle histories for each path line investigated in Figure 5.4. As mentioned above, the deformation history varies from one path to the other depending on its location across the width of the sample. The deformation gradient present in the work-piece angle clearly appears from this analysis. The theoretical value from the discontinuous shear approach (i.e. shear appears in a single plane, not over a zone) is shown for comparison. Also, the shear angle reached after passing through the die angle for the path line (1) is much lower than the two others due to increase of the effective value of ψ. The homogeneous zone, i.e. the volume of the work-piece carrying homogeneous deformation, can be considered as the volume of the sample where the shear strain angle is within ±10% of the theoretical value. As can be seen in Figure 5.3, the homogeneous zone is dependent on the friction conditions for the work-piece. The homogeneous zone, not counting the front end of the billet, i.e.

steady state deformation, is approximately 90% in high friction conditions and approximately 80% in the low friction condition (these values count for one-pass ECAP. For multi pass ECAP, geometrical considerations must be made).

Further, a comparison of deformation histories or flows along the same path line (path line (2) in Figure 5.4) for different friction/temper combinations is shown in Figure 5.6. The path line considered here is approximately located in the middle of the width of the sample, i.e. far from the edges. Although all element deformation histories appear similar, a closer look at the extent of stretch in the *n*-direction reveals friction dependence of the material flow through the deformation zone.

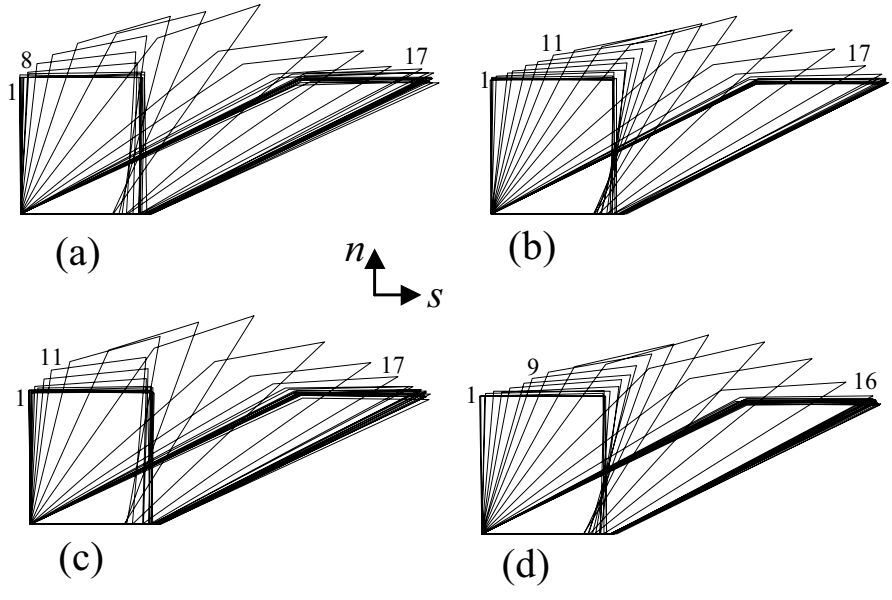

Figure 5.6: Experimental deformation history of material elements, path line (2) in Figure 5.4(a), in mid-samples, for different temper and friction conditions: (a) homogenized - high friction; (b) homogenized - low friction, (c) T4 - high friction and (d) T4 - low friction. *s* and *n* is the path line coordinate system. Numbers 1-17 are the grid numbers.

Moreover, the number of grid patterns in the deformation zone, e.g. 8 to 17 in Figure 5.6a), is slightly higher for low friction than for high friction. This is in agreement with the statements made in the previous section about the dependence of the strain gradient in the deformation zone on friction. Nevertheless, the material temper does not seem to affect the flow along this path, i.e. in the centre of the sample. The latter statement brings to the conclusion that material temper, hence the work hardening behaviour, does not affect, or very little, flow inside the work-piece, i.e. far from the bottom corner.

5.3 Conclusion

The above presentation described the experimental analysis of strain during one pass of ECAP at room temperature. For the first time, quasi-3D strains are observed, thus validating the assumption of plane-strain in ECAP, and the shear strain angle engendered during the process is measured.

Some typical features of ECAP have been corroborated, i.e. friction and material temper affect the strain distribution, the strain homogeneity and the work-piece corner angle, friction being the most significant here. Also, new conclusions have been drawn. The analysis of material element deformation histories along path lines reveals that ECAP can be interpreted as the combination of shearing and stretching (i.e. tension and/or compression). Furthermore, the final shear strain angle obtained in ECAP appears to be friction and material temper independent in the zone of homogeneous deformation.

Finally, since the results exposed here are based on a single set of experiments some of the observations may not be statistically significant. However, the main trends seem very likely.

6 MECHANICAL PROPERTIES IN AA6082 SUBJECTED TO ECAP

6.1 Introduction

Submicron grained aluminium alloys produced by severe plastic deformation (SPD) techniques have recently gained much attention due to some unique and promising mechanical properties [35]. Combinations of reasonable ductility and high strength, plus thermal resistance and high strain rate superplasticity in certain alloys are main driving forces for the research in this field. Another interesting effect is of course the unusually small high angle grain structure obtained in most SPD processed materials. It is believed that this is a direction the research on alloy and processing development will enter in coming years.

One of the most promising methods of SPD is Equal Channel Angular Pressing (ECAP), and was as mentioned in previous chapters, first explored by Segal [1, 4]. The billet pressed through the die experiences intense straining, mainly by simple shear in a zone at the juncture of the two channels composing the deformation tool. Most commonly, ECAP on aluminium is done between room temperature and 200°C.

As a part of a more comprehensive program on SPD processing, the aim of the present work is to investigate the potential of ECAP on a standard, commercial heat treatable 6082 alloy. The mechanical properties at room temperature after ECAP processing from different starting conditions are investigated and compared to similar results found in the literature. In addition, the effect of post ECAP artificial aging has been investigated for samples pressed in the solutionized state to N=1 and N=6 by route A.

Numerous works have been published on the mechanical properties of aluminium alloys after ECAP. Non-heat treatable alloys such as the Al-Mg

[22-34], Al-Mn [35], and Al-Mn-Mg [36] alloys have shown improvements in both strength and ductility after ECAP.

Heat treatable alloys such as Al-Cu-Zr [37], Al-Mg-Si [38-41], Al-Cu-Mg-Mn [42], Al-Mn-Si [43],Al-Zn-Mg [35, 44-46], Al-Li [18, 47-49] and Al-Mg-Sc [50-52] have been reported to achieve positive developments after ECAP. A majority of these studies show that tensile ductility is decreased after multiple ECAP presses, and flow stress is generally increasing with plastic strain accumulation.

Moreover, the effects of SPD on heat treatable alloys are complex multifactor phenomena. There is a combined effect of strengthening due to the refined grain size, dynamic precipitation during pressing, and the precipitation strengthening arising from isothermal heat treatments. One dilemma is that heat treatment after pressing tends to reduce the strength increase effect of SPD, probably due to recovery and release of residual stresses. The highest mechanical strength of heat treatable alloys have been found when the material has been processed in the solutionized state followed by post SPD aging at low temperatures, typically about 100°C for aluminium, e.g. [38, 42].

The effect of strain rate on the mechanical properties during tensile testing after ECAP has also been investigated. Further, a comparison to cold rolling in regard to the development in mechanical properties with increasing accumulated strain is made. This has also been done by Horita et al. [35], but on a non-heat treatable 3xxx series alloy.

Finally, two different processing routes, A and Bc, as defined in Langdon et al. [6] are employed and compared in regard to the mechanical properties achieved.

The ECAP processed samples are compared to tabulated values of commercial 6082 alloy (Al 0.9Mg 1.0Si 0.7Mn) in the T6 condition.

6.2 Results

The ECA pressing has been performed on different initial material states and the mechanical properties are followed press by press, ranging from N=1 (first press) to N=8 (last press). The mechanical properties of ECA processed material are after testing plotted as a function of equivalent strain, which corresponds directly to the number of passes through the die (ε=1 for N=1 etc.). The values recorded at an equivalent strain of zero, represent the testing of samples in the initial state, prior to ECAP.

6.2.1 The effect of ECAP on different initial material states

All initial tempers (homogenized, solutionized, T4 and soft-annealed) processed by route A and Bc, show an abrupt increase in yield stress (Figure 6.1) and ultimate tensile stress (Figure 6.2) after N=1, followed by a more gradual increase for increasing number of passes. Moreover, the elongation to failure decreases abruptly after the first pass, but there is no further reduction with additional passes. Instead, the elongation to failure remains essentially constant after higher equivalent strains, except for the soft-annealed samples, which show a slight increase after 4 passes and the homogenized samples which show a gradual decrease (Figure 6.3). The soft annealed condition demonstrates the highest ductility after ECAP and stays at ~8-9% up to N=8.

Highest strength is obtained in the initially solutionized samples, followed by T4, homogenized and soft-annealed in decreasing order. It seems that more alloying elements in solid solution prior to ECAP results in higher strengths after the maximum number of passes achieved.

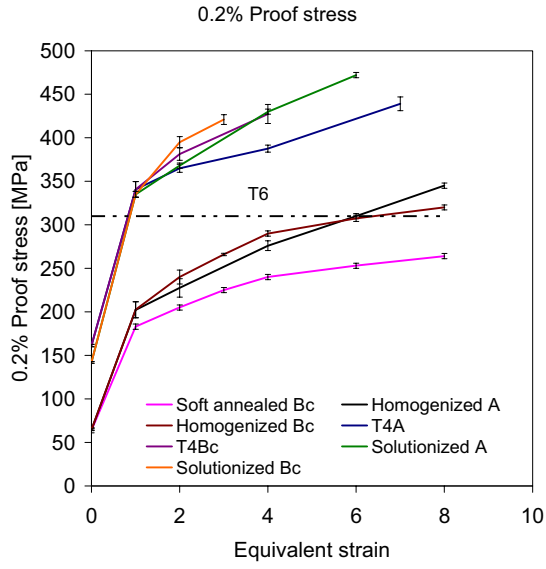

Figure 6.1: Yield stress as a function of equivalent strain. Initial strain rate ~0.001s^{-1}. The points in the graphs are average values from two to four measurements. Error bars give the standard deviation of the measurements.

An interesting observation is the curve crossing of the T4 and the solutionized condition. The T4 material has higher UTS and yield stress up to an equivalent strain of 2, and the curves cross between ε=2 and ε=3, whereupon the solutionized material shows higher strength for increasing number of passes. Further, the increase in the yield stress for N=1 compared to non-ECAP'ed material is much higher than for the UTS, thus indicating that tensile work hardening reduces after the first ECAP pass, as also shown in Figure 6.1. It should also be remarked that the maximum strength level (i.e. T6 condition) of the un-deformed material is exhausted by the materials processed by ECAP. This is further commented in a separate paragraph below.

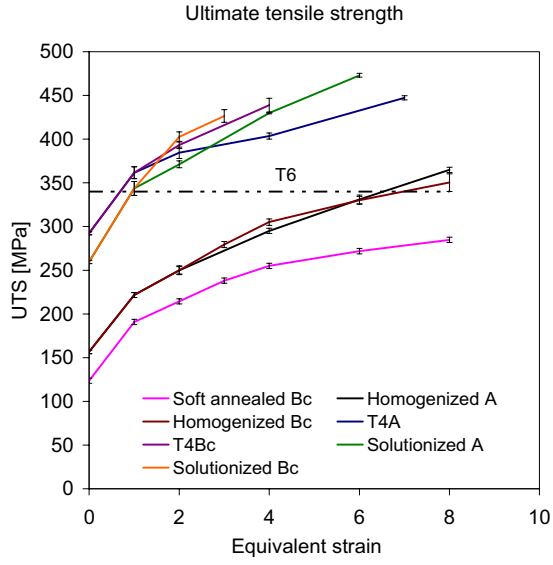

Figure 6.2: Ultimate tensile strength as a function of equivalent strain. Initial strain rate ~0.001s^{-1}. The points in the graphs are average values from two to four measurements. Error bars give the standard deviation of the measurements.

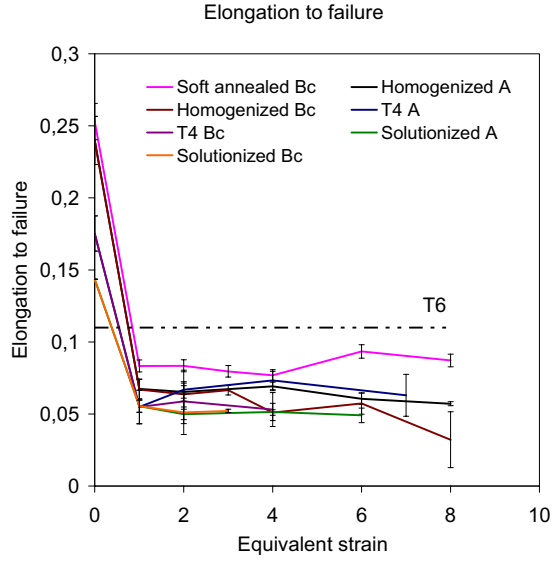

Figure 6.3: Nominal elongation to failure as a function of equivalent strain. Initial strain rate ~0.001s^{-1}. The points in the graphs are average values from two to four measurements. Error bars give the standard deviation of the measurements.

The uniform strain (Figure 6.4) shows a large drop after the first ECAP pass and stays almost constant at this level, i.e. independent of the imposed strain. The T4 samples processed by route A show the highest uniform strain, with a peak after 2 passes, followed by a slight decrease with increasing strain. The solutionized samples tend to exhibit the lowest uniform strains.

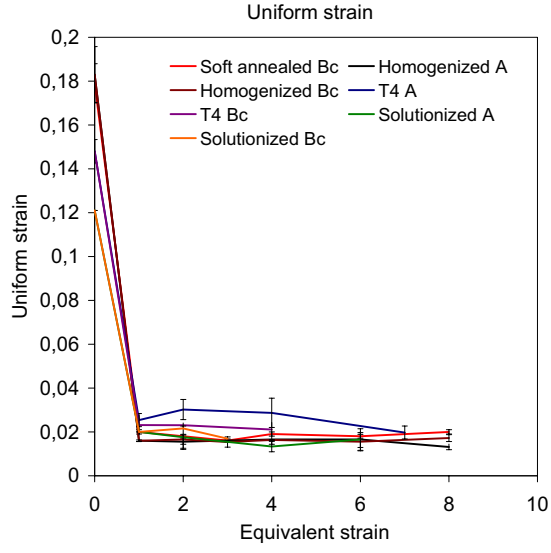

Figure 6.4: Uniform strain as a function of equivalent strain. Initial strain rate ~0.001s^{-1}. The points in the graphs are average values from two to four measurements. Error bars give the standard deviation of the measurements.

The true stress at failure for the T4 and the solutionized samples is calculated based on the measured cross section area and the load at failure and is shown in Figure 6.5. The T4 condition shows higher stress values than the solutionized samples, indicating less strain localization and more contraction during necking. This is verified by the contraction strain at failure in Figure 6.6. The contraction strain after the first pass is equal for both the T4 and the solutionized samples. For an imposed strain of 2 or more, the contraction strain is highest for the T4 samples (~35%) while the solutionized samples shows more variation and a lower level at about 25%.

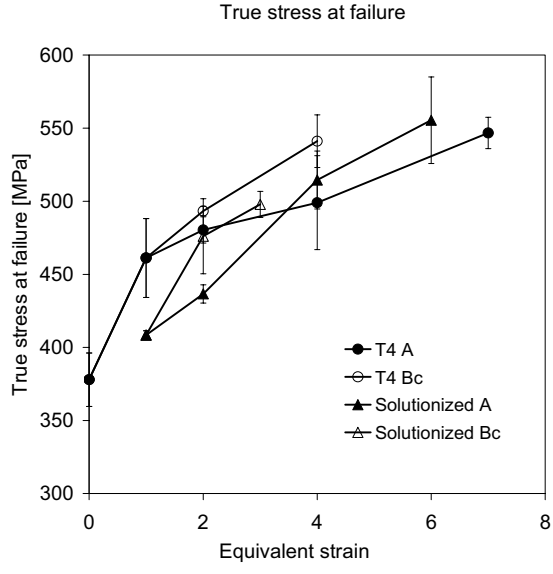

Figure 6.5: True stress at failure as a function of equivalent strain calculated from the cross section area after failure. Initial strain rate ~0.001s^{-1}. The points in the graphs are average values from two to four measurements. Error bars give the standard deviation of the measurements.

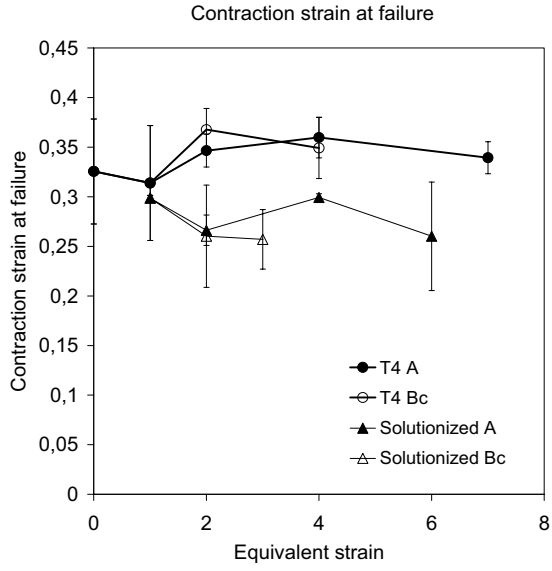

Figure 6.6: True contraction strain at failure as a function of equivalent strain calculated from the cross section area after failure. Initial strain rate ~0.001s^{-1}. The points in the graphs are average values from two to four measurements. Error bars give the standard deviation of the measurements.

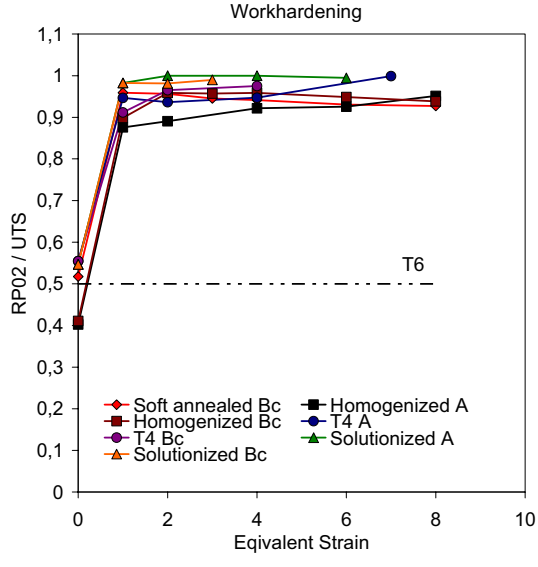

Figure 6.7: Work hardening displayed as RP_{02} / UTS, calculated from average values of yield stress and ultimate tensile stress. Initial strain rate ~0.001s^{-1}.

As a measure of the work hardening potential of ECAP'ed materials, the ratio R_{P02}/UTS is presented (Figure 6.7). The value 1 indicates no work hardening and lower numbers indicates higher work hardening. In general, all ECAP processed samples yield low work hardening and then significantly less than non-ECAP'ed conditions T4, T0 and T6. The extreme case is that of the solutionized samples, which contain almost the same yield stress and UTS after an imposed strain of 2 and higher.

6.2.2 The effect of processing route and tensile test strain rate

The post ECAP tensile test results show that route Bc gives a higher rise in strength than route A up to N=4 (Figure 6.2 and Figure 6.1). Billets processed by route A can be pressed to a higher total strain before cracking occurs, and reaches higher values of yield stress and UTS at the maximum obtainable strain. In the case of the homogenized material, samples could be pressed up to N=8 by both route A and route Bc, but at this strain, the route A processed samples revealed the highest values of both yield stress and UTS. Concerning work hardening potential after ECAP, route Bc tends to achieve slightly higher values than route A for the homogenized condition. However, there is no difference between the two routes for solutionized material (Figure 6.7). Furthermore, samples processed by route Bc also demonstrate higher variation in ductility but show similar values as for samples processed by route A (Figure 6.3). It should also be remarked that the uniform strain is independent of the processing route, i.e. strain path.

Tensile samples were tested at initial strain rates 10^{-4} to $10^{-1}s^{-1}$. At these strain rates, there are no significant or systematic variations in either strength or ductility. The variations in tensile strength are in all cases less than 5% and are difficult to separate from experimental scatter.

6.2.3 Comparison to conventional T6 heat treated non-ECAP'ed material

The homogenized and ECAP'ed material reach the UTS and yield stress values of the conventionally processed T6-temper after an imposed strain of 6, while the elongation to failure is about 50% of that of T6 material, as shown in Figure 6.3. The T4 and ECAP'ed and the solutionized and ECAP'ed material reach the UTS and yield stress values of commercially processed T6-temper after an imposed strain of 2 and continues to increase with increasing number of passes. The solutionized and ECAP'ed sample processed by route A to N=6, gives a 40% rise in the UTS and 50% increase in yield stress compared to a conventional T6-temper, while the elongation to failure is approximately 50% less.

6.2.4 Comparison with cold rolling

For comparison with cold rolling, a soft-annealed sample was chosen due to the highest cold working potential. As can be seen from Figure 6.8, cold rolled and ECAP processed samples show approximately the same values for yield stress, UTS, work hardening and elongation to failure for similar imposed strains. However, it should be remarked that the nominal stress-strain curves have different shapes after reaching the maximum load, as shown in Figure 6.8. The ECAP'ed materials tend to drop load continuously and exhibit larger post-uniform deformation. CR materials seem to have a two-stage post-uniform elongation, i.e. first a low load drop region and finally a promptly load drop before fracture. This difference might be partly due to the different test specimen geometry applied in the two cases (round for ECAP'ed and flat for CR material). However, the CR material reached a maximum equivalent strain of 4.2 before severe cracking occurred, while the ECAP processed samples show only minor evidence of cracking after 8 passes. Therefore the latter processing achieved higher strength since the material can accumulate more strain before it fails.

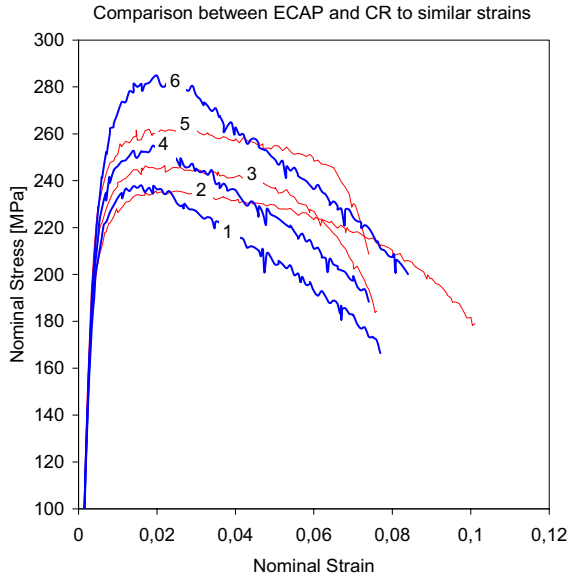

Figure 6.8: Soft annealed and cold rolled (red) to different strains, compared to ECAP'ed (blue) samples from route Bc of similar strain. (1) ECAP N=3, (2) CR to 2.7, (3) CR to 3.5, (4) ECAP N=4, (5) CR to 4.2, (6) ECAP N=8, Initial strain rate ~0.001s^{-1}.

6.2.5 The effect of post-ECAP artificial aging

The effect of post ECAP artificial aging was investigated for samples pressed in the solutionized state to N=1 and N=6 by route A. Three different post ECAP aging temperatures were investigated; 90, 110 and 130°C in addition to natural aging at room temperature. Tensile tests were made at different aging times, corresponding to peaks in the post ECAP aging curves. The results from N=1 are shown in Figure 6.9 as nominal stress-strain curves. It is clear that samples pressed to N=1 has an aging potential. Artificial post ECAP aging results in an increase in tensile strength, tensile ductility and increased tensile work hardening.

For the samples pressed to N=6 (Figure 6.10), the effect of low temperature post ECAP aging is quite remarkable. The tensile ductility can be more than doubled (from 8% to 18% tensile elongation to failure), while

the ultimate tensile strength only decreases slightly (from ~425MPa to ~410MPa). It is interesting though that the samples having the highest ultimate tensile strength, also possess the highest tensile ductility.

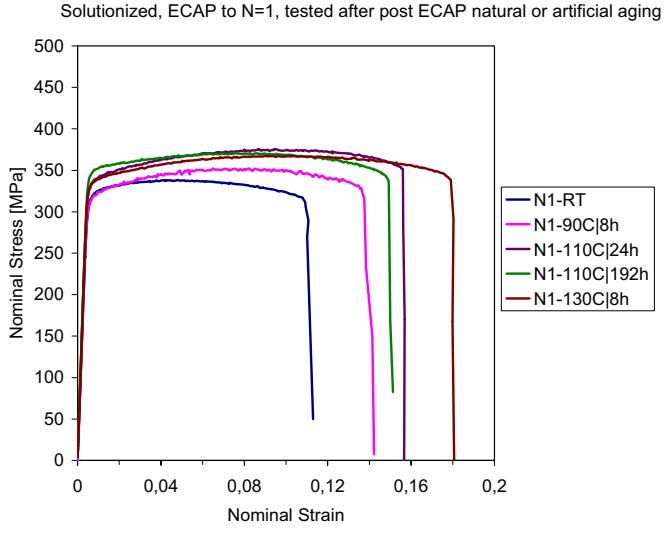

Figure 6.9: Nominal stress-strain curves for samples ECAP'ed in the solutionized state to N=1, followed by low temperature artificial aging. Initial strain rate ~0.01s^{-1}.

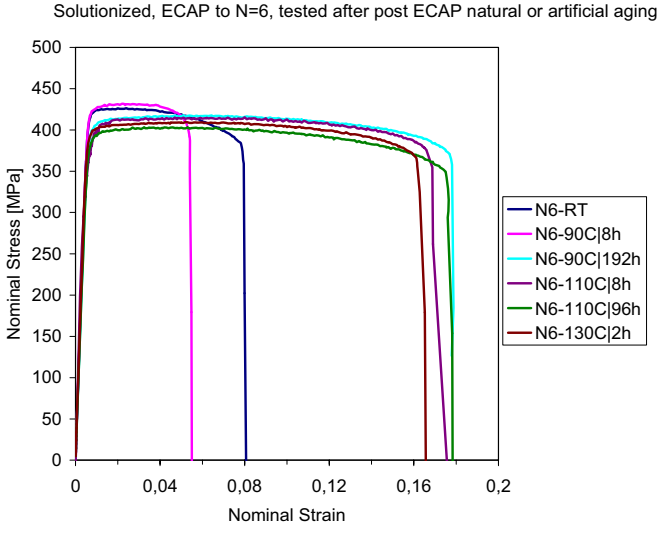

Figure 6.10: Nominal stress-strain curves for samples ECAP'ed in the solutionized state to N=6, followed by low temperature artificial aging. Initial strain rate ~0.01s^{-1}.

6.3 Discussion

The experimental findings presented above give important information on the effect of ECAP and the severe plastic deformation (SPD) on mechanical properties for the selected commercial Al-Mg-Si alloy. It should be pointed out that material states involved are selected in such a way that the effects of precipitates can be minimized. However, the solutionized and T4 conditions have both potentials for dynamic precipitation during SPD. Thus, the post-ECAP aging potential regarding properties is discussed briefly.

6.3.1 Influence of SPD strain accumulation

For all samples processed in this study an increase in imposed strain results in an expected strength increase as shown in Figure 6.11. This increase is influenced by both initial material condition and the deformation path (i.e. processing route).

Due to the sub-micron grain size obtained by SPD, the interaction length is short, the dislocation generation rate is high (geometrically necessary) and the dislocations can easily migrate to the grain boundaries and contribute to increase the misorientation between grains and across dense dislocation walls. A normal assumption is that the dislocation barrier strength is increasing with increasing misorientation. Therefore, the accumulation of misorientation with increasing strain is believed to contribute to the observed strength increase.

It is clear from Figure 6.2 and Figure 6.1 that the soft annealed and homogenized materials are about to reach maximum strength after 8 passes which means that the grains approach the smallest possible size obtainable by the present processing conditions. In addition one will expect dynamic precipitation to play a role, as will be discussed below.

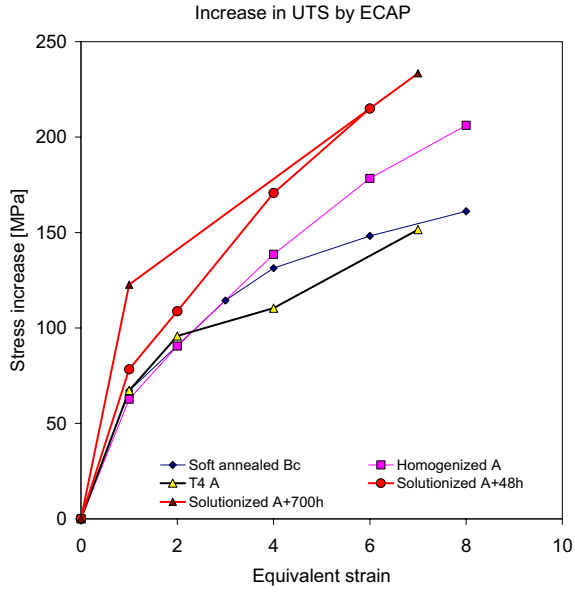

Figure 6.11: Increase in UTS after ECAP from different initial conditions, calculated from average values of ultimate tensile stress.

The largest increase in yield stress and UTS is observed after the first pass. The very large increase in yield stress compared to UTS after the first pass indicates a reduction in work hardening capability of ECAP processed materials i.e. the dislocation accumulation rate is already high and can not develop at the same rate when deformed in tension after processing. Also, a general trend is that necking appears at low tensile strain (close to the yield point) and is followed by a substantial post-uniform elongation before fracture.

The ductility has a large drop after the first pass, and is almost independent of the initial material temper. The values for elongation to failure drop to values between 9% and 4%, and stay almost constant with increasing SPD strain. However, the results presented above (Figure 6.9 and Figure 6.10) shows that the ductility can recover to ~18%, while keeping

mostly the tensile strength, if aged at low temperatures. The same behaviour is also observed for the uniform strain.

6.3.2 Influence of initial temper

Ferrasse et al. [40] studied the effect of pre-ECAP heat treatment (i.e. peak-aging and over-aging) on the development of sub-microstructure in the ECA processed 6061 Al alloy. They found that the ECA processed peak-aged material exhibited much higher strength than the ECA processed over-aged material, although both materials had similar dislocation barrier separation length of ~0.4μm. The increase in strength after ECAP, however, was more pronounced in the over-aged material (180%) compared to the peak-aged material (15%). They attributed this result to differences in the primary obstacles to dislocation motion. In the peak-aged state, fine particles formed during heat treatment serve more efficiently as obstacles to plastic flow than new dislocations created during the ECAP process, while in the soft annealed state, the new dislocations formed during ECAP are more effective than the precipitate particles which are now coarser and less dense.

There are four important matters on investigating the influence of initial material temper prior to ECAP: **a)** alloying elements in solid solution, **b)** size and distribution of hardening precipitates and particles, **c)** dynamic precipitation during ECAP processing, and **d)** the post ECAP aging potential.

The total effect of ECAP on the strength development, starting from different initial conditions, is best shown in Figure 6.12. Here the UTS is plotted against the initial temper for non-ECAP'ed and the two ECAP'ed conditions; N=1 and maximum imposed strain. The largest strength increase from ECAP is obtained from the solutionized state combined with natural aging at room temperature. The materials processed from underaged

condition have a potential for precipitation hardening, while material processed from T6 or overaged conditions cannot improve the strength by any sort of heat treatment. Also, the effect of ECAP on the tensile strength is lowest when the material is processed in the peak aged condition.

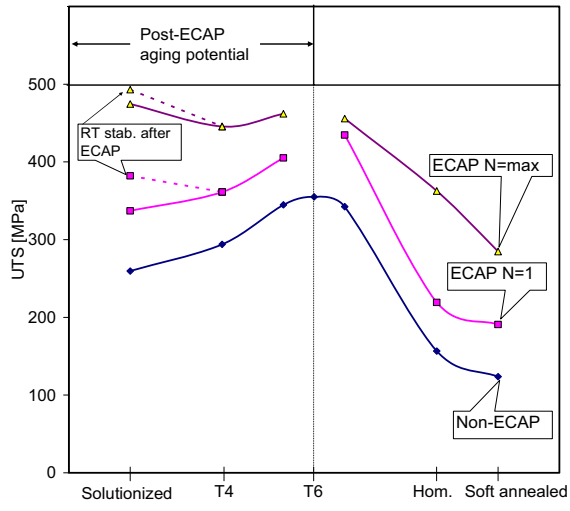

Figure 6.12: UTS as a function of initial material temper (average values of ultimate tensile stress).

Aging phenomena is accelerated in ECAP material. Increased dislocation density facilitates enhanced diffusion rates and nucleation of strengthening precipitates. Hence, incubation time for precipitate nucleation and the aging time to peak hardness are therefore reduced by SPD.

Comparing the tensile strain hardening behaviour between the T4 and solutionized material this is different. While the solutionized material shows no strain hardening after ECAP, the T4 material shows some strain hardening up to N=4 (see Figure 6.7). Condition T4 also gives the highest uniform strain and contraction strain at failure.

The difference in stress levels in Figure 6.2 and Figure 6.1 for the different initial tempers can to a large extent be explained by the amount of

alloying elements in solid solution. The soft annealed material has just the equilibrium amount of elements in solid solution. Coarse particles and the primary particles and dispersoids are distributed by the severe plastic deformation. This material has the lowest values of yield stress and UTS over the whole strain range investigated. Very low chemical potential for precipitation and less efficient dislocation barriers (particles) can explain these observations.

The homogenized material has also a small amount of alloying elements in solid solution before ECAP and the alloying elements are mainly presented as large primary particles along with dispersoids. Hence, the ECAP processed material shows the same development in yield stress and UTS as the soft annealed, but rises to a higher level of stress after large strains. The latter is probably due to a refinement of particle structure (i.e. strain induced particle break-up) which can contribute to work hardening. The grain refinement may also be affected by particle break-up, leading to a finer grain size, thus contributing to the strength increase.

The difference between the T4 and the solutionized material is somewhat more complex (Figure 1 to 4). In this case the different behaviour has to be explained as a combination of the amount of alloying elements in solid solution and post ECAP natural aging or dynamic precipitation during ECAP processing. The solutionized material has the highest amount in solid solution before ECAP, and therefore has a lower initial strength than T4, and higher work hardening potential. The two curves for UTS are crossing between the second and third pass (Figure 1). Here, the work hardening of the solutionized material is confining at higher rate and at the same time dynamic precipitation is occurring to a large extent (the solutionized material has also a driving force for dynamic precipitation during ECAP and natural aging after ECAP). The sample temperature during ECAP was monitored and never exceeded 40°C in the solutionized sample; however,

still dynamic precipitation is believed to occur at higher rate in the solutionized material. Please note that the solutionized samples were tested 48 hours after ECAP processing and thus had time for some natural aging to occur. The same material was also tested after post-ECAP room temperature stabilizing for 700h after one pass. In this case, post ECAP precipitation occurs concurrently with internal stress relaxation and precipitation hardening dominates the softening effect by stress relaxation. This leads to an increase in ductility from 5% for 48h to 6.5% after 700h storage at room temperature. Simultaneously, an increase in UTS from 340MPa to 380MPa is achieved. These properties are already higher than the T4 plus ECAP'ed material processed to the same strain ($\varepsilon = 1$).

As the imposed strain increases for each pass, the grain size and so the interaction length is becoming smaller and the activation energy for precipitation will decrease. Thus the potential for dynamic precipitation during ECA processing will increase with increasing strain until the solution content is starting to deplete and reduces the chemical potential for precipitation. The point where the dynamic precipitation hardening becomes more pronounced is where the T4 and solutionized curves cross, i.e. after a strain of 3.

The situation with regard to strength development with increasing SPD strain where different potentials for precipitation is presented can be visualized by the curves in Figure 6.12.

6.3.3 Strain path and cold rolling

In order to compare the influence of SPD strain path on the strength and ductility development, additional tests following the ECAP route Bc and classical cold rolling (CR) were performed.

For all tempers, the route Bc processed samples reach saturation first and cracking occurs at lower strains than in route A. For the homogenized

samples, route Bc gives higher yield stress and UTS up to 4 passes and then lower values at higher imposed strains. Route Bc gives a larger increase in yield stress and UTS for the T4 and solutionized samples. However, cracking occurs for the 5^{th} and 4^{th} pass respectively, while route A can be safely processed to 7 and 6 passes respectively, thus giving the highest values of yield stress and UTS since these conditions reach a higher maximum imposed strain.

It is also observed that the Bc processed samples in most cases yield lower elongation to failure, and in all cases give a lower strain at failure at the maximum imposed strain. There are also tendencies that the route Bc processed samples yields lower work hardening capabilities than route A at similar imposed strains. Generally the 6082 alloy in the present study reveals that route A seems to gain slightly better mechanical properties than route Bc, but no conclusion regarding the most efficient processing route can be drawn.

The reason why route A pressed samples can be processed to higher strains than route Bc is believed to be an effect of texture development. In route A, the majority of the active slip systems (measured from the texture) are aligned with a <110> slip direction in the pressing direction (up to 8 times random at N=8) or with a (111) plane parallel to the macroscopic shear plane and with the effective Burgers vector in the shear direction (8 times random at N=2). The reader can refer to chapter 7 for details on the texture development. Since no sample rotation is introduced between successive pressings, the crystallographic rotation needed to accommodate a high slip activity in the shear plane is low compared to samples processed by rout Bc, i.e. the textural hardening is higher in route Bc.

When comparing cold rolled material to ECAP'ed material at the same effective imposed strains, the textural difference may affect the mechanical properties differently. Cold rolled material is known to possess a strong

texture, while the ECAP'ed material has a relatively weak texture in comparison. However, the textures are different; in ECAP, the crystalographic slip direction tends to align with the macroscopic shear plane, while for cold rolling there are more than one shear plane. This means that the texture strength is not necessarily comparable between the two processes. Also, the fractions of high and low angle boundaries are different for the two processes. This will probably affect the tensile strain behaviour as well as the tensile work hardening. Generally, cold rolled materials and ECAP'ed materials are responding similarly to strain accumulation when strength is under concern. Ductility and post uniform deformation is however different in the two processes.

6.3.4 Further comments on precipitation

It is well known that alloys containing supersaturated solutes tend to form precipitates upon plastic deformation (i.e. dynamic precipitation). This effect is, of course, exhibiting higher kinetics and growth rates at elevated temperatures due to enhanced diffusion rates.

Kim et al. [38, 39] studied the effect of post-ECAP aging on mechanical properties in the 6061 Al alloy and later the 2024 Al alloy [42], and found that pre-ECAP solution treatment combined with post-ECAP low-temperature aging is very efficient in enhancing the room temperature strength of these heat treatable alloys. The 2024 alloy with post-ECAP heat treatment achieved higher strength in combination with higher ductility compared to the ECA processed alloy without post ECAP heat treatment.

In the present study, an increase both in strength and ductility was observed at N=1, while at higher strains, N=6, the strength dropped slightly while the ductility increased by a factor 2 or more.

Comparing the results from Kim et al. [42] with the results from [35] on the 2024 Al alloy, the ECAP'ed samples processed from the fully annealed

state by Horita et al. exhibits much lower yield stress than the 2024 Al alloy ECA-processed in the solutionized state by Kim et al. (~320 vs. 570MPa) even though the former material was processed to higher strains (4 vs. 1) and at lower temperature (293 vs. 433K). This is supposed to be related with the difference in dislocation accumulation rate during ECA processing [42].

These results are comparable to the present observations; solutionized material pressed to $\varepsilon=1$ has higher UTS than the soft annealed material pressed to $\varepsilon=8$.

Due to the fact that the nucleation of incoherent precipitates causes considerable increase of the surface enthalpy [148] the precipitation of these types of precipitates is hindered at undisturbed parts of the lattice. In the vicinity of grain boundaries, dislocation loops, and the cores of both edge and screw dislocations, the coherency of the lattice is more or less destroyed, therefore, the nucleation of precipitates with interfaces partially or even totally incoherent with regard to the ambient matrix, is favoured by these types of lattice faults. In these cases the increase in surface energy required to form nuclei of these types of precipitates is significantly lower at these lattice faults as compared to fault free parts of the matrix. In other words, the critical size of nuclei is much smaller in disturbed regions of the lattice as opposed to the undisturbed parts. In addition can two-dimensional faults such as grain and twin boundaries, stacking faults, interfaces or zero dimensional vacancies interstitials support heterogeneous precipitation.

In the case of SPD processing, the fault generation and dislocation density is very high. This will facilitate heterogeneous nucleation during and after SPD processing. The nucleation rate for heterogeneous precipitation will most likely overpower the rates for homogeneous precipitation.

For a more comprehensive treatment of the mechanisms and quantitative description of heterogeneous precipitation in solids, the reader could see [148, 149].

Since the grain boundaries tend to occupy increasing volumes with increasing strain, these sites may serve effectively to enhanced heterogeneous nucleation. If the free energy for nucleation of a spherical nucleus is taken as ΔG_H and that of the grain boundary is ΔG_B, then the nucleation rate for a given grain size $\overline{D}$ is changed from homogeneous rate by the amount [148]:

$$\frac{\delta}{\overline{D}} \exp\left(\frac{\Delta G_H - \Delta G_B}{kT} \right)$$

Equation 6.1

where δ is the grain boundary thickness, k is the Boltzman constant and T is the temperature in Kelvin. Hence, assuming $\delta = 0.05 \mu m$ the heterogeneous nucleation rate will be faster than homogeneous nucleation if:

$\Delta G_H - \Delta G_B \geq 8kT$ for a grain size $\overline{D} = 100 \mu m$ and

$\Delta G_H - \Delta G_B \geq 2kT$ if the grain size is reduced to $\overline{D} = 0.3 \mu m$

This indicates a factor 4 increase in heterogeneous nucleation probability by lowering the grain size from $100 \mu m$ to $0.3 \mu m$.

The barrier to nucleation of the new phase is reduced because of its formation at a grain boundary. The required diffusion of solute takes place along the grain boundary and thus, since it involves lower activation energy, will tend to be the dominant diffusion mechanism at relatively low temperatures.

Furthermore, the strain energy around dislocations is considered to assist the nucleation process at the dislocations because it is assumed that forming

precipitates lower the strain around the core of the dislocation [150]. It is obvious that nucleation at dislocations is favoured with respect to the undisturbed parts of the matrix, because the strains associated with the homogeneous nucleation is a barrier to precipitation. The precipitation rate at dislocations will be high; presuming the density of dislocations is sufficiently large.

As suggested by Cahn (1957) [151], the strain energy of the forming precipitate can balance the strain energy of the dislocation and hence reduce the total strain energy and increase the nucleation rate $\dot{N}_V$ of the precipitate. A dimensionless parameter α was introduced by Cahn to describe the effectiveness of dislocations to lower the free activation energy for nucleation, ΔG^*, of spherical precipitates:

$$\alpha = \frac{\Delta G_C \cdot G \cdot b^2}{2\pi^2 \cdot \sigma^2}$$

Equation 6.2

where ΔG_C is the specific chemical free energy of the precipitate, G is the shear modulus, b is the Burgers vector and σ is the specific surface energy of the precipitate / matrix interface.

A large value of α favours an activation energy reduction, i.e. higher nucleation rate at dislocations. If the nucleation can take place in an event where a dislocation is dissociated into two partials, this is believed to be the most effective nucleation [148].

Discontinuous precipitation may also occur on the grain boundaries and grow into the grains. In this case, nodules of a lamellar structure form at the grain boundaries and grow into the grains. The lamellae consist of plates or laths of precipitate embedded in the matrix, and the structure can form when

the temperature is so low that nucleation and growth of individual precipitate particles within the matrix occurs at a negligible rate. The precipitate only forms at an advancing interface [148], so that this mechanism may likely occur during grain subdivision, when new grain boundaries are formed and existing grains rotate against each other.

According to Cahn [152], the greatest volume nucleation rates for precipitates increase in the order; corner defects, edge / surface defects and grain boundaries. This may illustrate that small grained SPD processed alloys tend to favour heterogeneous nucleation. The present results give strong support to this suggestion.

6.3.5 The grain size effect: Homogenized, route A

The effect of grain size on tensile yield stress is empirically described as:

$$\sigma_Y = \sigma_i + \frac{k'}{\sqrt{D}}$$

Equation 6.3

commonly known as the Hall-Petch relation, where σ_Y is the yield stress, σ_i is the friction stress opposing motion of dislocations, k' is the "unpinning constant", measuring the extent to which dislocations are piled up at barriers and D is the high angle grain diameter. However, the Hall-Petch equation fails to describe correctly the grain size dependence at very small grain sizes. By extrapolating the Hall-Petch equation to the smallest imaginable grain sizes, the predicted yield stress approaches the theoretical shear strength. Results from molecular dynamics simulations suggest that maximum strength is achieved at the cross-over grain size ~20nm [153]. It has been reported by several authors [154]that the yield stress follows closer

to a $1/D$ relation at sub-micron grain sizes, where D is the boundary separation length, including both low angle and high angle boundaries:

$$\sigma_Y = \sigma_i + \frac{k}{D}$$

Equation 6.4

In the present work, the boundary separation length is calculated from the grain area, which is defined as areas surrounded by continuous boundaries with misorientations larger than 2°, as the diameter of a circle having the same area.

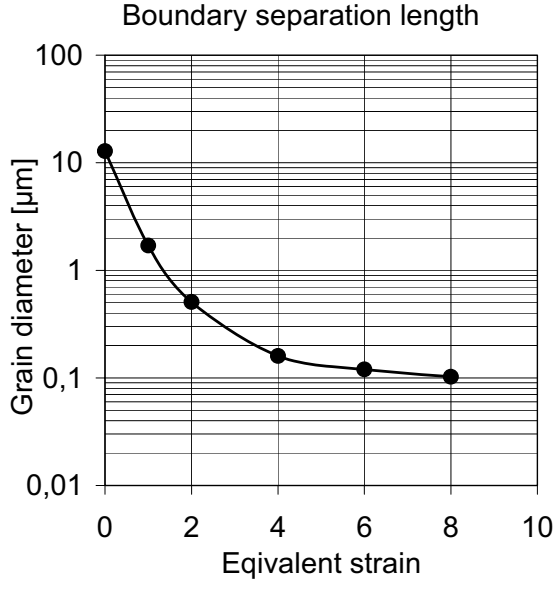

Figure 6.13: Development of boundary separation length with equivalent strain in homogenized material (from 2° misorientation).

The separation length is measured to ~1.7μm after the first pass and decreases continuously by increasing strain to a value of ~0.12μm after 8 passes (Figure 6.13).

A simple 1/*D* relation fits reasonably well with the measured boundary separation length and yield stress, starting from the first pass (i.e. at an equivalent strain of 1) with a *k* value of $13 \cdot 10^{-6}\, MPa \cdot m^{-1}$ and σ_0 value of 205MPa. The 1/*D* relation over-predicts slightly the yield stress at equivalent strains between 2 to 7 and under-predicts at an equivalent strain of 8. Equation 4 does not take into account the fact that high angle boundaries may act as stronger barriers for dislocation movement than typical low angle boundaries.

An attempt was made to consider the different strengths of high angle and low angle boundaries by modifying Equation 6.4 to Equation 6.5:

$$\sigma_Y = \sigma_0 + f_{HAB} \frac{k_{HAB}}{\overline{D}_{2^\circ}} + f_{LAB} \frac{k_{LAB}}{\overline{D}_{2^\circ}}$$

Equation 6.5

σ_Y = yield stress

σ_0 = friction stress opposing motion of dislocations = 205MPa

f_{HAB} = fraction high angle boundaries (15°<θ<62.8°), measured

f_{LAB} = fraction low angle boundaries (2°<θ<15°), measured

$\overline{D}_{2^\circ}$ = Boundary separation length (grain diameter), boundaries > 2°, measured

k_{HAB} = Strength factor for high angle boundaries = $16 \cdot 10^{-6}\, MPa \cdot m^{-1}$

k_{LAB} = Strength factor for low angle boundaries = $5 \cdot 10^{-6}\, MPa \cdot m^{-1}$

Here, the *k/D* term is divided into two parts, one for high angle boundaries and one part for low angle boundaries. Also introduced is a normalizing of the respective parts represented by the fraction high angle boundaries and low angle boundaries respectively. Theses fractions are measured values. A good fit between the modelled and measured values for tensile yield stress was reached by assuming the high angle boundaries possess barrier strength 3.2 times stronger than low angle boundaries. The results are presented in Figure 6.14 and Figure 6.15.

Please note that the results presented below are based on a single set of experiments. The curve fitting based on Equation 6.5 should be tested on an independent set of experiments and compared to the results presented in Figure 6.14 and Figure 6.15.

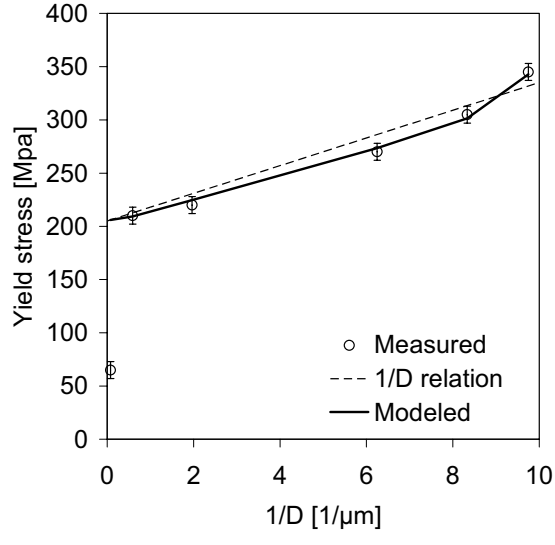

Figure 6.14: Yield stress dependency on boundary separation length from homogenized and ECAP'ed material (Route A). Circles are measured values, solid line is modelled from Equation 5 and stippled line is the 1/D relation.

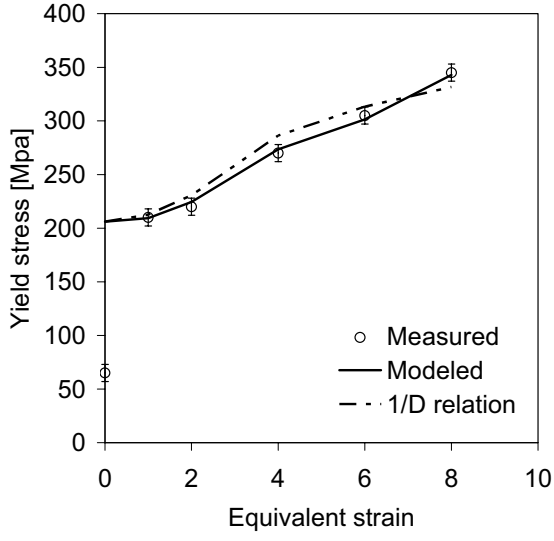

Figure 6.15: Yield stress as a function of equivalent strain from homogenized and ECAP'ed material (Route A). Circles are measured values, stippled line is the 1/*D* relation and the solid line is modelled from Equation 6.5.

6.4 Conclusions

The commercial AA6082 Al-Mg-Si alloy has been processed successfully by ECAP at room temperature to strains ε=6 to ε=8. The alloy has been processed in the solutionized, T4, homogenized and soft annealed states. The highest tensile strength was obtained from the solutionized material, followed by T4, homogenized and soft annealed. This behaviour is linked to the solid solution content prior to ECAP and the potential for dynamic precipitation during ECAP processing.

The tensile elongation to failure drops to a constant level between 4% and 9% after ECAP and is highest for the soft annealed and lowest for the solutionized material. The ductility in the solutionized material can, however, recover to ~18% elongation to failure by low temperature heat treatment with only a small drop in tensile strength.

Soft annealed and ECAP'ed material has been compared to cold rolling to similar strains. The tensile strength response to accumulated strain is similar, but the ductility and post uniform deformation is different. However, the ECAP'ed material can be processed to higher strains and, thus, achieving higher strength.

7 MICROSTRUCTURE AND TEXTURE DEVELOPMENT IN THE DEFORMATION ZONE

7.1 Introduction

Recent years, lots of work has been published concerning the microstructure and texture of ECAP'ed materials [for references, please refer to section 2]. The deformation mechanisms are not yet fully understood neither is the texture development. All work, so to say, has been made on samples pressed one or several times through the die and the conclusions have been made on the basis of fully pressed samples. In this work, the microstructural and textural developments are followed trough the deformation zone in the first and second pass of route A, so as to cover the full deformation history and revealing in more detail the mechanisms of early grain subdivision coupled with the local and global texture development. The scientific approach has been to fully map the microstructure and all crystal orientations in the deformation zone by use of high resolution EBSD measurements coupled with strain measurements and XRD texture data. In the following, the most important findings are presented and discussed, but there are still lots of details hidden in the obtained EBSD maps, that reach beyond the scope and time limit of the present work.

7.2 Experimental

All data in this work is referred to the global orthogonal XYZ-coordinate system (Figure 7.1). Some parameters, however, is referred in the local stream-line coordinate system, ED-TD-ND, where ED is the extrusion direction and follows the stream lines. This direction is the same as the grid lines in the longitudinal direction. The TD and ND directions are

normal to the ED direction. The two coordinate systems are shown in Figure 7.1.

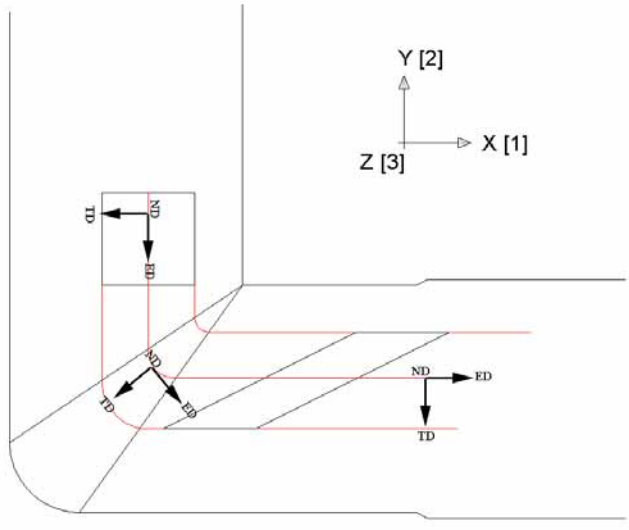

Figure 7.1: The orthogonal (X, Y, Z) indicates the global coordinate system, while (ED, TD, ND) refers to the local streamline coordinate system. Red lines show the streamlines. Positive rotation direction is from X towards Y. ***Positive X direction is in the direction of the exit channel.***

All observations are made in the XY plane. In the texture measurements, all (111) pole-figures are given in the XY-frame and all (110) pole-figures are given in the XZ-frame (by rotating the data sets). **Please note that the EBSD maps in this work are recorded in the XY-plane, rotated 45° about the Z axis, as shown in Figure 7.32.** The (111) pole-figures shown in relation to EBSD maps are oriented according to the maps, i.e. rotated 45° about Z (left on the map corresponds to left in the pole figure and up to up etc.). All pole figures have their coordinate axis drawn onto them.

EBSD mapping has been performed on a coarse scale for texture measurements (step-size 2-4μm) and fine scale for detailed microstructure (step-size 0.03-0.4μm). The EBSD maps are linked to the strain

measurements in order to have texture / microstructure development as a function of strain.

The term orientation describes here the orientation of the principle axes of a crystal ($\mathbf{e}_i^C$) relative to the principle axes of the sample ($\mathbf{e}_i^S$). The Euler angles are the three rotations about the principle axes of the crystal that will bring the crystal axes into coincidence with the principle axes of the sample. In the case of Bunge's form of the Euler angles (φ_1, Φ, φ_2) this is a rotation (φ_1) about the $\mathbf{e}_3^C$ axis followed by a rotation (Φ) about the new $\mathbf{e}_1^C$ axis followed by a third rotation (φ_2) about the rotated $\mathbf{e}_3^C$ axis again. The angles φ_1 and φ_2 range from 0 to 2π and Φ ranges from 0 to π. These limits form a bounded space referred to as Euler space (Figure 7.2).

The orientation notation may also be given as (hkl)/θ, where (hkl) is the crystal plane normal which corresponds to the Z-axis, and θ is the angle describing rotation around the plane normal. In this special case, the angle θ corresponds to φ_1 in Bunge's description of the Euler angles.

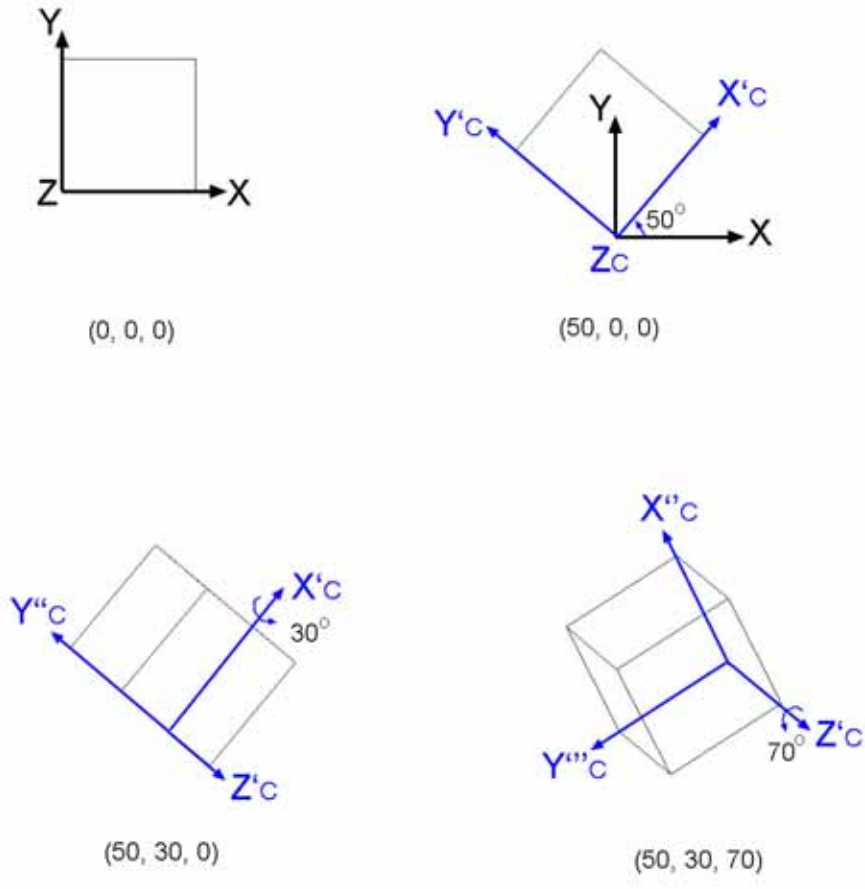

Figure 7.2: Definition of the Euler angles in the Bunge notation. Above is an example of the rotations for the orientation (50,30,70). Firstly, the crystal is rotated 50° (φ_1) about the e_3^C axis (Z). The new crystal axis are now denoted X'c, Y'c and Zc. Secondly, the crystal is rotated 30° (Φ) about the new e_1^C axis (X'c), moving Y'c into Y''c and Zc into Z'c. Finally, the crystal is rotated 70° (φ_2) about the rotated e_3^C axis (Z'c), moving Y''c into Y'''c and X'c into X''c.

7.3 Strain measurements in the deformation zone

The actual strain history of an element moving through the die was calculated from the scribed grids and analyzed using the commercially available strain analysis software ASAME® [147]. The effective plastic strain is determined using the following relationship:

$$\varepsilon_{eff} = \frac{2\sqrt{\varepsilon_x^2 + \varepsilon_y^2 + \varepsilon_x \varepsilon_y}}{\sqrt{3}}$$

Equation 7.1

where ε_x, ε_y and ε_{xy} are the strains along the x and y axis and the shear strain in the (xy) plane, respectively. The strain measurement accuracy is ±2%. A closer look at the sample shape and strain contours(Figure 7.3) reveals and validates some typical features of ECAP already observed in experiments and simulations [9, 13, 141, 145, 146].

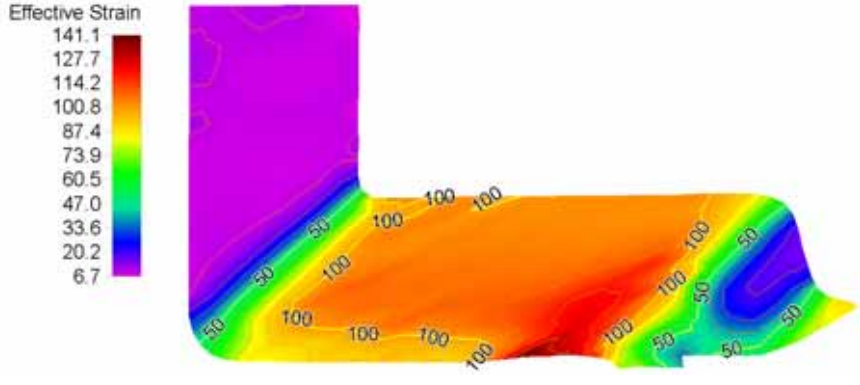

Figure 7.3: Measured strain distribution (effective strain in % values, nodal strains) in ECAP'ed sample, homogenized, 1st pass.

The process does not provide homogeneous strains in the whole sample, especially in the front-end part, but only in a zone located in the upper part of the sample. The sample front-end is slightly bent up and experiences low strains. The lower part of the sample undergoes heterogeneous strains due to friction and flow path dissimilarity over the die corner. Moreover, the shear deformation occurs over a wide zone, or fan, rather than along a line (Figure 7.4). However, a strain gradient is present across the work-piece corner and high strains in the order of 1.1 are reached at the exit of the deformation zone.

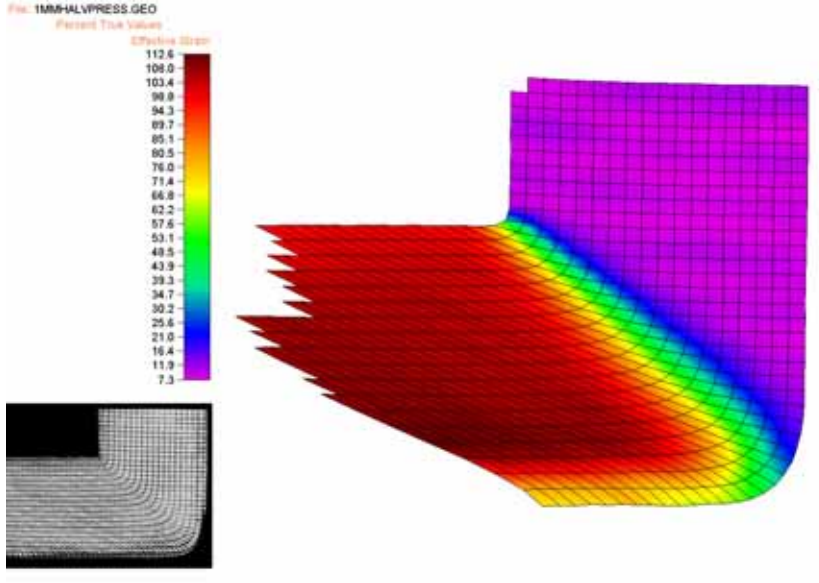

Figure 7.4: Strain measurement of the whole deformation zone from the first pass. Grid size 1×1 mm^2. Effective nodal strain colour-map.

Special attention has been made to the deformation zone. Separate measurements were made on the same sample which was investigated by EBSD (see the following sections). The deformation zone from the first pass

is shown in Figure 7.4 and the specific area analyzed by EBSD is shown in Figure 7.5 and Figure 7.6.

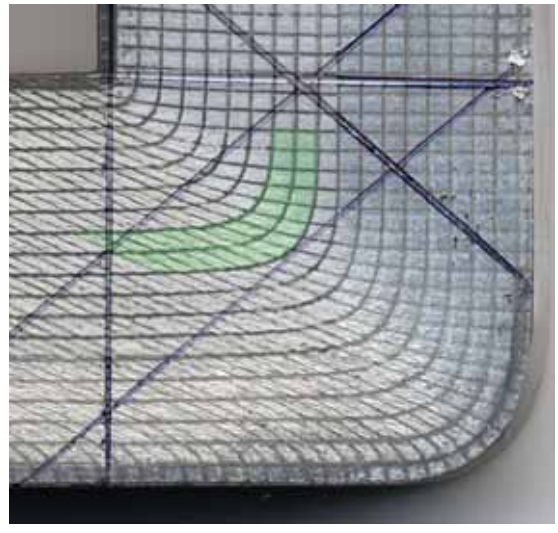

Figure 7.5: Sample for EBSD drawn onto the deformed billet. The green marked area corresponds to Figure 7.6.

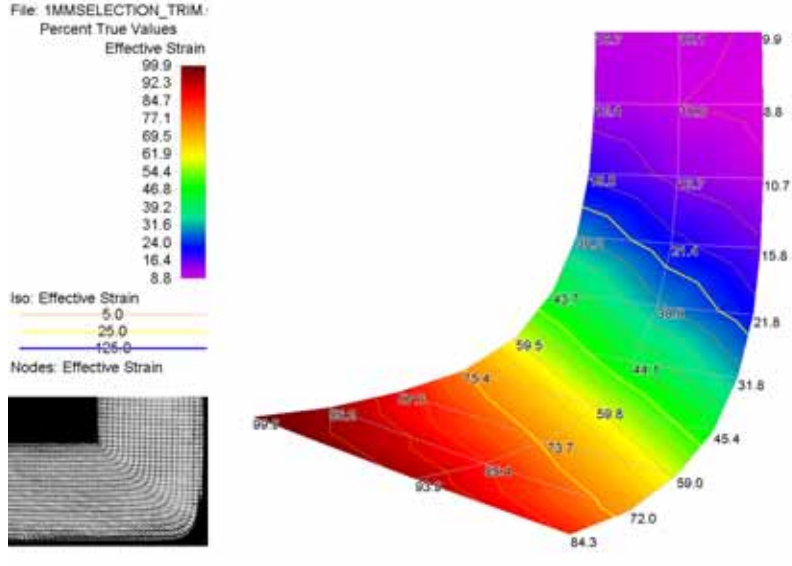

Figure 7.6: Strain measurements along two neighbouring flow paths, which have been redrawn in the streamline coordinate system in the following two figures. The lower path corresponds to Figure 7.8 and the upper path to Figure 7.9.

The deformation mode can be interpreted by the logarithmic strain tensor components (Figure 7.7) calculated in the ED-TD frame from the two central grid lines in Figure 7.6. The measured strain tensor is later used for calculation of Taylor factors in section 7.5.

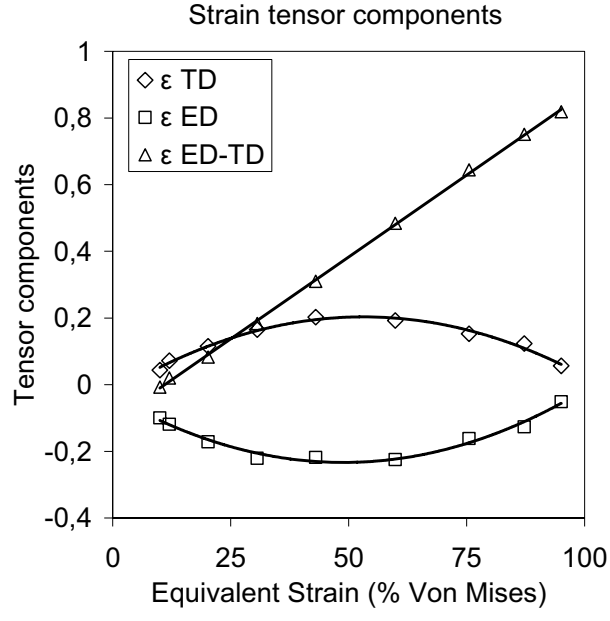

Figure 7.7: Measured strain tensor components as a function of equivalent strain. Positive=tension, negative=compression.

The strain accumulation is gradual and increasing to an effective strain of ~1.1. The starting values are non-zero, due to compression of the sample in the upper die-channel. The deformation mode is not simple shear as has been commonly assumed, but is in fact a combination of pure and simple shear combined with tension and compression. The material elements start off by experiencing compression along ED and tension in TD. (By incremental values, the derivatives, the compressive and tensile components

change sign at ~50% strain). The shear component is continuously increasing through the deformation zone.

The two central grid lines (Figure 7.6) have been redrawn in the stream line coordinates to visualize the actual strain path (Figure 7.8 and Figure 7.9).

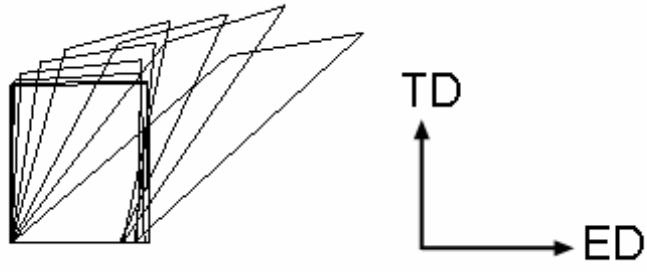

Figure 7.8: Strain path 1 in the stream line coordinate system.

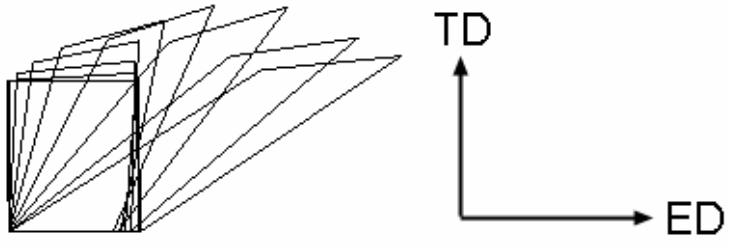

Figure 7.9: Strain path 2 in the stream line coordinate system.

7.4 Texture development

7.4.1 Introduction

The characterization of the texture development through the deformation zone is based on EBSD maps, covering a zone in the centre of the sample and throughout the deformation zone (Figure 7.5). From the *first pass*, overlapping maps were collected covering from ~200 to ~1000 original grains each (i.e. representing 2 to 6mm^2), and which are based on a 3 to 5 μm step-size. The crystalographic measurements are from selected areas separated at strain range intervals of ~0.1. The corresponding textures from the first pass are calculated using the harmonic series expansion with a series rank of 16 and Gaussian smoothing of 1°.

Due to a more refined microstructure, the texture development in the *second pass* (route A) was measured using different scan parameters. Three different maps were made at 10%, 50% and 100% effective strain into the 2nd pass. Each measurement was covering an area of 1x0.3mm^2, mapped with a step size of 8μm. The textures from the second pass are calculated using the harmonic series expansion with a series rank of 22 and Gaussian smoothing of 5°.

In addition, global XRD texture measurements were made at the end of first, second, third, fourth, sixth and eighth pass and ODF's were calculated using the harmonic series expansion with a series rank of 32 and Gaussian smoothing of 5°.

The different texture calculation parameters (series rank and Gaussian smoothing) were chosen as a result of different scan-parameters and measuring techniques in order to get comparable results regarding texture index.

The texture measurements are represented as (111) pole figures in the XY-plane and (110) pole figures in the XZ-plane as well as ODF sections

covering the most important part of the orientation space (φ1=0-180°, Φ=0-180° and φ2=45°). For definition of the sample orientation, see Figure 7.1, for orientation notations, please refer to Figure 7.2.

7.4.2 Identification of the ideal texture components

The typical ECAP texture (at the end of each pass, route A) has been elaborated by the present author, and is found to be a combination of a few stable orientations which are, in the present work, referred to as the ideal ECAP texture components. The components have been identified in the present work and are listed in Table 7.1.

Table 7.1: The ideal ECAP texture components in the present case for FCC aluminium pressed by route A. Here, eqv. is an equivalent orientation in the same section of Euler space. The components are given as crystal directions in the global X, Y and Z directions, Euler angles and as (hkl)/θ notation for easy reference in the following chapters.

	Crystal directions in the global X, Y and Z directions			Euler angles			(hkl)/θ
Texture component	X	Y	Z	φ1	Φ	φ2	
A_{2E}	[-3 3 25]	[25 -25 6]	[1 1 0]	99.74	90	45	(110)/105
A_{1E}	[-25 25 6]	[3 -3 25]	[1 1 0]	170.37	90	45	(110)/165
C_E	[71 -71 100]	[71 -71 -100]	[1 1 0]	**45**	90	**45**	(110)/45
A_E	[2 -20 9]	[20 -2 -9]	[1 1 2]	**45**	35.26	**45**	(112)/45
$-A_E$	[-2 20 -9]	[-20 2 9]	[1 1 2]	**45**	144.7	**45**	(112)/225
B_E	[27 -100 73]	[100 -27 -73]	[1 1 1]	**45**	54.74	**45**	(111)/45
			Eqv.	105	125.2	45	
			Eqv.	165	54.74	45	
$-B_E$	[-73 -27 100]	[73 -100 27]	[1 1 1]	105	54.74	45	(111)/105
			Eqv.	165	125.2	45	
			Eqv.	**45**	125.2	**45**	
D_E	[13 -12 7]	[8 4 -7]	[2 5 5]	**45**	105	**45**	(255)/120
Cube	[100]	[010]	[001]	**45**	0/180	**45**	(001)/45
			Eqv.	**135**	0/180	**45**	
Z-rotated cube	[-5-11 0]	[11-5 0]	[001]	**70**	0/180	**45**	(001)/70
			Eqv	**160**	0/180	**45**	

The active slip systems operating in the stable texture components when slip occurs at 45° to the X-axis are listed in Table 7.2.

Table 7.2: Active slip systems and corresponding Schmid factors operating in the stable texture components when slip occurs at 45° to the X-axis

Texture components	Active slip systems	Schmid factor
A_{2E}	(-111)<0-11> and (-111)<101>	0.433; 0.433
A_{1E}	(1-11)<011> and (1-11)<-101>	0.433; 0.433
C_E	(111)<0-11> and (-111)<0-11>	0.348; 0.348
A_E	(-1-11)<-110>	0.5
$-A_E$	(111)<-110>	0.5
B_E	(-1-11)<-110>	0.471
$-B_E$	(111)<-110>	0.471
D_E	(111)<0-11> and (111)<-110>	0.405; 0.384
Cube	(1-11)<011> and (-111)<011>	0.408; 0.408
Z-rotated Cube	N.A.	N.A.

The ideal texture components have one common feature, i.e. the principal shear direction. These ideal orientations all have a <110> crystal direction aligned in the principal shear direction (45° to the X-axis) and in the XY-plane. Exceptions are the $\mathbf{A_{1E}}$ and $\mathbf{A_{2E}}$ components, alternatively *(110)/105 and (110)/165*, which both have a (111) plane aligned parallel to the principal shear plane, with the resulting Burgers vector in the principal shear direction. The general notation of all orientations having a <110> direction in the principal shear direction may be written in the Euler angles as ***(SD, Φ, 45)***, where ***SD*** is the principal shear direction and ***Φ*** is the rotation angle about the <110> direction, from 0 to 180°.

The positions of the ideal texture components in the φ2=45° ODF section are shown in Figure 7.10. Illustrations of the crystal orientations through the ***(SD, Φ, 45)*** fibre is shown schematically in Figure 7.11. The crystal orientations along with the Burgers vectors for the $\mathbf{A_{2E}}$ and $\mathbf{A_{1E}}$

components are shown in Figure 7.12. The pole figure presentation of the ideal texture components are shown in Figure 7.13 to Figure 7.19.

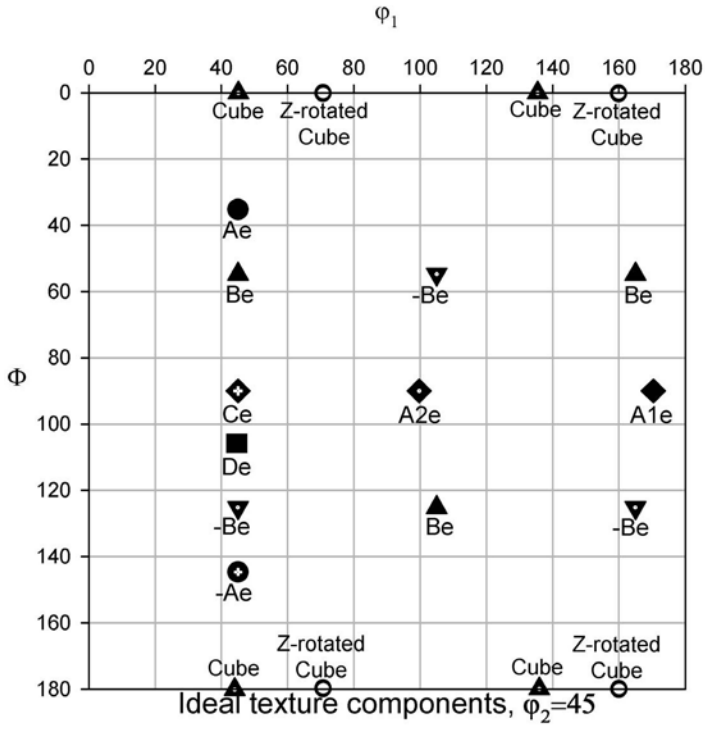

Figure 7.10: Location of the ideal texture components in the ODF section (0-180, 0-180, 45), based on observations and calculations of highest resolved shear stress in crystal orientations having either a slip direction or a slip plane aligned with the principal shear direction.

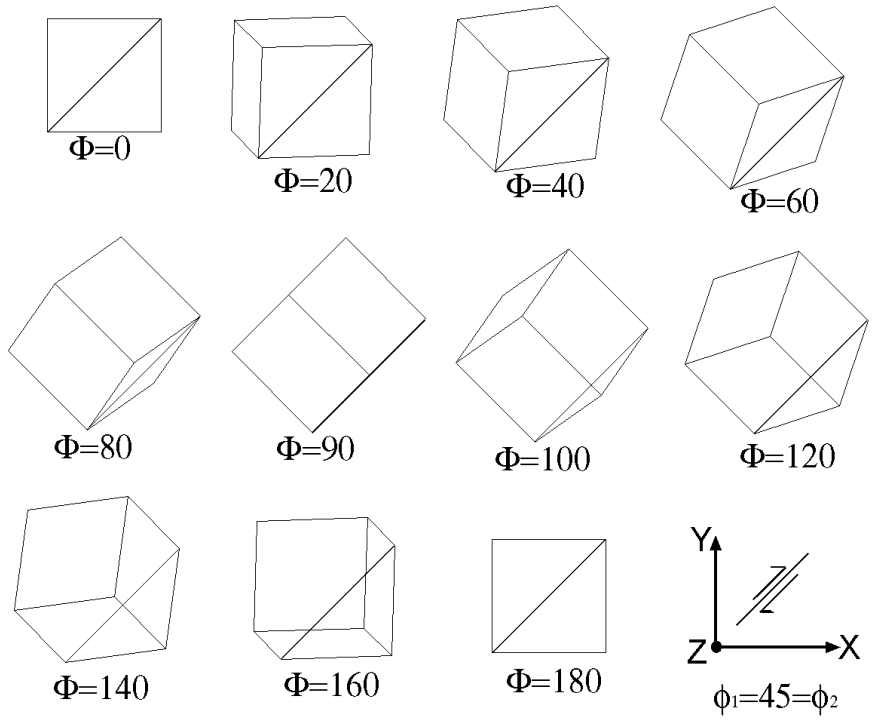

Figure 7.11: Illustration of the crystal orientations through the *(45, Φ, 45)* texture fibre. Shear is assumed to occur at 45° to the X-axis and in the XY-plane. The crystal rotates about the [110] crystal axis, which coincides with the principal shear direction.

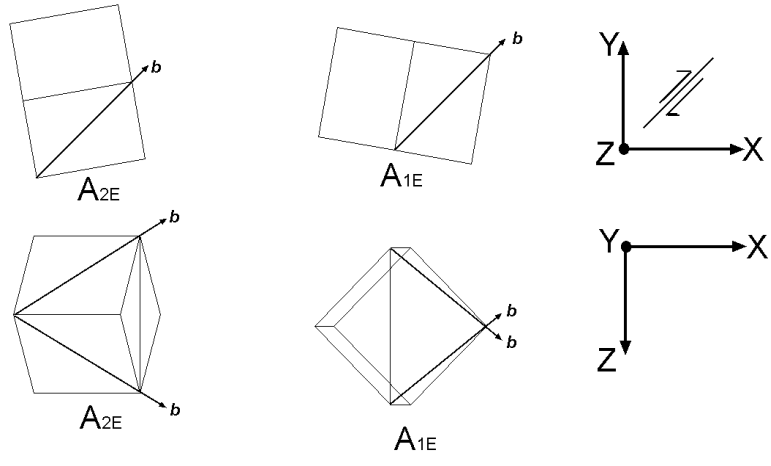

Figure 7.12: Illustration of the A_{1E} and A_{2E} crystal orientations. For ease of understanding, the crystals are projected in the XY and XZ plane, upper and lower figures respectively. *b* is the Burgers vector, i.e. the slip directions. The resulting Burgers vector is aligned at 45° to the X-axis and in the XY-plane.

Ideal texture components projected in the XY plane as (111) pole figures

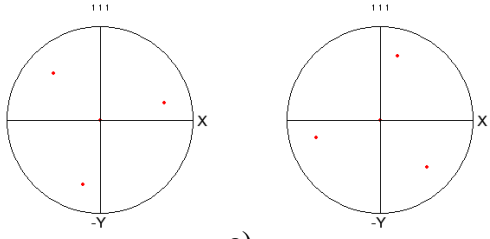

a) b)

Figure 7.13: a) (111)/45, B_E and b) (111)/105, $-B_E$

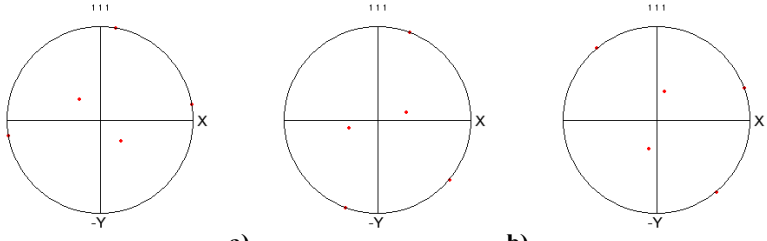

a) b) c)

Figure 7.14: a) (110)/45, C_E, b) (110)/105, A_{2E} and c) (110)/165, A_{1E}

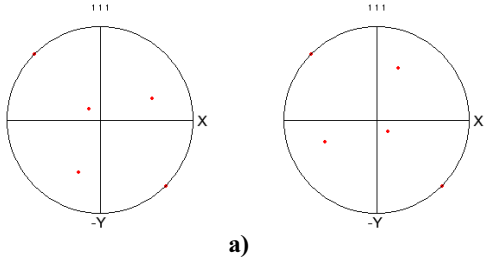

a) b)

Figure 7.15: a) (112)/45, A_E and b) (112)/225, $-A_E$

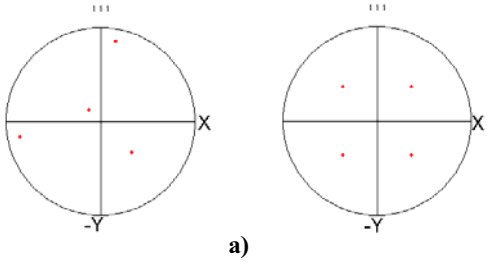

a) b)

Figure 7.16: a) (255)/120, D_E and b) (001)/45, Cube.

Ideal texture components projected in the XY plane as (110) pole figures

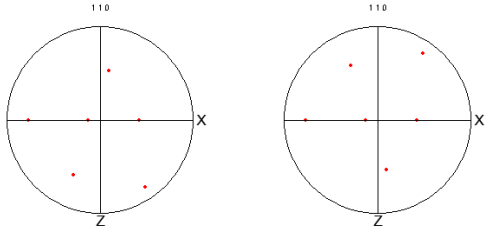

a) **b)**

Figure 7.17: a) (111)/45, B_E and b) (111)/105, $-B_E$

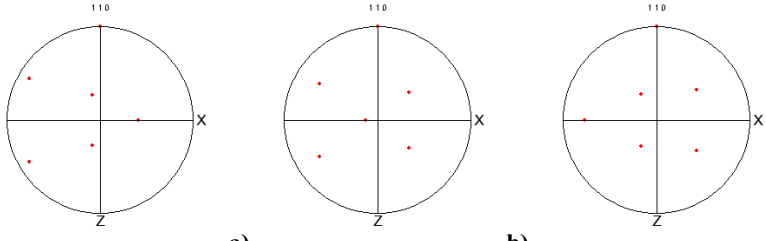

a) **b)** **c)**

Figure 7.18: a) (110)/45, C_E, b) (110)/105, A_{2E} and c) (110)/165, A_{1E}

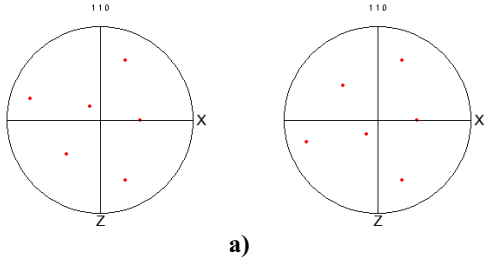

a) **b)**

Figure 7.19: a) (112)/45, A_E and b) (112)/225, $-A_E$

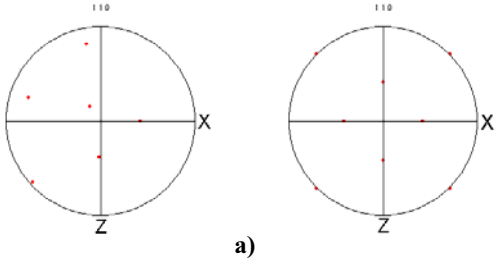

a) **b)**

Figure 7.20: a) (255)/120, D_E and b) (001)/45, Cube.

7.4.3 Texture development through the deformation zone in the 1st pass

The starting texture is very close to a random distribution (Figure 7.22a, Figure 7.23a and Figure 7.24a), which is as expected for a cast and homogenized billet. The texture strength increases continuously through the shear zone, as shown in Figure 7.21.

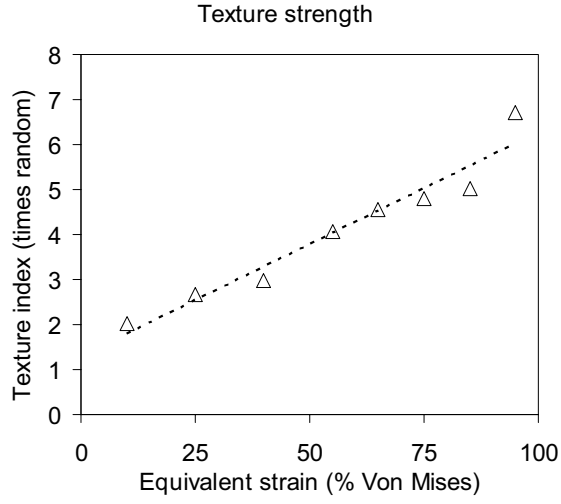

Figure 7.21: Observed EBSD texture strength as a function of equivalent strain in the central portion of the deformation zone through the first pass (taken as the (111) pole figure maxima). Open triangles are measured values; dotted line is a linear fit.

The typical ECAP texture appears at ~20% effective strain and increases in strength while becoming more well-defined with increasing strain (Figure 7.22a-h, Figure 7.23a-h and Figure 7.24a-h). All texture components are observed to rotate ~15° about the Z-direction (in the XYZ-frame) from the X-direction towards the Y-direction (positive rotation). This means that the principal shear direction starts at ~30° to the X-direction (at 20% strain), and rotates ~15° about Z-direction and ends up at ~45° to the X direction (at 100% strain). The angle of 45° corresponds to the intersection of the two ECAP channels.

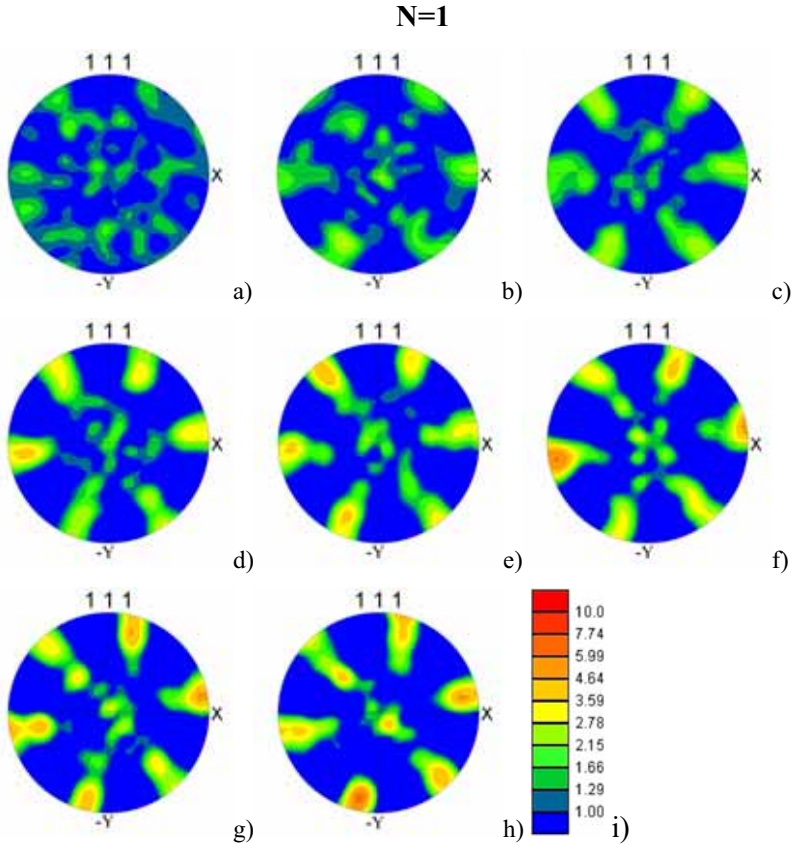

Figure 7.22: Observed EBSD (111) pole figures for a) 10%, b) 20%, c) 35%, d) 55%, e) 65%, f) 75%, g) 85% and h) 95% strain in first pass, i) Applied scale [times random]. Note that the pole figures are shown in the XY frame.

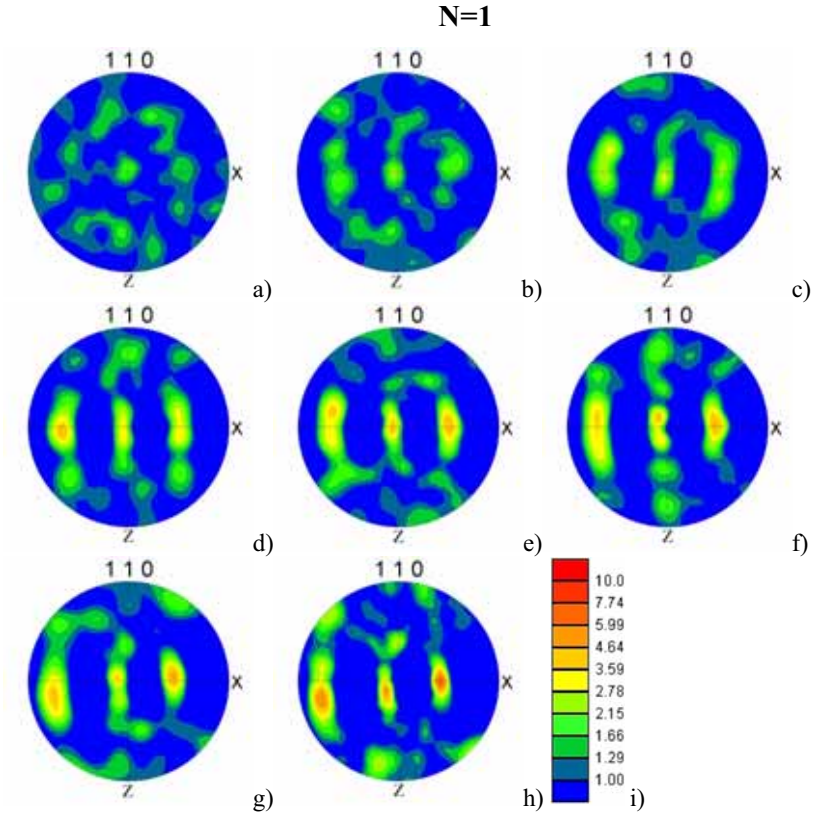

Figure 7.23: Corresponding observed EBSD (110) pole figures for a) 10%, b) 20%, c) 35%, d) 55%, e) 65%, f) 75%, g) 85% and h) 95% strain in first pass, i) Applied scale [times random]. Note that the pole figures are shown in the XZ frame.

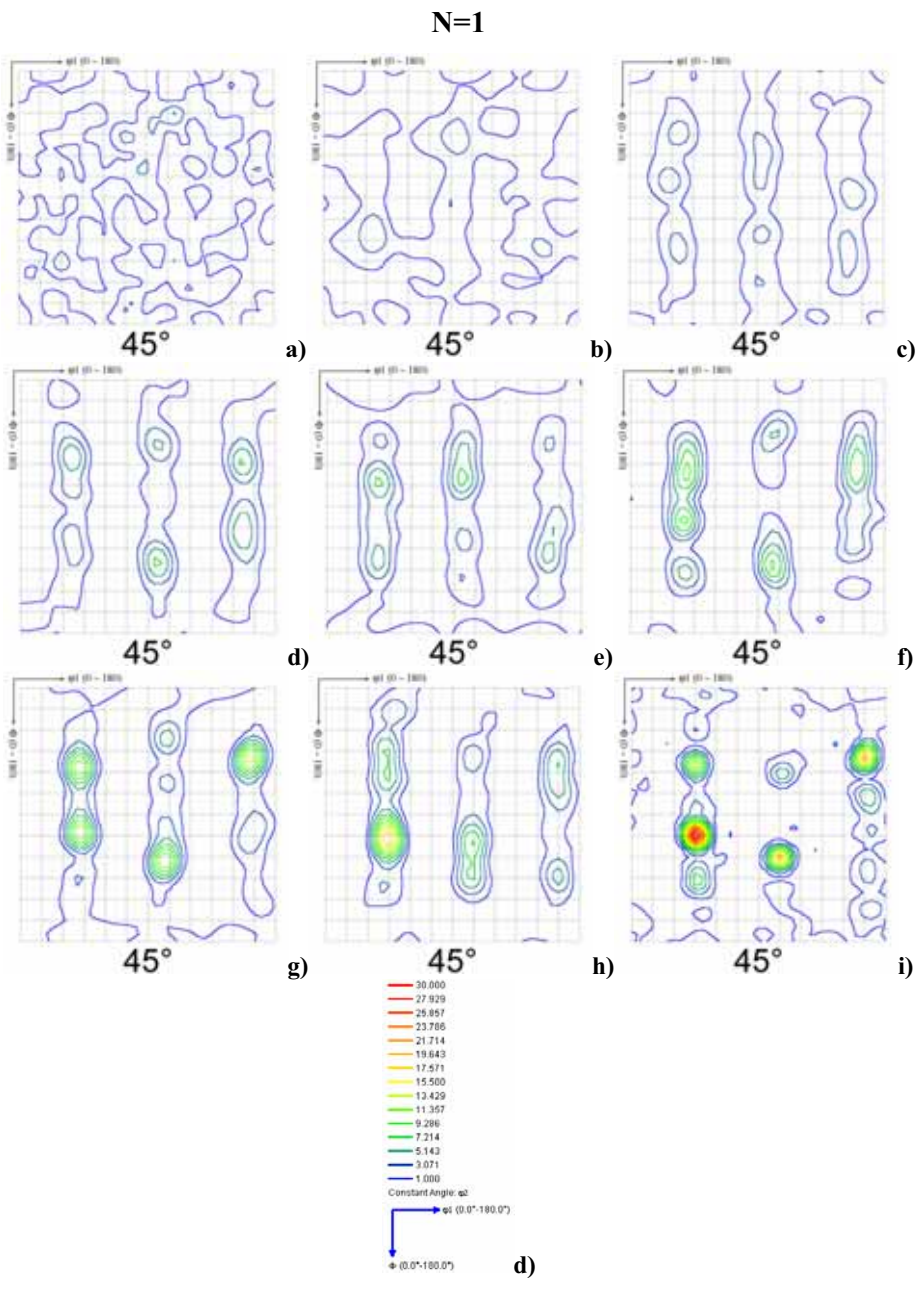

Figure 7.24: Measured EBSD ODF sections for φ_2=45° from the first pass, for a) 10%, b) 20%, c) 35%, d) 55%, e) 65%, f) 75%, g) 85%, h) 95% strain, i) 10% in to 2nd pass, rotated in to the coordinate system of first pass. d) Applied scale (times random)

The theoretical shear plane, as proposed by Langdon et al. [155], lies at 45° to the X direction at the intersection of the two channels, the (111) slip plane parallel to the shear plane, the <110> slip direction parallel to the direction of shear and the Z direction corresponds to the <112> direction. This crystal orientation corresponds to the $\mathbf{A_E}$ and $\mathbf{-A_E}$ texture components, which are only two of the ten observed texture components. At the same time, these components are observed (from the EBSD measurements) to be some of the weakest of them all. The latter can be seen from the observations in Figure 7.25, where the strength of the texture components along the (45, Φ, 45) fibre is shown. The strongest component is clearly the $\mathbf{D_E}$ component, followed by the $\mathbf{B_E}$ component.

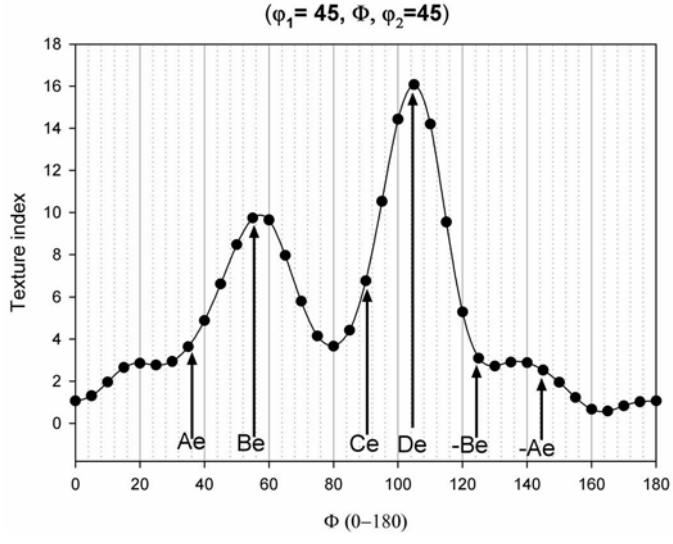

Figure 7.25: Measured intensities along the (45, Φ, 45) fibre after 1st pass (from EBSD). Arrows indicate the location of the texture component along the fibre.

However, the similar measurements made by XRD lists the $\mathbf{A_E}$ and $\mathbf{-A_E}$ components at the same intensity as the two $\mathbf{B_E}$ components, but still at only half the strength of the A_{1E} component (Table 7.3).

The gradual 15° rotation about the Z-axis suggests that the "shear plane" or more correct, the principal shear direction is not a single defined direction or plane, rather the deformation occurs over a finite "fan shaped" zone (Figure 7.26). This observation is also supported by the strain measurements, which shows that the width of the actual deformation zone in the specimen centreline is about ~5mm for this specific die design and high friction conditions. The actual width of the deformation zone is dependent upon the outer corner angle of the die, the friction in the die channels (hence also the back pressure) and the work hardening of the material [156].

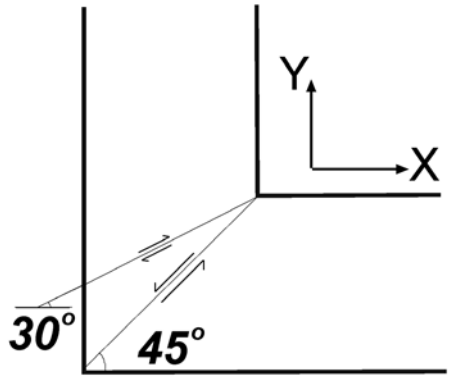

Figure 7.26: Illustration of the physical shear direction in the fan-shaped deformation zone, starting at 30°to the X-axis, finalizing at 45°to the X-axis. Note that the effective strain distribution is different as shown in Figure 7.4.

As pointed out in section 5.2.2, strain measurements also show that the deformation mode is not simply described by simple shear, rather a combination of shears along with tension and compression components. The measured strain tensor components (Figure 7.7) show that the shear component increases linearly with the equivalent strain, while a material element will experience compression in the ED direction and tension in the TD direction up till ~50% strain. Here the tension / compression is reversed, i.e. the material element will experience tension in the ED direction and

compression in the TD direction until the element has passed through the deformation zone where the final distortion of the element can be described by simple shear only.

It is believed that this mixed deformation mode, generated as a result of the fan-shaped deformation zone and ECAP geometry, is the reason behind the gradual texture component rotation. This is also supported by the texture modelling by Gholinia et al. [70], where they compared the texture generated from the mixed deformation mode generated by ECAP, and texture generated from simple shear. By using the actual observed strain tensor, they successfully reproduced the observed ECAP texture.

7.4.4 Texture development through the deformation zone in the 2nd pass

As expected, the measured starting texture in the second pass (Figure 7.27a, Figure 7.28a, and Figure 7.29a) is almost identical to the final texture from the first pass, but rotated -90° about the Z-axis according to route A. In the first pass, the texture components are observed to rotate ~15° about the Z-axis, according to the fan-shaped deformation zone which gradually changes the effective principal shear direction from 30 to 45° to the X-axis. In the second pass, the texture components are observed to rotate ~30° about the Z-axis, even though the angular width of the deformation zone is the same. By looking at the (111) pole figures in Figure 7.27, it appears like the whole texture rotates, however, by a closer look at the ODF sections in Figure 7.29, the process is more complex than that. The texture development during the second pass is partly a process of realignment of the stable texture components, i.e. by rotating the sample by route A, the already established texture components gets a new orientation in relation to the XYZ-coordinate system and may no longer be stable. At the same time as some components diminish due to their unstable orientation, other crystals will continue to rotate towards the stable components.

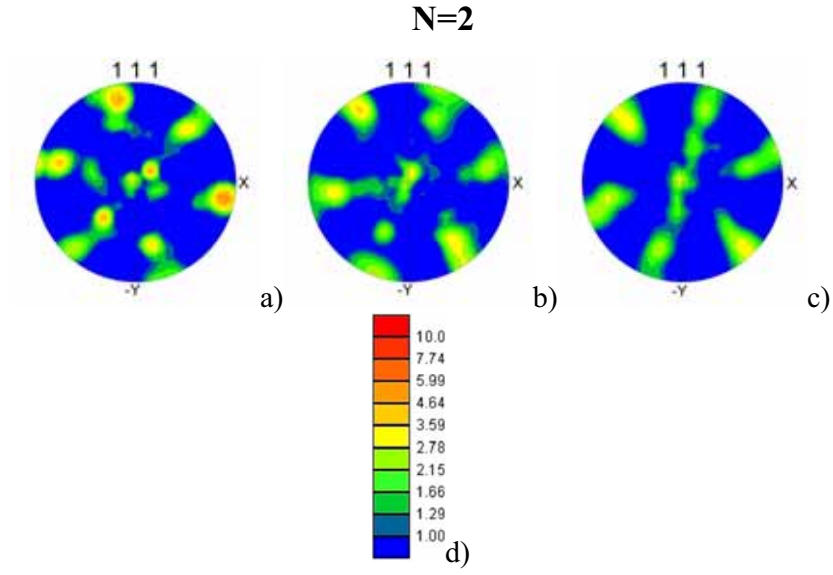

Figure 7.27: Observed EBSD (111) pole figures for a) 10%, b) 50% and c) 100% strain in second pass, d) applied scale [times random]. Note that the pole figures are shown in the XY frame.

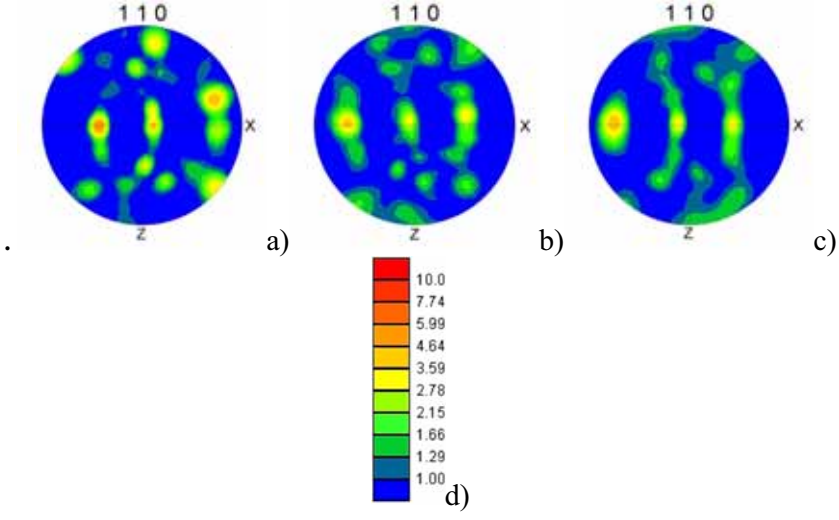

Figure 7.28: Corresponding observed EBSD (110) pole figures for a) 10%, b) 50% and c) 100% strain in second pass, d) applied scale [times random]. Note that the pole figures are shown in the XZ frame.

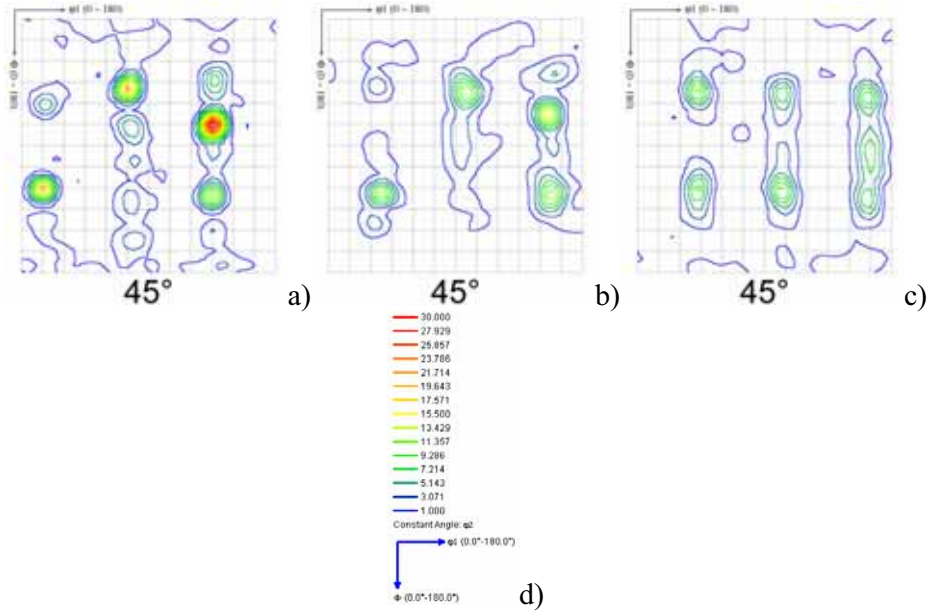

Figure 7.29: Measured EBSD ODF sections for φ_2=45° from the second pass, for a) 10%, b) 50%, c) 105% strain. d) Applied scale (times random).

By assuming that crystal rotation during the second pass will occur mainly as rotations about the Z-axis (in the XY-plane) due to the plane strain deformation mode, some predictions regarding the texture development can be made based on crystalographic considerations.

The $\mathbf{B_E}$ and $\mathbf{-B_E}$ components (***(111)/45*** and ***(111)/105***) are rotated -90° around the Z-axis (according to route A) into ***(111)75*** and ***(111)/15*** orientations. The "ideal" orientation for shear in the principal shear direction starts at ***(111)30*** and ***(111)/90*****,** i.e. the principal shear direction starts at 30° to the X-axis. These components may easily rotate about the Z-axis to the "ideal" orientations because the ***(111)/0*** components have three ***<110>*** slip directions located in the XY-plane. The $\mathbf{B_E}$ and $\mathbf{-B_E}$ orientations are therefore assumed to be stable orientations for ECAP by route A and therefore expected to increase in intensity with increasing number of ECAP passes.

Further, the $\mathbf{C_E}$ (***(110)/45***) component is rotated -90° around Z into ***(110)/315*** which is equivalent to ***(110)/135***. It is further believed that shear in the principal shear plane requires active ***<110>*** Burgers vectors parallel to the shear direction. The $\mathbf{C_E}$ component fulfils the ***<110>***||SD (shear direction) requirement, but the ***(110)/135*** orientation does not easily fulfil the requirement for <110> ||SD and is observed to diminish in the second pass and rotate into the ***(110)/165*** ($\mathbf{A_{1E}}$) or ***(110)/105*** ($\mathbf{A_{2E}}$) component.

Now, the $\mathbf{A_{2E}}$ (***(110)/105***) component is rotated -90° around Z into ***(110)/15.*** This orientation has a ***<110>*** direction at 15° to X, and will most probably rotate into ***(110)/30-45*** ($\mathbf{C_E}$) which fulfils the ***<110>***||SD requirement.

The $\mathbf{A_{1E}}$ (***(110)/165***) component is rotated -90° around Z into ***(110)/75***. This orientation has a ***<110>*** direction at 75° to X, and may rotate into the ideal $\mathbf{C_E}$ (***(110)/45***) orientation or into the $\mathbf{A_{2E}}$ (***(110)/105***) orientation.

The high resolved shear stress components, $\mathbf{A_E}$ and $\mathbf{-A_E}$ (***(112)/45*** and ***(112)//225***) are rotated -90° around Z into ***(112)/315*** and ***(112)/135***. These orientations will need to rotate ±17° about the Y-axis and 12-27° about the Z-axis to obtain a ***<110>***||SD. The $\mathbf{A_E}$ and $\mathbf{-A_E}$ components are observed to diminish in strength and may also rotate into the $\mathbf{B_E}$ and $\mathbf{-B_E}$ components.

The $\mathbf{D_E}$ (***(255)/120***) component is rotated -90° around Z into ***(255)/30***. This orientation has a ***<110>*** at 30° to the X-axis in the XY-plane and may thus be stable, but is observed to diminish in strength and rotate into the $\mathbf{B_E}$ or $\mathbf{A_{1E}}$ component during the second pass (Figure 7.29 a-c)

Finally, the **Cube** component is rotated -90° around Z into an equivalent orientation, i.e. the **Cube** component do not change its characteristic orientation by the sample rotation according to route A. However, the appearance of the **Z-rotated Cube** component in the second pass may be linked to the loss of intensity of the **Cube** component during the second pass.

By comparing the intensities of the different texture components from XRD texture measurements at the end of the first and second pass (Table 7.3 and Figure 7.30), one find support for the above assumptions and suggestions. Table 7.3 also includes intensities from the third, fourth, sixth and eight ECAP pass by route A. The respective ODF sections are shown in Figure 7.31.

Please note that the texture intensities from XRD measurements are lower than the respective intensities calculated from EBSD measurements. The reason for this is most likely due to different measurement methods. For the case of XRD, all reflections are measured, including particles, grain boundaries and other disturbances. In the case of EBSD, only the grain interior is measured and the measured area is much smaller. This combined effect is believed to result in higher intensities and larger variations in the textures calculated from EBSD measurements.

Table 7.3: Texture component intensities from XRD measurements, pass 1-8, route A

Intensities from XRD measurements (times random)						
Texture component	**1st pass**	**2nd pass**	3rd pass	4th pass	6th pass	8th pass
A_{2E}	**2**	**1.4**	4	2	2.5	1.4
A_{1E}	**6.4**	**8**	8	5	5.6	4
C_E	**5**	**4**	2.8	2.5	4	2.8
A_E	**3.2**	**2.8**	1	1	1.4	1.2
$-A_E$	**4**	**2.8**	1	1	1.4	1.2
B_E	**3.2**	**5.6**	5.6	6.4	8	8
$-B_E$	**3.2**	**4**	5.6	6.4	8	8
D_E	**4**	**2.8**	2	1.6	2	2
Cube	**2.5**	**1.4**	1	1.3	1.4	1.4
Z-rotated Cube	**1.6**	**2**	2.8	2.5	2	2

The $\mathbf{B_E/-B_E}$ components which were assumed to be stable are observed to continuously increase in strength by increasing number of passes. These components will also increase due to the $\mathbf{-A_E/A_E}$ and $\mathbf{D_E}$ components, which are assumed to rotate into the $\mathbf{-B_E/B_E}$ components.

The $\mathbf{A_{1E}}$ component is observed to increase in strength in the second pass, be stable in third pass and thereafter decrease slightly by increasing number of passes. $\mathbf{C_E}$ and $\mathbf{D_E}$ may rotate into $\mathbf{A_{1E}}$ in the second pass and may therefore contribute to the $\mathbf{A_{1E}}$ texture strength.

The $\mathbf{C_E}$ component decreases slightly in the second pass. The $\mathbf{A_{1E}}$ and $\mathbf{A_{2E}}$ may both rotate into the $\mathbf{C_E}$ component in the second pass and therefore contribute to the $\mathbf{C_E}$ texture strength.

The $\mathbf{A_E}$ and $\mathbf{-A_E}$ components decrease in the second and third pass and is thereafter stable at intensity ~1 times random. This is probably because none of the other components rotate into the $\mathbf{A_E}$/ $\mathbf{-A_E}$ components. This is also the case for the $\mathbf{D_E}$ component, which only seems to be stable in the first pass.

The $\mathbf{A_{2E}}$ component is low in the first pass and decreases slightly in the second pass. Here, the $\mathbf{A_{2E}}$ component rotates into the $\mathbf{C_E}$ component and only the $\mathbf{A_{1E}}$ component is likely to rotate into the $\mathbf{A_{2E}}$ component.

The **Cube** component reaches an intensity of 2.5 times random in the first pass, higher than the $\mathbf{A_{2E}}$ component. The **Cube** component is mainly observed in the micro structure as deformation bands developed from (001)/θ oriented grains. From geometrical considerations, one would expect the cube component to be stable at higher number of passes because the -90° sample rotation around the Z-axis (route A) will bring the orientation back to a symmetric **Cube** orientation. However, this is not observed; the **Cube** component decreases in intensity and becomes stable at~1.3 times random.

The decrease in the **Cube** component may be linked to the appearance of the **Z-rotated Cube** component, which is observed to increase in intensity when the **Cube** component decreases.

- ***Microstructural observations presented in the following chapters gives strong support to the above assumptions and will explain the mechanisms leading to the different texture components.***

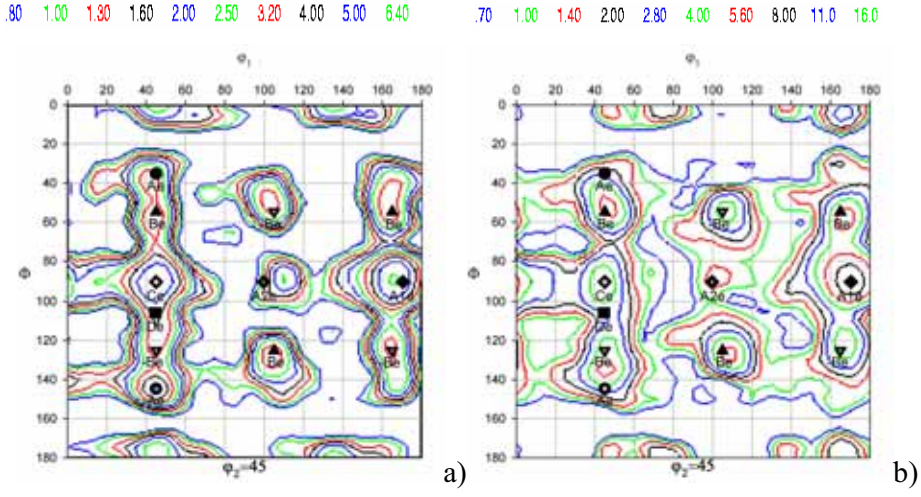

a) b)

Figure 7.30: XRD measurements at the end of a) 1st pass, b) 2nd pass (note the different scale). The locations of the ideal texture components are superimposed on the ODF sections. (ODF sections (0-180, 0-180, 45).

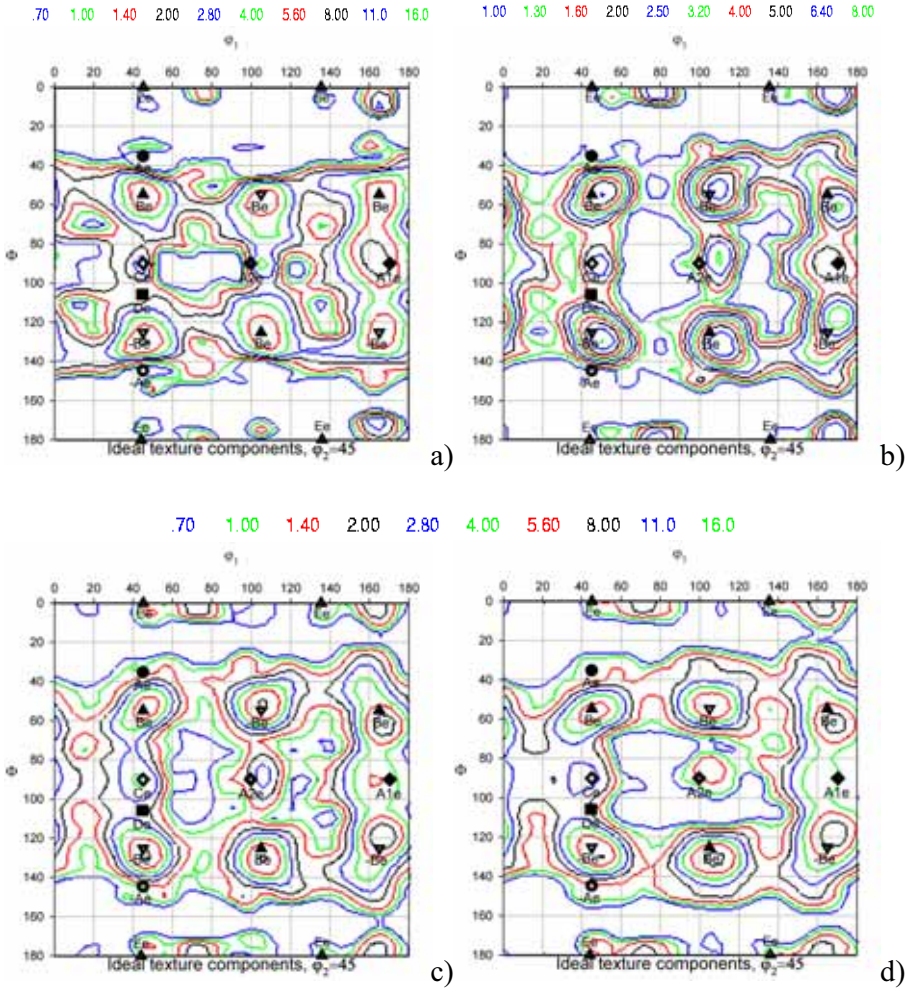

Figure 7.31: XRD measurements of ECAP'ed samples processed by route A for a) 3 passes, b) 4 passes, c) 6 passes and d) 8 passes. The ideal texture components are superimposed on the ODF sections. ODF sections (0-180, 0-180, 45). Note the different intensity scale for figure b).

7.5 Microstructural development

In the following, the microstructural development throughout the deformation zone (see Figure 7.5 for position of the investigated area) of the first and second ECAP pass (route A) will be presented. Detailed EBSD maps give information about the local texture and operating grain-fragmentation mechanisms. Selected grains throughout the deformation zone are analyzed in detail in order to characterize the fragmentation characteristics in different orientated grains as well as identifying stable orientations.

The full EBSD map from the deformation zone in the first pass (Figure 7.32) reveals the overall grain shape change through the zone. The grain morphology changes similar to the deformed grid. The grains become elongated with their long axis parallel to the longest grid-lines. After one full passage through the deformation zone, the grains are elongated and aligned at ~25-28° to the X-direction. Even though the deformation seems homogeneous at the scale of several millimetres, the local deformation of individual grains is different due to their crystallographic orientation and location relative to other grains, thus some grains deform more than others. Soft grains surrounding hard grains tend to deform more in order to sustain strain compatibility, i.e. there will be variations in the local strain tensor on the scale of individual grains.

The Taylor factor is calculated specifically for each crystal orientation in the orientation imaging maps (OIM maps), based on measured strain tensors (calculated from deformed grids). For a given strain, the strain tensor is calculated as the "accumulated" strain tensor, assuming a linearly increasing strain along one deformation path. This gives an idea of which structural elements have been active up to the given strain, according to the Taylor theory. There are basically two structural elements that appear in the

microstructure, namely an aligned cell structure (ACS) and deformation bands (DB's).

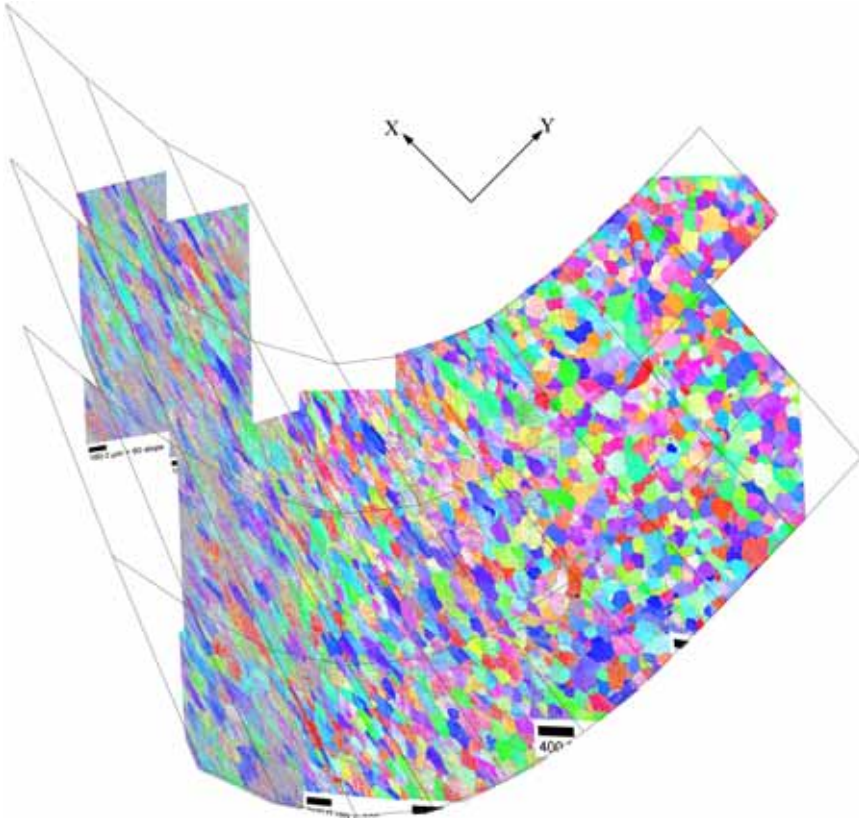

Figure 7.32: Overview of the mapped area in the deformation zone of the first pass with deformed superimposed. The figure is composed of different EBSD maps presented in the Inverse Pole Figure (IPF) colour coding. See next figure for description of the colour coding.

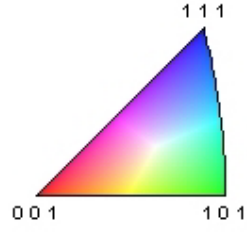

Figure 7.33: Inverse pole figure (IPF) colour coding used in all IPF maps presented throughout this chapter.

7.5.1 Introduction to the Aligned Cell Structure (ACS)

The aligned cell structure is observed in all grains (and resembles slip-traces). It appears at very small strains and is obvious from 20% effective strain. The structure is aligned along the physical principal shear direction and coincides with the direction of the active (110) poles in Figure 7.23, starting at 30° to the X-direction at 20% strain and finally aligning at 45° to the X-direction after a full passage through the deformation zone, which coincides with the theoretical shear plane (in a 90° die).

The cell structure is characterized by low angle of misorientation and is formed by trapping of mobile glide dislocations carrying deformation. The average cell size decrease with increasing strain accumulation, and is shown as low angle boundaries in the linear intercept measurements in Figure 7.34.

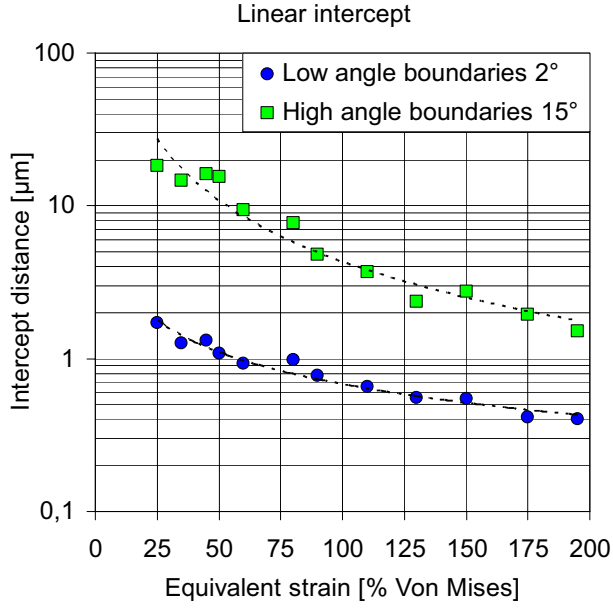

Figure 7.34: Boundary separation length by linear intercept for low-angle boundaries (>2°) and high-angle boundaries (>15°). The equivalent strain is the effective Von Mises strain accumulated up to two passes; first pass from 0-100%, second pass from 100-200%.

At lower strains, several grains have the cell structure aligned in two directions, probably as a result of the tension / compression strain components which dominates at low strains (Figure 7.7). The characteristic misorientation across cell boundaries is dependent on the average grain orientation and accumulated strain, but in general, the misorientation increases steadily with accumulated strain.

Those grains carrying homogeneous deformation by crystallographic slip on one or two slip systems (grains oriented within the stable texture components, Table 7.1) have the largest cell size with the lowest misorientation. Grains which deform on minimum 5 systems (according to the Taylor model) and have a high Taylor factor, have the smallest cell size and also higher misorientations across boundaries, due to crossing dislocations on different slip systems leading to dislocation pile-ups. The misorientations between cells are mainly alternating rotations about the Z-axis. Typical cell structures are shown in the following chapters, e.g. in Figure 7.58, Figure 7.59 and Figure 7.67, along with misorientation profiles and pole figures, and is shown schematically in Figure 7.35.

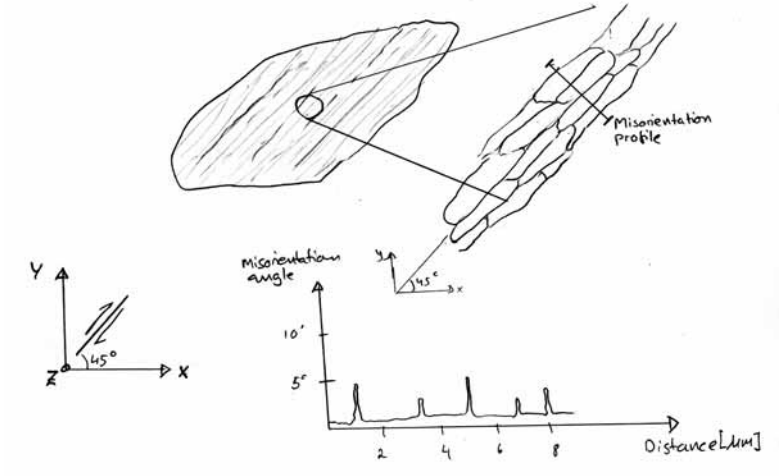

Figure 7.35: Schematically drawing of the aligned cell structure.

7.5.2 Introduction to Deformation Bands (DB)

Deformation bands are typical slab-shaped parallel sequences of volume elements with alternating average lattice orientation, which are caused by the local simultaneous operation of fewer slip systems than would be required for homogeneous deformation.

For the special case of ECAP, as presented here, the original grains become divided by deformation bands, appearing already at 20% strain and increases in population with increasing strain. The deformation bands are regions of different orientation originating inside or crossing through "original" grains. They often appear as several bands with alternating orientations. At higher strains, it may be impossible to separate the bands from the original grains because the remaining fragments of the original grains will also rotate towards a stable orientation, typically in the opposite direction compared to the deformation bands. Deformation bands are separated from the surrounding matrix by high angle boundaries. The width, alignment and population of deformation bands vary with accumulated strain and grain orientation.

Grains experiencing deformation banding show large variations in Taylor factors, i.e. the deformation bands have different Taylor factors than the matrix in which they are formed.

Most grains experience some degree of deformation banding during the first ECAP pass. All deformation bands may not be visible in the OIM maps presented in the XY-frame due to their orientation correlation to the parent grain. Pure Z-rotated crystals show no colour contrast when observed in the Z-direction and plotted with the inverse pole figure (IPF) colour map; therefore, as the majority of deformation bands form by crystal rotation about the Z-direction, IPF-maps presented are also projected in the XZ-frame in the following chapter.

The deformation bands carry deformation by crystal rotation, as shown schematically in Figure 7.39, but this is probably not the driving force for deformation band formation, rather a result of the crystal rotation necessary to bring the DB into a more favourable orientation. The deformation bands form mainly by crystal rotation about the Z-axis in such a way that a <110> slip direction is located in the direction of principal shear, thus facilitating deformation on fewer than 5 slip systems. Not all bands form in this manner, some rotates out of the XY-plane and into one of the stable orientations, as will be shown in the following chapter.

Deformation bands are treated in more detail in section 2.2.7 in relation to the low energy dislocation structures (LEDS) theory.

7.6 *Microstructural observations through the deformation zone: First pass*

7.6.1 25% strain

An example of the deformed grain structure at 25% strain is shown in Figure 7.36 a) and b) with inverse pole figure colour coding in the XY- and XZ-frame respectively.

At this strain, the grains have already established the typical cell structure and some grains have been subdivided by deformation bands.

The IPF maps (Figure 7.36) and the Taylor factor map (Figure 7.37) reveals deformation bands in four of the grains, which are shown in the following figures (Figure 7.38 to Figure 7.42).

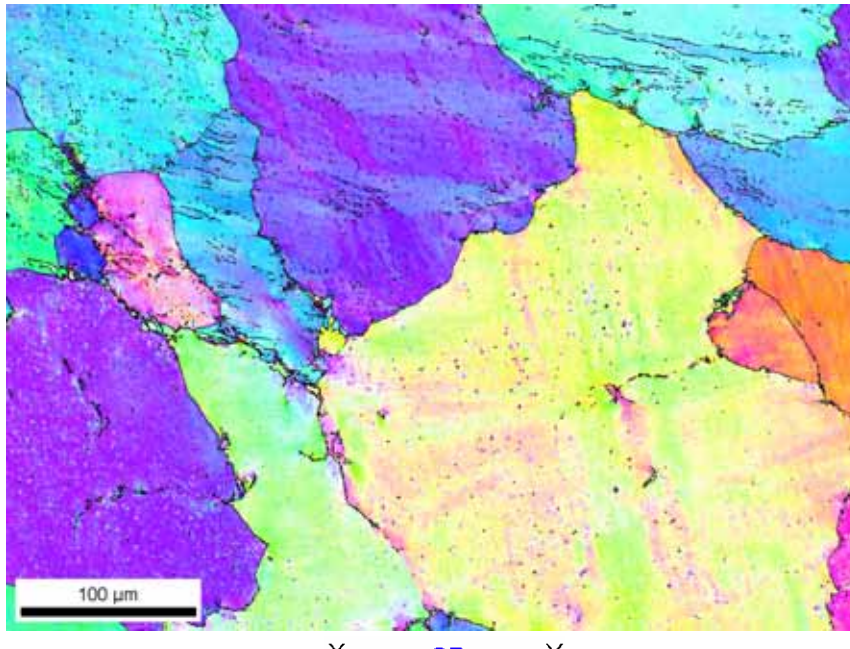

a)

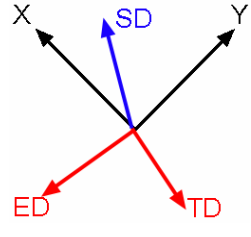

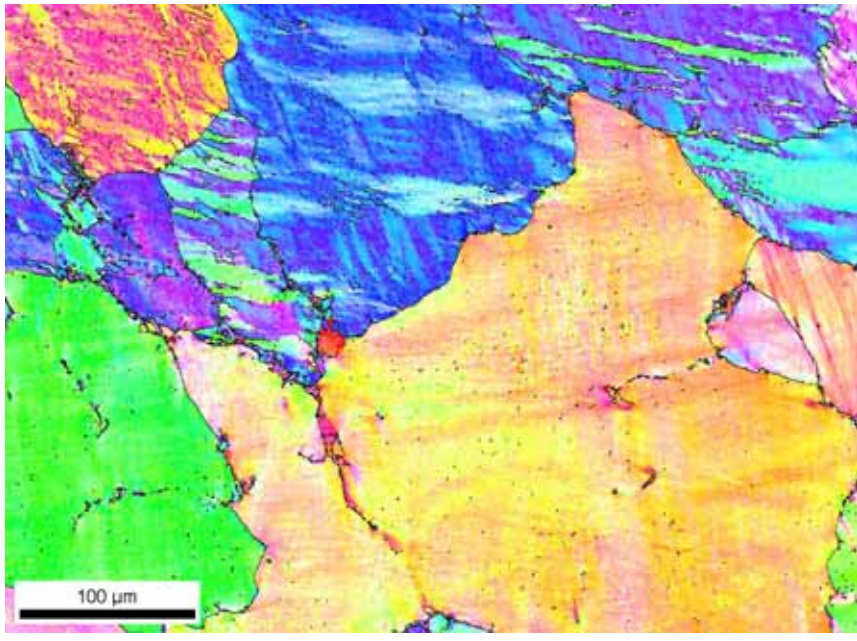

b)

Figure 7.36: Inverse pole figure (IPF) maps at ~25% strain, presented in a) the XY-frame (high angle boundaries superimposed as black lines) and b) the XZ-frame (high angle boundaries superimposed as black lines)

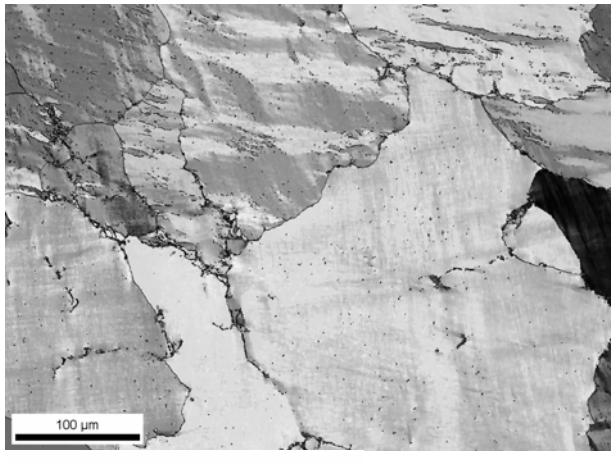

Gray Scale Map Type: <none>

Color Coded Map Type: Taylor Factor

	Min	Max	Total Fraction	Partition Fraction
	2.00698	4.85513	1.000	1.000

Boundaries: Rotation Angle

	Min	Max	Fraction	Number	Length
	15°	180°	0.040	71437	1.65 cm

Figure 7.37: Taylor factor map

The central grain in the last two figures is highlighted by applying a new colour coding to the grain and pole figures. This is done in order to easier reveal information about the deformation and orientations within the grain.

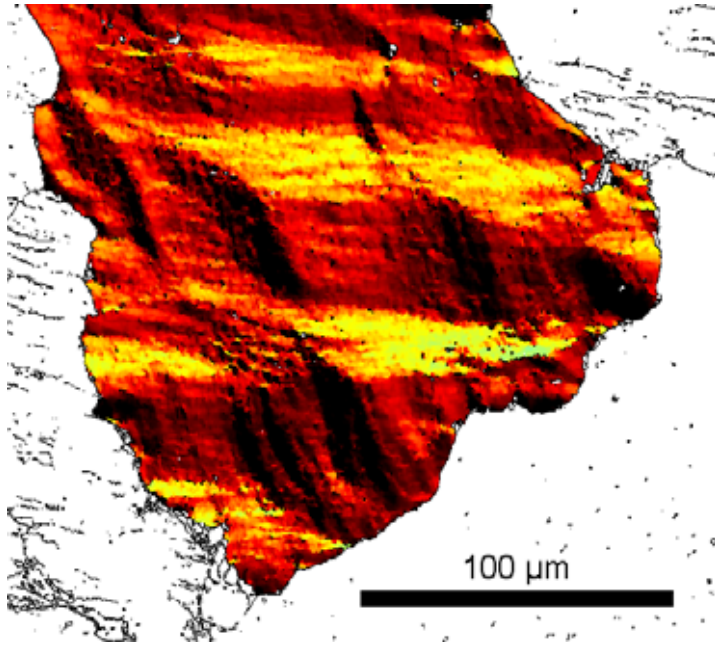

Figure 7.38: a) Highlighted grain from previous figures containing crossing deformation bands, b) and c) are corresponding pole figures. The average grain orientation is (335)/60 (red) and the deformation band orientations are (335)/30 (yellow) and (335)/90 (black)

The average orientation of the above grain (Figure 7.38) is *(335)/60* and including the full spread about Z, the orientation may be written *(335)/30-*

85. The grain is divided by two sets of crossing deformation bands and is shown schematically in Figure 7.39. At this strain, the closest "ideal" orientations are (111)/30 and (111)/90 for <110>||SD, which are within 15° of the orientation in the observed deformation bands.

From the measured strain tensor components at 25% strain, an element experiences compression in the ED direction and tension in the TD direction. The effect of the compression / tension components are shown in Figure 7.39, and results in the observed pure shear deformation mode. The element may adapt to the applied strain tensor components by simple shear in two directions, and is in fact observed to do so by the formation of two sets of deformation bands.

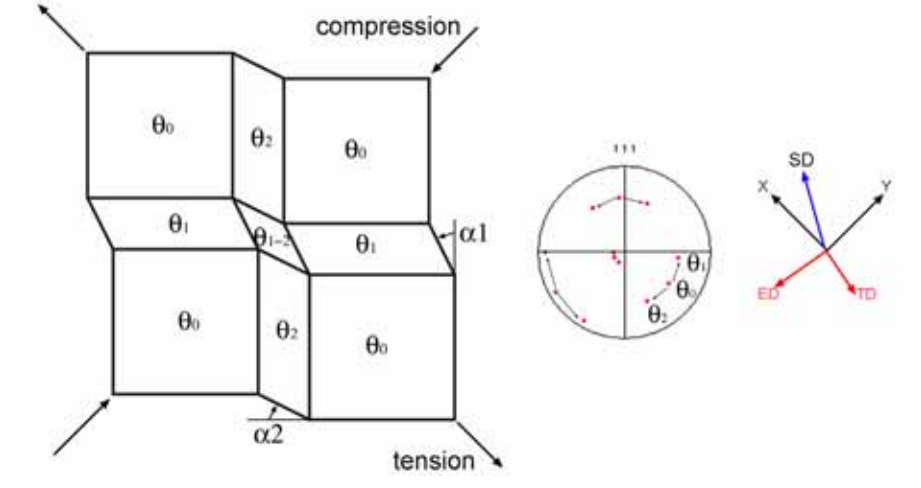

Figure 7.39: Schematic drawing of crystal orientation / rotation for deformation by crossing deformation bands in a grain with orientation θ_0 as identified from Figure 7.38. The symbols are discussed in the text.

The crystal orientation in the deformation bands have rotated in opposite directions, α1 and α2 respectively, and are separated by a 60°rotation about the Z-axis. One can follow the structure of the bands, and the crystal rotation about Z describes the macroscopic deformation of the grain. Thus, the deformation bands carry a macroscopic deformation by crystal rotation.

This means that the rotation α_1 in a band having a width w_1, rotating the orientation θ_0 into θ_1, results in an equivalent shear deformation, by displacing the crystal on one side of the deformation band relative to the crystal on the other side of the deformation band by an amount: $w_1 \tan(\alpha_1)$.

The rotations α_1 and α_2 of orientation θ_0 into orientation θ_1 and θ_2 is energetically favourable according to the LEDS theory, by the simultaneous operation of fewer than 5 slip systems (see section 2.2.7 for details).

The (110) pole figure in Figure 7.38c) reveals that the orientation θ_0 is unfavourable for slip in the principal shear direction, which at 25% strain is located at ~30° to the X-axis in the XY-plane. The initial grain orientation, θ_0, is located at ~60° to the X-axis. The grain splits into two sets of deformation bands, one set of bands rotating towards the X-axis by ~30° (α1) and the other set of bands rotating towards the Y-axis by ~25° (α2), each set of bands now having a <110> direction closely aligned to the direction of principal shear.

The similar subdivision of grains by deformation bands is also observed in the grains highlighted in Figure 7.40 to Figure 7.42 and is shown with the corresponding (111) and (110) pole figures in the following.

The highlighted grain in Figure 7.40 has one set of primary deformation bands at (331)/270 (blue-yellow) which is within 15° of <110>||SD, and shows tendencies of a crossing structure with orientation ~(331)/320 (black).

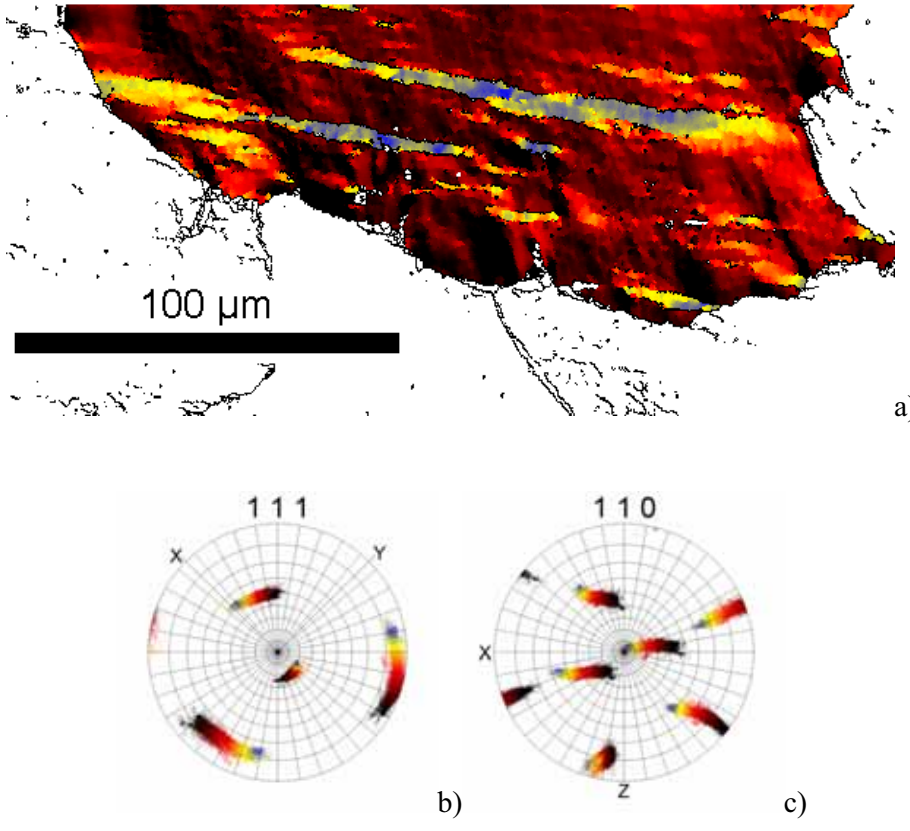

Figure 7.40: a) Highlighted grain with one set of deformation bands, b) and c) pole figures. The average grain orientation is close to (331)/300 and the new orientations are (331)/270 (blue) and (331)/320 (black)

Another example is the highlighted grain in Figure 7.41. The grain is severely divided by deformation bands in one direction only. However, in this case, the bands (blue-yellow) and "matrix" (red) have probably rotated in opposite directions into (478)/30 (blue-yellow) and (478)/85 (black) in order to have both "matrix" and deformation bands within ~15° of <110>||SD.

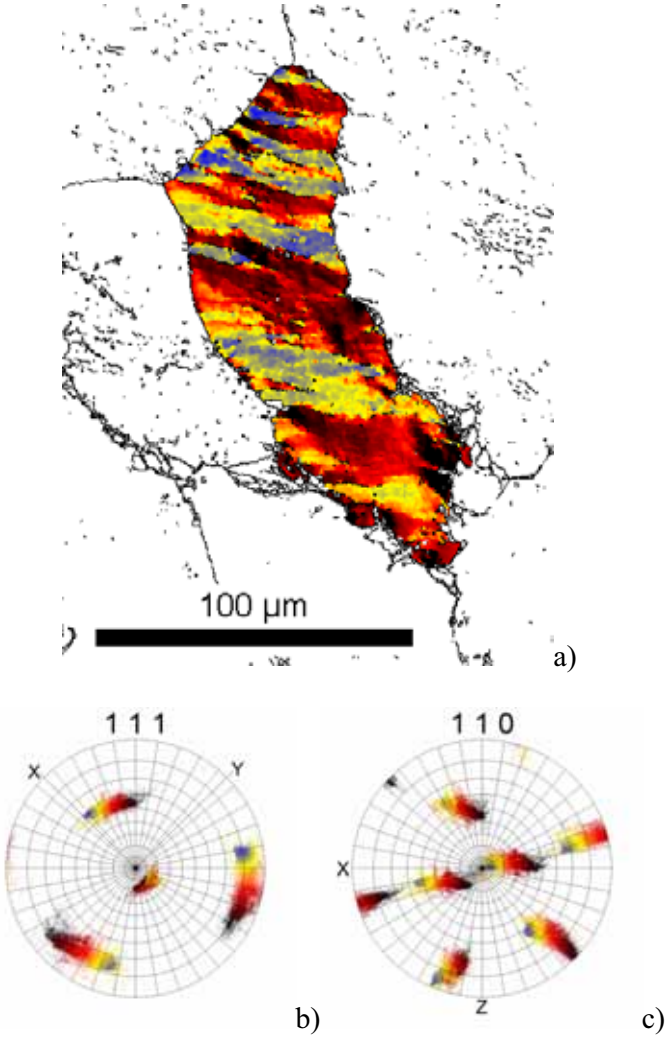

Figure 7.41: Highlighted grain with deformation bands rotating in opposite directions, b) and c) corresponding pole figures. Deformation band orientations are (478)/30 (blue-yellow) and (478)/85 (black).

Also, the grain in Figure 7.42 shows early stages of grain subdivision by deformation bands close to ~(255)/75 (blue) orientation. The bands are still not fully rotated into the stable orientation and the bands do not have sharp boundaries but show some orientation gradients towards the banded structures (may be denoted hybrid transition / deformation bands).

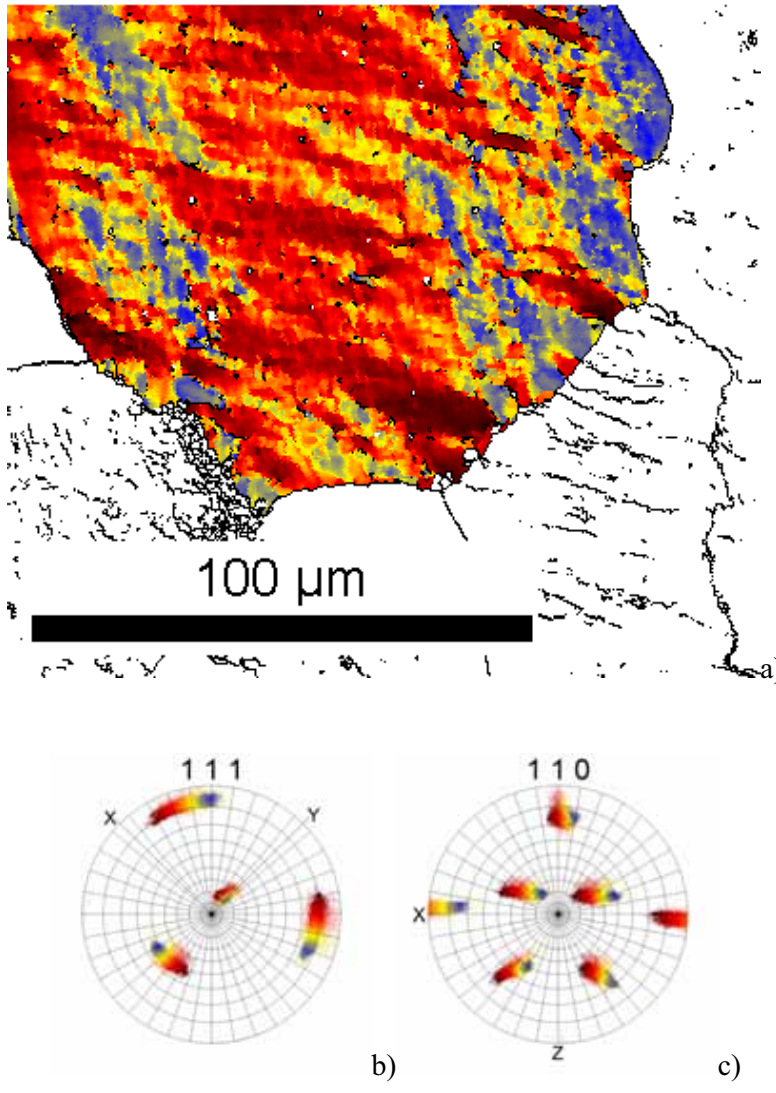

Figure 7.42: Highlighted grain in the early stage of deformation banding, b) and c) corresponding pole figures. Original grain orientation is ~(255)/35 (red) and deformation bands close to (255)/75 (blue).

Grains oriented within 15° of the stable texture components (except A_{1E} and $\mathbf{A_{2E}}$) can be revealed by highlighting crystal orientations which have a <110> direction aligned within 15° of the principal shear direction, and are shown in Figure 7.43, along with the <110> pole figure in the XZ frame. One can see that all fully developed deformation bands observed in this scan fulfils the <110>||SD criterion.

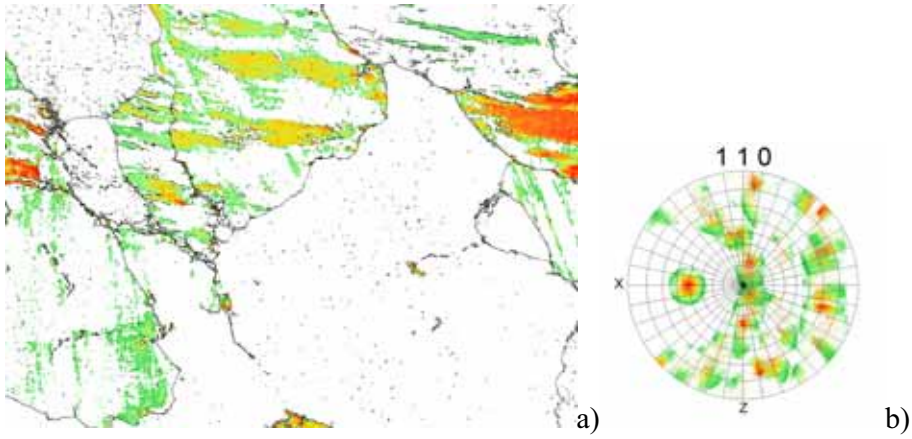

a) b)

Figure 7.43: Highlighting of orientations within 15° of the principal shear direction, a) highlighted map and b) highlighted orientations.

7.6.2 50% strain

At 50% strain, the grains have clearly become more elongated in shape, as can bee seen in Figure 7.44. Some grains show clear traces of the principal shear direction in the form of aligned cell structures and in a few grains also deformation bands, even though the DB's tend to align in the principal strain direction. It also becomes clear that different grain orientations have different deformation characteristics. Some grains are severely subdivided by deformation bands while other grains seem to deform more homogeneously by crystalographic slip, generating a cell structure separated by low angle boundaries.

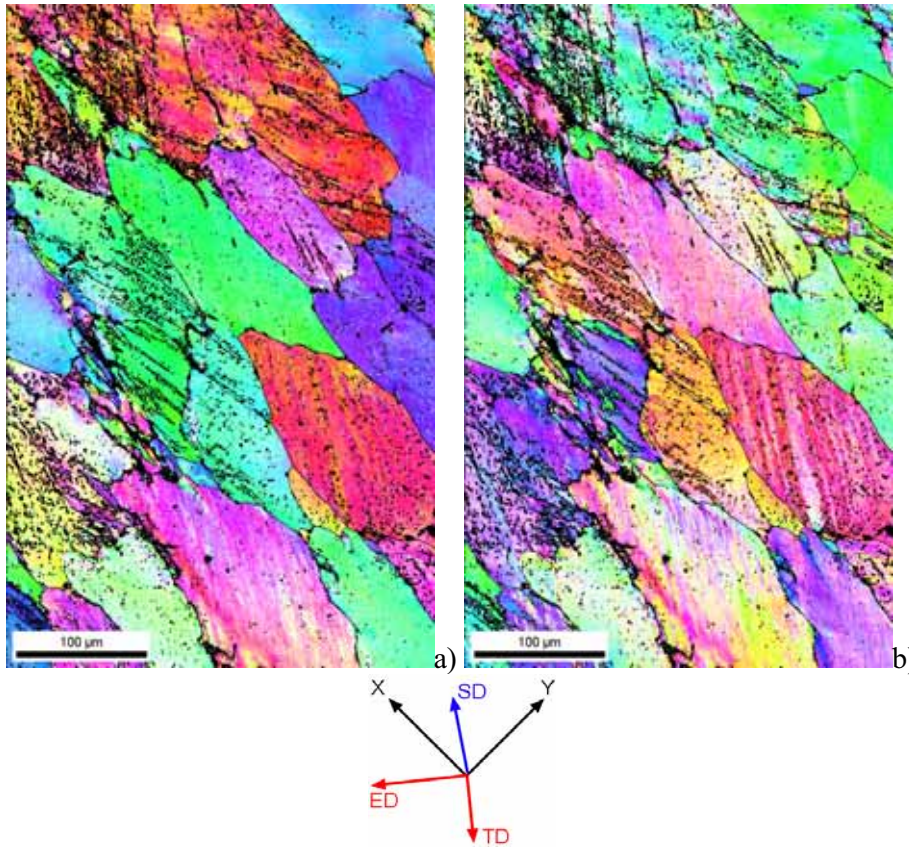

Figure 7.44: Inverse pole figure (IPF) maps at ~50% strain, presented in a) the XY-frame (high angle boundaries superimposed as black lines) and b) the XZ-frame (high angle boundaries superimposed as black lines)

All corresponding crystal orientations aligned with a <110> direction within 15° of the principal shear direction are highlighted in Figure 7.45. Again, most deformation bands show up by this highlighting, along with some grains which have not been subdivided because they are already oriented within a stable orientation. Two of the grains which have not been highlighted appear to be "clean", i.e. no deformation banding (marked $\mathbf{A_{1E}}$ on the map). These two grains are oriented within the stable $\mathbf{A_{1E}}$ texture component. This supports the assumptions and observations in section 7.4.2.

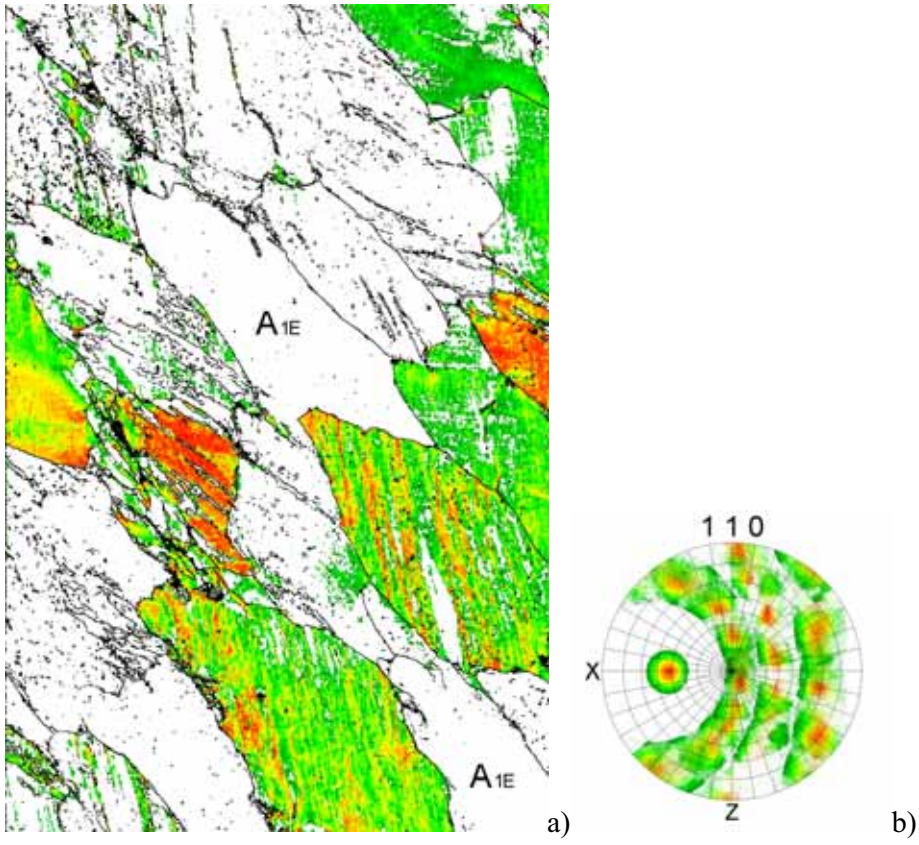

Figure 7.45: Highlighting of orientations in the previous figure lying within 15° of the principal shear direction, a) highlighted map, b) highlighted orientations. The grains labelled $\mathbf{A_{1E}}$ have deformed homogeneously but are not highlighted. These grains are oriented within the $\mathbf{A_{1E}}$ texture component.

Moreover, the (3-21 8)/20 oriented grain shown in Figure 7.46 is divided by deformation bands with average orientation (-29 9 1)/96, but these bands are not yet clearly defined. The (110) pole figure (Figure 7.46c) shows that this grain already have a <110> direction aligned in the XY-plane but at ~15-20° to the X direction. The deformation bands, where the slip activity has been highest, have rotated towards a stable **Cube** component (orientation (001)/45), with the <110>||SD at ~45° to the X-direction. The alignment of these bands is also in the direction of principal shear, i.e. the same direction as the aligned cell structure. **This special alignment of the deformation bands seems to be typical for DB's having Cube orientation.**

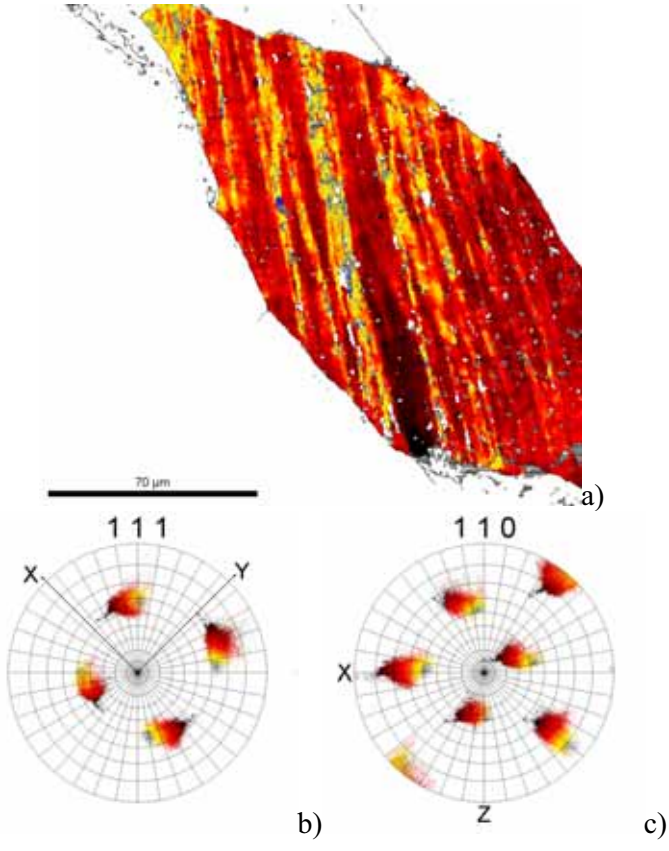

Figure 7.46: Deformation banding in a grain with original orientation ~(3 -2 18)/19 (dark red), deformation band orientation close to ~(001)/45 Cube (blue).

A different example of subdivision of a ~(-2 3 17)/35 oriented grain is given in Figure 7.47, where the main crystal rotation appears out of the XY-plane. There are a few narrow bands in the principal shear direction with orientation (1 12 -3)/130 (black) while the other crossing band (the blue – yellow) has an orientation close to (205)/240 giving a misorientation between the two orientations of 35.2° rotation about the <5-4-8> crystal axis. **This rotation out of the XY-plane will show to be typical for grains oriented with a <001> crystal axis aligned closely parallel to the Z-axis.**

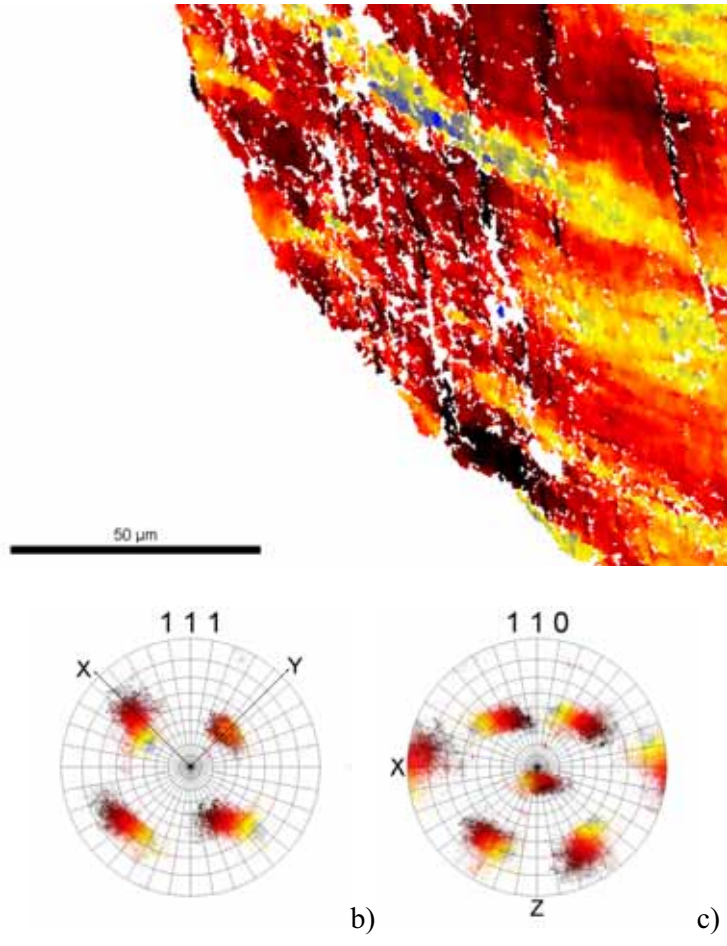

Figure 7.47: Subdivision of a ~(-2 3 17)/35 oriented grain by deformation bands with orientation ~(1 12 -3)/130 (yellow-blue) and most probably shear bands with orientation close to ~(205)/240 (black)

One of the grains that seem to have a **stable orientation** is shown in Figure 7.48. The grain orientation is given as (110)/135-165, in which the (110)/165 is the $\mathbf{A_{1E}}$ stable texture component.

The grain shows alignment of a cell structure in two directions; SD and at 68.5° to SD. This corresponds to the angle between two (111) planes. We may therefore assume from the alignment of the cell structure that this grain deforms by crystalographic slip on four systems; the two slip systems given for the $\mathbf{A_{1E}}$ component and two more on the neighbouring {111} plane.

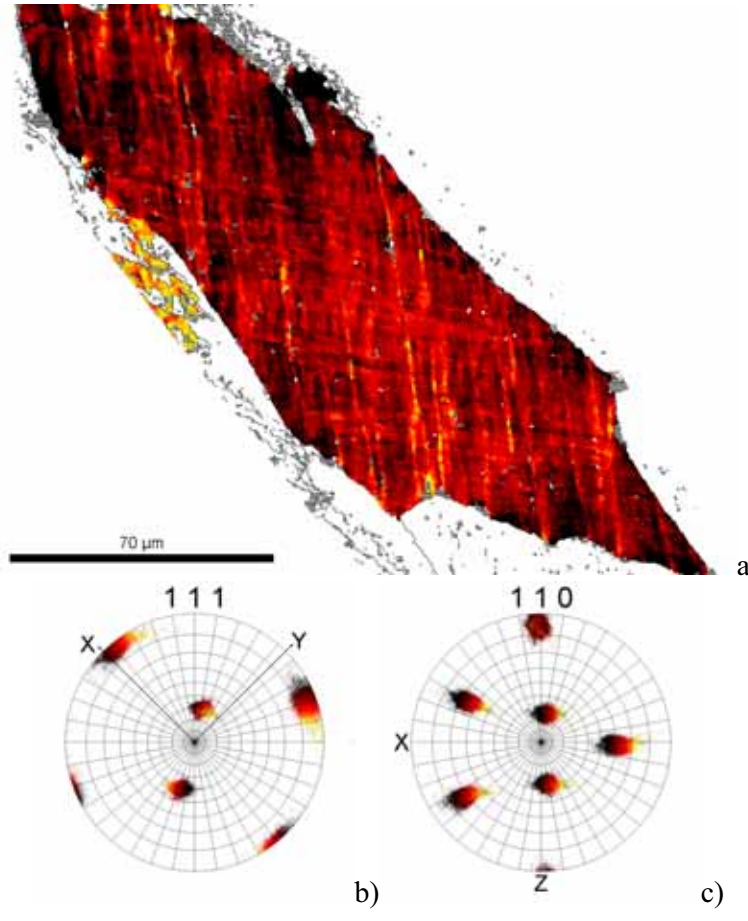

Figure 7.48: Deformation by simple shear in a grain oriented within the stable texture component A_{1E}, (110)/135-165. The total spread is ~30° about <110>.

Grains oriented with a (110) plane normal aligned parallel to the Z-axis, (110)/θ orientation, may also develop deformation bands as shown in Figure 7.49. The red area of this grain has a (110)/45 orientation (**C_E** component) which also is a stable orientation from the assumptions made in chapter 7.4. Still, there are deformation bands present in this grain. The orientation of these bands is identified as (110)/85, i.e. the DB's and matrix is separated by a ~40° rotation around <110>. A closer look at the boundaries separating the DB's and the matrix reveals that they are in fact **Σ9 boundaries**, characterized by a 38.9° rotation around <110>. This specific case is treated in more detail in section 7.9.3.

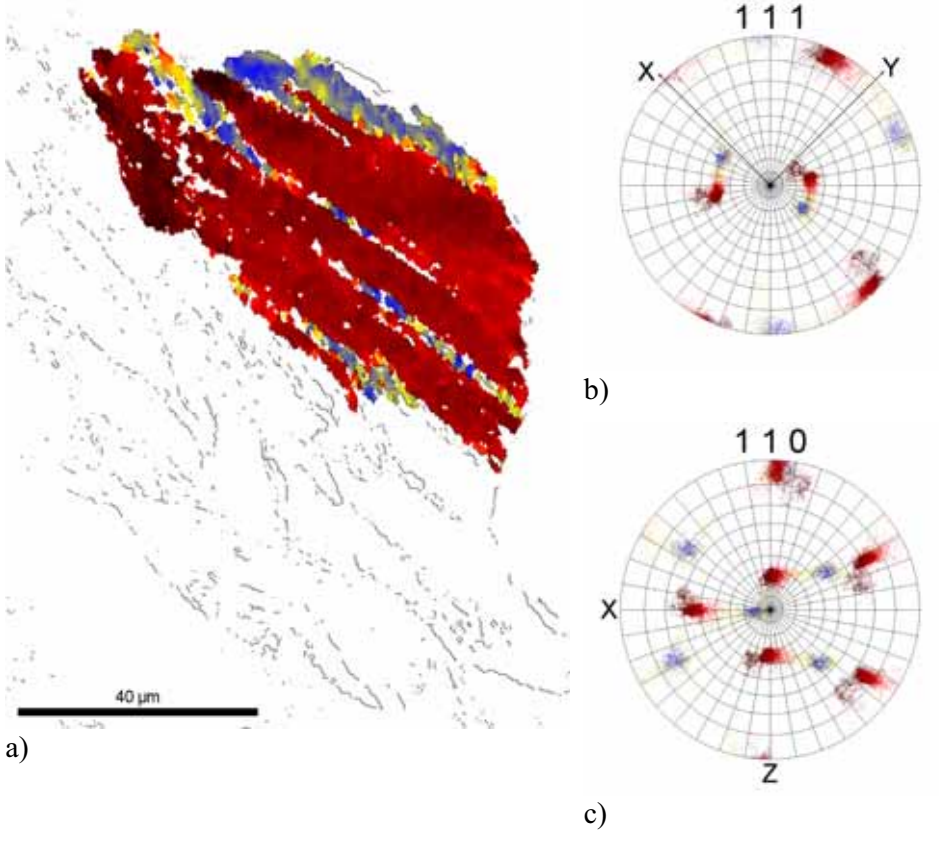

Figure 7.49: Deformation banding in a grain oriented in the stable texture component C_E, (110)/45. The deformation bands have orientation (110)/85 and are separated from the grain matrix by low energy Σ9 boundaries (38.9° around <110>).

In some regions, small high angle grains may be present in the grain interior which have not been formed by deformation banding. These grains have formed as a result of collapse of large orientation gradients, as shown in Figure 7.50. The misorientation profile shows a gradual orientation gradient (on both sides of the collapsed region), spanning several microns in length, thus steadily building up a ~20° rotation about the Z-axis, followed by a **collapsed region of different orientation**, separated by high angle boundaries. This mechanism of high angle grain boundaries formation will be treated in section 7.9.2.

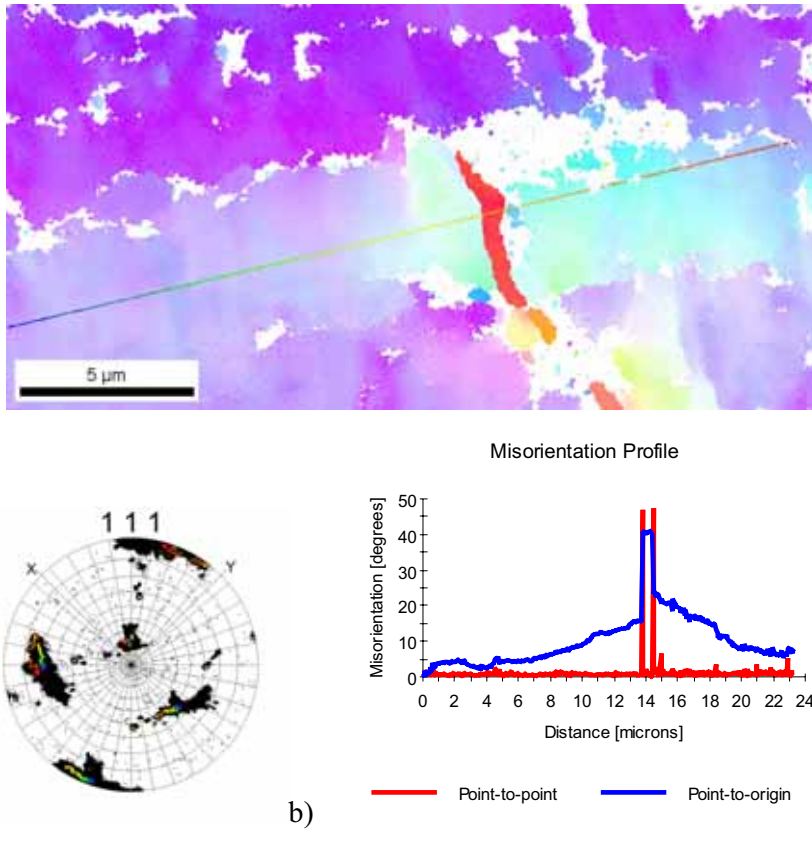

Figure 7.50: Long range orientation gradients in a grain with orientation (112)/305-355, with a collapsed region with orientation (001)/45 Cube. a) IPF map, b) corresponding pole figure and c) misorientation profile.

7.6.3 60% strain

A section of the microstructure at 60% strain is shown in Figure 7.51 in the inverse pole figure colour coding in the XY- and XZ-frame respectively.

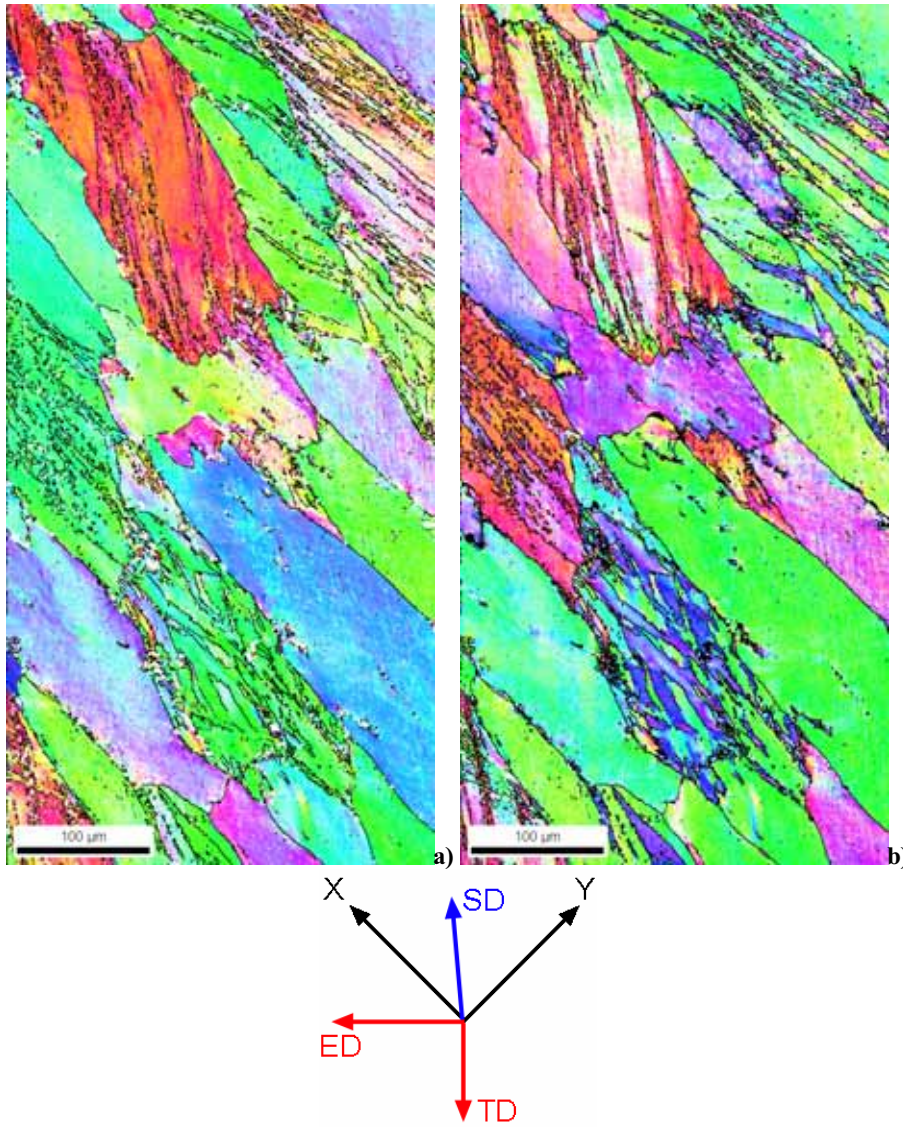

Figure 7.51: Inverse pole figure (IPF) maps at ~60% strain, presented in a) the XY-frame (high angle boundaries superimposed as black lines) and b) the XZ-frame (high angle boundaries superimposed as black lines).

There are several interesting features to note; at this strain most grains are subdivided by deformation bands. The grains which are not subdivided are oriented within one of the stable texture components. Again, crystal orientations having a <110> direction aligned within 15° of the principal shear direction are highlighted (Figure 7.52), and we observe that most deformation bands show up in the highlighted orientations, along with some larger non subdivided grains already oriented within a stable texture component.

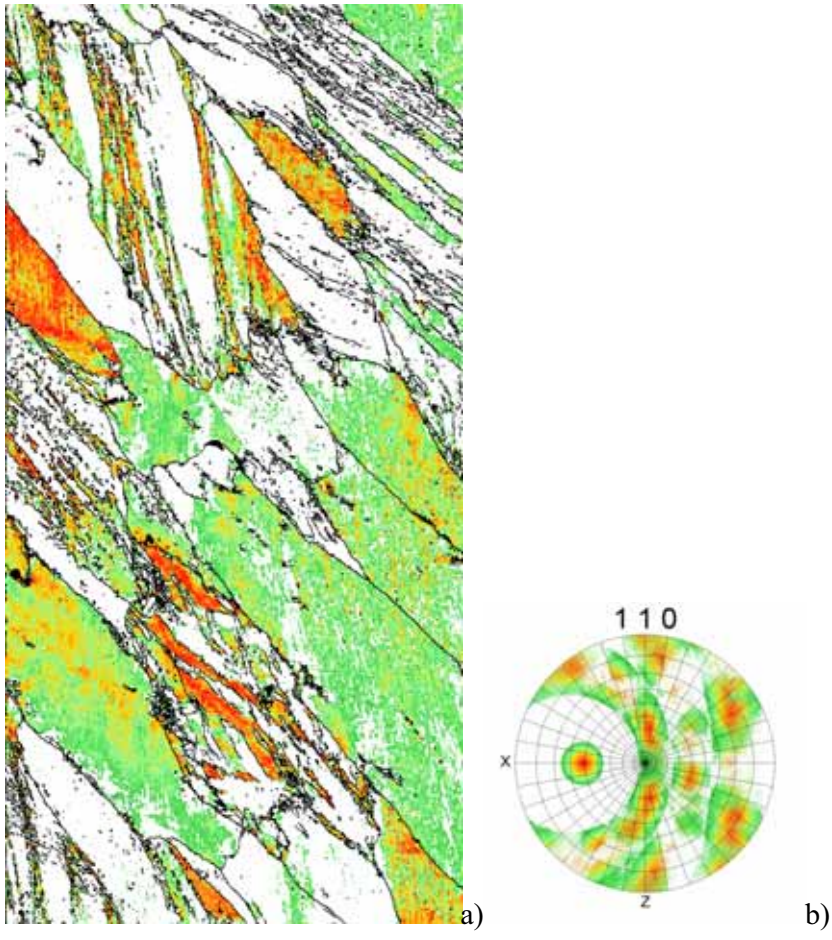

a) b)

Figure 7.52: Same area as in the previous figure: Highlighting of orientations within 15° of the principal shear direction, a) highlighted map, b) highlighted orientations.

The banded grain in the upper right corner in Figure 7.51 is shown in Figure 7.53 along with the corresponding pole figures and misorientation profile. This grain probably started out as a "rotated cube" grain with orientation (001)/90, and has been **severely divided by two sets of deformation bands with orientations close to (110)/105 (A_{2E}) and (110)/165 (A_{1E})**, again indicating that these are stable orientations. The rotation in this grain has been "out of plane", i.e. the deformation bands are formed by rotation out of the XY-plane. The misorientations across the deformation bands are shown in the misorientation profile in Figure 7.53e). High angle boundaries with misorientation up to 40° are observed and the orientation spread about Z is as much as 80°.

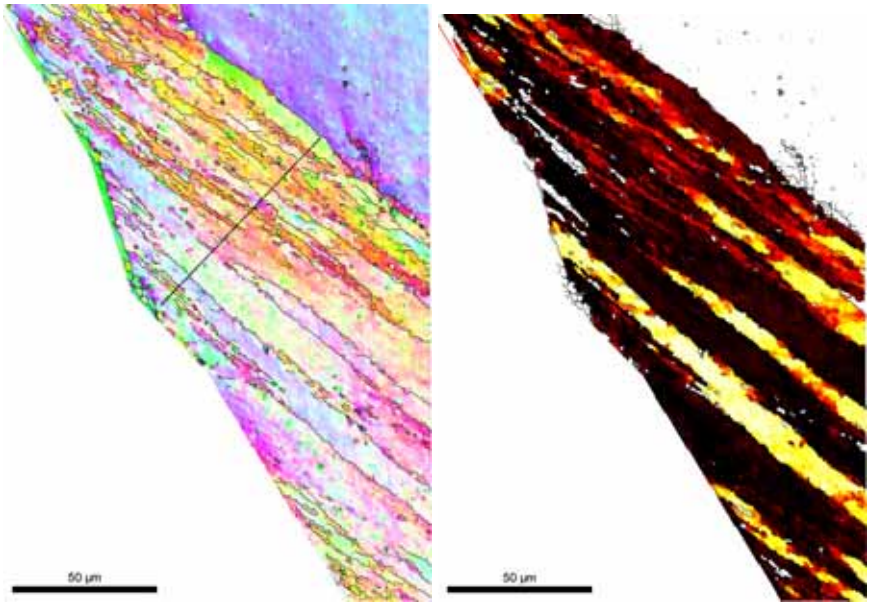

a) b)

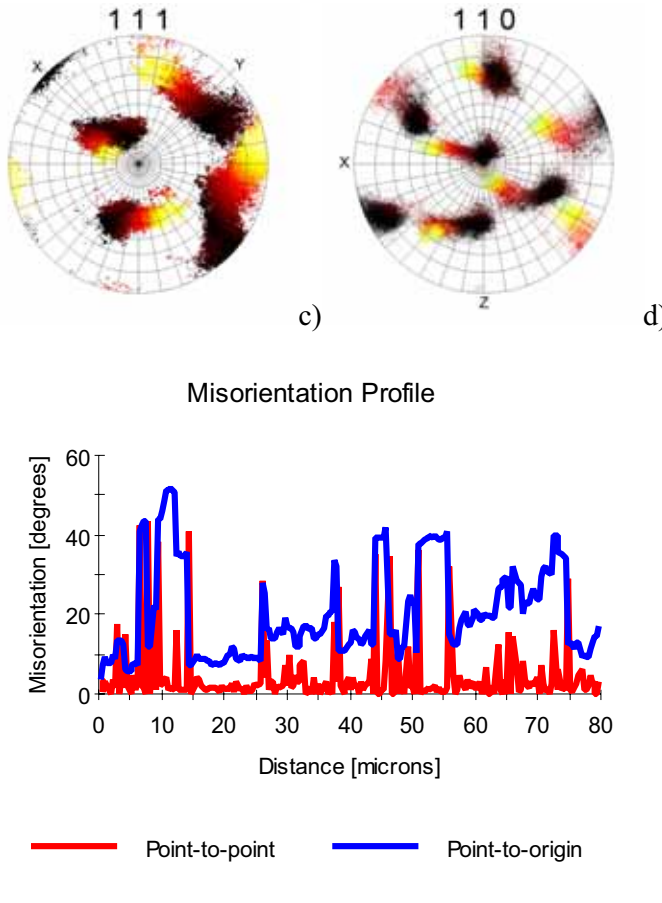

Figure 7.53: Example of deformation banding in a "rotated cube" oriented grain (001)/90. a) IPF map, b) highlighted grain, c) and d) corresponding pole figures. The original grain orientation was close to (001)/90. The grain is subdivided into two new orientations, both stable texture components; A_{2E} (110)/105 (yellow) and A_{1E} (110)/165 (black). e) Misorientation profile through deformation bands in a).

Furthermore, the grain in Figure 7.54 shows an example of severe subdivision by **crossing deformation bands** in a typical (110)/θ oriented grain. The mechanism is the same as the schematic drawing in Figure 7.39. Again, one can see how the DB's rotate into more stable orientations with a <110> direction aligned in the direction of principal shear. **The subdivision can be written (110)/θ→(110)/45+(110)/105**. The original orientation of the grain (θ) is unknown, but from the pole figure and the fact that

deformation bands are crossing and thus probably have rotated in opposite directions, the original orientation may have been close to (110)/70.

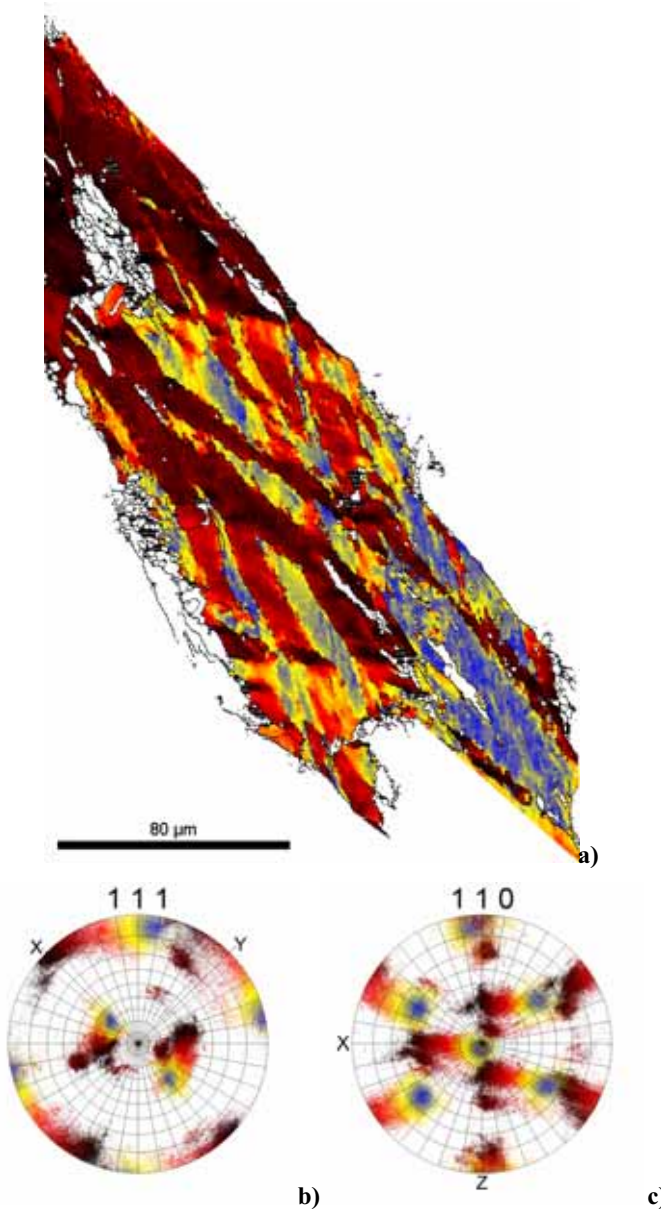

Figure 7.54: Example of crossing deformation bands in (110)/θ grain ((110)/25-110). The two sets of bands have rotated in opposite directions towards the stable C_E and A_{2E} texture components. a) Highlighted grain, b) and c) corresponding pole figures.

The (001)/90 oriented grain in Figure 7.55 has experienced crystal rotation in very narrow deformation bands. The grain is split by deformation bands (yellow-blue), rotating towards the stable (001)/45 **Cube** orientation. This orientation fulfils the <110>||SD criteria, as can be seen in the (110) pole figure in Figure 7.55c). Also, the misorientation profile across the bands is shown in Figure 7.55d).

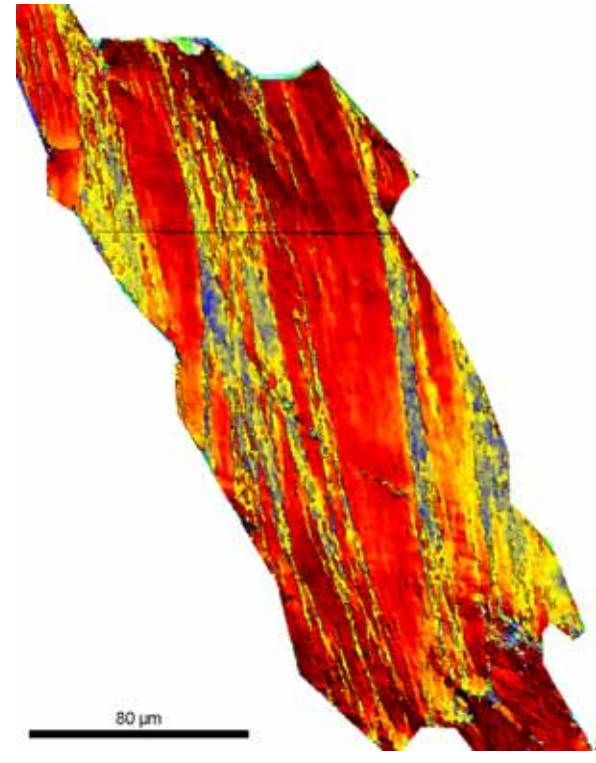

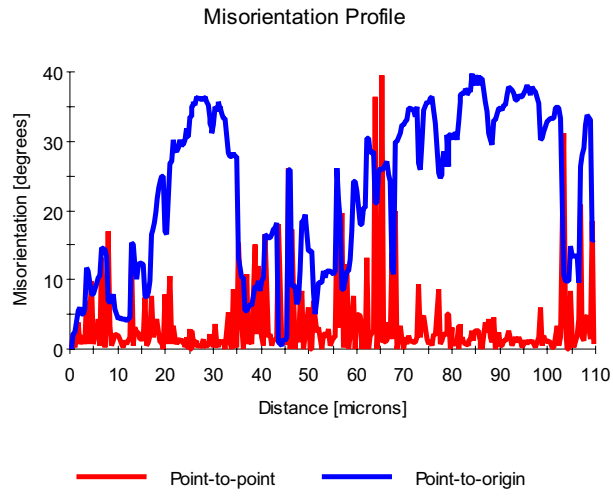

d)

Figure 7.55: a) Example of deformation bands in a (001)/90 oriented grain (red). The deformation bands (blue-yellow) are oriented close to the (001)/45 cube orientation. b) and c) corresponding pole figures, d) misorientation profile

Another interesting observation is the (122)/160 oriented grain presented in Figure 7.56. This grain has experienced simple shear by crystalographic slip, in the direction of principal shear.

The deformation is shown schematically in Figure 7.57. This deformation mode is believed to generate the typical aligned cell structure. The average orientation spread in such a grain is relatively small, typically 10-15°. The long range orientation gradients are small, and the cells have alternating orientations about the Z-axis, as shown in the misorientation profile in Figure 7.56. At this strain (60%), the misorientation across the cells in a stable grain is usually ~3-5° with a cell size of ~1μm. A detailed view of the cell structure is shown in Figure 7.58 along with the corresponding (111) pole figure and misorientation profiles in the two characteristic directions, i.e. the principal shear direction and the principal strain direction. In non-stable regions, the cell misorientation is usually somewhat larger, typically ~5-8°.

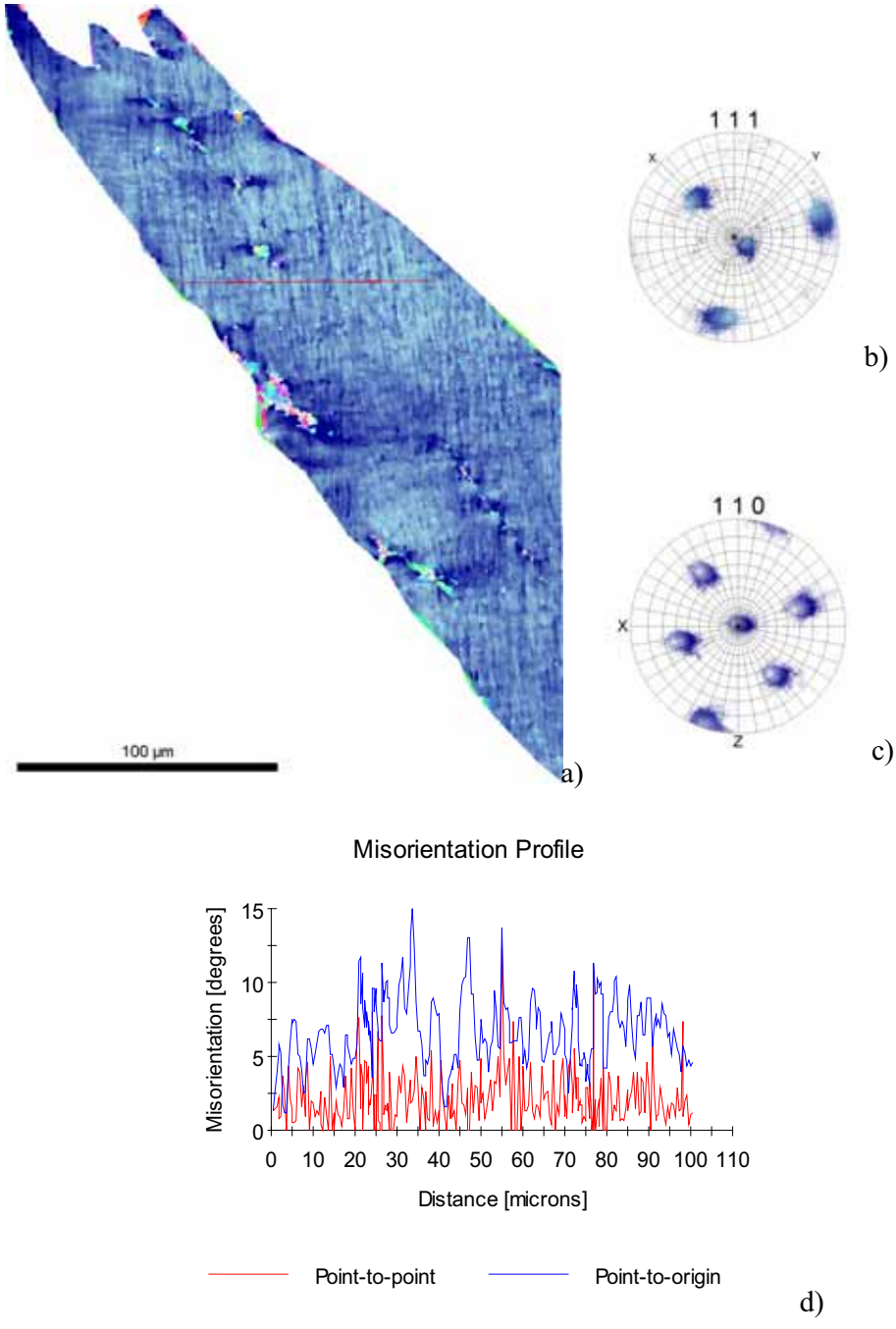

Figure 7.56: Example of simple shear by crystalographic slip in a stable (122)/160 oriented grain developing the aligned cell structure. a) Highlighted grain, b) and c) pole figures and d) misorientation profile along the red line (left to right).

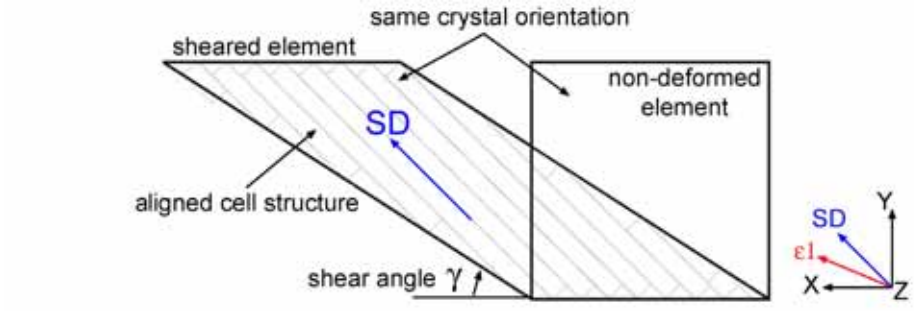

Figure 7.57: Schematic presentation of deformation by crystalographic slip in a grain oriented for development of aligned cell structure. SD indicates the shear direction and ε1 indicates the first principal strain direction.

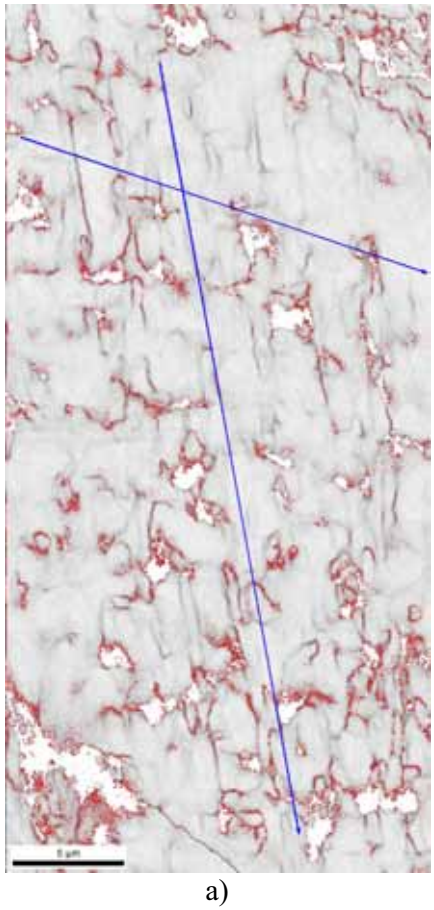

a)

Gray Scale Map Type: <none>

Color Coded Map Type: Kernel Average Misorientation

	Min	Max	Total Fraction	Partition Fraction
	0	4.97965	0.925	1.000

Boundaries: Rotation Angle

	Min	Max	Fraction	Number	Length
	15°	180°	0.076	5114	88.58 microns
	2°	15°	0.924	62409	1.08 mm

*For statistics - any point pair with misorientation exceeding 1° is considered a boundary (total number = 67523, total length = 1.17 mm)

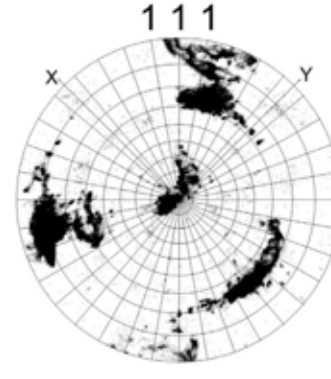

b)

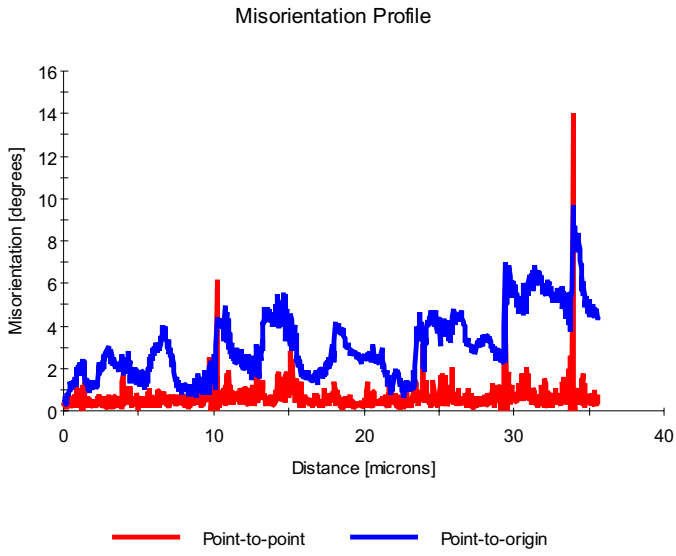

c)

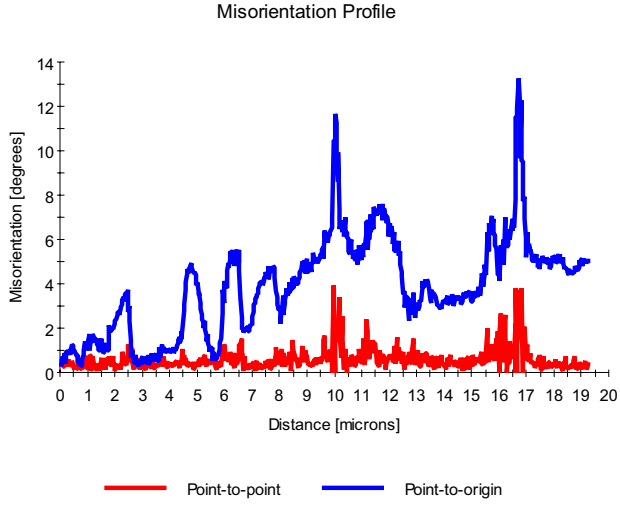

d)

Figure 7.58: Cell structure and misorientation profiles from a stable (111)/θ oriented grain. a) Kernl average misorientation map with low angle boundaries superimposed (red lines), b) corresponding (111) pole figure, c) and d) misorientation profiles in the shear direction and principal strain direction respectively.

7.6.4 70% strain

Generally, with increasing strain the sub-structure appears more refined and more distinguishable orientations appear more frequently. Here, some observations need to be commented.

The cell structure in a grain with orientation (035)/175-225 at 70% strain is shown in Figure 7.59, along with misorientation profiles across the structure (Figure 7.60).

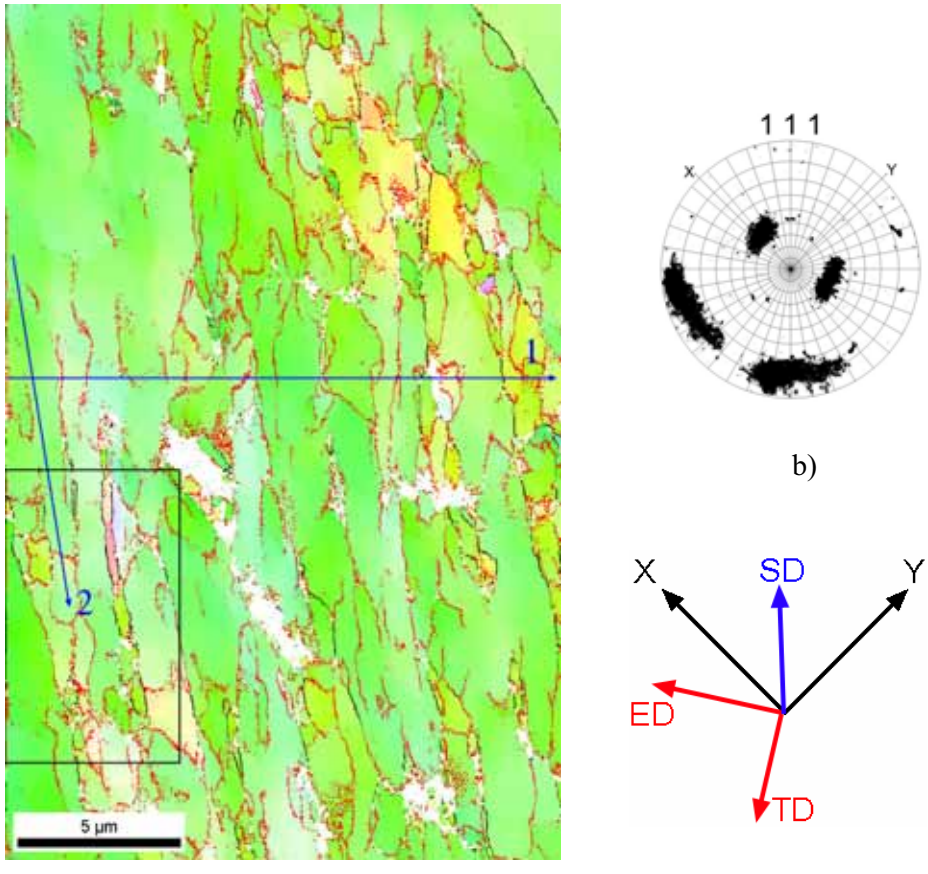

Figure 7.59: Cell structure in a grain at ~70% strain. a) IPF map with low (>2°) and high (>15°) angle boundaries represented as red and black lines, b) corresponding (111) pole figure from the whole map. The average orientation is (035)/175-225. The lines marked 1 and 2 represents misorientation profiles shown in the following figures. The marked area is shown in detail in Figure 7.61.

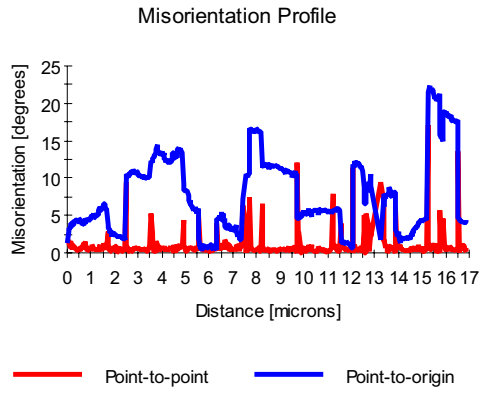

a)

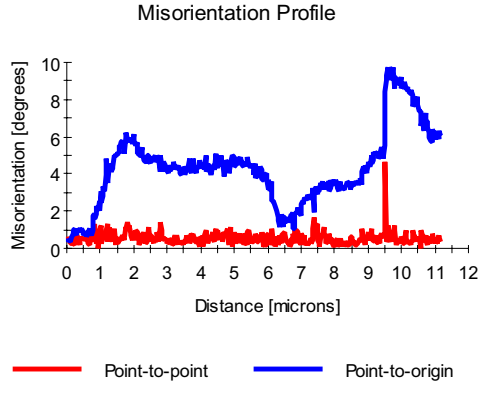

b)

Figure 7.60: Misorientation profiles from Figure 7.59; a) horizontal line (1), b) vertical line (2).

The mapped area shows a large spread about the Z-axis (~50°). The misorientation profiles in Figure 7.60 reveal some interesting information about the microstructure. The horizontal profile (marked "1" in Figure 7.59) is made nearly perpendicular to the shear direction. The misorientation across sub-grains is typically between 5 and 10°. The misorientation profile marked "2" is made in the shear direction and clearly shows the presence of orientation gradients rather than sharp boundaries.

From the first misorientation profile ("1") here are also a few high angle boundaries (20-30° misorientation), separating some very small, elongated individual grains, as shown in more detail in Figure 7.61. The

misorientation profile crossing through these grains (Figure 7.61b-d) reveals orientation gradients ranging a few microns to each side of the grains. The small grains are probably a result of reordering of dislocations due to high internal stresses and are probably not formed as deformation bands, as these grains do not have a <110> direction aligned with the principal shear direction, neither are they oriented within any of the stable texture components. The grains have a width in the order of 0.09 to 0.2μm in width and 0.5 to 1.5 μm in length.

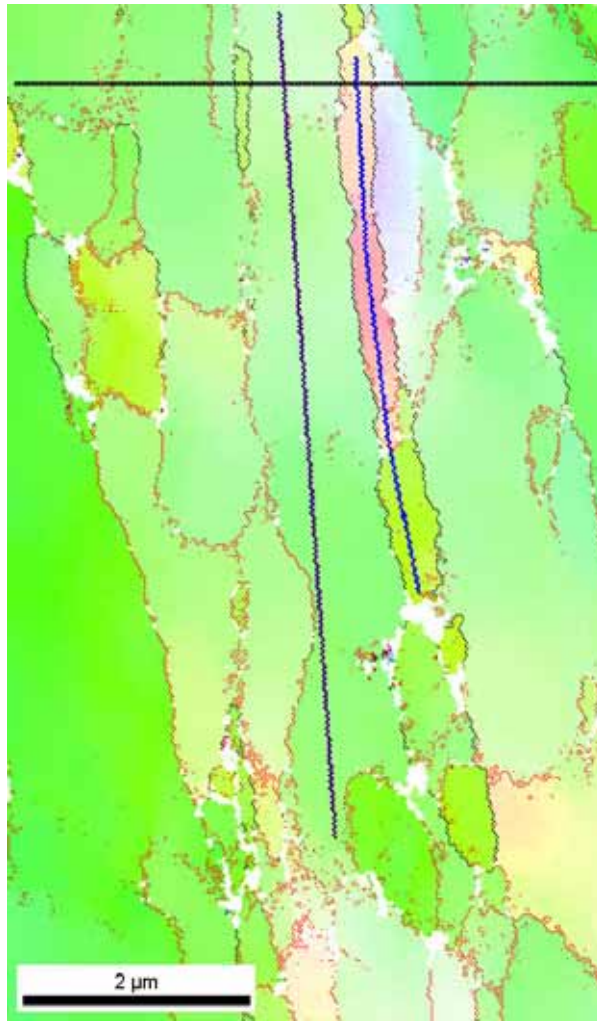

a)

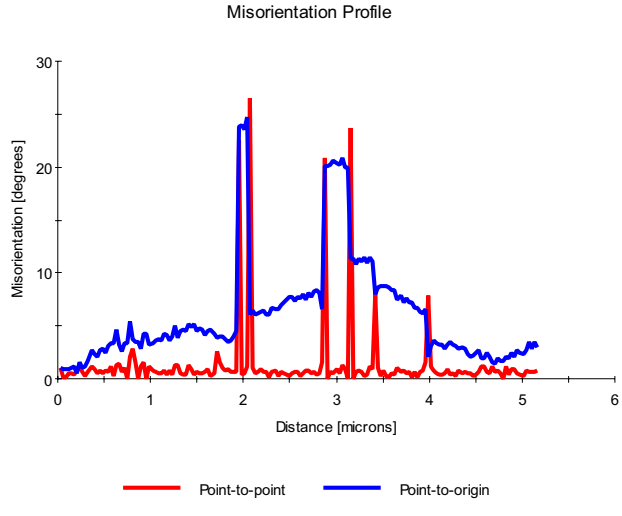
Misorientation Profile
Misorientation [degrees]
Distance [microns]
Point-to-point
Point-to-origin

b)

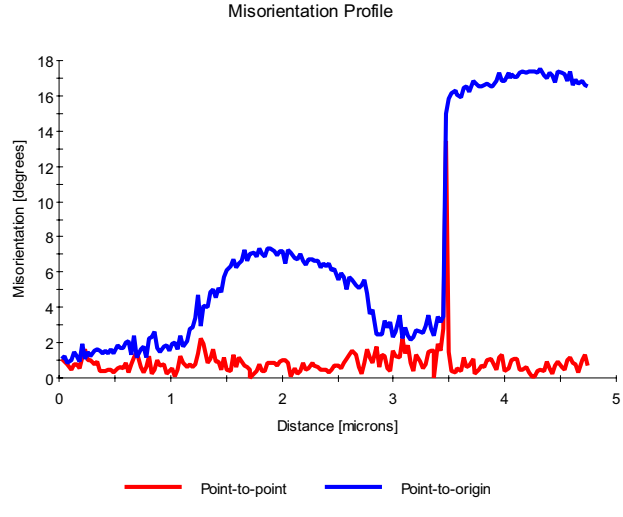
Misorientation Profile
Misorientation [degrees]
Distance [microns]
Point-to-point
Point-to-origin

c)

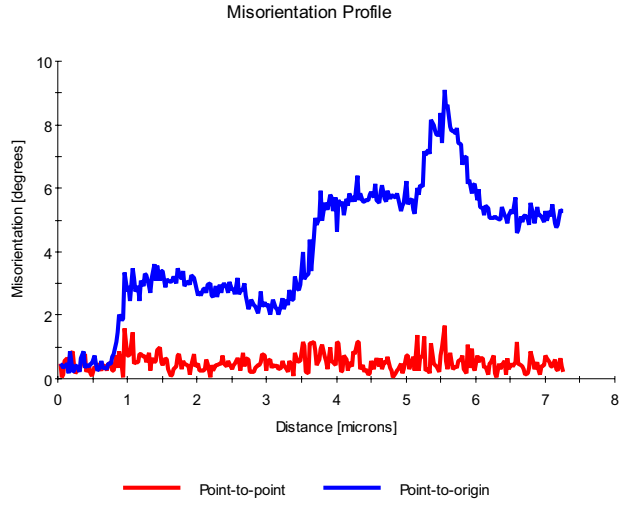

d)

Figure 7.61: Detail at 70% strain. a) IPF map with >2° and >15° boundaries in red and black respectively. b) Misorientation profiles for horizontal, c) blue line and d) lilac line.

The horizontal misorientation profile (Figure 7.61a) reveals the presence of orientation gradients when approaching the high angle grains. Further, the two following misorientation profiles reveal large orientation gradients in the elongation direction. These profiles will probably collapse into sharp sub grain boundaries at higher strains, thereby releasing some of the internal strains.

7.6.5 80% strain

The microstructure at 80% strain is heavily deformed: **(i) the grains have either been divided by deformation bands or (ii) grains oriented within the stable texture components have developed a strong cell structure**. It is still possible to trace most of the original grain boundaries. The new high angle boundaries are mainly formed by deformation bands. An example of this microstructure is shown in Figure 7.62 as IPF maps in the XY and XZ frame.

There are several features worth noting: in the upper right part of Figure 7.62, there are several grains of nearly the same orientation, oriented within the $\pm\mathbf{B}_{\mathbf{E}}$ texture components. These grains have developed a strong cell structure, and the elongation direction (corresponding to the shear direction) can be seen directly in the IPF map (Figure 7.62b). One can also see the alignment of the deformation bands, which tend to align in the grain elongation direction, close to the first principal strain direction. However, some deformation bands align in the shear direction as seen in the grains in the lower left and upper left corners of Figure 7.62. These deformation bands are always rotated into the component (001)/45 **Cube** component, and are formed in grains having a **rotated cube** orientation, i.e. (001)/θ, $\theta \neq 45$.

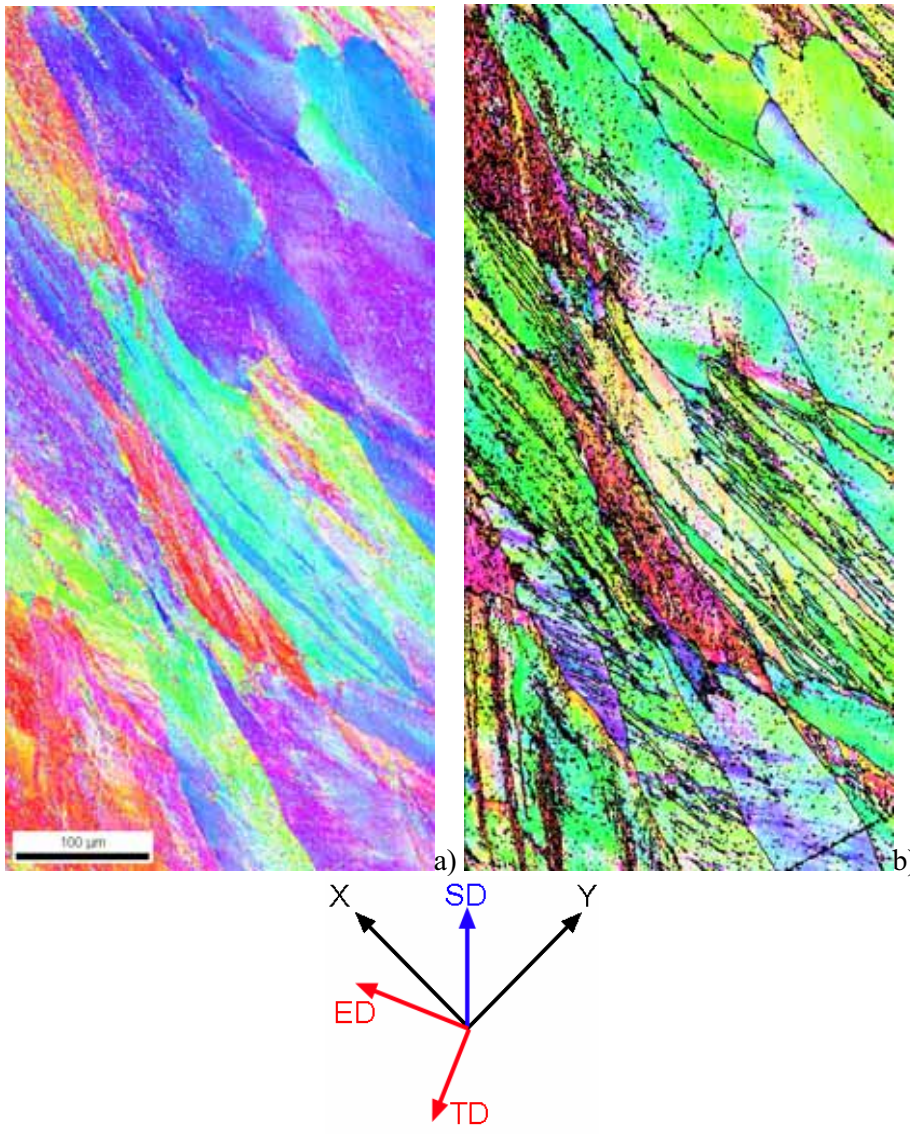

Figure 7.62: Microstructure at 80% strain. a) IPF map in XY-frame, b) IPF map in XZ-frame with high angle boundaries superimposed as black lines.

All orientations having a <110> direction aligned within 15° of the principal shear direction have also been highlighted as shown in Figure 7.63. Again, the deformation bands show up in the highlighted map along with some grains having a stable orientation and therefore are not prone to

deformation banding. The deformation bands tend to align in two directions; along the grain elongation direction or along the principal shear direction, as pointed out above.

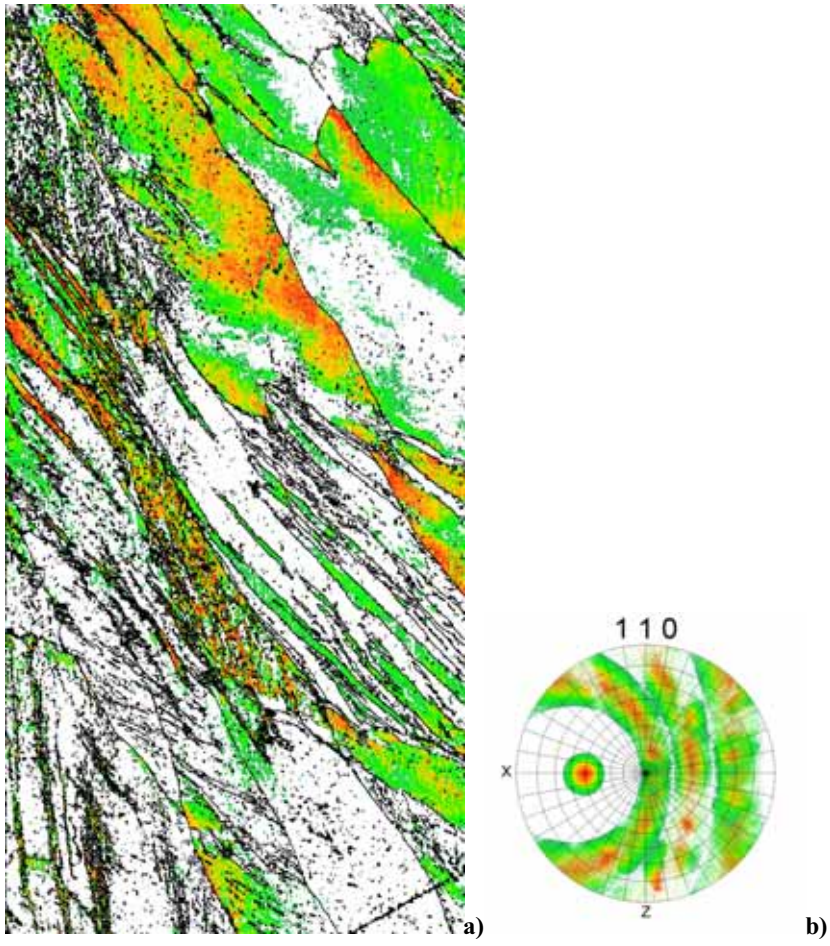

a) b)

Figure 7.63: Highlighting of all orientations within 15° of the principal shear direction, a) highlighted map, b) highlighted orientations.

An example of a highly subdivided area with (112)/θ orientation observed at this strain is shown in Figure 7.64. It is difficult to observe the large orientation differences in the area from the inverse pole figure maps in this figure, therefore the different orientations are highlighted in the following Figure 7.65.

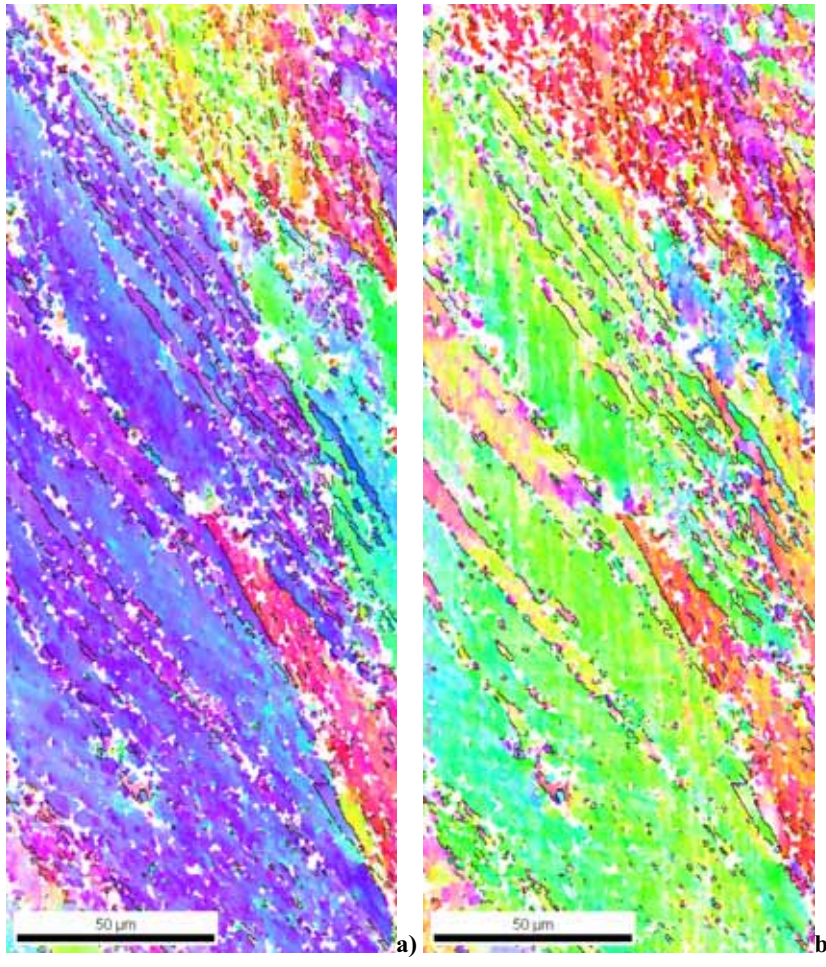

a) b)

Figure 7.64: Detail of a severely subdivided grain represented as a) IPF map in XY-frame and b) XZ-frame. High angle boundaries are superimposed as black lines.

The green and red highlighted areas have a symmetric orientation, (112)/105 and (112)/285 respectively (180° rotation around the Z-axis / <112> crystal axis). The deformation bands are shown in blue colour. The DB's are created by rotating into the stable orientation with a <110> direction aligned at ~45° to the X-axis in the XY plane, hence fulfilling the <110>||SD criteria.

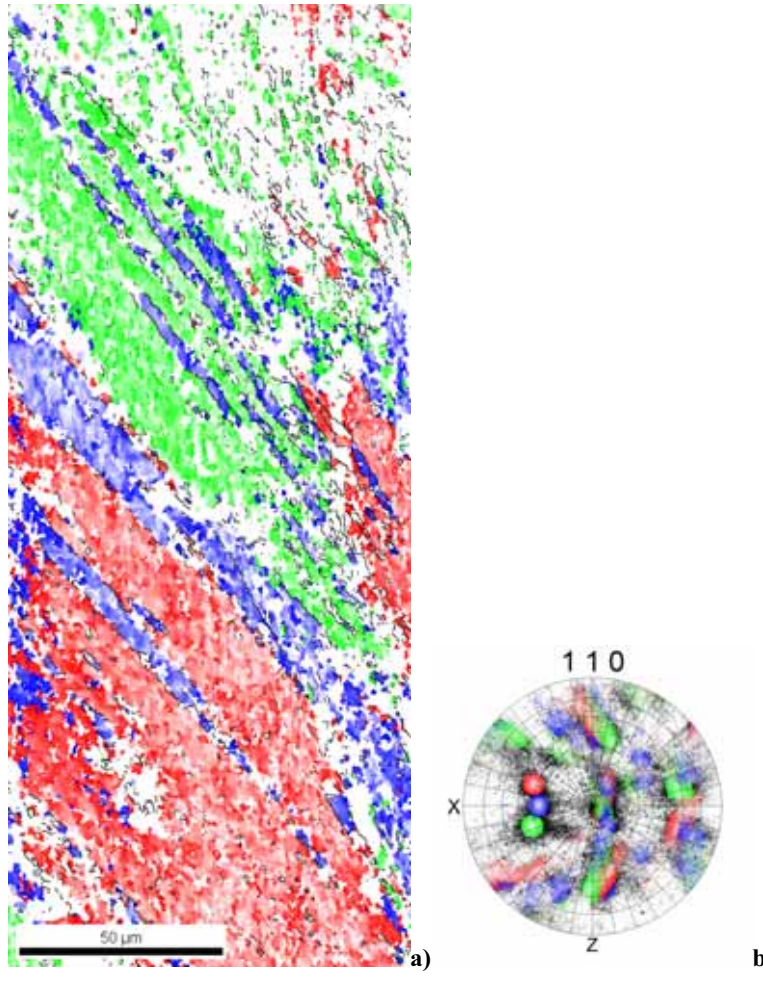

Figure 7.65: Highlighted orientations of the same area as shown in Figure 7.64, a) map, b) corresponding highlighted (110) pole figure. The highlighting was made by applying a colour coding to the selected orientations in the pole figure, shown as green, blue and red circles.

The deformation bands in the green grain have different orientation than the deformation bands in the red grain, and are highlighted as blue and lilac in Figure 7.66; in fact the two sets of deformation bands are separated by a **60° rotation about a <111> axis**, i.e. a **twin relation** having (112)/45 and (112)/225 orientations. The red and green areas are also separated by a ~60° misorientation, within 5° from the 60° twin relation.

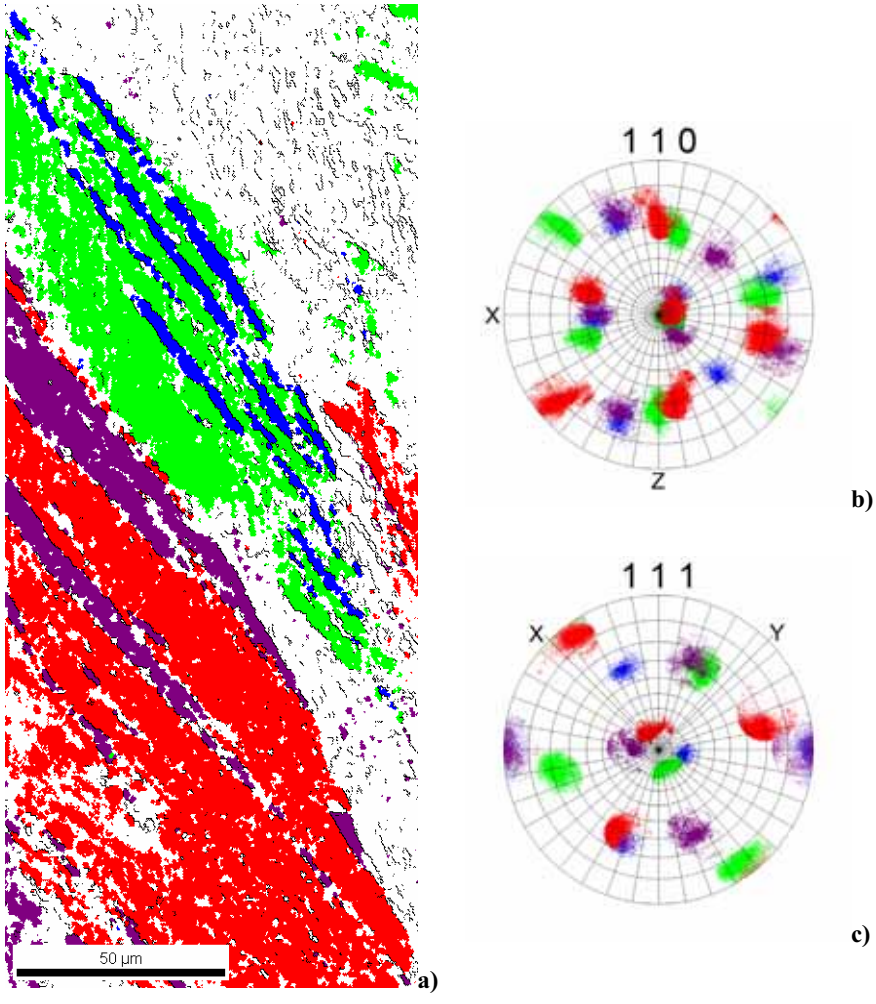

Figure 7.66: Highlighted areas, a) map, b) and c) pole figures. Lilac: (112)/225, red: (112)/285, green: (112)/105, blue: (112)/45.

One can observe some very small fragments having twin orientation relations where the red and the green grain meet. These may have been formed by a twinning mechanism or simply be a result of crystals rotating into symmetrically stable orientations. It is however clear that the deformation bands formed in the green and red highlighted grains are formed by the exact same mechanism as they are related to their parent grain in the exact same way.

A detail of the aligned cell structure in a (112)/165 oriented grain close to a grain boundary is shown in Figure 7.67. Medium angle boundaries (10-20°) separate narrow elongated grains (typically ~0.5μm in width) aligned with the principal shear direction. A misorientation profile across the boundaries shows the presence of orientation gradients in the cell structure (Figure 7.68).

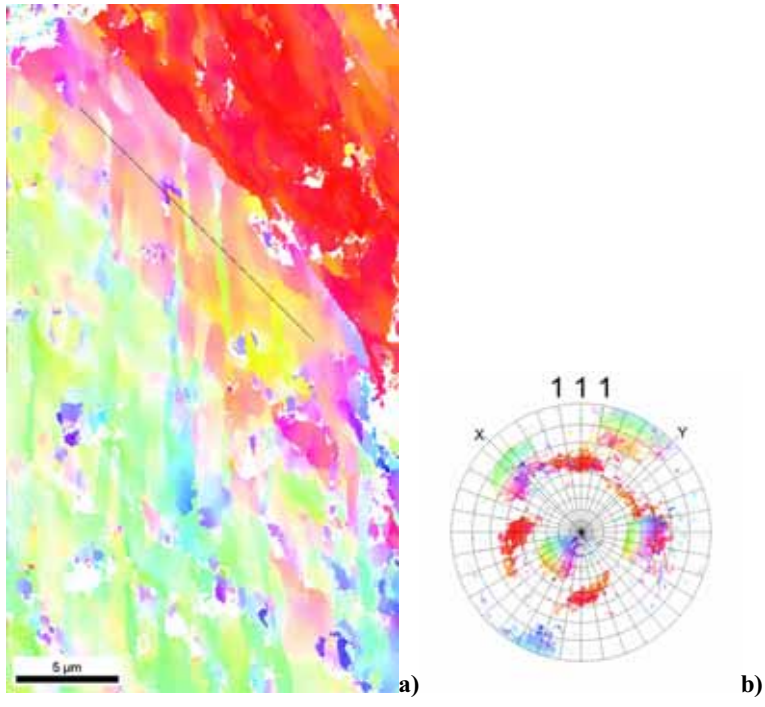

a) b)

Figure 7.67: Cell structure close to a grain boundary at 80%. a) IPF map and b) pole figure with IPF colours applied as highlight. Grain orientations (112)/165 and (100)/45 (red).

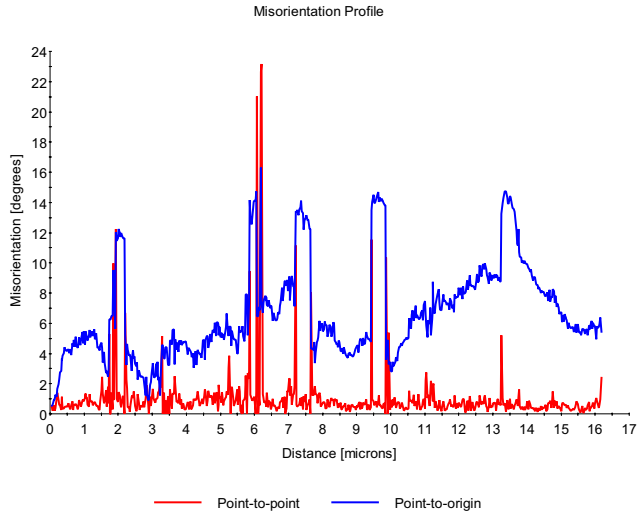

Figure 7.68: Misorientation profile from Figure 7.67.

7.6.6 100% strain (full passage through the deformation zone)

The microstructure after one completed pass does not deviate much from what was observed at 80% strain. A detail of the microstructure is shown in Figure 7.69 as IPF maps in the XY and XZ-frame. There are several observations resembling what have been seen alt lower strains, i.e. the typical break up of the (001)/θ oriented grain into **Cube** oriented deformation bands aligned in the principal shear direction. This is seen in the red grain in the IPF maps. One can see the remaining fragments in the IPF map in the XZ frame (Figure 7.69b), which still carry the original grain orientation, i.e. most of the grain has rotated into the **Cube** component. Another typical feature is the homogeneous deformation by crystalographic slip in grains oriented within the stable texture components. This is shown in Figure 7.70, where orientations having a <110> direction aligned within 15° of the principal shear direction are highlighted.

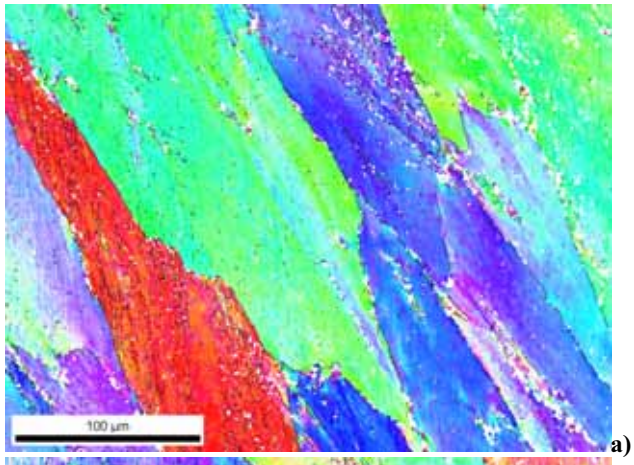

a)

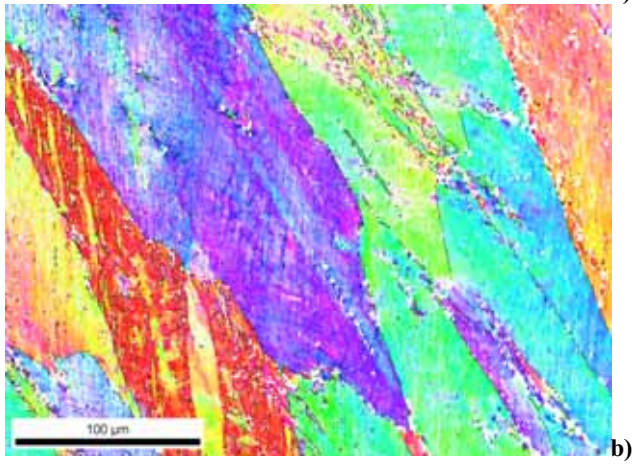

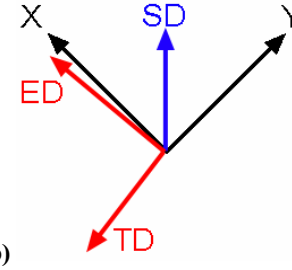

b)

Figure 7.69: Section of the microstructure at 100% strain. a) IPF map in the XY-frame, high angle boundaries presented as black lines, b) IPF map in the XZ frame, high angle boundaries presented as black lines.

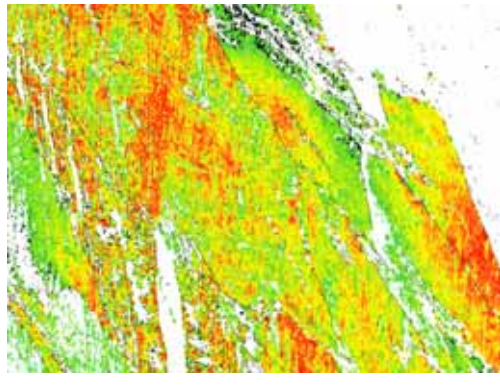

a)

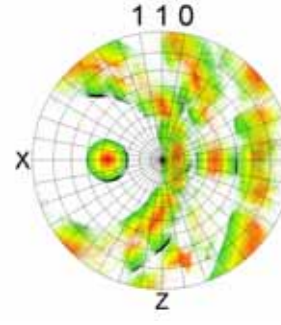

b)

Figure 7.70: Highlighting of orientations within 15° of the principal shear direction, a) highlighted map, b) corresponding highlighted orientations.

7.7 Microstructural observations through the deformation zone: Second pass

The microstructural development appearing in the second pass (Route A) differs somewhat from the development in the first pass. The starting texture is already well developed and the microstructure is highly deformed. Please note that all measurements made in the second pass are made in the mirror plane of the first pass, i.e. the XYZ-coordinate system is flipped vertically.

7.7.1 10% strain in 2nd pass

The starting microstructure and texture in the second pass is of course equal to the final micro structure and texture from the first pass, but rotated -90° about the Z-axis according to route A. The aligned cell structure from the first pass, which was aligned at 45° to the X-direction, is now aligned at -45° to the X direction. From the observations made during the first ECAP pass, the preferential active shear direction is located between 30 and 45° to the X-direction and in the XY-plane. The established texture from the first pass has resulted in an increased population of <110> slip directions now aligned at 15 and 75° to the X direction (~6 times random), and a very low population of <110> directions between 30 and 45° to the X-direction (~0.5 times random, values taken from Figure 7.28). One may assume that any new aligned cell structure forming during the earliest stages of deformation in the second pass will either form in the direction of the already established population of <110> directions located 15° to the X-direction, or in any grain already oriented with a <110> direction aligned at ~30° to the X-direction (in the XY-plane). This means that one will expect a spread in the alignment of the cell structure during the early stages of the second pass.

An example of the microstructure at 10% strain in the second pass is shown in Figure 7.71. One can easily see the aligned cell structure from the first pass aligned -45° to the X-direction. (Judging from the width and

direction of the band in the middle of Figure 7.71, this is assumed to be part of a deformation band or transition band.)

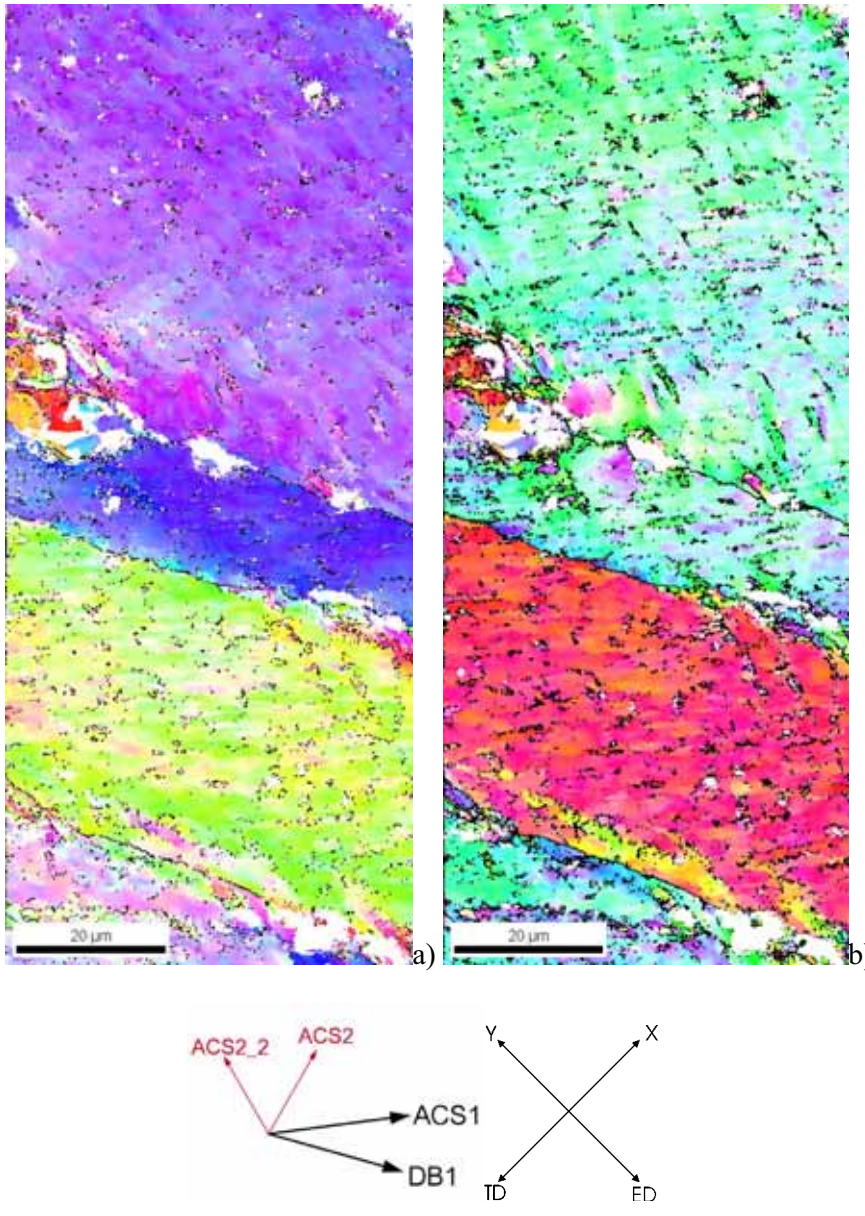

Figure 7.71: a) IPF map in XY-frame, b) IPF map in XZ-frame (DB1: direction of deformation bands formed during the first pass, ACS1: direction of aligned cell structure formed during the first pass, ACS2: direction of new forming cell structure). High angle boundaries presented as black lines.

7.7.2 30% strain in 2nd pass

At 30% strain in the second pass, one can clearly see the results of new structures formed in the second pass, crossing structures formed in the first pass. A section of the microstructure at 30% strain is shown in Figure 7.72 as IPF maps in the XY- and XZ-frame respectively.

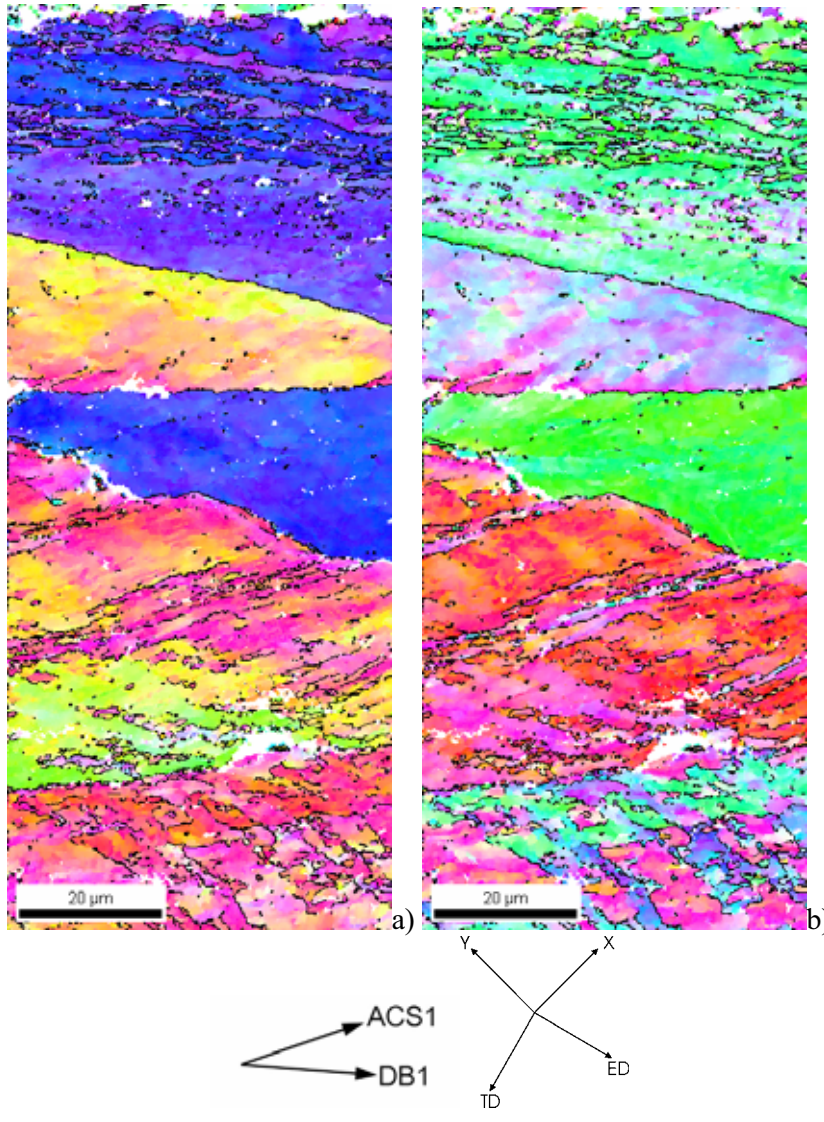

Figure 7.72: Section of the microstructure at 30% strain in the second pass. a) IPF map in the XY-frame, b) IPF map in the XZ-frame. High angle boundaries are superimposed as black lines.

These EBSD maps show the large variations in microstructure present in different areas. One can observe deformation bands, homogeneously deformed areas with aligned cell structure, macroscopic deformation by deformation bands and crossing deformation bands in highly disturbed regions.

The deformation bands observed in Figure 7.73 are probably formed during the first pass and are realigning some of the bands during the second pass.

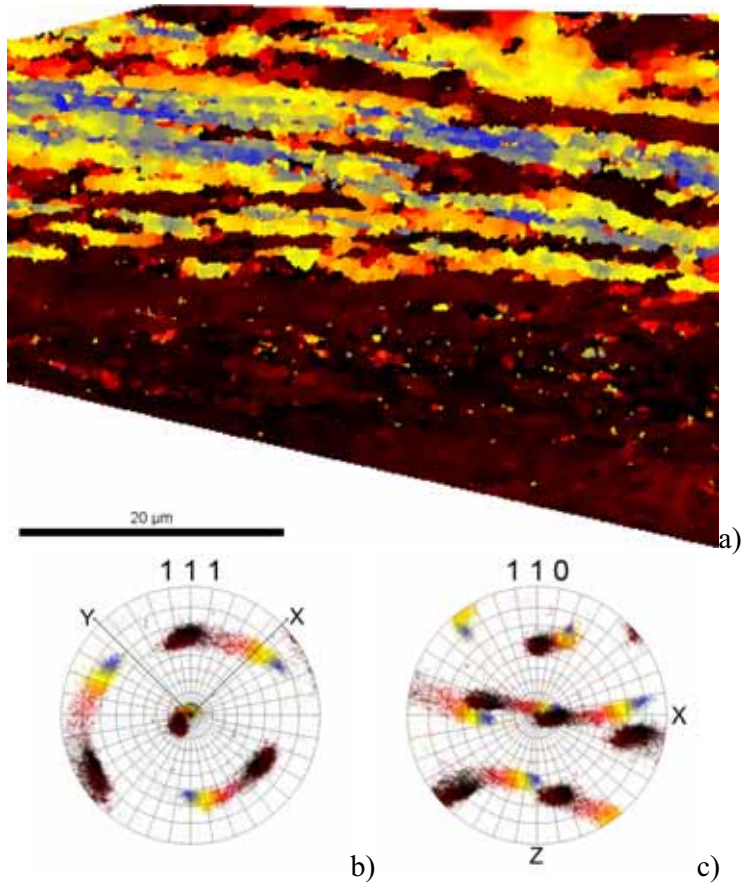

Figure 7.73: Example of a grain which was subdivided by deformation bands during the first pass ((112)/165 oriented grain with $-B_E$ (111)/105 oriented deformation bands) and is now realigning towards the new stable B_E (111)/45 orientation. a) Highlighted map, b) and c) corresponding pole figures.

The area highlighted in the darkest colour has an orientation (112)/75, the red has a (111)/45 $\mathbf{B_E}$ orientation, and the blue has a (111)/15 orientation. The (111)/15 orientation had a stable (111)/105 ($\mathbf{-B_E}$) orientation during the first passes and is now rotating towards the new stable (111)/45 $\mathbf{B_E}$ orientation. The (112)/75 orientation had a (112)/165 orientation during the first pass, and was likely to be the original grain orientation in which the (111)/105 ($\mathbf{-B_E}$) deformation bands formed during the first pass.

The effect of **banding by grain rotation** is shown in Figure 7.74, where the displacement along a grain boundary clearly illustrates how deformation is carried by large crystal rotations and concentrated slip in narrow bands. **The bands (DB2) form on the aligned cell structure generated during the first pass** (ACS1). This may be due to the fact that the direction of ACS1 coincide with the first principal strain direction (ε1) in the second pass.

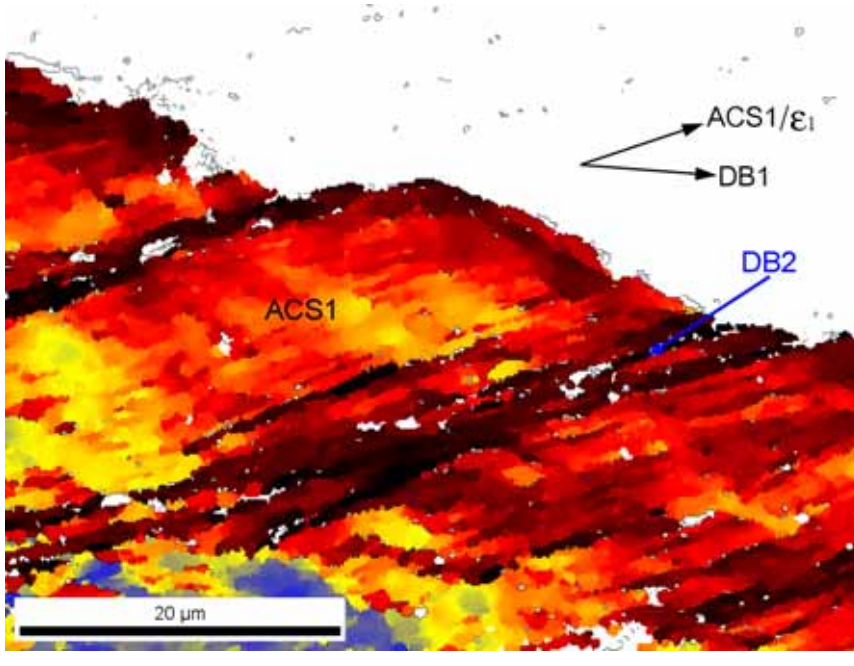

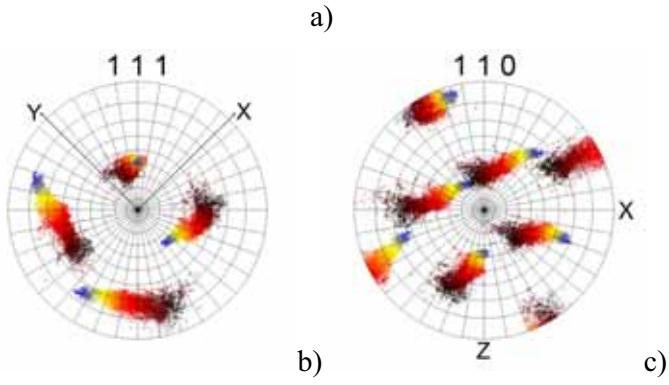

Figure 7.74: Banding on cell structure from the first pass. a) Highlighted grain, b) and c) corresponding pole figures. Key orientations (-7 0 1)/175 (red) and (3 -4 16)/335 (dark red-black, DB2).

Large deformations occur in the dark-red highlighted areas. These areas have not rotated into or towards stable orientations, but have probably occurred as a result of the macroscopic deformation. The **crystal rotation occurs around a <111> axis**, i.e. the crystals rotate on a (111) plane and thus have three <110> slip directions available for rotation in that plane.

Another interesting observation is found in the area in Figure 7.75. This grain has been severely subdivided by crossing deformation bands. From the pole figures in Figure 7.75 b) and c), we observe that the total crystal rotation is occurring out of the XY-plane, and resembles the subdivision from Figure 7.53, in this case however, the grain has been split towards (112)/25 and (112)/315. These orientations correspond to (112)/115 and (112)/45 in the *first pass* respectively, i.e. before the -90° sample rotation by route A. It is thus likely that this is an example of the **(112)/45 A_E texture component formed during the *first pass,* splitting and rotating towards the A_E component in the *second pass***. The crystal rotation occurring here is a **rotation around a <111> axis** which supports the above assumption, as

the crystal rotates on a (111) plane and thus has three <110> slip directions available for rotation in the plane.

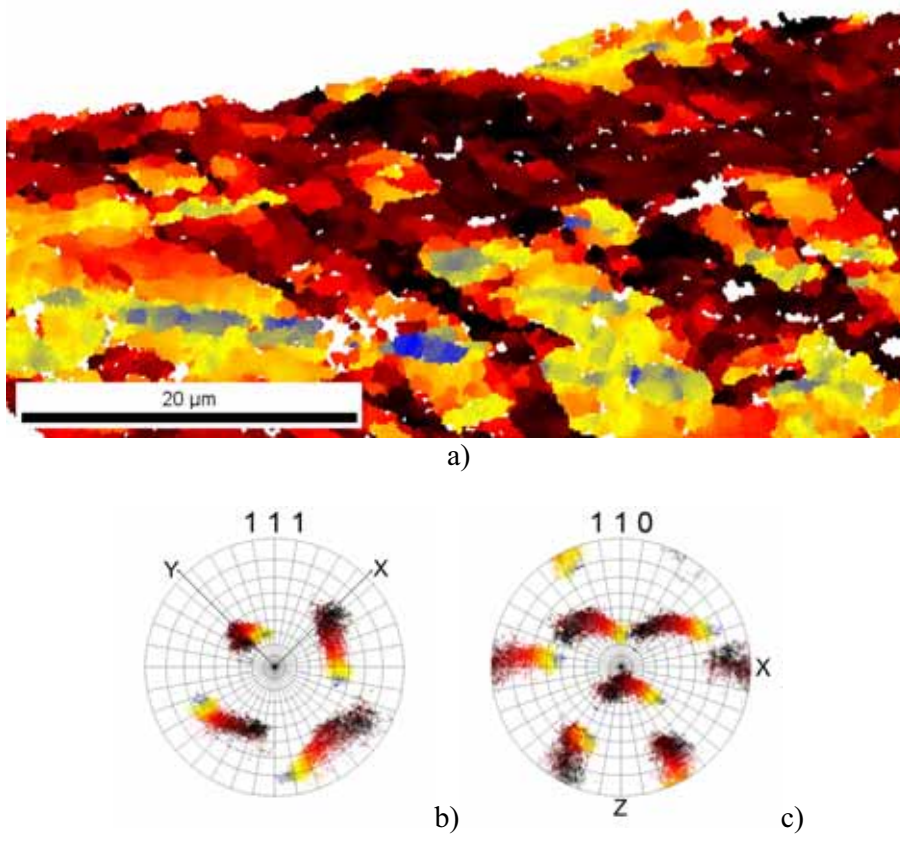

Figure 7.75: Severe subdivision of a grain by crossing deformation bands. a) Highlighted map, b) and c) corresponding pole figures. Key orientations (5 -11 2)/200 blue, (-1 15 -2)/310 red, and (-4 7 -16)/210 dark red.

7.7.3 50% strain in 2nd pass

A section of the microstructure at 50% strain into the second pass is shown in Figure 7.76 as inverse pole figure maps in the XY- and XZ-frame and a grey scale fit-parameter map superimposed. This aids in revealing the substructure without drawing all the low angle boundaries on the map. The white areas represent non-indexed primary particles. The complexity of the microstructure makes it difficult to interpret; however, there are still identifiable structures.

In this map, it is also possible so see the effect of the primary particles on the surrounding microstructure. The blue grain in the upper half of Figure 7.76a) is oriented within the stable $\mathbf{B_E}$ texture component and may therefore deform by crystalographic slip in the shear direction. This grain shows no additional effect from the neighbouring particles. The material on the lower side of the particles however, has undergone severe plastic deformation and poses a very refined structure. The average crystal orientations in this area appear to be close to (001)/90, i.e. a very hard orientation. Thus, it is reasonable to assume that soft oriented grains are not affected by the hard, non-deformable primary particles while the hard oriented grains break up and become severely subdivided.

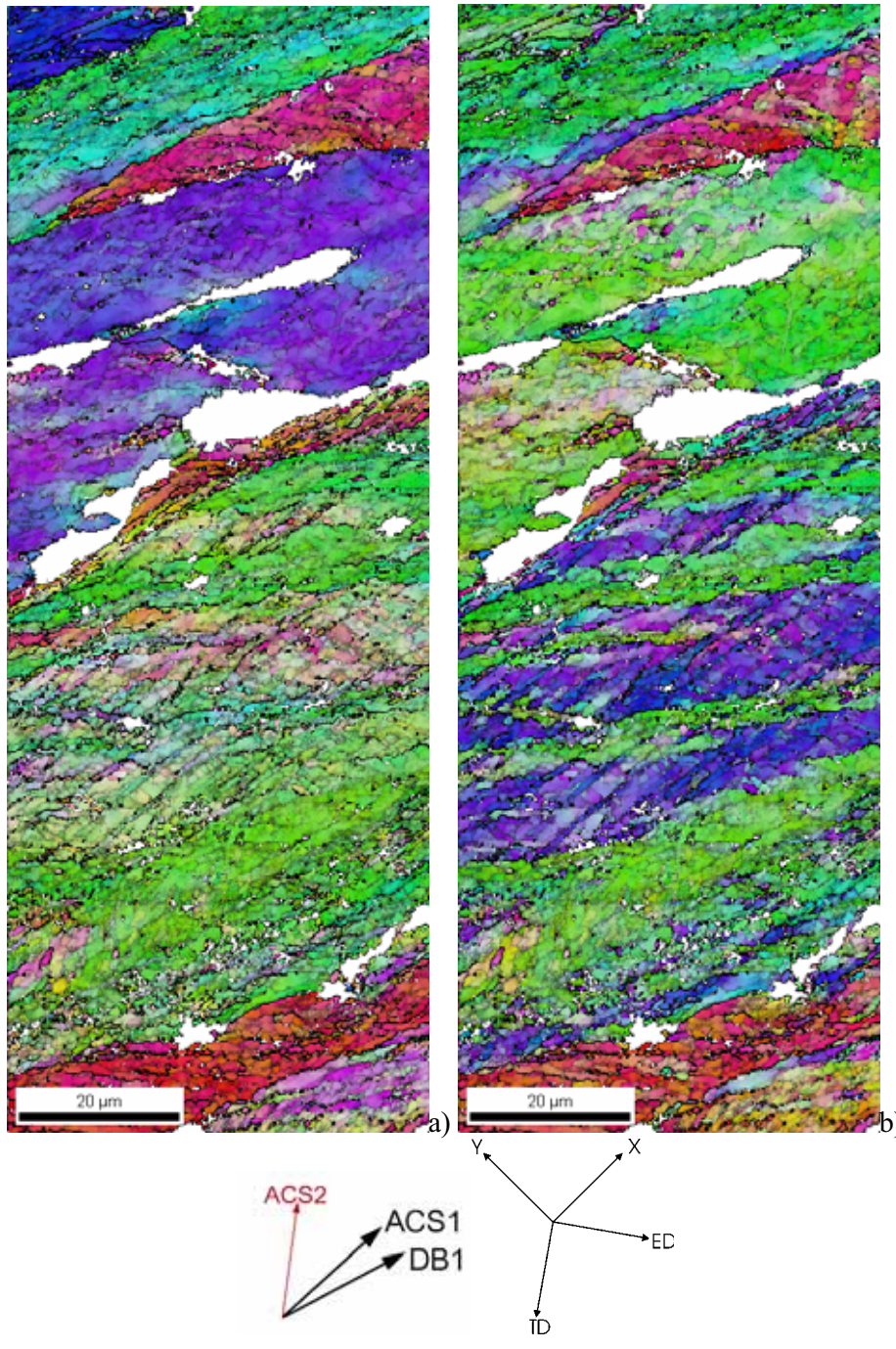

Figure 7.76: Microstructure at 50% strain in second pass presented as IPF map and superimposed fit parameter in grey-scale to reveal the sub-structure in a) the XY-frame and b) the XZ-frame. High angle boundaries are superimposed as black lines.

Another typical feature observed at this strain level is the **stair-step structure**. The deformation carried by the cell structure results in disturbance of crossing structures such as deformation bands. The effect results in a "stair-step" structure along the boundaries of the DB's as shown in Figure 7.77. This indicates that slip has occurred extensively in the red bands. The crystalographic orientation in these bands does not deviate significantly from the surrounding cell structure. The alignment of the bands is in the direction of the cell structure formed during the first pass. The cell structure in the turquoise area is aligned normal to the direction of the red bands. This can be seen in more detail in Figure 7.79.

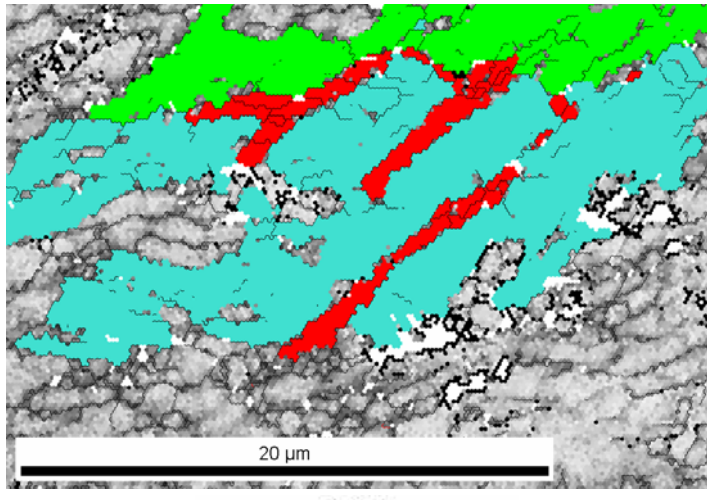

a)

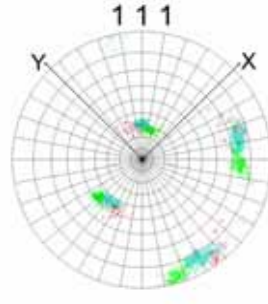

b)

Figure 7.77: a) stair step structure by concentrated slip in collapsed ACS's: turquoise=ACS region, red=collapsed ACS, green=deformation band from first pass, b) highlighted pole figure

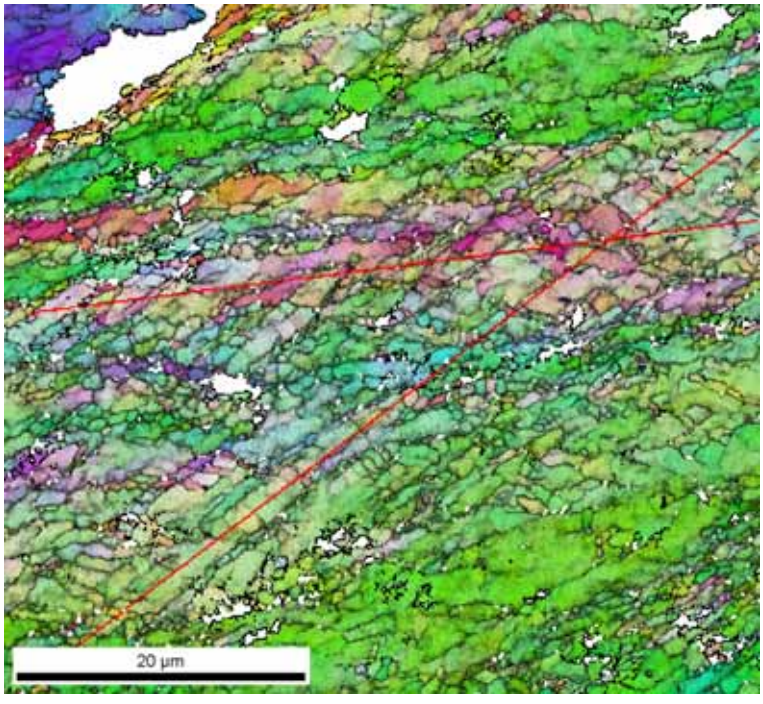

a)

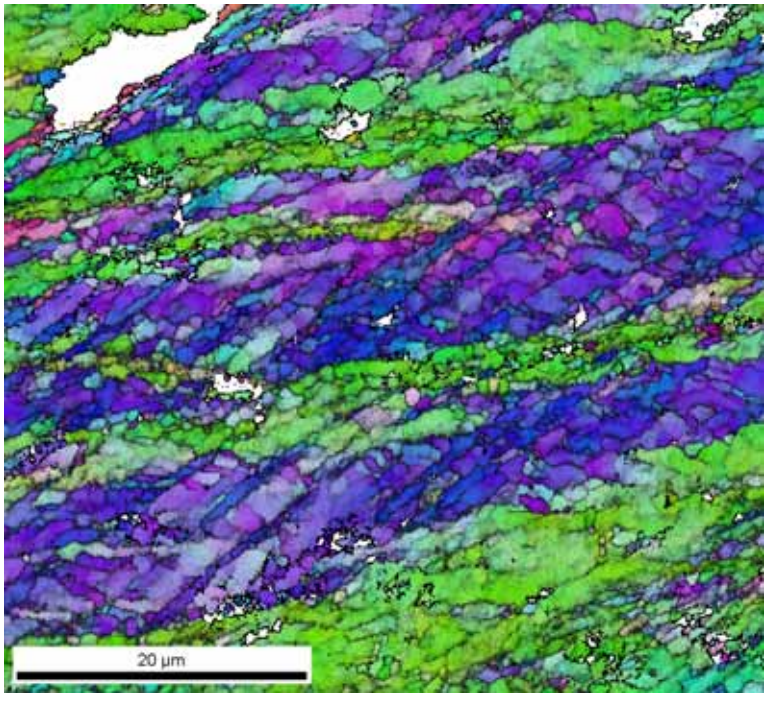

b)

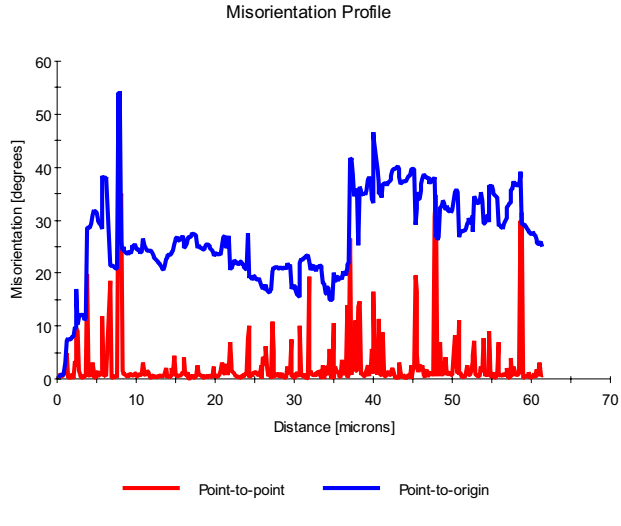

c)

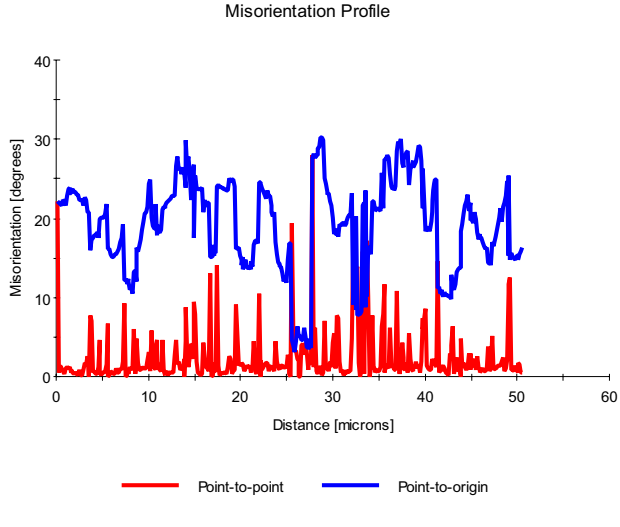

d)

Figure 7.78: IPF map in a) the XY- and b) the XZ-frame with boundaries >5° superimposed as black lines. Misorientation profiles: c) horizontal line, d) diagonal line.

The ~horizontal misorientation profile (drawn left to right) shows that the typical misorientation between the turquoise and red bans in the previous figure is less than 15°, however there are some bands which have developed high angle boundaries (20-35°). The diagonal misorientation profile (drawn bottom to top) reveals the cell misorientation in one of the

wide bands. The typical cell misorientation is 8-12°. The band is disrupted halfway through the misorientation profile by a crossing deformation band, and can bee seen in the misorientation profile by the large drop in the blue "point to origin" curve.

The section shown in Figure 7.79 shows how this grain, oriented as (110)/45 $\mathbf{C_E}$ component in the *first pass* (now oriented (110)/125 and shown in dark-red colour), splits by deformation bands rotating towards the stable $\mathbf{A_{2E}}$ texture component, which at 50% strain is located at (110)/90 (shown in blue-yellow colour).

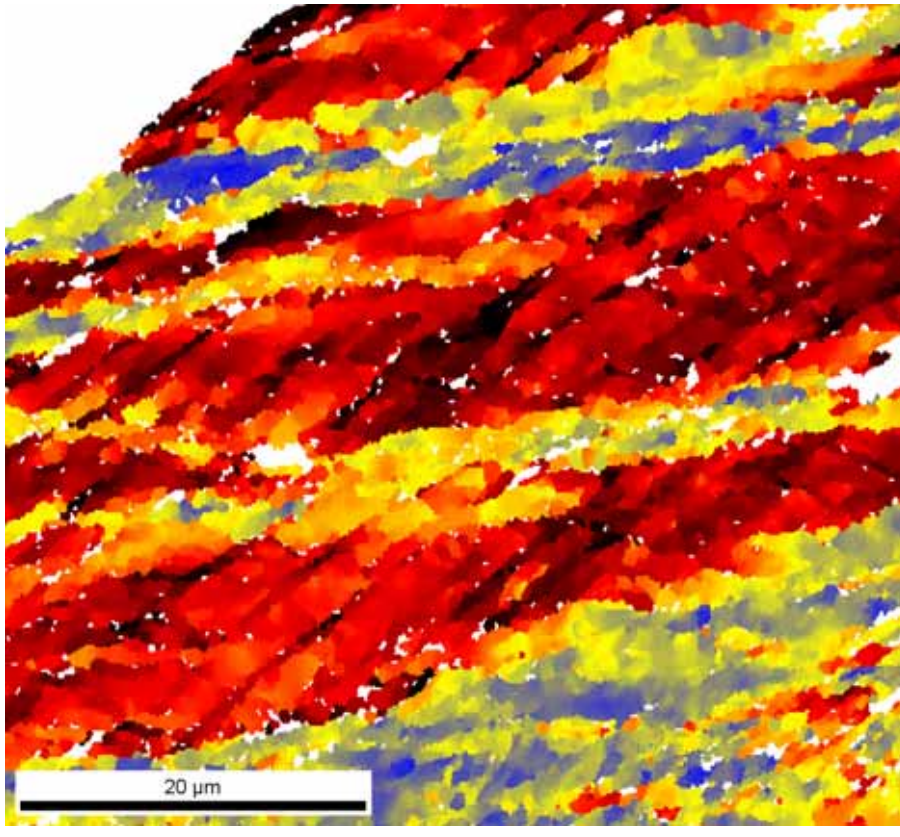

a)

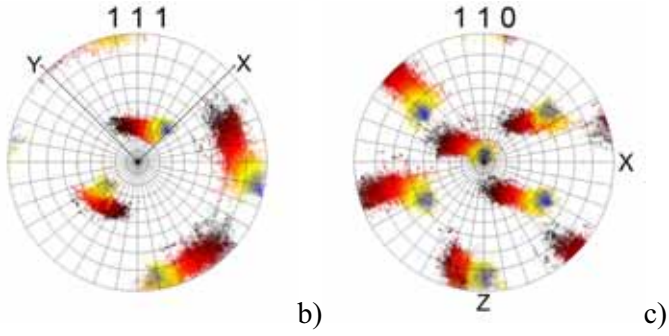

Figure 7.79: Example of a grain oriented within the C_E component in the first pass, now being divided by deformation bands rotating towards the A_{2E} component. a) Highlighted grain, b) and c) corresponding pole figures. Key orientations Blue-yellow (110)/65-95 A2e; dark red (110)/125.

7.7.4 75% strain in 2nd pass

A section of the microstructure after 75% strain is the second pass is shown in Figure 7.80 presented as IPF maps in the XY- and the XZ-frame with superimposed grey-scale fit parameter in order to reveal the sub-structure.

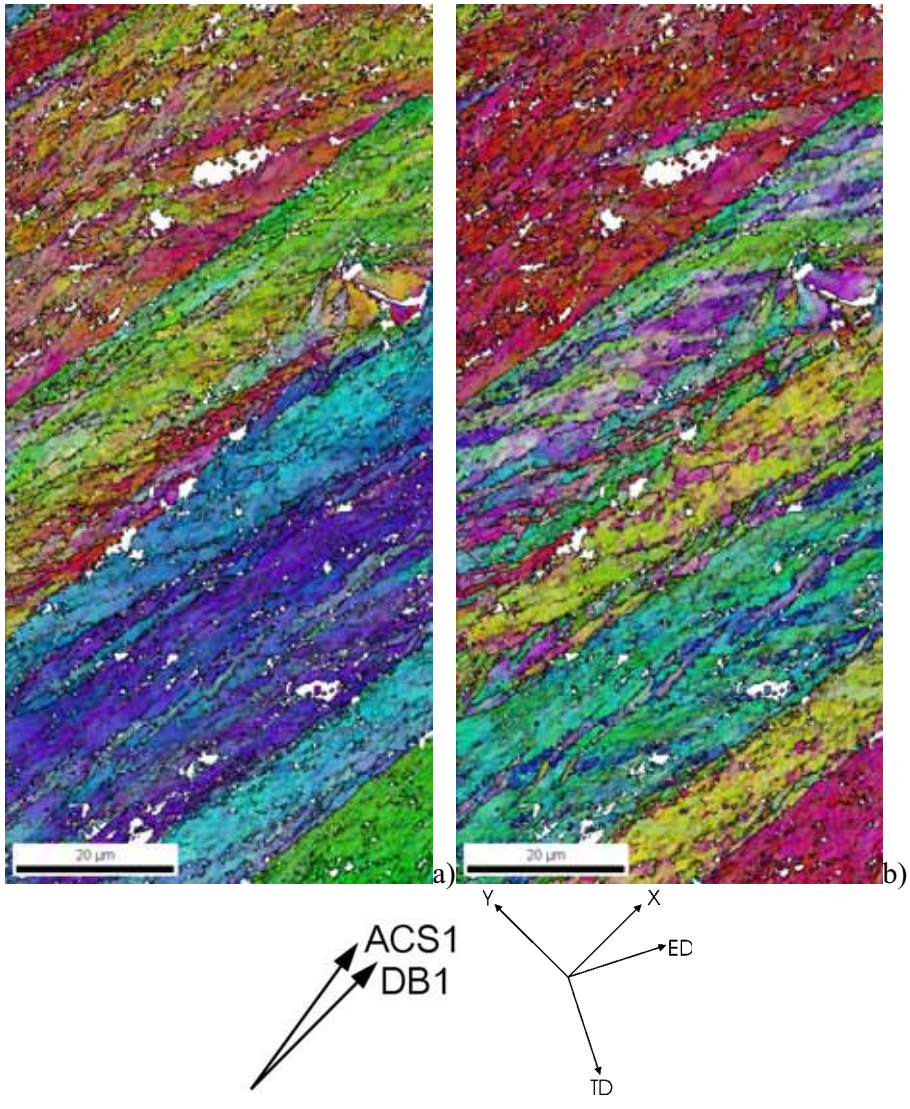

Figure 7.80: Microstructure at 75% strain in second pass presented as IPF map and superimposed fit parameter in grey-scale to reveal the sub-structure in a) the XY-frame and b) the XZ-frame. High angle boundaries are superimposed as black lines.

The traces of the aligned cell structure formed during the first pass are still visible, but have gradually developed into aligned grains separated by low to medium angle boundaries, typically ~5-15°. We observe an increasing population of **small band-like fragments separated from the matrix by high angle boundaries**. These are not deformation bands as observed during the first pass, but fragments showing a large spread in orientation. **These fragments are often aligned clusters of small grains separated by high angle boundaries.** A typical example is shown in Figure 7.81 and Figure 7.82. The green and blue highlighted areas are deformation bands formed during the first pass while the red highlighted areas are aligned grain clusters. The large spreads in orientation in these areas are shown in the two pole figures and corresponds to 120° rotation about the Z-axis, though the actual misorientation is of course smaller.

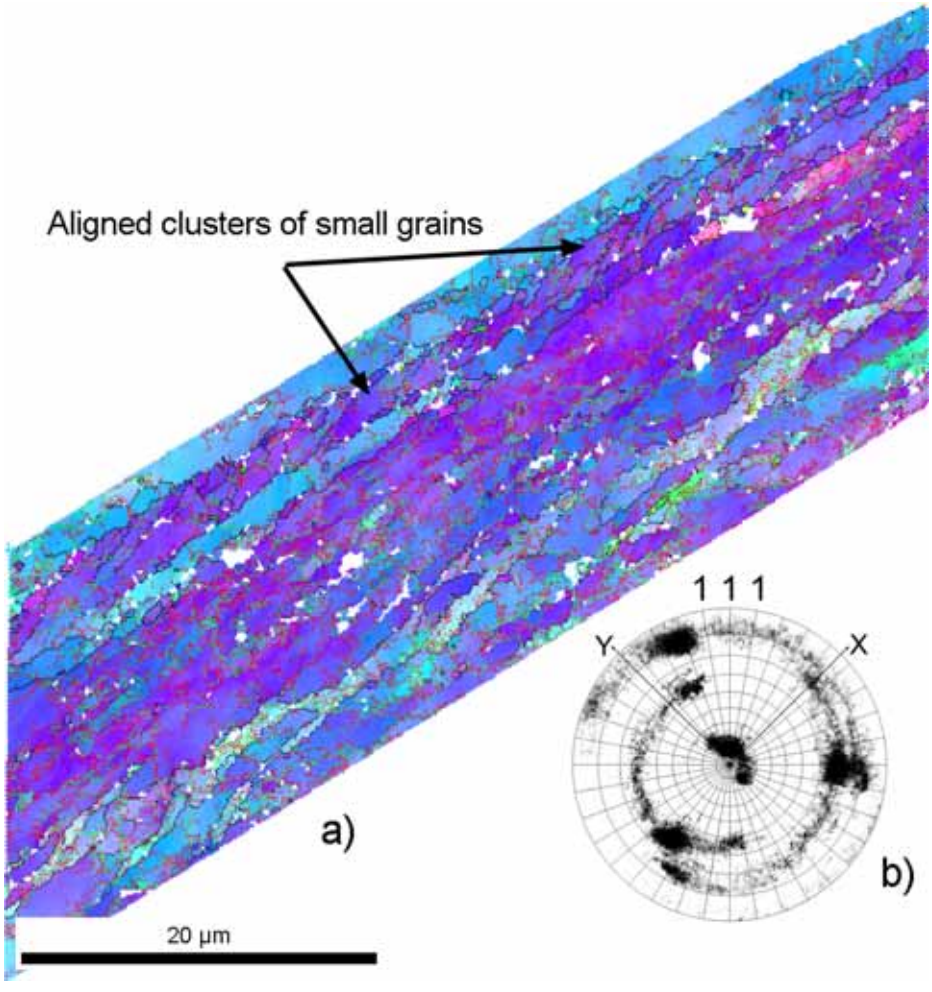

Figure 7.81: a) Selected subdivided area presented as IPF map in the XY-frame with low (2-5°), medium (5-15°) and high angle boundaries as red, green and black lines respectively, b) corresponding (111) pole figure.

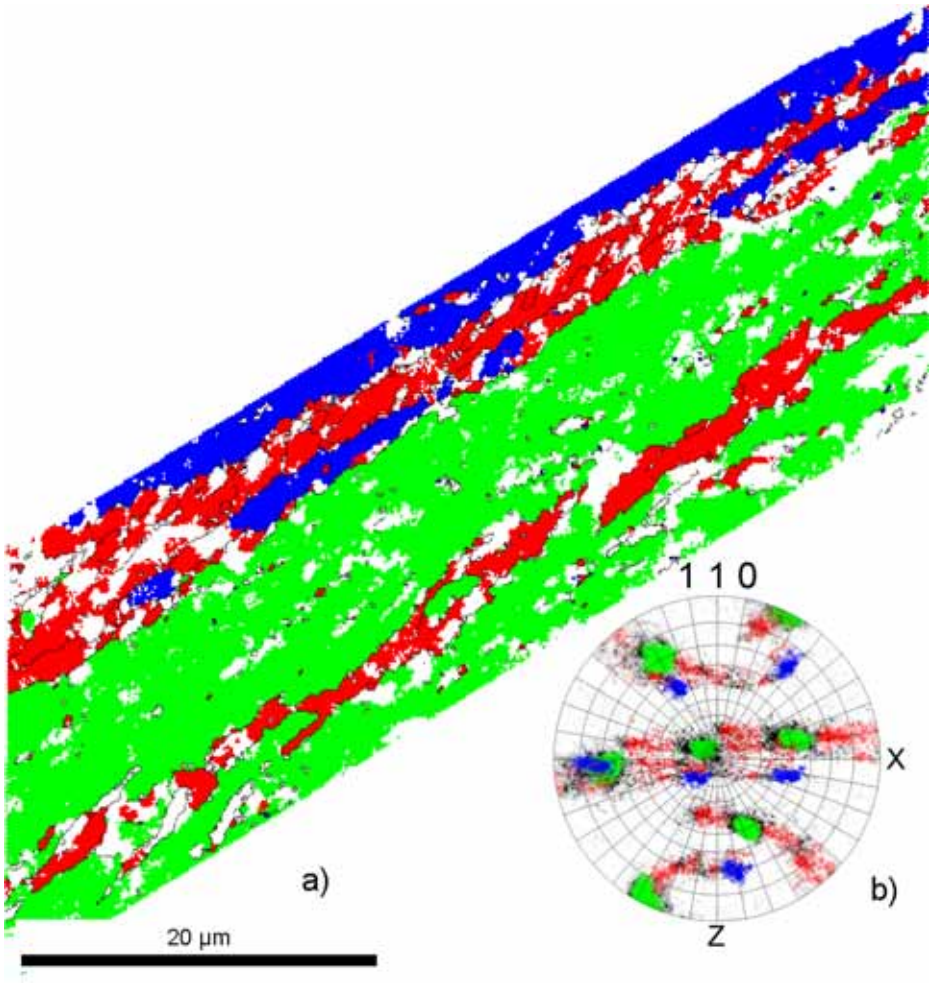

Figure 7.82: Highlighted orientations shown in a) map with high angle boundaries superimposed as black lines and b) corresponding (110) pole figure. Key orientations (8 5 -9)/53 blue and (10 8 -15)/165 green. Note the large spread in orientation in the red highlighted grain clusters.

7.7.5 95% to 105% strain in 2nd pass

A section of the microstructure after 95% strain in the second pass is shown in Figure 7.83 presented as IPF maps in the XY- and the XZ-frame with superimposed grey-scale fit parameter in order to reveal the sub-structure. The microstructure has become very complex and consists of several different structural elements. Some areas oriented within the stable texture components carry the aligned cell structure in the direction of principal shear, as shown in the following example. Deformation bands formed during the second pass are observed aligning in different directions. Many of the deformation bands seem to be divided into smaller fragments, probably as a result of the shear deformation acting at an angle to the direction of the bands. There are also some areas which have been severely subdivided by crossing deformation bands and carrying the earlier mentioned “stair step” structure.

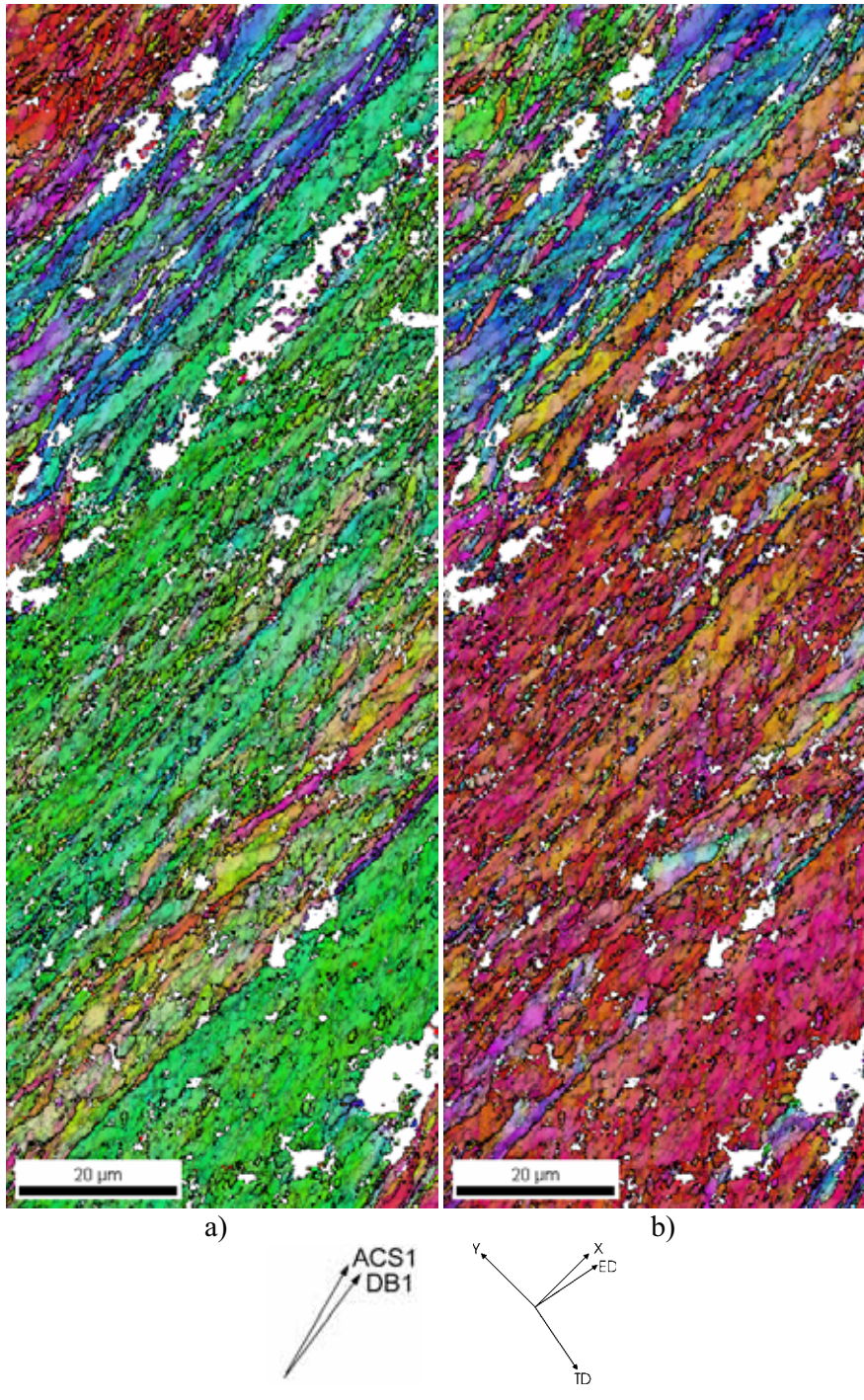

Figure 7.83: Microstructure at 95% strain in second pass presented as IPF map and superimposed fit parameter in grey-scale to reveal the sub-structure in a) the XY-frame and b) the XZ-frame.

An example of an area carrying the aligned cell structure formed during the second pass is shown in Figure 7.84. The orientation is within $\mathbf{A_{1E}}$ texture component ((110)/165) and is highlighted in blue-yellow colour. The IPF map (Figure 7.84a) also reveals some deformation band fragments. The (111) pole figure also shows the typical "out of plane" rotation which has been observed earlier, e.g. Figure 7.53, Figure 7.75 and Figure 7.79. The dark red highlighting also has a stable orientation, (110)/105 $\mathbf{A_{2E}}$.

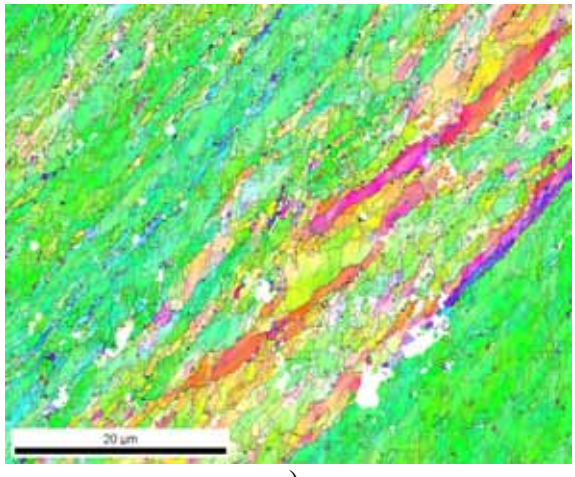

a)

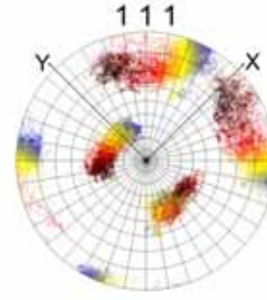

c)

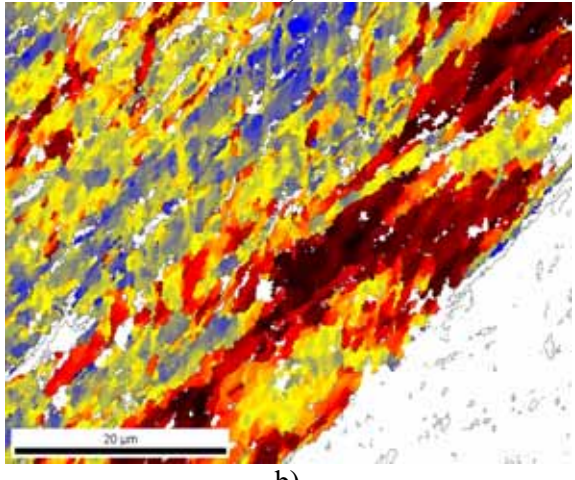

b)

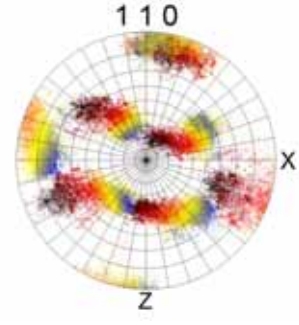

d)

Figure 7.84: Selected area presented as a) IPF map in the XY-frame with low and high angle boundaries superimposed as grey and black lines respectively. b) Highlighted area, c) and d) corresponding pole figures. Key orientations (110)/165 A_{1E} blue; (110)/105 A_{2E} dark-red; (0 -6 -1)/100 red.

A section of the microstructure the end of the second pass is shown in Figure 7.85, presented as IPF maps in the XY- and the XZ-frame with superimposed grey-scale fit parameter in order to reveal the sub-structure.

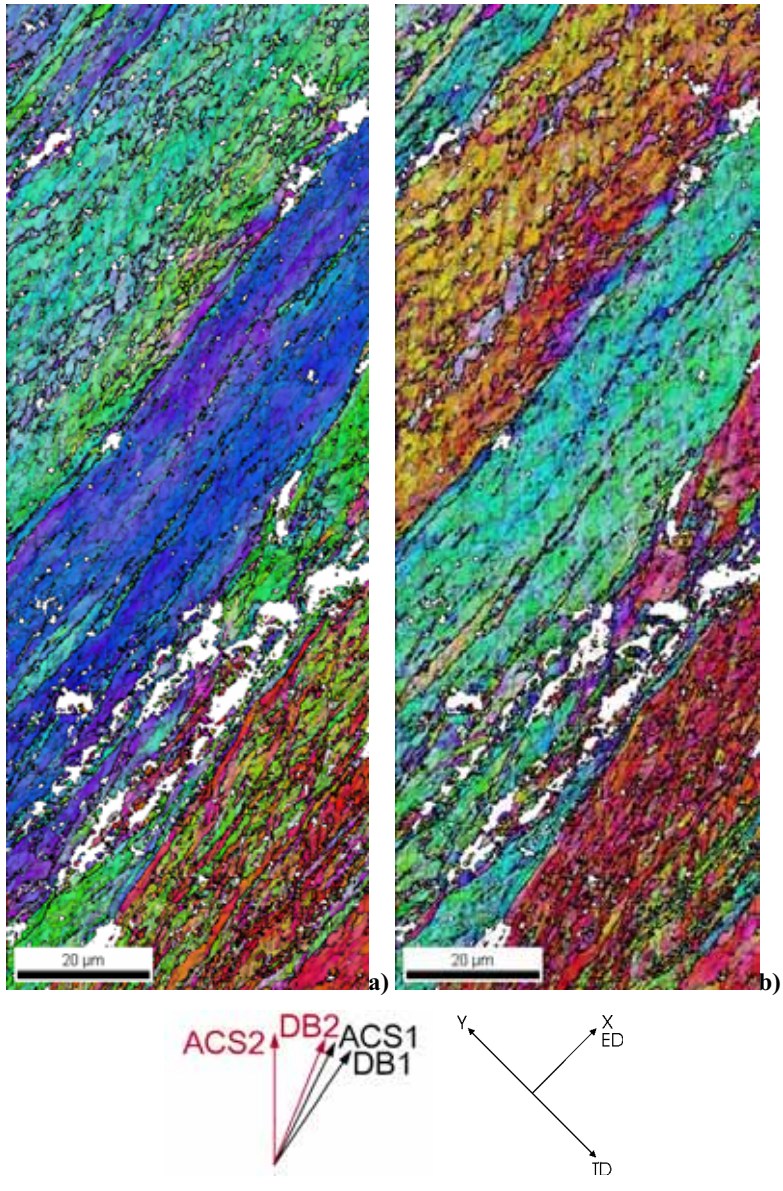

Figure 7.85: Microstructure at 105% strain in second pass presented as IPF map and superimposed fit parameter in grey-scale to reveal the sub-structure in a) the XY-frame and b) the XZ-frame.

There are some large sections showing aligned cell structure formed during the second pass in addition to some severely subdivided areas. A section from the aligned cell structure is shown in Figure 7.86. The lower section has a stable orientation within 10° of the $\mathbf{B_E}$ texture component, while the upper section is close to the $\mathbf{A_{1E}}$ texture component. There are also some very small deformation bands present in the $\mathbf{B_E}$ oriented grain. These deformation bands are oriented within the $\mathbf{A_{1E}}$ texture component.

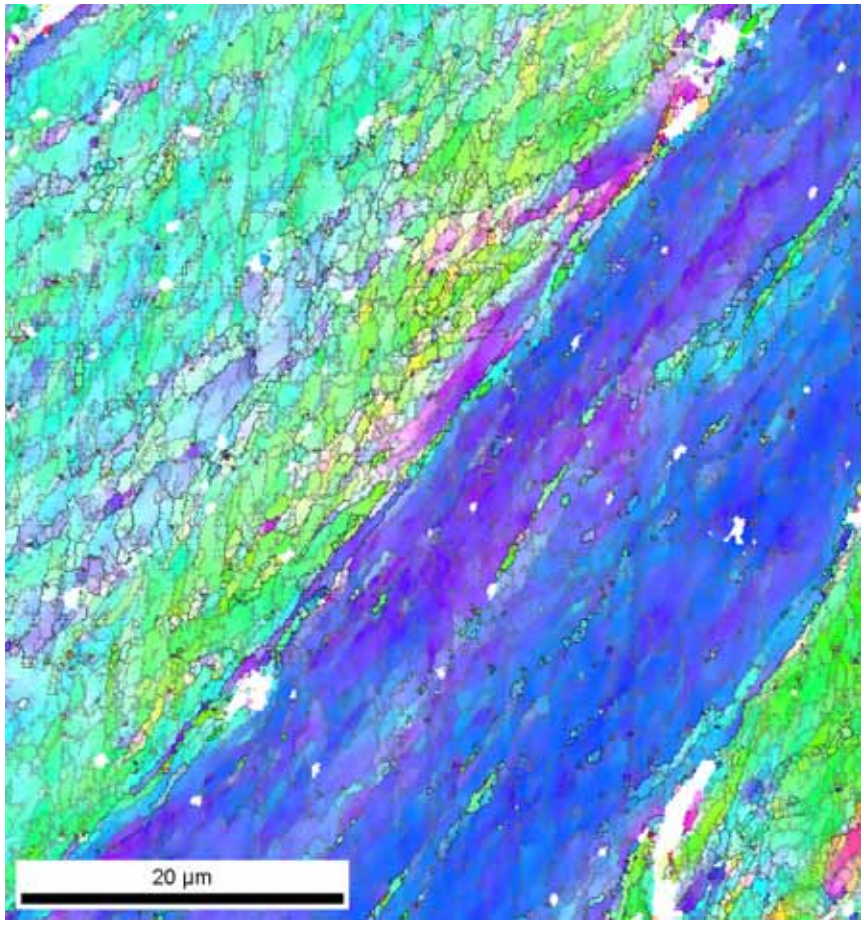

a)

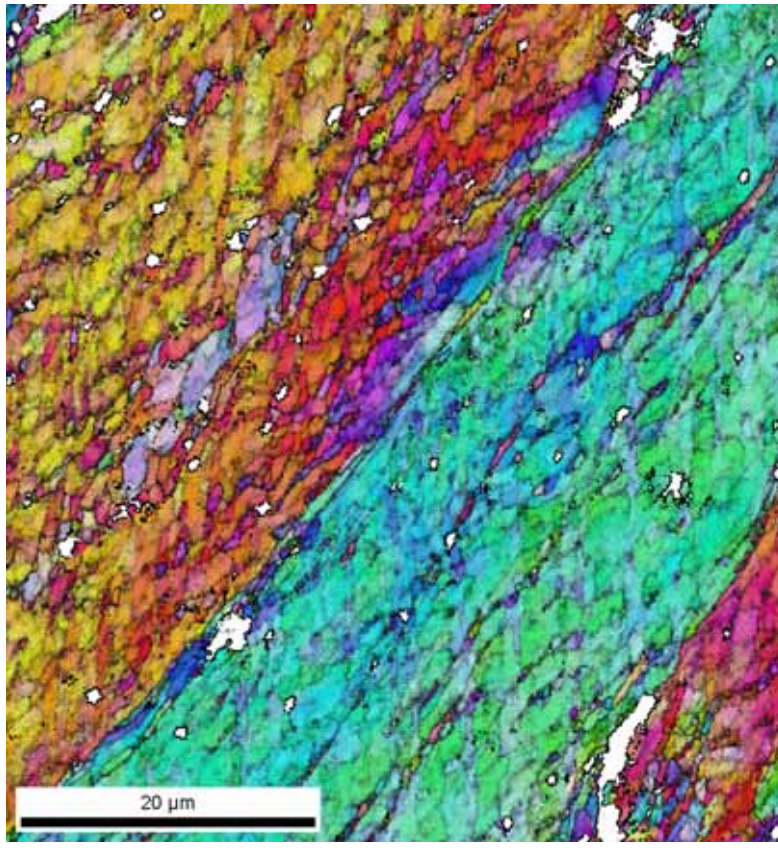

Figure 7.86: Selected area presented as IPF maps in a) the XY-frame with low and high angle boundaries as grey and black lines and b) in the XZ-frame with the fit-parameter superimposed as grey scale. c) and d) Pole figures with the colours in b) applied as highlight. (Blue (111)/45)

The last example is of a very refined area which has been split by crossing deformation bands at a very fine scale (Figure 7.87). The spread in

orientation is very large as may be seen in the pole figures in Figure 7.87c-d. The boundary spacing in this area is 0.25μm for low angle boundaries (higher than 2°) and 0.39μm for high angle boundaries (higher than 15°). It is obvious that the initial grain orientation is very important regarding the efficiency of grain subdivision.

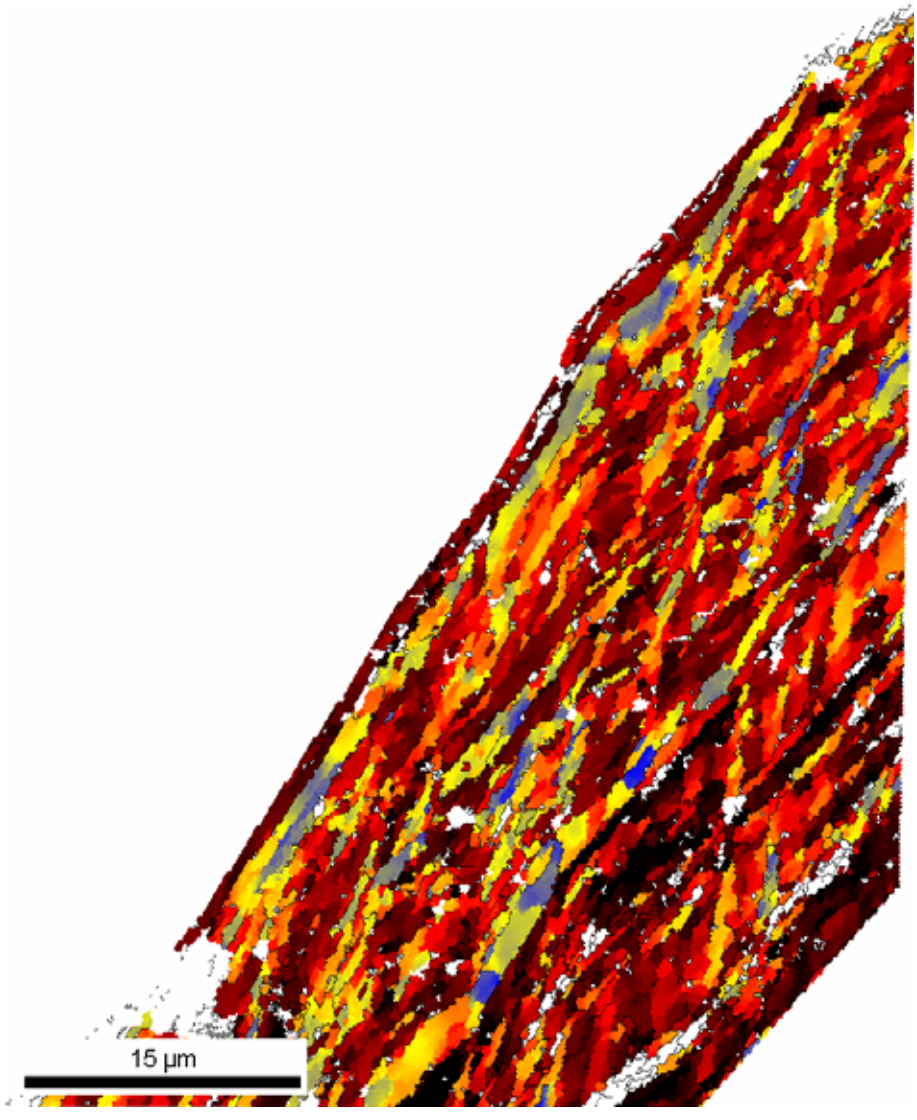

a)

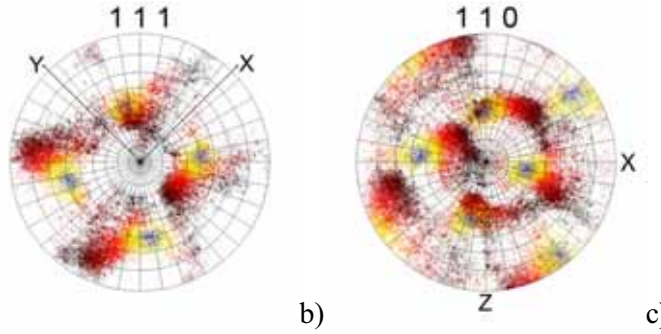

Figure 7.87: Severely subdivided grain by crossing deformation bands presented as a) highlighted orientations, b) and c) corresponding pole figures.

7.8 Deformation twins

In some highly deformed regions of special orientation, primarily crystal orientations where the <111> crystal axis is aligned parallel to the Z-axis, we can observe grains with a 60° rotation about a <111> crystal axis twin configuration. Areas containing twins are generally divided in a very fine lamellar deformation band structure. It is difficult to state whether these twin configurations have developed by a twinning mechanism or by gradual rotation towards the two equally stable orientations. The twined areas always have an ideal, textural stable, orientation. However, some of the twins are very small compared to the general grain size at the same strain. A twinned area is shown in Figure 7.88, where red boundaries correspond to Σ3 twin boundaries and green boundaries to other CSL configurations.

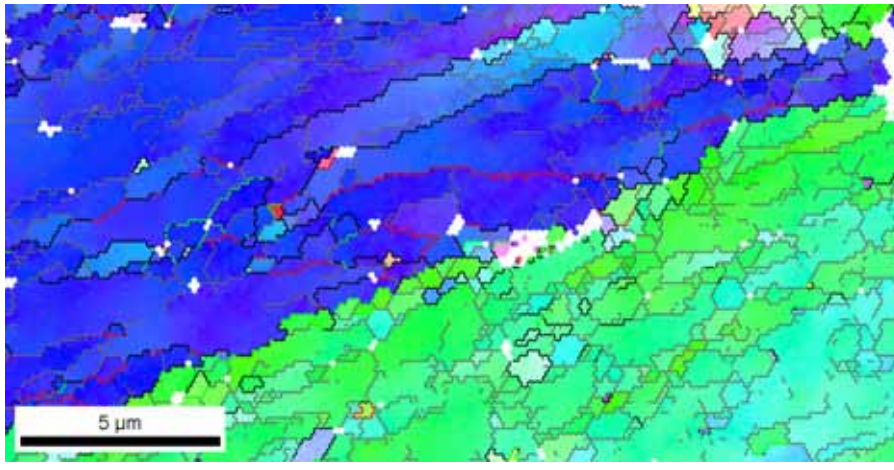

a)

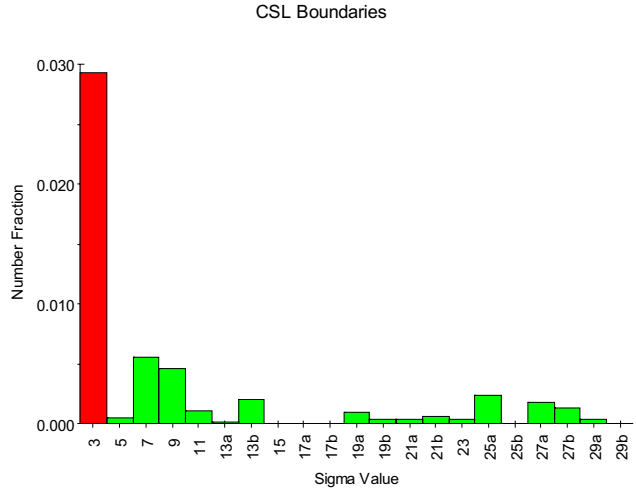

b)

Figure 7.88: a) Selected area containing twins and other CSL boundaries presented as IPF map with high angle boundaries as black lines, low angle boundaries as grey, CSL boundaries as green and twins as red. b) CSL boundary chart.

The different areas are highlighted and shown in Figure 7.89 along with the corresponding pole figures. A detail of a twin is shown in Figure 7.90 along with reconstructed EBSD patterns (Figure 7.91), simulated EBSD patterns (Figure 7.92) and (111) pole figures (Figure 7.93). Due to the high symmetry of twins, it is necessary to check the reconstructed EBSD patterns (recorded from the Hough peaks) for possible miss-indexing during

indexing. In ~50% of the twins recorded by the EBSD software, primarily the smallest ones from 1 to 3 points, miss-indexing is possible and one must assume that the software has miss-indexed the points. In this case however, the indexing is correct.

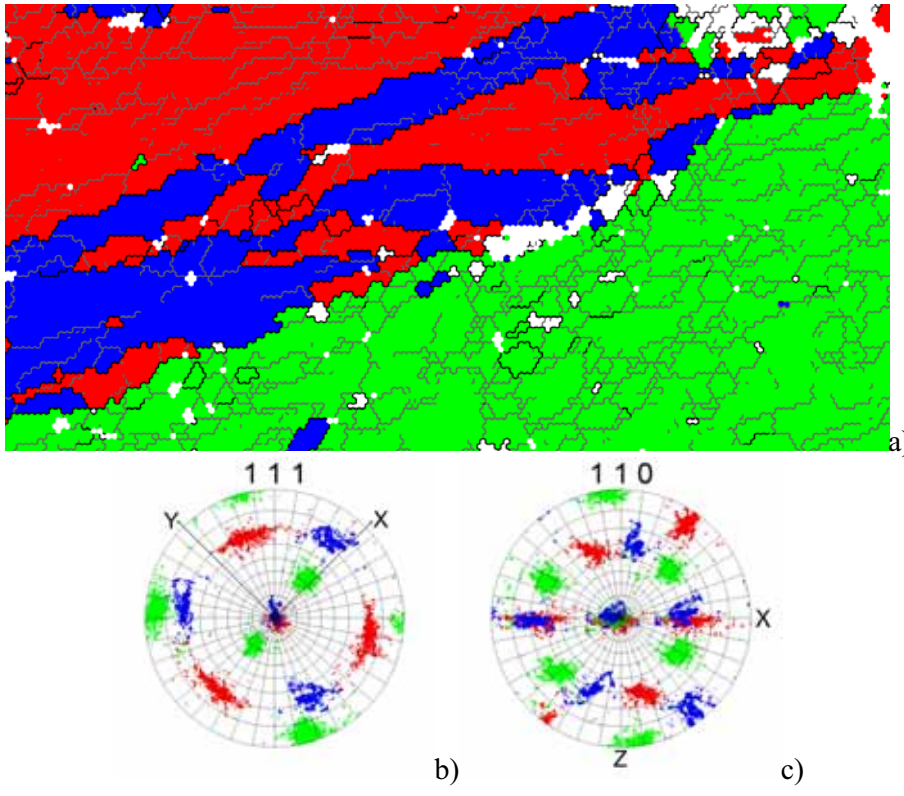

Figure 7.89: a) Highlighted orientations, b) pole figures. (Green (110)/270; blue (111)/115; red (111)/55)

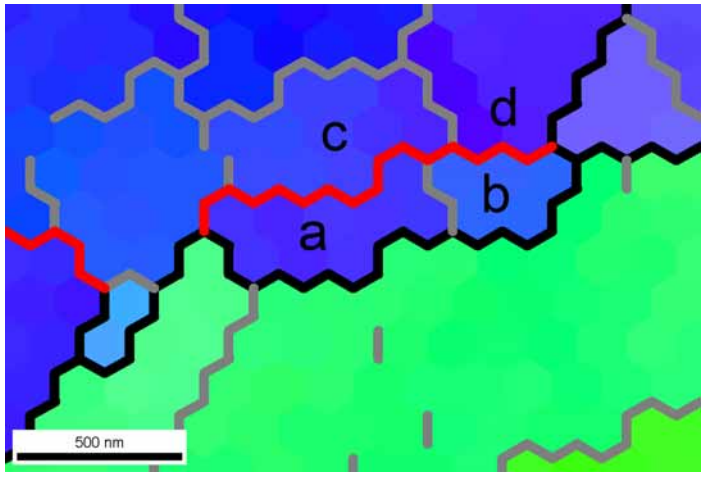

Figure 7.90: Deformation twin: Boundary *a-c*: 60° [111], Boundary *b-d*: 60° [111], Boundary *b-c*: 60° [111], Boundary *a-b*: 3,9° [100], Boundary *c-d*: 4,2° [243]

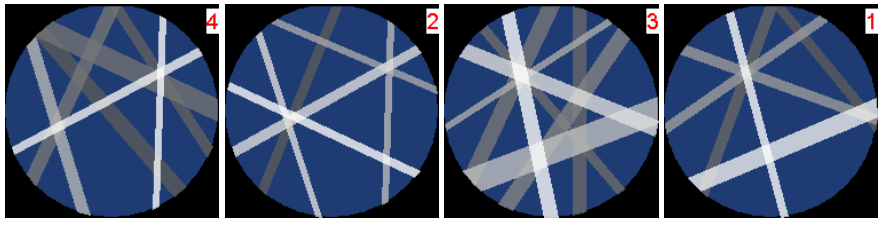

Figure 7.91: EBSD patterns for region a, b, c and d

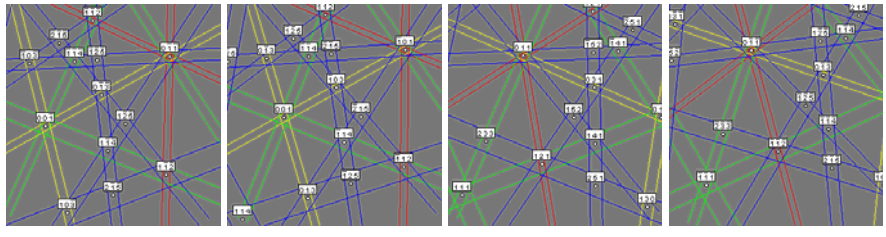

Figure 7.92: Simulated patterns for region a, b, c and d

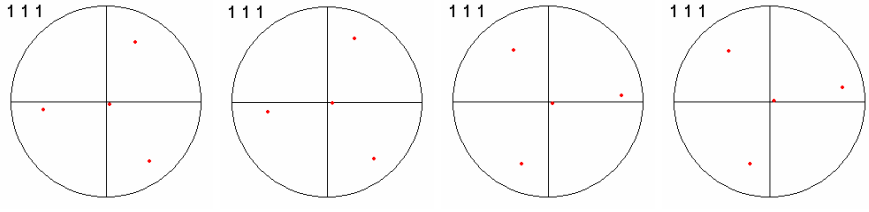

Figure 7.93: Pole figures for region a, b, c and d

7.9 Discussion

Numerous works have been published on the description of deformation structures in cold worked FCC metals, e.g. [93, 104-107]. These works are dealing with cold rolled pure aluminium and nickel. In ECAP the deformation structures are different, even though there are many similarities. In the following discussion, emphasis has been set on explaining the textural and microstructural evolution during the two first ECAP passes of route A. The author has chosen to use descriptions common for deformation structures found in ECAP. Therefore the microstructural evolution will not be compared or discussed against typical cold rolled deformation structures.

Further, much work has been reported in the literature aiming at describing the deformation structure in ECAP'ed materials at very high strains, i.e. at six or more passes. These works include dislocation density based modelling [157] and disclination based modelling [158-160] and articles describing deformation mechanisms in nanocrystalline aluminium, e.g. [161-163]. In the following discussion, the author focuses on the microstructural evolution in the early stages of grain subdivision and all reported results originate from experimental observations. Therefore, the discussion will not compare with the results obtained from microstructural modelling in the literature.

7.9.1 Texture evolution

Much work has been reported in the literature concerning the texture development in ECAP'ed materials, with the main emphasis on texture modelling. Maybe the most important experimental work is that of Tóth et al. [67] in identifying the stable texture components in ECAP'ed copper, processed by route A.

In the present work, the author has identified the presence of the same ideal texture components. The texture components can be identified as the ideal component for simple shear textures, rotated 45° around the Z-axis such that the shear plane in ECAP corresponds to the shear plane for torsion. Tóth et al. reported the presence of the $\mathbf{A_{1E}}$, $\mathbf{A_{2E}}$, ± $\mathbf{A_E}$, $\mathbf{C_E}$, and ± $\mathbf{B_E}$ components. In the present work three other components have been identified. These are referred to as $\mathbf{D_E}$, **Cube** and **Z-rotated Cube**. The $\mathbf{D_E}$ and **Cube** components are both part of the **(45, Φ, 45)** fibre, i.e. the two components fulfil the <110>||SD criteria discussed in section 7.4.2. A closer inspection of the experimental ODF sections presented in Figure 3 in [67] reveals the presence of the **Z-rotated Cube** component after one ECAP pass, but disappears at higher strains. It is also present, however with low intensity, in the simulations made by the discontinuous shear approach, while it is not present in the simulations made by the other approaches, e.g. self consistent modelling using the discontinuous shear model, flow line approach using the Taylor model or the flow line approach using the self consistent modelling [67].

The results in the present work clearly show the presence of both the Cube and the Z-rotated Cube components.

The intensities of the other texture components observed in the present work are comparable to the experimental values reported in [67], such as the drop in intensity for the $\pm\mathbf{A_E}$ and $\mathbf{C_E}$ components with increasing number of passes. In the present work, the $\pm\mathbf{B_E}$ component seems to increase continuously, whereas in [67] it is increasing in the second pass and decreases again in the third pass.

However, the work by Tóth et al. is made on OFHC copper, while the present work is made on a commercial 6xxx series aluminium alloy, thus one can not expect a perfect match between the observed textures, although they both are FCC atomic arrangements. Copper is known to possess lower

stacking fault energy and is therefore more prone to twinning, which may affect the texture development to some degree.

To the authors knowledge this is the only published work [67] which presents the intensities of the different texture components in such a way that the results are directly comparable. Most other important works on texture have presented the modelled and experimental textures in the form of pole figures making the results difficult to compare as several of the texture components overlap.

Furthermore, the presence of the $\mathbf{D_E}$ component in the ODF sections from EBSD measurements requires some attention. The $\mathbf{D_E}$ component is not clearly visible in the XRD measurements, but is found to be very strong in the two samples investigated by EBSD (from the first and second pass).

From the assumptions made in section 7.4.2, the ideal texture components would lie on the **(45, Φ, 45)** fibre or with a (111) plane in the shear plane, having the resulting Burgers vector in the shear direction. This assumption includes the $\mathbf{D_E}$ component; however, the intensity of this component cannot readily be explained. One possibility is that the occurrence of the $\mathbf{D_E}$ component is a direct result of the experimental technique involving pressing of split samples. This may lead to some material flow in the Z-direction between the two sub-specimens or to local deformations from friction effects, thus slightly altering the actual strain components in this area and therefore altering the texture. This will, in that case, also explain why the $\mathbf{D_E}$ component is not clearly defined in the XRD measurements, as the measured samples are cut from the mid section of regularly pressed samples.

Also, the textures developed in ECAP differ from those found in torsion as they exhibit a significant rotation about the Z-axis, e.g. the order of ~15° away from the X-direction (direction of the exit channel), commonly referred to as the “tilts” of the texture. Similar rotations about the Z-axis has

been reported in other publications [67, 164-167], and has previously been explained in terms of an idealized view of the deformation taking place during ECAP. In this idealized interpretation it is assumed that shear occurs approximately parallel to the plane of intersection of the two die channels, commonly referred to as the die's shear plane [164-166]. The reason behind the observed tilt was later explained by Prangnell et al. [70] as a direct effect of the actual deformation mode generated in ECAP. They state that the underlying reason for the tilts must be related to the presence of tension and compression components acting simultaneously with simple shear through the deformation zone. This was also supported by texture modelling using the Taylor model with the actual (measured) strain history through the deformation zone.

Based on the texture measurements presented in section 7.4.3 and 7.4.4 and the measured strain tensor components from Figure 7.7, the present author partially agrees on a few aspects of the observations made by Prangnell et al. [70]. In the present observations of texture development through the first pass, one observes a continuous rotation of the texture components, rotating ~15° in the positive direction (X towards Y). One also observes that this rotation coincides with the alignment of the cell structure. This means that the (SD, Φ, 45) texture fibre (where SD is the alignment of the <110> crystal direction in respect to the global XY-coordinate system) rotates the shear direction (SD) from 30° to 45° through the deformation zone, and the cell structure is parallel to the shear direction through the deformation zone. This again implies that the tilts can be explained by alignment of the (SD, Φ, 45) fibre to the *actual physical shear direction*. The latter which is observed to rotate as a result of the actual deformation mode, i.e. the combination of tension / compression and shears. Thus, the deformation mode is the reason behind the tilts, but the texture still aligns with the actual physical shear direction.

What happens in the second pass with respect to realignment of the textures is even more complex. Prangnell et al. [70] also stated clearly that the textures does not try to realign between each alternating pass as this would lead to a weakening of the texture every odd number of passes. This seems only partially true; the texture components do not realign to the same components, i.e. the $\mathbf{A_{1E}}$ component does not realign to $\mathbf{A_{1E}}$. However, in the present work, microstructural evidence is presented showing that some components realign into other stable texture components, as will be discussed in detail below. It is also clear from the measured ODF sections that some components get weaker due to this realignment while other components get stronger. This can not easily be seen by examining the pole intensities in regular pole figures, as many of the identified texture components overlap when presented as pole figures, which is unfortunately the most common way of presenting ECAP textures in the literature [70, 74, 78, 167].

7.9.2 Microstructural development

There seem to be several possible deformation and microstructure development mechanisms operating during the first ECAP pass of the present alloy. The mechanisms operating will depend on the initial microstructure and texture, hence dependent on the local crystal orientation of the grain (in which they operate) and the surrounding grain orientations.

In the present case the initial microstructure had a near random texture, large grains and no thermomechanical pre- processing.

Deformation by *crystallographic slip*, leading to the aligned cell structure, is observed to occur mainly in grains having an orientation within the stable texture components. For orientations $\mathbf{A_{2E}}$ and $\mathbf{A_{1E}}$, slip operates

ideally on one plane and in two equally active <110> directions and the cell structure tends to align in two directions. However, the other stable texture components deform ideally by slip on mainly one slip system or in only one direction, and therefore align only in one direction: the physical shear direction. The above statements are based on the crystalographic considerations presented in section 7.4.2 (described schematically in Figure 7.11 and Figure 7.12) and careful examination of the EBSD data presented in section 7.6 and 7.7. As a summary, crystalographic slip occurs on *one* slip system when the deforming crystal is oriented with a crystalographic *slip direction*, i.e. a <110> direction, in the principal (actual) shear direction. Crystalographic slip occurs on *two* slip systems when the deforming crystal is oriented with a *slip plane*, i.e. a (111) plane in the principal (actual) shear plane and having the resulting Burgers vector in the principal (actual) shear direction.

Deformation by crystalographic slip during the first pass results in a network of cells separated by low angle boundaries with cell orientations alternating about the average grain orientation. These rotations are observed to mainly take place around the Z-axis. This is believed to be a result of the plane strain deformation mode, whereby dislocations are travelling in the direction of shear which coincides with the a <110> crystal direction for crystals oriented within the (SD, Φ, 45) fibre.

Aligned cell structure is commonly reported in the literature and is commonly described as bands of subgrains elongated and aligned with the shearing direction. This structure was reported in pure aluminium after one pass ECAP in [5, 7, 155, 168, 169] and for Al-0.3%Mg in [170]. This structure is easiest revealed when the grain size is fairly large, typically larger than 10μm. The bands of subgrains and the cells within them are observed to have alternating orientations, and which corresponds to the observations reported by Prangnell and Bowen (2002) [170].

On a smaller length scale, incidental dislocation boundaries are formed within the cell blocks, as also described in [104].

Langdon and co-workers [155] suggested that this mechanism of substructure development in ECAP is generated by glissile dislocations generated on the primary slip planes (the direction of alignment) during pressing and these dislocations combine to create the subgrain / cell boundaries. This mechanism is supported by the present author.

On the larger size scale, deformation by *deformation banding* leads to grain subdivision and results in macroscopic shear deformation by crystal rotation in the deformation bands. The deformation bands are separated from the grain matrix by high angle boundaries. Further, **the deformation bands are observed to form by crystal rotation towards one of the stable texture components**. The rotation may be in both the positive and negative direction (positive rotation defined from X towards Y), dependent on the orientation of the grain in which they form and the macroscopic deformation occurring in the neighbouring grains, i.e. the local deformation mode may wary on the scale of a grain resulting in e.g. more tension / compression than what is found from the (average) measured strain tensor.

The presence of deformation bands was also reported in [155, 170, 171], however, no explanation of why these bands form or the special orientations were given, except for the work of Langdon and co-workers (2004) [155]. However, in the work of Langdon and co-workers on ECAP of an aluminium single crystal, the formation of deformation bands are observed in a crystal orientated within in the $\mathbf{A_{2E}}$ texture component. The new deformation bands are oriented closer to the $\pm\mathbf{B_E}$ component. This can be explained if one assumes the same rotation of the physical shear direction as in the present work. This means that the initial $\mathbf{A_{2E}}$ texture component is ideal for shear at 45° to the X-axis, however, the present observations reveal

that the physical shear direction starts at ~30° to the X-axis, meaning that the initial $\mathbf{A_{2E}}$ texture component is in fact unstable for shear by crystalographic slip. This results in deformation bands forming, having orientations closer to the the $\pm\mathbf{B_E}$ components, and the original crystal matrix now embedded between the deformation bands remains stable or rotate in the opposite direction towards the closest stable orientation.

These observations made on an aluminium single crystal in [155] give strong support for the observations made in the present work concerning both the texture development and deformation banding.

A detailed and general description of deformation bands formed in cold deformation described by the LEDS theory was reported by Kuhlmann-Wilsdorf [118]. This theory has been discussed in detail for orientation splitting in plane strain compression in fcc metals by Akef and Driver (1991) [119], Maurice and Driver (1992) [120], Basson and Driver (2000) [121], Paul, Driver and Jasienski (2002) [122] and Paul, Driver, Maurice and Jasienski (2003) [123]. The main findings are:

- Plane strain compression of (001)[010] and (001)[110] aluminium single crystals leads to the development of deformation bands by lattice rotations of opposite sign about the transverse axis [100]. The decomposition process is preceded by a stage of relatively homogeneous deformation up to a critical strain $\varepsilon_c \approx 0.2\text{-}0.3$.

This is in accordance of the present findings; the first signs of deformation banding are observed at a strain of ~0.25 and are shown in Figure 7.38.

- The decomposition process can in certain cases be related to the type of dislocation interactions; within a given band the number of active slip systems is reduced either to one or two which interact weakly.

This is supported by the present observation of deformation bands; the deformation bands form by rotation into one of the stable texture components which deform on one or two slip systems as discussed above.

In the present work, deformation banding is also observed to occur in grains already oriented within one of the stable texture components. In this case, the deformation bands tend to form low energy boundaries, CSL boundaries, to the parent grain, and the deformation bands form symmetric orientations. This has, to the present authors knowledge not previously been noted in the literature.

When a grain is subdivided by deformation bands, the original grain matrix separating the bands will also rotate, towards a symmetric but also stable orientation. The theory of deformation banding is treated in more detail in section 2.2.7. A summary of some of the observed subdivisions by deformation banding is presented in Table 7.4. Again, no such observations seem to be reported earlier in regard to ECAP. Examples of calculations on deformation bands by the theory presented in section 2.2.7 will be discussed further below.

Table 7.4: Observed subdivisions (from the present work) by deformation banding during the 1st pass. DB orientation=average orientation of the observed deformation bands, MOA is the deviation in orientation from the closest ideal texture component.

Grain orientation: $(\varphi_1,\Phi,\varphi_2)$	DB orientation: $(\varphi_1,\Phi,\varphi_2)$	Texture comp/MOA
(85,40,45)	(45,40,45) + (105,40,45)	$\mathbf{A_E}$ /5° + $\mathbf{-B_E}$ /15°
(135,103,45)	(105,103,45) + (155,103,45)	$\mathbf{A_{2E}}$ /14° + $\mathbf{A_{1E}}$ /20°
(45,90,45): $\mathbf{C_E}$	(45,90,45) + (85,90,45)	$\mathbf{C_E}$ /0° + Σ9 to $\mathbf{C_E}$
(45,0,0)	(100,90,45) + (170,90,45)	$\mathbf{A_{2E}}$ /0° + $\mathbf{A_{1E}}$ /0°
(70,90,45)	(45,90,45) + (100,90,45)	$\mathbf{C_E}$ /0° + $\mathbf{A_{2E}}$ /0°
(45,0,0)	(45,0,45)	**Cube**/0°
(160,35,45)	Stable	N.A.
(105,145,45)	(45,145,45)	$\mathbf{-A_E}$ /0°
(105,35,45)	(45,35,45)	$\mathbf{A_E}$ /0°
(20,11,124)	(96,88,73)	**Cube**/18°

The deformation bands tend to align in the direction of the first principal strain direction or close to the average grain elongation direction. However, the **Cube** oriented deformation bands are **always observed to align in the direction of principal shear**. To the present author's knowledge, this observation has not previously been reported in the literature. The reason for this special alignment is not yet fully understood.

Further, small elongated grains, separated from the matrix by high angle boundaries, typically ~20°, are observed to form inside original grains. These small grains are not small deformation bands or classical recrystallized grains, but are most probably formed by collapse of longer range orientation gradients present across the cell structure. They do not have any typical orientation relation to the parent grain in which they form. The formation of these grains occurs when orientation gradients build up as a result of stored dislocations in an ordered pattern. The misorientation, related to the average orientation of the parent grain, may build up by ~1-2° per micron over a range of up to 10-20μm. The orientation gradient builds up from two sides and results in a "peak", which collapses into a high angle

boundary when the orientation gradients reach a critical value of ~20°. By the formation of a new grain, the internal stresses from the lattice bending are released and the formation of a new grain will result in a lower energy state of the system and may thus be explained by the LEDS hypothesis.

Similar grain structures were observed by Prangnell and Bowen (2002) [170], however, no explanations of the origin of these grains were given.

Based on the observations, the present author believes that the texture evolution and the formation of new high angle boundaries during the first ECAP pass are mainly driven by deformation banding. High angle boundaries formed by the collapse of orientation gradients only counts for a very small amount of the new boundaries observed, and seem not to contribute to the formation of stable texture components.

The deformation mechanisms operating during the second ECAP pass, are in principal much the same as in the first pass, but operate at a smaller dimensional scale. There are however some important differences:

Deformation banding during the second pass operates on a much smaller scale than in the first pass and the new deformation bands which form are not “clean”, i.e. they may be obstructed by crossing structures and in general show a larger spread in orientation compared to deformation bands observed in the first pass.

The bands formed during the second pass can be separated in two groups; those formed on the cell structure from the first pass (formed in the same direction), see e.g. the bands noted DB2 in Figure 7.74, and those formed as new elements, crossing the cell structure formed in the first pass, see e.g. the blue-yellow bands in Figure 7.79.

However, it may be may be inaccurate to characterize the bands in Figure 7.74 as deformation bands, as they do not posses a stable orientation.

The bands formed on the cell structure typically have the same size scale as the cell structure, i.e. ~1-3μm in width and several microns in length, thus creating high angle boundaries along the direction of the "old" cell structure. Some bands still form by crystal rotation towards a stable texture component, while others seem to form by concentrated slip in narrow bands (aligned in the direction of the first principal strain) by rotation around a <111> crystal axis, leading to a typical "stair step" structure as seen in Figure 7.74 and Figure 7.77. This mechanism has to the present author's knowledge not previously reported.

The new deformation bands formed by crossing the cell structure are typically larger and act much the same way as the deformation bands formed during the first pass (see e.g. Figure 7.79).

A summary of some subdivisions by deformation banding observed during the second pass is presented in Table 7.5.

Table 7.5: Observed realignment of grains / deformation bands during the 2nd pass. DB1 is the deformation bands formed during the first pass, DB2 is the orientation of deformation bands formed during the second pass.

Grain orientation, 1st pass. (φ_1,Φ,φ_2): component	DB1 orientation, 1st pass. (φ_1,Φ,φ_2): component	Grain orientation, 2nd pass. (φ_1,Φ,φ_2): component	DB1 orientation 2nd pass. (φ_1,Φ,φ_2): component	DB2 orientation, 2nd pass. (φ_1,Φ,φ_2): component
(165,35,45)	(105,55,45): $\mathbf{-B_E}$	(75,35,45)	(15,55,45)	(45,55,45): $\mathbf{B_E}$
(115,35,45)	(45,35,45): $\mathbf{A_E}$	(25,35,45)	(315,35,45)	(45,35,45): $\mathbf{A_E}$
(45,90,45): $\mathbf{C_E}$	N.A.	(125,90,45)	N.A.	(105,90,45): $\mathbf{A_{2E}}$

One still observe crystalographic slip in the principal shear direction in grains oriented within the stable texture components. This again results in an aligned cell structure as seen during the first pass. The aligned cell structure formed during the second pass, however, is only observed at strains higher than 50% into the second pass, see e.g. Figure 7.86.

The last deformation mechanism observed during the second pass is twinning and formation of low energy CSL boundaries. Due to the relatively high stacking fault energy of aluminium, twinning is not expected to be a contributing mechanism. However, twin configurations are observed in the present work in the microstructure both as larger deformation bands rotated into a twin configuration, typically the $\mathbf{B_E}$ and $\mathbf{-B_E}$ component, and as small twins, with a typical size of ~0.15μm in width and 0.45μm in length. Twins may be much smaller than this, but this is the smallest scale in which the EBSD measurements were performed.

Twinning in aluminium at moderate strains, such as two ECAP passes has not previously been reported in the literature, however, twinning in pure aluminium during high pressure severe plastic deformation has been observed recently by Zuh et al. [161-163, 172]. This is considered to be an important mechanism when the grain size reaches the nano-scale at very high plastic strains.

The formation of CSL boundaries also seems to be a mechanism driven by lowering the energy of the system. Deformation bands have in the present work been observed to form in grains already in a stable orientation by rotation into a non-stable orientation. However, these deformation bands are observed to be CSL boundaries, typically a Σ9 configuration, see Figure 7.49 for further details. To the author's knowledge, no reports of the occurrence of CSL boundaries in aluminium at lower number of ECAP passes have been published in the open literature.

Interestingly, typical shear bands, crossing through numerous grains, are not observed in the investigated alloy. Shear banding has been reported by several authors in different metals, primarily copper alloys, after ECAP, [173-179] and in Al-Mg-Sc [180]. However, shear banding has been observed in a 5xxx series alloy containing 4 wt% Mg, currently under

investigation. This is in accordance with the assumption that magnesium promotes shear banding [125].

The grain refining effect obtainable by severe plastic deformation is the main driving force for research in this field. The ECAP process can be used to reduce the grain size in aluminium to the sub-micron scale, typically down to ~0.1μm and with a high fraction of high angle boundaries [8, 31, 35, 78, 164, 181-200].

In the present work, similar results on grain size have been reported. The grain size evolution is shown in Figure 6.13 and Figure 7.34. The reported grain size in the first figure (Figure 6.13) is based on calculations from EBSD measurements of the grain area defined as areas separated by a continuous boundary of 2° misorientation or more, normalized to the number fraction of grains. The second figure (Figure 7.34) is based on linear intercept values from selected EBSD maps through the deformation zone in the first and second pass. The two methods are not directly comparable, but the trends are very similar. Two different methods were used because the applied EBSD mapping techniques are different at low and high strains, making the linear intercept method inaccurate at higher strains and the area method inaccurate at lower strains.

The typical trend is a large reduction in the grain size during the first ECAP passes and a much slower reduction of grain size at higher strains. During the last passes, typically from N=6 to N=8, the grain size is more or less stable, while the fraction of high angle boundaries increases. This trend is commonly reported in the literature.

Examples of the microstructure after 8 passes by route A (pressed in the homogenized state) is shown as a TEM micrograph (bright field) and as EBSD inverse pole figure map in Figure 7.94 and Figure 7.95 respectively. The TEM micrograph is directly comparable to microstructures presented in

the literature on ECAP'ed aluminium to similar strain by route A, see e.g. [201].

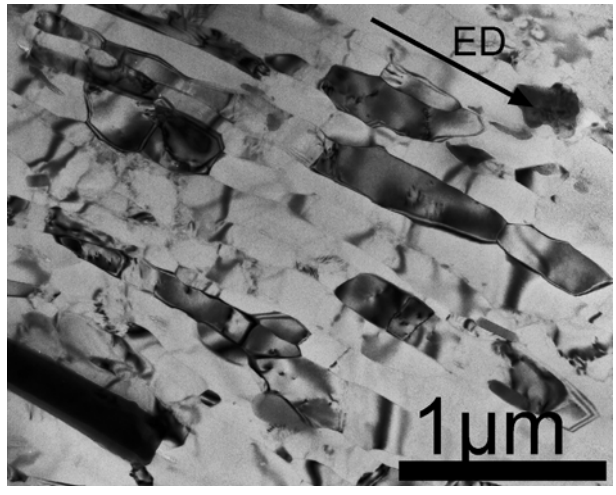

Figure 7.94: TEM micrograph of the grain structure in the XY-plane from the homogenized and ECAP'ed sample. 8 passes by route A.

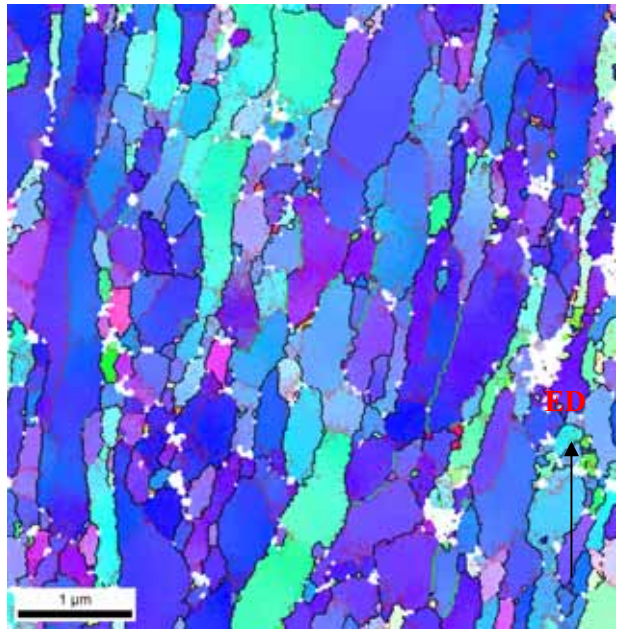

Figure 7.95: EBSD map of the grain structure in the XY-plane from the homogenized and ECAP'ed sample. 8 passes by route A. The colours are presented with the inverse pole figure coding (see Figure 7.33). Black and red lines represents high angle and low angle boundaries respectively. Green lines represent twin boundaries. White areas are non-indexed points.

By comparing the TEM micrograph and high resolution EBSD map, one can see that the two techniques reveals the same structure and may be compared directly (at the given magnification). Note that no clean-up routines were necessary on the EBSD map presented in Figure 7.95. Please also note the presence of twin boundaries (green lines in Figure 7.95) in the EBSD map.

7.9.3 Deformation banding in ECAP explained by the LEDS theory

To the present author's knowledge, no work has been reported in the literature attempting to describe the microstructural evolution and grain refinement in ECAP based on deformation banding and the LEDS theory.

Based on the theory of deformation banding presented in section 2.2.7, one may calculate from Equation 2.10 and Equation 2.18 the energies related to the formation of the observed deformation bands. The parameter δ_N may be calculated from the Taylor factors of the actual deformation band and the parent grain, based on the actual strain tensor and DB / grain orientation. In such a calculation, the Taylor factors can be based on the lowest number of slip systems needed to accommodate the actual strain. The shear stress is estimated from the yield stress at the time of DB formation, as $\sigma_{yDB} / \overline{M}$ where $\overline{M} \approx 3$ is the presumed average Taylor factor. The yield stress at the time of DB formation is estimated from tensile tests and the equivalent strain at the time of DB formation. Further, the F parameter can be estimated from the observed cell misorientation in the deformation bands and parameters presented in Figure 2.28. The redundancy factor M_r is taken as 2 from [118], except for the case of Σ- boundaries, which are low energy boundary configurations and thus the redundancy factor M_r may be as low

as 1, i.e. the boundary consists of only the geometrically necessary dislocations. The parameters used for calculations of some selected grains are given in Table 7.6 (L.S and R.S refers to the left and right hand side of Equation 2.10 respectively).

Table 7.6: Calculated (estimated) DB energies from selected grains. For definition of parameters please see section 2.2.7.

Figure	*W* [μm]	*L* [μm]	M_{grain}	M_{DB}	δ_N	τ_{DB} [MPa]	ζ	*F*	φ_{DB}	Γ_{DB}	M_r	*L.S* [kJm^{-3}]	*R.S* [kJm^{-3}]
7.38	17	180	3.38	2.01	0.408	~50	1.843	0.75	30°	0.411	2	37.8	30.8
7.47	2.5	45	2.81	2.4	0.146	~60	14.8	0.25	30°	0.054	2	19.4	29.3
7.49	2	40	3.52	2.38	0.32	~60	20.55	0.24	39°	0.068	1	43.2	39.5
7.53	6	200	3.52	2.31	0.34	~65	9.73	0.5	35°	0.27	2	53.7	50.4
7.55	6	180	3.03	2.45	0.19	~65	8.76	0.25	35°	0.137	2	29.9	28.1
7.66	3	120	3.62	2	0.447	~65	23.35	0.35	51°	0.19	2	70.0	67.9
7.66	5.5	140	3.62	2	0.447	~65	8.11	0.35	51°	0.192	2	70.0	41.0

The first deformation-bands appear at ~25% strain (Figure 7.38), and is the widest bands observed, with a width of ~17μm. This is in accordance with the observations from Driver and co-workers [119-123] as pointed out earlier in the discussion.

The thin vertical bands in Figure 7.47 do not fulfil the necessary condition for deformation banding by the LEDS theory, even if the *F* and M_r parameters are set at values well below reasonable values. These bands may therefore have been formed by some other mechanism, i.e. by plastic instability in shear bands at the grain size level.

The DB's in Figure 7.49 have different characteristics compared to the typical observed DB's. The DB's form in a grain already in a stable orientation ($\mathbf{C_E}$) by 38.9° rotation about a <110> axis, corresponding to a Σ9 boundary. The new DB orientation actually requires 5 slip systems; however, the Taylor factor is still lower than for the parent grain. The typical cell misorientation inside the band is ~8° resulting in lowering of the *F* factor to 0.24. The shear stress is here estimated to 60MPa. With these

parameters, Equation 2.10 is not fulfilled. However, as mentioned above, the DB boundary configuration is a Σ9 boundary which is a low energy boundary configuration and thus the redundancy factor M_r ~1. With these parameters, Equation 2.10 and the necessary conditions for deformation banding by the LEDS theory are again fulfilled.

The rest of the deformation bands listed in Table 7.6 fulfils Equation 2.10, but the ζ-parameter reaches too high values, indicating that the assumptions made regarding the accommodation energy may be inaccurate and that the accommodation energy is in fact lower than predicted by Equation 2.8.

By assuming equilibrium conditions in Equation 2.10 and introducing a parameter $K = W/L$, where W is the band width and L is the band length, the minimum band width may be expressed as a function of the shear stress at the time of DB formation and *K* as:

$$W = \frac{0.035 F M_r G^2 b}{\tau_{DB}^2 (\delta_N - K)}$$

Equation 7.2

where all parameters are defined in section 2.2.7.

In addition, one must remember that the upper limit of *W* is given by the grain size as $D_G K \geq W$ and $\delta_N > \approx 2K \geq 2\frac{W}{D_G}$.

The present dependence of *W* on *F* and M_r as a function of shear stress is shown in Figure 7.96 as iso-*K* and iso-*F* curves. As can be seen, the effect of the *K*-parameter is very small and the curves seem to converge to the same value at a shear stress of ~150MPa. The effect of the *F*-parameter is very significant, indicating that higher cell misorientations are likely to promote smaller deformation bands.

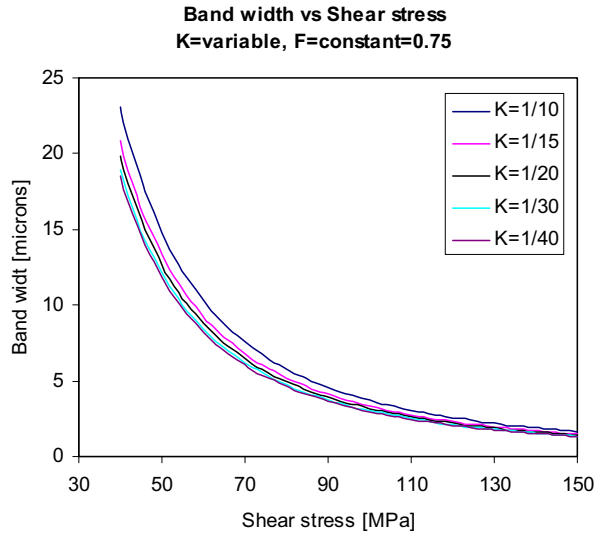

a)

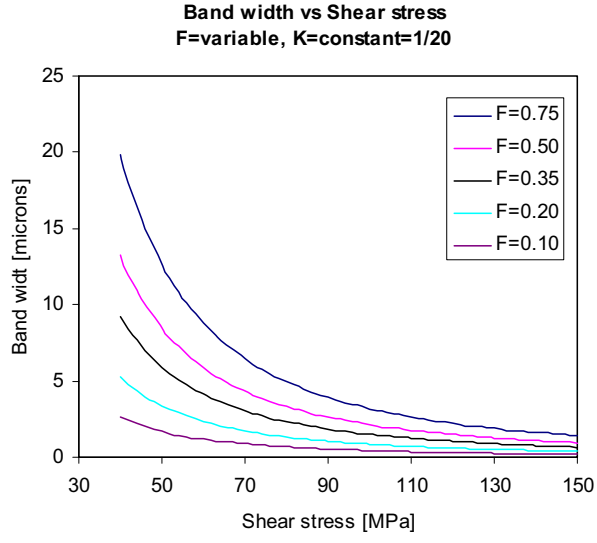

b)

Figure 7.96: Estimated (calculated according to the LEDS-theory) band width as a function of shear stress at equilibrium for δ_N=0.4, M_r=2 and a) F=0.75 and K=variable and b) K=1/20 and F=variable. The curves give lower bound values of the band width.

It becomes clear from Equation 7.2 and Figure 7.96 that the most important factor regarding the DB size is the shear stress which is proportional to $1/\tau^2$, i.e. when the material strength increases due to grain refinement and work hardening, smaller deformation bands may form. The cell misorientation also increases with strain and thus the F parameter decreases. It is also clear that by reducing M_r by creation of Σ-boundaries, deformation banding may still be a deformation mechanism at very high strains when the grain size has reached sub-micron sizes, i.e. one can expect to observe an increasing number of twin configurations and CSL boundaries at very high strains (from 2 to 8 ECAP passes). This is supported by the microstructural observations made on samples pressed 8 time by route A, and can be seen in the relatively large number of twin boundaries in Figure 7.95.

However, one gets trouble with reasonable parameters regarding the accommodation energies, i.e. the parameter ζ becomes unreasonably high for small DB's. The reason for this may be the assumptions made regarding the accommodation energy; when a DB terminates in a grain boundary, U_a may be close to zero, also, the DB's terminating in the grain matrix tends to have a highly reduced width in the end regions, thus lowering the effective band width used in the calculations of U_a in Equation 2.8.

The size of the smallest deformation bands that may form with reasonable parameters according to the LEDS-theory is given in Figure 7.97 with K=1/20, F=0.2, δ_N=0.5 and M_r=2.

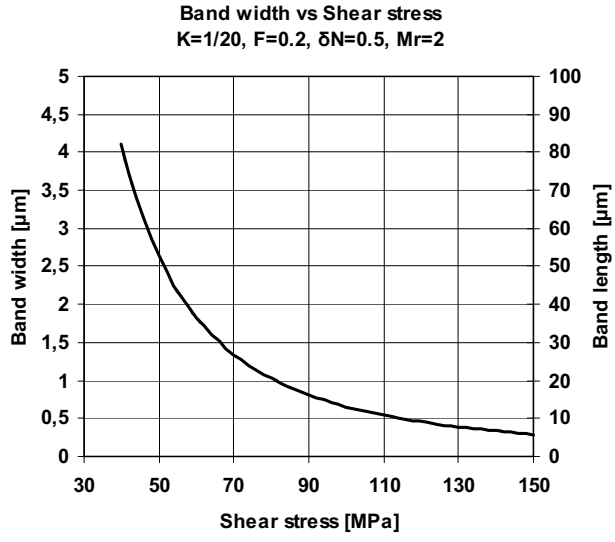

Figure 7.97: Smallest deformation bands which may form within reasonable parameters as a function of the shear stress at the time of DB formation. K=1/20, F=0.2, δ_N=0.5, Mr=2.

The estimated values of the minimum band width from Figure 7.97 shows a very good agreement with the observed (high angle) grain size presented in Figure 7.34, and (high angle) grain sizes measured up to a strain of ~6. This supports the idea of deformation banding as the main source of high angle grain boundary formation in the early stages of ECAP processing.

One may pose a few important questions regarding deformation banding as a grain refinement mechanism in ECAP processing.

- Is it possible to form a new DB inside an old DB assuming the shear strength increases? The answer to this is assumed to be yes, it may be possible to form a new BD inside an old DB if, and only if Equation 2.10 is fulfilled. This may be the case when a sample is rotated -90° when reinserted in the ECAP die, thereby rotating the texture components with respect to the global coordinate system, resulting in a change of the local Taylor factors.

- Can deformation bands form on the already developed aligned cell structure, going from the first to the second pass? The answer to this seems to be yes. The *F*-parameter decreases when the cell misorientation increases. The typical cell misorientation developed during the first pass is ~5-10°, thereby reducing the *F*-factor, allowing for smaller deformation bands to form. This is probably the most important factor regarding DB formation in the second pass and at even higher strains.
- Accommodation energy: how small can it be? Equation 2.8 is based on the elastic strain energy assuming the DB terminates in the grain matrix and creates an elastic strain field in the end zones. However, most of the observed DB's terminate at grain boundaries, where the strain field may easily be minimized. The DB's terminating in the grain matrix tends to have a greatly reduced width in the end zones so as to minimize the strain field, thus the accommodation energy is likely to be lower than predicted by Equation 2.8.
- What is a reasonable value for the redundancy parameter? A reasonable value is M_r=2, but low energy CSL configurations such as twin boundaries may have a value closer to Mr~1, thus reducing the minimum band width by a factor 2. This is supported by the observations in Figure 7.49. The number of twin boundaries and other CSL configurations are observed to increase with accumulated strain (and increased shear stress). Thus, lowering the redundancy factor may promote the formation of CSL boundaries at higher strains where DB formation otherwise would be impossible.
- At what size can we expect the grains to stabilize, according to LEDS and DB formation? From Figure 7.97 at τ~130MPa (shear stress after 8 passes) the minimum band width is ~0.4μm. However, we se no trace of DB formation at the corresponding strain, i.e. after

8 passes, but the DB size may stabilize at ~0.8 to ~0.6μm in width (somewhere between the fourth and sixth ECAP pass) and become more elongated in the last ECAP passes, hereby reducing the band width from geometrical considerations, and become divided in the length direction by low to medium angle boundaries from excess dislocations generated during the last ECAP passes.

From the above considerations, it is likely that the microstructure, generated as a result of severe plastic deformation by ECAP, can be described by the LEDS hypothesis [118] and is in fact an equilibrium structure:

”*Among all microstructures that are in equilibrium with the applied stresses and are in principal accessible to dislocations, those are formed which minimize the energy of the system composed of the deforming material and the applied tractions”.*

7.10 Conclusions

The typical ECAP texture starts to develop already at ~25% strain and increases in intensity during the first pass. The strongest texture components in the first pass are given as $\mathbf{A_{1E}}$, $\mathbf{C_E}$, $\pm\mathbf{A_E}$, $\mathbf{D_E}$, $\pm\mathbf{B_E}$ and $\mathbf{A_{2E}}$ in decreasing order. In the second pass, $\mathbf{A_{1E}}$ and $\pm\mathbf{B_E}$ increase in intensity while all other components decrease. This is believed to be a result of realignment of the different texture components to the closest stable component in the second pass. At higher strains, up to 8 passes, the $\pm\mathbf{B_E}$ component continuous to increase in intensity while all other components, including $\mathbf{A_{1E}}$ decrease in intensity. The $\pm\mathbf{B_E}$ component is stable in route A, which is believed to be a result of the special alignment of the component in regard to the shear zone; the $\pm\mathbf{B_E}$ component has three slip directions aligned in the XY-plane and may therefore easily rotate about the Z-direction.

The microstructural development during the first pass is dominated by deformation banding leading to grain-subdivision. The average linear intercept distance is reduced from ~80μm to ~4μm for high angle boundaries and from ~10μm to ~0.7μm for low angle boundaries. During the second pass, the linear intercept distance is further reduced to ~1.8μm for high angle and ~0.3μm for low angle boundaries.

Deformation twins are observed during the second pass and are believed to play an important role in severe plastic deformation when the grains reach the sub-micron or nano-scale.

The deformation banding have bee explained in terms of the LEDS theory, and has been shown to be an important mechanism in the early stages of grain subdivision, and is further believed to be the main source of high angle grain boundary formation by grain subdivision down to a grain size of approximately ~0.6μm, when other deformation mechanisms, such as twinning, may be energetically more favourable.

8 GENERAL CONCLUSION

Strain measurements were made on partially pressed (ECAP'ed) samples by analysis of deformed grids applied onto the surface of split samples. For the first time, quasi-3D strains are observed, and the assumption of plane-strain in ECAP has been verified. Further, the shear strain angle engendered during the ECAP process was measured.

Some typical features of ECAP have been corroborated, i.e. friction and material temper affect the strain distribution, the strain homogeneity and the work-piece corner angle, friction being the most significant here. Also, new conclusions have been drawn. The analysis of material element deformation histories along path lines reveals that ECAP can be interpreted as the combination of shearing and stretching (i.e. tension and/or compression). Furthermore, the final shear strain angle obtained in ECAP appears to be friction and material temper independent in the zone of homogeneous deformation.

The mechanical properties of ECAP'ed billets have been investigated. The commercial AA6082 Al-Mg-Si alloy has been processed successfully by ECAP at room temperature to strains $\varepsilon=6$ to $\varepsilon=8$. The alloy has been processed in the solutionized, T4, homogenized and soft annealed states. The highest tensile strength was obtained from the solutionized material, followed by T4, homogenized and soft annealed. This behaviour is linked to the solid solution content prior to ECAP and the potential for dynamic precipitation during ECAP processing.

The tensile elongation to failure drops to a constant level between 4% and 9% after ECAP and is highest for the soft annealed and lowest for the solutionized material. The ductility in the solutionized material can,

however, recover to ~18% elongation to failure by low temperature heat treatment with only a small drop in tensile strength.

Soft annealed and ECAP'ed material has been compared to cold rolling to similar strains. The tensile strength response to accumulated strain is similar, but the ductility and post uniform deformation is different. However, the ECAP'ed material can be processed to higher strains and, thus, achieving higher strength.

The tensile yield strength behaviour of the homogenized and ECAP'ed material can be described by a simple relation to the grain size and the fraction high and low angle boundaries.

The texture development throughout the deformation zone in the first and second pass of route A was investigated and the ideal texture components were corroborated. The typical ECAP texture starts to develop already at ~25% strain (ε_{eff}=0.25 into the first pass) and increases in intensity during the first pass. The strongest texture components in the first pass are given as $\mathbf{A_{1E}}$, $\mathbf{C_E}$, $\pm\mathbf{A_E}$, $\mathbf{D_E}$, $\pm\mathbf{B_E}$ and $\mathbf{A_{2E}}$ in decreasing order. In the second pass, $\mathbf{A_{1E}}$ and $\pm\mathbf{B_E}$ increase in intensity while all other components are observed to decrease. This is believed to be a result of realignment of the different texture components to the closest stable component in the second pass. At higher strains, up to 8 passes, the $\pm\mathbf{B_E}$ component continuous to increase in intensity while all other components, including $\mathbf{A_{1E}}$ decrease in intensity.

The microstructural development during the first pass is dominated by deformation banding leading to grain-subdivision. The average linear intercept distance is reduced from ~80μm to ~4μm for high angle boundaries and from ~10μm to ~0.7μm for low angle boundaries. During the second pass, the linear intercept distance is further reduced to ~1.8μm for high angle and ~0.3μm for low angle boundaries.

Deformation twins are observed during the second pass and are believed to play an important role in severe plastic deformation when the grains reach the sub-micron or nano-metre scale.

The deformation banding can be explained in terms of the LEDS theory, and has been shown to be an important mechanism in the early stages of grain subdivision, and is further believed to be the main source of high angle grain boundary formation by grain subdivision down to a grain size of approximately ~0.6μm, when other deformation mechanisms may be energetically more favourable.

9 REFERENCES

[1] Segal V.M.: Patent of the USSR, No 575892, (1977),

[2] Nadai A., *Theory of Flow and Fracture*. Mc-Graw-Hill.New York: (1950)

[3] Segal V.M., Reznikov V.I., Drobyshevskiy A.E., Kopylov V.I.: Russian Metallurgy(engl Transl), (1981), **1**, pp. 115.

[4] Segal V.M.: Materials Science and Engineering A, (1995), **197**, pp. 157-164.

[5] Iwahashi Y., Horita Z., Nemoto M., Langdon T.G.: Acta Materialia, (1998), **46**, pp. 3317-3331.

[6] Langdon T.G., Furukawa M., Iwahashi Y., Horita Z., Nemoto M.: Materials Science and Engineering A, (1998), **257**, pp. 328-332.

[7] Iwahashi Y., Horita Z., Nemoto M., Langdon T.G.: Acta Materialia, (1997), **45**, pp. 4733-4741.

[8] Ferrasse S., Hartwig T., Goforth R.E., Segal V.M.: Metallurgical and Materials Transactions A, (1997), **28A**, pp. 1047-1057.

[9] Semiatin S.L., Delo D.P., Shell E.B.: Acta Materialia, (2000), **48**, pp. 1841-1851.

[10] Prangnell P.B., Harris C., Roberts S.M.: Scripta Materialia, (1997), **37**, pp. 983-989.

[11] Kim H.S., Seo M.H., Hong S.I.: Materials Science and Engineering A, (2000), **291**, pp. 86-90.

[12] Kim H.S.: Materials Science and Engineering A, (2001), **315**, pp. 122-128.

[13] Srinivasan R.: Scripta Materialia, (2001), **44**, pp. 91-96.

[14] Wang J., Iwahashi Y., Horita Z., Furukawa M., Nemoto M., Valiv R.Z., Langdon T.G.: Acta Materialia, (1996), **44**, pp. 2973-2982.

[15] Wang J., Horita Z., Furukawa M., Valiev R.Z., Ma Y., Langdon T.G.: Journal of Materials Research, (1993), **8**, pp. 2810.

[16] Wang J., Horita Z., Furukawa M., Nemoto M., Valiev R.Z., Langdon T.G.: Materials Science and Engineering, (1996), **A216**, pp. 41.

[17] Furukawa M., Horita Z., Nemoto M., Valiev R.Z., Langdon T.G.: Acta Materialia, (1996), **44**, pp. 4619-4629.

[18] Berbon P., Furukawa M., Horita Z., Nemoto M., Tsenev N.K., Valiev R.Z., Langdon T.G.: Materials Science Forum, vol 217-222, no 2, (1996), pp. 1013-1018.

[19] Hansen N., Horsewell A., Leffers T., Lilholt H.: 2nd Riso International Symposium on Metallurgy and Materials Science, (1981), pp. 137.

[20] Barlow C.Y.J., Bay B., Hansen N.: Philos Mag A, (1985), **51**, pp. 253-275.
[21] Bay B., Hansen N., in: Hansen N., Juul Jensen D., Leffers T., Ralph B. (Eds), *Annealing Processes*, Risø National Laboratory, Roskilde, Denmark, (1986), pp. 215.
[22] Kang H.G., Bachelard L., Kim H.W., Kang S.B.: Journal of the Korean Institute of Metals and Materials (South Korea), (2001), **39**, pp. 553-559.
[23] Demura Y., Kitagawa K., Kawazoe M.: Journal of Japan Institute of Light Metals, (2001), **51**, pp. 324-328.
[24] Mukai T., Kawazoe M., Higashi K.: Materials Science and Engineering A, (1998), **247**, pp. 270-274.
[25] Chinh N.Q., Illy J., Kovacs Z., Horita Z., Langdon T.G.: Materials Science Forum, (2002), **396-402**, pp. 1007-1012.
[26] Morris D.G., Munoz-Morris M.A.: Acta Materialia, (2002), **50**, pp. 4047-4060.
[27] Morris D.G., Munoz-Morris M.A., Garcia Oca C.: Scripta Materialia, (2003), **48**, pp. 213-218.
[28] Dupuy L., Blandin J.J., Rauch E.F.: Materials Science and Technology (UK), vol 16, no 11-12, (2000), pp. 1256-1258.
[29] Vevecka A., Cavaliere P., Cabbibo M., Evangelista E., Langdon T.G.: Journal of Materials Science Letters, (2001), **20**, pp. 1601-1603.
[30] Kawazoe M., Shibara T., Higashi K.: Materials Science Forum (Switzerland), vol 233-234, (1997), pp. 207-214.
[31] Chang S.-Y., Lee J.G., Park K.-T., Shin D.H.: Materials Transactions, (2001), **42**, pp. 1074-1080.
[32] Tsai T.L., Sun P.L., Kao P.W., Chang C.P.: Materials Science and Engineering A, (2003), **342**, pp. 144-151.
[33] Wang Z.C., Prangnell P.B.: Materials Science and Engineering A, (2002), **328**, pp. 87-97.
[34] Furukawa M., Horita Z., Nemoto M., Langdon T.G.: Materials Science and Technology (UK), vol 16, no 11-12, (2000), pp. 1330-1333.
[35] Horita Z., Fujinami T., Nemoto M., Langdon T.G.: Metallurgical and Materials Transactions A, (2000), **31A**, pp. 691-701.
[36] Park K.-T., Hwang D.-Y., Chang S.-Y., Shin D.H.: Metallurgical and Materials Transactions A, (2002), **33A**, pp. 2859-2867.
[37] Xu C., Lee S., Langdon T.G.: Trans Tech Publications, Materials Science Forum (Switzerland), vol 357-359, (2001), pp. 521-526.
[38] Kim J.K., Jeong H.G., Hong S.I., Kim Y.S., Kim W.J.: Scripta Materialia, (2001), **45**, pp. 901-907.

[39] Kim W.J., Kim J.K., Park T.Y., Hong S.I., Kim D.I., Kim Y.S., Lee J.D.: Metallurgical and Materials Transactions A, (2002), **33A**, pp. 3155-3164.
[40] Ferrasse S., Segal V.M., Hartwig T., Goforth R.E.: Journal of Materials Research, (1997), **12**, pp. 1253-1261.
[41] Chang J.-Y., Shan A.: Materials Science and Engineering A, (2003), **347**, pp. 165-170.
[42] Kim W.J., Chung C.S., Ma D.S., Hong S.I., Kim H.K.: Scripta Materialia, (2003), **49**, pp. 333-338.
[43] Cabibbo M., Di Sabatino M., Evangelista E., Latini V.: Metallurgia Italiana, (2003), **95**, pp. 25-30.
[44] Kim B.-K., Szpunar J.A., Alexandra B., Takayama Y.: Materials Science Forum, (2002), **408-412**, pp. 1513-1518.
[45] Wang J., Xu C., Zhang Z., Zhao X., Wang J., Langdon T.G.: Minerals, Metals and Materials Society/AIME, Ultrafine Grained Materials II, (2002), pp. 429-438.
[46] Xu C., Furukawa M., Horita Z., Langdon T.G.: Acta Materialia, (2003), **51**, pp. 6139-6149.
[47] Fan W., Chaturvedi M.C., Goel N.C., Richards N.L.: Materials Science Forum (Switzerland), vol 243-245, (1997), pp. 563-568.
[48] Salem H.G., Lyons J.S.: Journal of Materials Engineering and Performance, (2002), **11**, pp. 384-391.
[49] Musin F., Kaibyshev R., Motohashi Y., Sakuma T., Itoh G.: Materials Transactions A, (2002), **43**, pp. 2370-2377.
[50] Mukai T., Nieh T.G., Watanabe H., Higashi K.: Materials Science Forum (Switzerland), vol 304-306, (1999), pp. 109-114.
[51] Horita Z., Lee S., Ota S., Neishi K., Langdon T.G.: Trans Tech Publications, Materials Science Forum (Switzerland), vol 357-359, (2001), pp. 471-476.
[52] Ota S., Akamatsu H., Neishi K., Furukawa M., Horita Z., Langdon T.G.: Materials Transactions, (2002), **43**, pp. 2364-2369.
[53] Komura S., Furukawa M., Horita Z., Nemoto M., Langdon T.G.: Materials Science and Engineering A, (2001), **297**, pp. 111-118.
[54] Mohamed F.A., Ahmed M.M.I., Langdon T.G.: Metall Trans A, (1977), **8A**, pp. 933-938.
[55] Valiev R.Z., Salimonenko U.S.A.T.U., Tsenev N.K., Berbon P.B., Langdon T.G.: Scripta Materialia, (1997), **37**, pp. 1945-1950.
[56] Komura S., Berbon P.B., Furukawa M., Horita Z., Nemoto M., Langdon T.G.: Scripta Materialia, (1998), **38**, pp. 1851-1856.
[57] Berbon P.B., Furukawa M., Horita Z., Nemoto M., Tesnev N.K., Valiev R.Z., Langdon T.G.: Phil Mag Lett, (1998), **78**, pp. 313.

[58] Berbon P.B., Langdon T.G., Tsenev N.K., Valiev R.Z., Furukawa M., Horita Z., Nemoto M.: Metallurgical and Materials Transactions A (USA), vol 29A, no 9, (1998), pp. 2237-2243.
[59] Berbon P.B., Komura S., Utsunomiya A., Horita Z., Furukawa M., Nemoto M., Langdon T.G.: Materials Transactions, JIM, (1999), **40**, pp. 772-778.
[60] Langdon T.G., Lee S., Berbon P.B., Furukawa M., Horita Z., Nemoto M., Tsenev N.K., Valiev R.Z.: Materials Science and Engineering A, (1999), **272**, pp. 63-72.
[61] Langdon T.G., Neishi K., Uchida T., Yamauchi A., Nakamura K., Horita Z.: Materials Science and Engineering A, (2001), **307**, pp. 23-28.
[62] Matsuki K., Aida T., Takeuchi T., Kusui J., Yokoe K.: Acta Materialia, (2000), **48**, pp. 2625-2632.
[63] Langdon T.G., Horita Z., Furukawa M., Nemoto M., Barnes A.J.: Acta Materialia, (2000), **48**, pp. 3633-3640.
[64] Langdon T.G., Furukawa M., Horita Z., Nemoto M.: JOM Journal of Metals, (1998), **50(6)**, pp. 41-45.
[65] Langdon T.G., Nakashima K., Horita Z., Nemoto M.: Acta Materialia, (1998), **46**, pp. 1589-1599.
[66] Oh-Ishi K., Horita Z., Nemoto M., Furukawa M., Langdon T.G.: Metallurgical and Materials Transactions A, (1998), **29A**, pp. 2011-2013.
[67] Toth L.S., Massion R.A., Germain L., Baik S.C., Suwas S.: Acta Materialia, (2004), **52**, pp. 1885-1898.
[68] Agnew S.R., in: Szpunar J.A. (Ed), *Proceedings of the ICOTOM12, the 12th International Conference on Textures of Materials*, Montreal, (1999), pp. 575.
[69] Baik S.C., Estrin Y., Hellmig H.G., Kim H.S.: Materials Science and Engineering A, (2003), **351**, pp. 86.
[70] Gholinia A., Bate P., Prangnell P.B.: Acta Materialia, (2002), **50**, pp. 2121-2136.
[71] Beyerlein I.J., Lebensohn R.A., Tome C.N.: Ultrafine Grained Materials II, (2002), pp. 585-594.
[72] Ferrasse S., Segal V.M., Alford F.: Materials Science and Engineering A, (2004), **372**, pp. 235-244.
[73] Apps P.J., Heason C.P., Prangnell P.B.: Materials Science Forum, (2004), **447-448**, pp. 423-428.
[74] Ferrasse S., Segal V.M., Kalidindi S.R., Alford F.: Materials Science and Engineering A, (2004), **368**, pp. 28-40.
[75] Beyerlein I.J., Li S., Alexander D.J., Necker C.T., Tome C.N., Bourke M.A.: Ultrafine Grained Materials III, (2003), pp. 185-192.

[76] Estrin Y., Hellmig R.J., Baik S.C., Kim H.S., Brokmeier H.G., Zi A.: Ultrafine Grained Materials III, (2003), pp. 247-253.
[77] Suwas S., Toth L.S., Fundenberger J.J., Eberhardt A., Skrotzki W.: Scripta Materialia, (2002) **47**, pp. 1203-1208.
[78] Cao W.Q., Godfrey A., Liu Q.: Materials Science and Engineering A, (2003), **361**, pp. 9-14.
[79] Suh J.Y., Han J.H., Oh K.H., Lee J.C.: Scripta Materialia, (2003), **49**, pp. 185-190.
[80] Toth L.S.: Advanced Engineering Materials, (2003), **5(5)**, pp. 308-316.
[81] Alexandrov I.V., Dubravina A.A., Kilmametov A.R., Kazykhanov V.U., Valiev R.Z.: Metals and materials, (2003), **9(2)**, pp. 151-156.
[82] Kusnierz J.: Materials Science Forum, (2002) **426-432**, pp. 2807-2812.
[83] Miyamoto H., Erb U., Koyama T., Mimaki T., Vmogradov A., Hashimoto S.: Materials Science Forum, (2002) **426-432**, pp. 2795-2800.
[84] Baeck S.M., Seok H.K., Lee J.C., Kim D.L., Lee H.C., Oh K.H.: Materials Science Forum, (2002), **408-412**, pp. 685-690.
[85] Skrotzki W., Tamm R., Klemm R., Thiele E., Holste C., Baum H.: Materials Science Forum, (2002), **408-412**, pp. 667-672.
[86] Chakkingal U., Thomson P.P.: Journal of Materials Processing Technology, (2001), **117**, pp. 169-177.
[87] Pithan C., Hashimoto T., Kawazoe M., Nagahora J., Higashi K.: Materials Science and Engineering A, (2000), **280**, pp. 62-68.
[88] Li S., Beyerlein I.J., Necker C.T., Alexander D.J., Bourke M.: Acta Materialia, (2004), **52**, pp. 4859-4875.
[89] Anonymous. Aluminun Association Inc.Washington D.C.: (1986)
[90] Dieter G.E., *Mechanical Metallurgy*. Mc Graw-Hill.London: (1988)
[91] Humphreys F.J., Hatherly M., *Recrystallization and related annealingphenomena*. Pergamon.Oxford: (1996)
[92] Maurice C.L., Driver J.H.: Acta Materialia, (1997), **45**, pp. 4627-4638.
[93] Hansen N.: Mater Sci Technol, (1990), **6**, pp. 1039.
[94] Hughes D.A., Hansen N.: Acta Materialia, (1997), **45**, pp. 3871-3886.
[95] Kulhman-Wilsdorf D., Hansen N.: Scripta Metallurgica et Materialia, (1991), **25**, pp. 1557.
[96] Gil Sevillano J., van Houtte P., Aernoudt E.: Prog Mat Sci, (1980), **25**, pp. 69.
[97] Forbord B., *Dr.ing. thesis*. NTNU.Trondheim: (1999)
[98] Furu T., Ørsund R., Nes E.: Acta Metallurgica et Materialia, (1995), **43**, pp. 2209.

[99] Furu T., Ørsund R., Nes E.: Materials Science and Engineering A, (1996), **214**, pp. 122.
[100] Nes E., Dons A.L., Ryum N., in: Gifkins R.C. (Ed), *Proc. ICSMA 6*, Pergamon press, Oxford, (1982),
[101] Schuh F., von Heimendahl M.: ZMetallk, (1974), **65**, pp. 346.
[102] Sæter J.A., *Dr.ing. thesis*. NTNU.Trondheim: (1997)
[103] Ryen Ø., *Work hardening and mechanical anisotropy of aluminium sheets and profiles*. NTNU.Trondheim: (2003)
[104] Bay B., Hansen N., Hughes D.A., Kuhlmann-Wilsdorf D.: Acta Metallurgica et Materialia, (1992), **40**, pp. 205.
[105] Bay B., Hansen N., Kuhlmann-Wilsdorf D.: Materials Science and Engineering A, (1992), **158**, pp. 139.
[106] Liu Q., Jensen D.J., Hansen N.: Acta Materialia, (1998), **46**, pp. 5819-5838.
[107] Hughes D.A., Hansen N.: Acta Materialia, (2000), **48**, pp. 2985.
[108] Hughes D.A.: Acta Metallurgica et Materialia, (1993), **41**, pp. 1421.
[109] Korbel O.A., Embury J.D., Hatherly M., Martin P.L., Erbsloh H.W.: Acta Metallurgica, (1986), **34**, pp. 1999-2009.
[110] Ashby M.F., in: Kelly A., Nicholson R.B. (Eds), *Strengthening Methods in Crystals*, Elsevier, Amsterdam, (1971), pp. 136.
[111] Nord-Vardhaug K., Forbord B.: Materials Science Forum, (2000), **331-337**, pp. 551-556.
[112] Langford G., Cohen M.: ASM TRANS QUART, (1969), **62**, pp. 623-638.
[113] Chen N.K., Mathewson C.H.: JMetals, (1951), **3**, pp. 653.
[114] Honeycombe R.W.K.: J Inst Metals, (1951), **50**, pp. 45-49.
[115] Higashida K., Takamura J., Narita N.: Materials Science and Engineering A, (1986), **81**, pp. 239.
[116] Sawkill J., Honeycombe R.W.K.: Acta Metallurgica, (1954), **2**, pp. 854.
[117] Søreng A., *Localized deformation and mechanical anisotropy in aluminium and AlZnMg alloys, PhD thesis*. NTNU.Trondheim: (1997)
[118] Kuhlmann-Wilsdorf D.: Acta Materialia, (1999), **47**, pp. 1697-1712.
[119] Akef A., Driver J.H.: Materials Science and Engineering A, (1991), **A132**, pp. 245-255.
[120] Maurice C.L., Driver J.H.: Acta Metallurgia et Materialia, (1653), **41**, pp. 1653-1664.
[121] Driver J.H., Basson F.: Acta Materialia, (2001), **48**, pp. 2101-2115.
[122] Paul H., Driver J.H., Jasienski Z.: Acta Materialia, (2002), **50**, pp. 815-830.
[123] Paul H., Driver J.H., Maurice C., Jasienski Z.: Materials Science and Engineering A, (2003), **359**, pp. 178-191.

[124] Dillamore I.L., Roberts J.G., Busch A.C.: Met Sci, (1979), **13**, pp. 73-77.
[125] Inagaki H., Kohara S.: ZMetallk, (1997), **88**, pp. 570-.
[126] Inagaki H., Koizumi M., Chang C.S.T., Duggan B.J.: Materials Science Forum, (2002), **396-402**, pp. 587-592.
[127] Harren S.V., Déve H.E., Asaro R.J.: Acta Metallurgica, (1988), **35**, pp. 2435.
[128] Lloyd D.J., in: Sachdev A.K., Embury J.D. (Eds), *Formability and metallurgical structure*, The Metallurgical Society, Inc., (1986), pp. 193.
[129] Ranganathan S.: Acta Crystallographica, (1966), **21**, pp. 197-199.
[130] Schmid E.: Proc IntConf Appl Mech, Delft, (1924), pp. 342.
[131] Sachs G.: Z Verein Deut Ing, (1928), **72**, pp. 734.
[132] Leffers T.: Scripta Metallurgica, (1968), **2**, pp. 447-452.
[133] Taylor G.I.: J Inst Mater, (1938), **62**, pp. 307.
[134] Raabe D., *Computational Materials Science*. Wiley-CH.Weinheim: (1998)
[135] Van Houtte P.: Textures and Microstructures, (1988), **8-9**, pp. 313.
[136] Aida T., Matsuki K., Horita Z., Langdon T.G.: Scripta Materialia, (2001), **44**, pp. 575-579.
[137] Iwahashi Y., Wang J., Horita Z., Nemoto M., Langdon T.G.: Scripta Materialia, (1996), **35**, pp. 143-146.
[138] Segal V.M.: Materials Science and Engineering A, (1999), **271**, pp. 322-333.
[139] Segal V.M.: Materials Science and Engineering A, (2003), **345**, pp. 36-46.
[140] Stoica G.M., Liaw P.K.: JOM Journal of Metals, (2001), **53(3)**, pp. 36-40.
[141] Bowen J.R., Gholinia A., Roberts S.M., Prangnell P.B.: Materials Science and Engineering A, (2000), **278**, pp. 78-99.
[142] Kim H.S.: Materials Transactions, (2001), **42**, pp. 536-538.
[143] Kim H.S., Seo M.H., Hong S.I.: Journal of Materials Processing Technology (Netherlands), vol 130, (2002), pp. 497-503.
[144] Oh S.J., Kang S.B.: Materials Science and Engineering A, (2003), **343**, pp. 107-115.
[145] Suh J.-Y., Kim H.-S., Park J.-W., Chang J.-Y.: Scripta Materialia, (2001), **44**, pp. 677-681.
[146] Shan A., Moon I.G., Ko H.S., Park JW.: Scripta Materialia, (1999), **41**, pp. 353-357.
[147] Camsys Inc., *ASAME 4.1 Reference Manual*. Hitchcock-Manthey LLC.New-York: (2000)
[148] Martin J.W., *Micro mechanisms in particle hardened alloys*. Cambridge University press. Cambridge: (1980)

[149] Christian J.W., *The theory of transformations in metals and alloys, Part 1 (second edition)*. Pergamon. Oxford: (1975)
[150] Löffler H., *Structure and structure development of Al-Zn alloys*. Akademie Verlag GmbH. Berlin: (1995)
[151] Cahn J.W.: Acta Metallurgica, (1957), **5**, pp. 169-172.
[152] Cahn J.W.: Acta Metallurgica, (1956), **4**, pp. 449-459.
[153] Yamakov V., Wolf D., Phillpot S.R., Mukherjee A.K., Gleiter H.: Philosophical Magazine Letters, (2003), **83**, pp. 385-393.
[154] Nes E., Marthinsen K., Holmedal B.: Materials science and technology, (2004),
[155] Langdon T.G., Fukada Y., Oh-ishi K., Furukawa M., Horita Z.: Acta Materialia, (2004), **52**, pp. 1387-1395.
[156] Roven H.J., Dumoulin S., Werenskiold J.C., in: Zhu Y.T., Langdon T.G., Valiev R.Z., Semiatin S.L., Shin D.H., Lowe T.C. (Eds), *Ultrafine Grained Materials III*, TMS, The Minerals, Metals & Materials Society, (2004), pp. 117-124.
[157] Baik S.C., Estrin Y., Kim H.S., Hellmig R.J.: Materials Science and Engineering A, (2003), **351**, pp. 86-97.
[158] Seefeldt M., Delannay L., Peeters B., Kalidinidi S.R., Van Houtte P.: Materials Science and Engineering A, (2001), **319-321**, pp. 192-196.
[159] Romanov A.E.: Advanced Engineering Materials, (2003), **5(5)**, pp. 301-307.
[160] Romanov A.E., Orlova T.S., Enikeev N.A., Nazarov A.A., Alexandrov I.V., Valiev R.Z., in: Zhu Y.T., Langdon T.G., Valiev R.Z., Semiatin S.L., Shin D.H., Lowe T.C. (Eds), *Ultrafine grained materials III*, TMS, . (2004), pp. 211-216.
[161] Zhu Y.T., He D.W., Liao X.Z., Zhou F., Lavernia E.J.: Applied physics letters, (2003), **83**, pp. 5062-5064.
[162] Zhu Y.T., Liao X.Z., Srinivasan S.G., Zhao Y.H., Baskes M.I., Zhou F., Lavernia E.J., Xu H.F.: Applied physics letters, (2004), **84**, pp. 3564-3566.
[163] Zhu Y.T., Srinivasan S.G., Baskes M.I., He D.W., Liao X.Z., Zhou F., Lavernia E.J.: Applied physics letters, (2003), **83**, pp. 632-634.
[164] Dupuy L., PhD thesis. *Comportement mécanique d'un alliage d'aluminium hyper-déformé*. INPG.Grenoble: (2000) pp. 96.
[165] Kao P.W., Huang W.H., Chang L., Chang C.P.: Materials Science and Engineering A, (2001), **307**, pp. 113-118.
[166] Agnew S.R., Kocks U.F., Hartwig K.T., Weertman J.R.: Riso National Laboratory, Modelling of Structure and Mechanics of Materials from Microscale to Product, (1998), pp. 201-206.
[167] Beyerlein I.J., Lebensohn R.A., Tome C.N.: Materials Science and Engineering A, (2003), **345**, pp. 122-138.

[168] Terhune S.D., Swisher D.L., Oh-Ishi K., Horita Z., Langdon T.G., MCNelley T.R.: Metallurgical and Materials Transactions A, (2002), **33A**, pp. 2173-2184.
[169] MCNelley T.R., Swisher D.L., Horita Z., Langdon T.G.: Minerals, Metals and Materials Society/AIME, Ultrafine Grained Materials II, (2002), pp. 15-24.
[170] Prangnell P.B., Bowen J.R.: Minerals, Metals and Materials Society/AIME, Ultrafine Grained Materials II, (2002), pp. 89-98.
[171] Apps P.J., Bowen J.R., Prangnell P.B., in: Zehetbauer M., Valiev R.Z. (Eds), *Nanomaterials by severe plastic deformation*, wiley-vch, Weinheim, (2002), pp. 138-144.
[172] Zhu Y.T., Liao X.Z., Zhao Y.H., Srinivasan S.G., Valiev R.Z., Gunderov D.V.: Applied physics letters, (2004), **84**, pp. 592-594.
[173] Wang J.T., Kang S.B., Kim H.W.: Ultrafine Grained Materials III, (2003), pp. 351-356.
[174] Kusnierz J., Bogucka J.: Archives of Metallurgy, (2003), **48**, pp. 173-182.
[175] Bieler T.R., Glavicic M.G., Semiatin S.L.: JOM Journal of Metals, (2002), **54(1)**, pp. 31-36.
[176] Semiatin S.L., DeLo D.P.: Materials and Design, (2000), **21**, pp. 311-322.
[177] Frey N.D., Fagin P.N., Semiatin S.L.: JJ Jonas Symposium on Thermomechanical Processing of Steel as held at the 39th Annual Conference of Metallurgists of CIM, (2000), pp. 541-556.
[178] Wu S., Li Q., Jiang C., Li G., Wang Z.: Acta Metallurgica Sinica, (2000), **36**, pp. 602-607.
[179] Wu S., Wang Z., Li G., Alexandrov I.V., Valiev R.Z.: Acta Metallurgica Sinica, (1999), **35**, pp. 960-963.
[180] Vinogradov A., Washikita A., Kitagawa K., Kopylov V.I.: Materials Science and Engineering A, (2003), **349**, pp. 318-326.
[181] Berbon P.B., Furukawa M., Horita Z., Nemoto M., Langdon T.G.: Metallurgical and Materials Transactions A, (1999), **30A**, pp. 1989-1997.
[182] Berbon P.B., Furukawa M., Horita Z., Nemoto M., Tsenev N.K., Valiev R.Z., Langdon T.G.: Minerals, Metals and Materials Society/AIME, Hot Deformation of Aluminum Alloys II, (1998), pp. 111-124.
[183] Brodova I.G., Bashlykov D.V., Manukhin A.B., Stolyarov V.V., Soshnikova E.P.: Scripta Materialia (USA), vol 44, no 8-9, (2001), pp. 1761-1764.
[184] Chang J.-Y., Yoon J.-S., Kim G.-H.: Scripta Materialia, (2001), **45**, pp. 347-354.

[185] Furukawa M., Berbon P.B., Horita Z., Nemoto M., Tsenev N.K., Valiev R.Z., Langdon T.G.: Materials Science Forum (Switzerland), vol 233-234, (1997), pp. 177-184.
[186] Furukawa M., Horita Z., Nemoto M., Langdon T.G.: Minerals, Metals and Materials Society/AIME, (1998), pp. 165-172.
[187] Horita Z., Fujinami T., Langdon T.G.: Materials Science and Engineering A, (2001), **318**, pp. 34-41.
[188] Horita Z., Fujinami T., Nemoto M., Langdon T.G.: Japan Institute of Light Metals, Aluminium Alloys: Their Physical and Mechanical Properties, (1998), pp. 449-454.
[189] Horita Z., Fujinami T., Sato K., Kang S.B., Kim H.W., Langdon T.G.: ASM International, Advances in the Metallurgy of Aluminum Alloys, (2001), pp. 271-275.
[190] Horita Z., Furukawa M., Nemoto M., Langdon T.G.: Materials Research Society, Superplasticity--Current Status and Future Potential, (2000), pp. 311-322.
[191] Horita Z., Furukawa M., Nemoto M., Tsenev N.K., Valiev R.Z., Berbon P.B., Langdon T.G.: Materials Science Forum (Switzerland), vol 243-245, (1997), pp. 239-244.
[192] Iwahashi Y., Furukawa M., Horita Z., Nemoto M., Langdon T.G.: Metallurgical and Materials Transactions A (USA), vol 29A, no 9, (1998), pp. 2245-2252.
[193] Langdon T.G., Furukawa M., Nemoto M., Horita Z.: Trans Tech Publications, Materials Science Forum (Switzerland), vol 357-359, (2001), pp. 489-498.
[194] Segal V.M.: Minerals, Metals and Materials Society/AIME, Ultrafine Grained Materials II, (2002), pp. 533-538.
[195] Valiev R.Z.: Kluwer Academic Publishers Group, (1993), pp. 303-308.
[196] Valiev R.Z.: Japan Institute of Metals, (1994), pp. 881-884.
[197] Valiev R.Z.: Minerals, Metals and Materials Society/AIME, Synthesis and Processing of Nanocrystalline Powder, (1996), pp. 153-161.
[198] Valiev R.Z., Alexandrov I.V., Zhu Y.T., Lowe T.C.: Journal of Materials Research, (2002), **17**, pp. 5-8.
[199] Valiev R.Z., Islamgaliev R.K., Kuzmina N.F., Li Y., Langdon T.G.: Scripta Materialia, (1998), **40**, pp. 117-122.
[200] Valiev R.Z., Korznikov A.V., Mulyukov R.R.: Mater Sci Eng A,, (1993), **A168**, pp. 141-148.
[201] Furukawa M., Horita Z., Langdon T.G.: Minerals, Metals and Materials Society/AIME, Ultrafine Grained Materials II, (2002), pp. 459-468.